Multilaser Conformer-Selective Spectroscopy of Cold Biomolecular Ions in the Gas Phase

THÈSE N⁰ 8012 (2017)

PRÉSENTÉE LE 27 OCTOBRE 2017
À LA FACULTÉ DES SCIENCES DE BASE
LABORATOIRE DE CHIMIE PHYSIQUE MOLÉCULAIRE
PROGRAMME DOCTORAL EN CHIMIE ET GÉNIE CHIMIQUE

ÉCOLE POLYTECHNIQUE FÉDÉRALE DE LAUSANNE

POUR L'OBTENTION DU GRADE DE DOCTEUR ÈS SCIENCES

PAR

Aleksandr PEREVERZEV

acceptée sur proposition du jury:

Dr A.-S. Chauvin, présidente du jury
Dr O. Boyarkine, directeur de thèse
Prof. G. Niedner-Schatteburg, rapporteur
Prof. J. Oomens, rapporteur
Dr D. Ortiz, rapporteur

ÉCOLE POLYTECHNIQUE
FÉDÉRALE DE LAUSANNE

Suisse
2017

To my most loving and patient family:
Anna, Susana, Zlata, and Nika

Abstract

Proteins and even small peptides play crucial role in almost any biological process involved in transformation of living matter. Biological activity and functionality of these building blocks of life are determined not only by their primary structure (i.e., amino acid sequence), but also by their three-dimensional orientation: secondary, tertiary, and quaternary structural motifs. This structure-function relationship is one of the most important paradigms in structural biology and makes characterization of the geometry of biological molecules an extremely important task. In contrast to experimental techniques in condensed phase, Cold Ion Spectroscopy studies biomolecular ions that are isolated in the gas phase and provides vibrational fingerprints specific for each conformer. This allows for a direct comparison of experimental data with high-level calculations. The method, widely known as "double-resonance" spectroscopy, has several fundamental and practical limitations – it is applicable in practice only to small peptides (shorter then 10 - 15 amino acids) that contain at least one aromatic amino acid and have vibrationally resolved electronic spectrum.

The main goal of this thesis is the development and demonstration of a novel conformer-selective spectroscopic technique – IR-IR-(D)UV hole-burning spectroscopy. This multilaser experiment has an important advantage over the double-resonance approach, because it does not depend on the shape or resolution of the electronic spectrum of peptide, and allows extending the application of Cold Ion Spectroscopy to peptides with any amino acid composition.

The first part of this work describes the application of this novel technique for recording conformer-selective vibrational spectra of the protonated aromatic amino acids tryptophan and histidine, for which the double-resonance cold ion spectroscopy is precluded because of their unstructured electronic spectra resulting from lifetime broadening. Combined with high-level

anharmonic calculations, conformer specific vibrational spectra allowed for solving structures of gas-phase conformers of these biomolecular ions.

The second part describes the use of peptide bond as an alternative natural chromophore, present in any peptide. Electronic gas-phase spectra of protonated peptides without aromatic residues as well as the influence of an IR pre-excitation are explored in details. The use of peptide bonds as a UV absorbers allows recording high-quality linear vibrational spectra of peptides without aromatic amino acids, for which only IRMPD and tagging spectroscopies were available until recently. This feature makes IR-IR-DUV hole-burning spectroscopy the most universal conformer-selective spectroscopic tool.

The third part of this thesis is dedicated to the relationship of gas-phase and native structures of biomolecular ions. The lack of solvent in the gas-phase mimics, to some extent, hydrophobic media of cell membranes or receptors where intramolecular hydrogen bonds, rather than interaction with solvent, largely determine the structure of peptides. In such cases, general structural motifs can survive the transfer to the gas phase. Experimental data and theoretical calculations for stereoisomers of an opioid peptide drug leucine enkephalin and an intrinsically disordered peptide neurokinin A are the first steps towards testing this hypothesis.

Finally, the presence of more than one conformer at cryogenic temperatures for almost all peptides suggests that collisional cooling is a fast, non-adiabatic process. In the last part the efficiency of the energy transfer during the collisional cooling of ions in a buffer gas is explored.

Key words: cold ion spectroscopy, electronic spectroscopy, vibrational spectroscopy, IR-IR-UV hole-burning, gas-phase, conformers, tryptophan, histidine, peptide bond, hydrophobic peptides, receptors, vacuum hydrophobicity, leucine enkephalin, neurokinin A, intrinsically disordered peptide, collisional cooling efficiency, gramicidin S, Monte-Carlo simulations, non-adiabatic cooling.

Zusammenfassung

Proteine und auch kleine Peptide spielen wichtige Rollen in beinahe jedem biologischen Umwandlungsprozess in lebenden Organismen. Die biologische Aktivität und Funktionalität dieser Bausteine des Lebens beruhen nicht nur auf ihrer Primärstruktur (die Aminosäurensequenz), sondern auch auf ihrer dreidimensionalen Form – den sekundären, tertiären und quaternären Strukturmotiven. Diese Beziehung zwischen Struktur und Funktion ist einer der wichtigsten Grundsätze der Strukturbiologie. Aufgrund dessen ist die Charakterisierung der Geometrie von biologischen Molekülen eine äusserst wichtige Aufgabe. Im Gegensatz zu experimentellen Methoden in Lösung befasst sich die Spektroskopie kalter Ionen mit isolierten biomolekularen Ionen in der Gasphase und liefert Vibrationsfingerabdrücke, die für jedes Konformer spezifisch sind. Dies ermöglicht den direkten Vergleich mit anspruchsvollen Strukturberechnungen. Die Methode, die als „Doppelresonanzspektroskopie" bekannt ist, weist mehrere grundlegende und praktische Einschränkungen auf und lässt sich in der Praxis nur auf Peptide anwenden, die kürzer als 10-15 Aminosäuren sind. Ausserdem müssen diese Sequenzen zumindest eine aromatische Aminosäure enthalten und ein vibrationsaufgelöstes elektronisches Spektrum aufweisen.

Das vorrangige Ziel dieser Arbeit ist die Entwicklung und Anwendung einer neuartigen konformerselektiven spektroskopischen Technik, IR-IR-(D)UV „hole-burning" Spektroskopie. Dieses multi-Laser Experiment weist einen bedeutenden Vorteil gegenüber der Doppelresonanztechnik auf: Es hängt nicht von Form oder Auflösung des elektronischen Spektrums des Peptids ab und ermöglicht, die Spektroskopie kalter Ionen auf Peptide mit beliebiger Aminosäurensequenz anzuwenden.

Der erste Teil dieser Arbeit beschreibt die Anwendung dieser neuartigen Technik auf die Aufnahme von konformerselektiven Vibrationsspektren der protonierten aromatischen

Aminosäuren Tryptophan und Histidin. Bei diesen Spezies kann Doppelresonanzspektroskopie kalter Ionen aufgrund der unstrukturierten elektronischen Spektren – eine Folge der Lebensdauerverbreiterung – nicht angewandt werden. In Kombination mit anspruchsvollen anharmonischen Strukturberechnungen konnten anhand konformerspezifischer Schwingungsspektren die Strukturen von Konformeren dieser Biomolekülionen in der Gasphase aufgeklärt werden.

Der zweite Teil beschreibt die Nutzung der Peptidbindung als alternatives Chromophor, das in jedem Peptid vorhanden ist. Die elektronischen Spektren von Peptidbindungen in kalten protonierten Peptiden in der Gasphase und der Einfluss von IR Voranregung werden im Detail untersucht. Die Benutzung der Peptidbindung gestattet das Aufnehmen von hochqualitativen linearen Schwingungsspektren von Peptiden, die keine aromatischen Aminosäuren enthalten. Für diese Substanzen standen bis vor kurzer Zeit nur IRMPD und „tagging"-Spektroskopie zur Verfügung. Diese Eigenschaft macht IR-IR-DUV „hole-burning" Spektroskopie zur universellsten konformerspezifischen spektroskopischen Methode.

Der dritte Teil dieser Arbeit widmet sich der Beziehung zwischen den Strukturen biomolekularer Ionen in der Gasphase und im nativen Zustand. Die Abwesenheit eines Lösungsmittels in der Gasphase ähnelt in gewisser Weise den hydrophoben Umgebungen von Zellmembranen oder Rezeptoren. Dort wird die Struktur hauptsächlich durch intramolekulare Wasserstoffbrücken und nicht durch Wechselwirkung mit dem Lösungsmittel bestimmt. In diesen Fällen können allgemeine Strukturmotive den Übergang in die Gasphase unbeschadet überstehen. Experimentelle Daten und theoretische Berechnungen an einem Stereoisomer des Opioidpeptid-Arzneistoffes Leucin Enkephalin sowie dem intrinsisch ungeordneten Peptid Neurokinin A stellen die ersten Schritte in Richtung der Überprüfung dieser Hypothese dar.

Im abschliessenden Teil untersuchen wir die Effizienz der Energieübertragung während der Kühlung von Ionen durch Stösse in einem Puffergas. Die Anwesenheit mehrerer Konformere bei kryogenischen Temperaturen, die bei beinahe allen Peptiden beobachtet werden kann, weist darauf hin, dass Stosskühlung ein schneller, nichtadiabatischer Prozess ist.

Schlüsselwörter: Spektroskopie kalter Ionen, Elektronenspektroskopie, Vibrationsspektroskopie, IR-IR-UV „hole-burning", Gasphase, Konformere, Tryptophan, Histidin, Peptidbindung, hydrophobe Peptide, Rezeptoren, Hydrophobe Eigenschaften des Vakuums, Leucin Enkephalin, Neurokinin A, intrinsisch ungeordnete Peptide, Effizienz der Stosskühlung, Gramicidin S, Monte-Carlo-Simulationen, nichtadiabatisches Kühlen.

Résumé

Les protéines et même les petits peptides jouent un rôle crucial dans presque tous les processus biologiques impliqués dans la transformation de la matière vivante. L'activité biologique et la fonctionnalité de ces éléments constitutifs de la vie sont déterminées non seulement par leur structure primaire (c'est-à-dire, par la séquence d'acides aminés), mais aussi par leur orientation tridimensionnelle: motifs structuraux secondaires, tertiaires et quaternaires. Cette relation structure-fonction est l'un des paradigmes les plus importants de la biologie structurale et rend la caractérisation de la géométrie des molécules biologiques une tâche extrêmement importante. Contrairement aux techniques expérimentales en phase condensée, la spectroscopie à l'ion froid étudie les ions biomoléculaires isolés dans la phase gazeuse et fournit des empreintes vibrationnel spécifiques à chaque conformant, ce qui permet une comparaison directe avec des calculs de haut niveau. La méthode, largement connue sous le nom de spectroscopie à double résonance, a plusieurs limitations fondamentales et pratiques – en pratique, elle ne s'applique que pour les peptides plus petits que 10 à 15 acides aminés, contenant nécessairement au moins un des acides aminés aromatiques et ayant un spectre électronique résolu par vibration.

L'objectif principal de cette thèse est le développement et la démonstration d'une technique de spectroscopie sélective de conformant, IR-IR- (D)UV spectroscopie de combustion des trous. Cette expérience multi-laser présente un avantage important par rapport à l'approche à double résonance car elle ne dépend pas de la forme ou de la résolution du spectre électronique du peptide et permet d'étendre l'application de la spectroscopie à l'ion froid aux peptides avec toute composition d'acides aminés.

La première partie de ce travail décrit l'application de cette nouvelle technique pour l'enregistrement des spectres vibrationnels sélectifs aux conformèrs d'acides aminés aromatiques protonés, le tryptophane et l'histidine, pour lesquels la spectroscopie à ions froid à double résonance était exclue en raison de leur spectre électronique non structuré résultant de l'élargissement à vie. Combinés avec des calculs anharmoniques de haut niveau, les spectres vibrationnels spécifiques aux conformères permettent de résoudre les structures des conformants en phase gazeuse de ces ions biomoléculaires.

La deuxième partie décrit l'utilisation de la liaison peptidique comme chromophore naturel alternatif, présent dans n'importe quel peptide. Les spectres électroniques des liaisons peptidiques dans les peptides protonés froids dans la phase gazeuse ainsi que l'influence d'une pré-excitation IR sont explorés en détail. L'utilisation de liaisons peptidiques permet d'enregistrer des spectres vibrationnels linéaires de haute qualité de peptides, même sans acides aminés aromatiques, pour lesquels seules des spectroscopes IRMPD et de marquage étaient disponibles jusqu'à récemment. Cette caractéristique rend la spectroscopie de combustion de trous IR-IR-DUV, l'outil spectroscopique sélectif de conformant le plus universel.

La troisième partie de cette thèse est dédiée à la relation entre la phase gazeuse et les structures indigènes des ions biomoléculaires. Le manque de solvant dans la phase gazeuse imite dans une certaine mesure les milieux hydrophobes des membranes ou des récepteurs cellulaires, où l'hydrogène intramoléculaire se lie plutôt que l'interaction avec le solvant, détermine en grande partie la structure des peptides. Dans ces cas des motifs structurels généraux peuvent survivre au transfert à la phase gazeuse. Les données expérimentales et les calculs théoriques pour les stéréo-isomères d'un médicament peptidique opioïde, la leucine-encéphaline et un peptide neurokinin A intrinsèquement désordonné sont les premières étapes vers le test de cette hypothèse.

Enfin, la présence de plus d'un conformant aux températures cryogéniques pour la quasi-totalité des peptides suggère que le refroidissement collisionnel est un processus rapide et non adiabatique. Dans la dernière partie, nous explorons l'efficacité du transfert d'énergie lors du refroidissement collisionnel des ions dans un gaz tampon.

Mots clés : spectroscopie à l'ion froid, spectroscopie électronique, spectroscopie vibrationnele combustion des trous IR-IR-UV, phase gazeuse, conformèr, tryptophane, histidine, liaison peptidique, peptides hydrophobes, récepteurs, hydrophobicité vacuum, leucine enképhaline, neurokinine A, intrinsèquement peptide désordonné, efficacité de refroidissement collisionnelle, gramicidine S, simulations de Monte-Carlo, refroidissement non adiabatique.

List of Abbreviations

CCS	Collisional Cross-Section
CID	Collision-Induced Dissociation
CIS	Cold Ion Spectroscopy
DFT	Density Functional Theory
DUV	Deep Ultraviolet
ESI	Electrospray Ionization
FRET	Förster Resonance Energy Transfer
FWHM	Full Width at Half of the Maximum
GS	Gramicidin S
IR	Infrared
IRMPD	Infrared Multiphoton Dissociation
MS	Mass Spectrometry
NKA	Neurokinin A
NMR	Nuclear Magnetic Resonance
OPO	Optical Parametric Oscillator
PDB	Protein Data Bank
PID	Photon-Induced Dissociation
RF	Radio Frequency
UV	Ultraviolet

Table of Contents

Chapter 1

Introduction

1.1. Structure-Function Relationship

Proteins play crucial role in virtually all biological processes, including gene transcription, enzymatic activity, signal transduction, post-translational modifications, transport of oxygen and chemical species, antibody-antigen complexation, etc.[1] Functionality of biological molecules *in vivo* is determined not only by their sequence, but also by their three-dimensional (3D) structures. This statement, known as the structure-function relationship, is the key concept in structural biology.

A poly-amino acid chain, longer than 50-100 monomers, is typically referred to as a protein, while shorter sequences are called peptides. The latter mainly act as signaling agents, such as neurotransmitters, hormones, antibiotics, and cell-penetrating agents.[2-10]

Because of the short length, peptides cannot form tertiary and quaternary structure, however, they do adopt certain secondary structure that determines their interaction with larger proteins, DNA, and lipids.[2, 3, 11-14] 3D structures of peptides *in vivo*, in turn, are determined by non-covalent intramolecular interactions (e.g., hydrogen bonds) and intermolecular interactions with the surrounding solvent molecules or binding pockets of ligands. Revealing those structures is necessary for developing practical implications, such as treatment of neurological diseases[15-18] and diabetes,[19] new antibiotics,[4, 6, 20, 21] targeted drug delivery,[13, 22, 23] and self-assembling materials.[24]

The next section provides general discussion and comparison of the advantages and disadvantages of modern techniques that are used for 3D structure identification of small to large biological molecules.

1.2. Methods of Structural Studies in Condensed Phase

1.2.1. X-Ray Crystallography

X-ray crystallography was the first technique that allowed determining 3D structure of large biomolecular species, such as DNA[25-27] and globular proteins,[28, 29] on atomic scale. It is currently the most widely used tool for structural elucidation of biomolecules (more than 10^5 entries in the Protein Data Bank (PDB)),[30, 31] because it provides an atomic resolution and structural information is obtained with a relatively simple mathematical procedure that allows avoiding molecular modeling.[32]

However, X-ray crystallography has some crucial limitations. The main disadvantage of this method is a need to crystallize samples. Obtaining large enough, well-ordered crystals of a molecule of interest remains a challenging task for many biological macromolecules because crystallization conditions are often not predictable.[32, 33] Furthermore, flexible regions (e.g., intrinsically disordered domains) of proteins often diffract so weakly, that they are invisible in crystallographic electron density maps.[34, 35] Finally, crystallization often requires specific solvents that are not usually present at biological conditions, and may significantly disturb native 3D structure of biomolecules. The latter is particularly true for peptides, because, due to their small size, they can be heavily influenced by solvent and additives used for crystallization.[36]

1.2.2. Nuclear Magnetic Resonance

Nuclear Magnetic Resonance (NMR) spectroscopy allows for studying 3D structure and dynamics of biomolecules directly in solution.[37, 38] In contrast to X-ray crystallography, NMR spectroscopy does not determine the 3D coordinates of the atoms in a molecule, but rather provides a list of restraints, such as internuclear distances and torsion angles. Thus, it requires molecular modeling for structure determination.[39, 40] Typically, this modeling results in an ensemble of structures, all of which are consistent with the experimentally determined restraints. Therefore, NMR lags behind X-ray crystallography in the number of structures submitted to the PDB,[30] even though the large variety of 2D and 3D methods allow for an unambiguous assignment of peaks in NMR spectra and, thus, analysis of the interactions between different parts of a molecule.[41-43]

It has been demonstrated that NMR can be employed to study macromolecular complexes with masses up to 1 MDa,[44, 45] however, in practice its application is limited to small- and medium-sized biomolecules, with molecular weight below 50 kDa.[46] Furthermore, it is still challenging for NMR spectroscopy to determine the 3D structure of flexible biomolecules, such as intrinsically

disordered proteins.[47] Moreover, NMR is very time-consuming and it usually cannot differentiate between different molecular conformations in solution.

1.3. Indirect Methods for Structural Identification

While X-ray crystallography provides structural data directly, all other techniques require complex calculations to predict precise molecular geometries, because they provide only experimental benchmarks that can be compared to theoretical predictions. Not only is the long computation time expensive, it also becomes a bottleneck in many studies. Over the last century, numerous techniques have been developed to facilitate the calculations by providing some structural constraints – overall shape, secondary structural motif, distance between specific sites in a molecule, etc.

Ion mobility,[48, 49] for example, allows for measuring Collisional Cross Section (CCS) of ions in the gas phase – a parameter that can be employed at early stages of computations. Another possible techniques in the gas phase include Förster resonance energy transfer[50] (FRET), which allows measuring the distance between the chromophores, hydrogen/deuterium (H/D) exchange.[51]

Circular dichroism (CD) is based on the different absorption of the left- and right-handed circularly polarized light by chiral molecules.[52] CD allows for a fast and efficient determination of secondary structure in terms of relative proportions of α-helices, β-sheets, and random coils for a large range of protein sizes.[53] Though the sample remains in solution and, thus, can be studied in native environment, CD provides neither atomic resolution nor residue-specific information, but rather an average signature of structural features.[54]

1.4. The Use of Optical Spectroscopy to Reveal Molecular Structure

Optical spectra of molecules are extremely sensitive to the 3D arrangement of their atoms. Even small differences between conformers give rise to detectable changes in spectroscopic properties. Vibrational spectroscopy, in particular, can reveal valuable structural information since the vibrational frequency of a given bond is highly dependent on its local environment. The characteristic shifts in the amide A (O-H and N-H stretching vibrations) and amide I and II regions (N-H bending and C=O stretching vibrations) reflect the hydrogen-bonding network that largely determines molecular structure. Experimentally obtained spectroscopic information can be directly compared to the accurate theoretical predictions of molecular structures, which are at the heart of *in silico* drug design.

Although UV and IR spectra in solution provide some structural information, they are usually very broad because of the inhomogeneous broadening. Therefore, the most rigorous comparison of theory to experiment can be achieved on isolated biological molecules, free from the complicating effects of interaction with the solvent.

1.4.1. Spectroscopy of Neutral Biomolecules

The first electronic spectrum of an amino acid in the gas-phase was reported in the mid 1980s by the group of Levy, who measured vibrationally resolved resonantly enhanced two-photon ionization spectra (R2PI) of jet-cooled neutral tryptophan[55, 56] and some of its derivatives.[57] In these experiments tryptophan was volatilized by heating and entrained in a molecular beam.[58] Different UV transitions showed different saturation behavior indicating the presence of several ground state conformations of tryptophan. Furthermore, different dispersed fluorescence spectra, obtained by pumping different conformers, indicated that several distinct conformations are also present in the excited state and do not interconvert on the time scale of the fluorescence lifetime.[59] Similar experiments were carried out later with tyrosine and phenylalanine.[60]

Following this pioneering work, many groups applied these methods to study larger biomolecules and developed innovative multi-resonance techniques for obtaining conformer-selective spectral information. UV-UV and IR-UV hole-burning techniques allowed for an assignment of different UV transitions to different conformers.[61-64] IR-UV depletion spectroscopy allowed for measuring conformer-selective vibrational spectra.[63-73] Furthermore, IR-IR-UV triple-resonance scheme has been employed to record conformer-specific vibrational spectra even when two (or more) conformers have indistinguishable UV transitions.[74] IR spectra of excited states have been recorded using the excited-state fluorescence dip technique.[75, 76] As one addition to the spectroscopic toolbox, Zwier and co-workers introduced population transfer spectroscopy,[77-81] in which absorption of an IR photon by a specific conformer is used to transfer part of its population into the potential wells of others. This technique allows for an estimation of the potential energy barriers between conformers and exploring isomerization dynamics in flexible biomolecules.

1.4.2. Spectroscopy of Charged Biomolecules at Room Temperature

Molecules *in vivo* are often globally or locally charged. At physiological conditions (pH ~7) most peptides in solution are zwitterions, having a deprotonated C-terminus (COO⁻) and a protonated ammonium group (NH_3^+). Moreover, residues with acidic (aspartic and glutamic acids) or basic (lysine, arginine and histidine) side chains can be charged, so that the entire molecule

generally possesses an overall net charge. Therefore, the study of charged biomolecules is at least equally important as that of their neutral counterparts. Soft ionization techniques, such as matrix assisted laser desorption ionization[82] (MALDI) and electrospray ionization[83, 84] (ESI), allow for a gentle transfer of large biomolecules into the gas phase.

The first electronic photofragmentation spectrum was measured by Andersen et al. to characterize green fluorescent protein chromophore ions, produced by electrospray.[85] At about the same time, McLafferty et al. reported infrared multiphoton dissociation (IRMPD) spectra of electrosprayed peptides and proteins in a Fourier transform ion-cyclotron resonance (FT-ICR) mass spectrometer, using an optical parametric oscillator[86] (OPO). Despite the fact that the observed bands at room temperature were about 30 cm^{-1} wide many light-atom stretching bands could be distinguished. High photon fluxes, delivered by free electron lasers[87, 88] (FELs), allowed for numerous IRMPD studies. Using FELIX, von Helden et al. extended IRMPD spectroscopy into the amide I and II spectral regions.[89] FELs were also coupled with 3D Paul traps and Fourier transform ion cyclotron resonance mass spectrometers[90] (FT-ICRs). Infrared spectra of solvated amino acid ions were also measured by detecting solvent loss subsequent to the absorption of IR photons, delivered by OPO.[91]

Room temperature IRMPD spectroscopy, although simple and convenient, does not provide the conformational selectivity and the spectral resolution sufficient for an unambiguous structural validation. On the other hand, total energy of multiple IR photons, absorbed by an ion, can cause interconversion of different isomers. Adding a second, low-energy IR source allows for probing the resulting ion ensemble. This two-colour IR-IR-MPD technique was demonstrated to provide useful insight into the details of population dynamics of model system.[92]

1.4.3. Cold Ion Spectroscopy

In contrast to small systems, the spectral resolution at room temperature does not allow for obtaining spectral features that yield structural information in larger biomolecules. Furthermore, because of the intrinsic nonlinearity of the IRMPD process, the band positions can be red-shifted and relative band intensities largely differ from the ones in linear spectra.[93] Moreover, the room-temperature UV spectra of peptides with aromatic side chains are broad,[94] so that IR-UV double-resonance technique cannot be applied to obtain conformer-selective spectra. Cooling, however, significantly simplifies spectroscopic characterization of even large peptides.

The most common way to cool the ions down is by confining them in a RF trap maintained at low temperature and allowing them to collide with a buffer gas for thermalization. Linear

multipole ion traps mounted onto a cryocooler allowed for attaining internal vibrational temperatures as low as 10 K. In their pioneering experiments, Boyarkin et al. demonstrated[94] that the cooling of protonated tyrosine in the 22-pole trap to ~12 K allows recording a sharp UV spectrum with transitions as narrow as 2.7 cm^{-1}. Electronic spectrum of protonated tryptophan remained broad even at 12 K because of its short excited state lifetime. However, solvation of the amino acid by only two water molecules drastically changes the photophysics of the exited state, allowing one to record its vibrationally resolved UV spectrum.[95]

The double-resonance depletion spectroscopy was applied to record conformer-selective vibrational spectra of solvated tryptophan[96] and, later, of protonated tyrosine and phenylalanine,[97] as well as the ones of tyrosine-containing protonated dipeptides.[98] The process of a secondary structure formation in polyalanine peptides demonstrated the applicability of the double-resonance approach for peptides as large as 12 amino acids.[99, 100]

One of the most fascinating achievements of the technique was an unambiguous assignment of the intrinsic structures of a decapeptide gramicidin S. This work involved studies of not only a bare peptide, but also of several isotopically substituted analogues and a huge computational effort.[101-103] Furthermore, CIS allowed studies of microsolvated gramicidin S with up to 50 water molecules attached to it.[104]

Large biomolecules often exhibit lower UV fragmentation yield, making their studies more difficult. An IR laser assisted photofragmentation spectroscopy (IRLAPS) can alleviate this problem. Irradiating the ions with a CO_2 laser pulse following UV excitation was shown to increase the photofragmentation yield by as much as two orders of magnitude. This technique allowed for recording well-resolved UV and IR spectra of a 17 amino acid peptide.[105]

As any experimental method, CIS has certain limitations. In particular, ions have to contain an aromatic residue (Trp, Tyr, Phe or His) to absorb UV light. Furthermore, one needs vibrational resolution in electronic spectra, because broad electronic transitions preclude the use of conformer-selective cold ion spectroscopy. Therefore, since the first demonstration, cold ion spectroscopy was mainly focused on peptides with Phe amino acid as a chromophore.

In search to overcome these disadvantages several novel directions have been explored. The use of highly-resolved electronic fingerprints of biomolecules together with high-resolution mass-spectrometry lead to the development of a novel method – 2D UV-MS.[106, 107] It provides either library-based or even "blind" identification of isomers of biomolecules. Furthermore, it allows even identification of conformers, though does not provide their vibrational spectra.[108]

On the other hand, many groups try to avoid using UV photodissociation, using IR-induced dissociation of weakly bound tags instead. One possible approach is an IR-IR hole-burning spectroscopy,[109, 110] first demonstrated by the group of prof. Johnson. Another possible strategy is employing ion mobility for spatial separation of conformers due to the differences in their CCSs prior to performing IR tagging spectroscopy.[111] Both techniques have significant disadvantages. While ion mobility often does not allow to separate conformers of peptides other than cis-/trans-isomers,[112] all tagging techniques suffer from low signal-to-noise (S/N) ratio and analyte-dependent parameters for efficient tagging. Furthermore, tags were shown to affect vibrational frequencies of ions, complicating their comparison with theoretical calculations.[113]

The main goal of this work is to develop a novel conformer-selective experimental approach that would applicable to peptides with any amino acid sequence.

1.5. Outline

This thesis is organized as follows.

In Chapter 2 the experimental setup used in this work to study spectroscopy of cold, biomolecular ions is presented. Its major constituents as well as the basic principles of operation are discussed in details. Also, we discuss the underlying mechanisms and describe the various spectroscopic techniques referred to as double-resonance cold ion spectroscopy.

In Chapter 3 the intrinsic limitations of the double-resonance approach are discussed and a novel conformer-selective spectroscopic technique, IR-IR-UV hole-burning spectroscopy, is presented. Following a general description of the principles of this technique, we describe two applications of the method – solving the structures of the two aromatic amino acids tryptophan and histidine, for which the cold ion spectroscopy was previously precluded due to the indistinguishable electronic spectra. Combined with high-level anharmonic calculations, the conformer-specific vibrational spectra, reported herein, allow for an unambiguous assignment of the geometries of the lowest-energy gas-phase conformers of these biomolecular ions.

In Chapter 4 we present a successful effort to extend the application range of cold ion spectroscopy toolbox to peptides that do not contain aromatic amino acids in their sequence. Instead, absorption of the peptide bond, a universal chromophore present in any peptide, is exploited. We present the electronic spectra of several model and natural peptides, as well as their IR-DUV vibrational spectra. Given some intrinsic difficulties due to the width of the electronic spectra, an optimal experimental workflow is described. Finally, we demonstrate the ability of the

IR-IR-DUV hole-burning spectroscopy to measure conformer-specific spectra of a natural six amino acid peptide.

In Chapter 5 we address one of the most vivid questions for the gas phase studies – how relevant are the intrinsic structures for biology? While numerous groups approach this question from the point of view of kinetic trapping, here an alternative idea is tested. Since the intrinsic structures are determined only by the intramolecular interactions, such geometries might be a good reflection of native geometries of molecules that are biologically active only in hydrophobic media. We provide evidence that the structures of opioid drugs in the gas phase correlate with their physiological activity and present conformational assignment of the spectra of a ten amino acid neurotransmitter peptide.

In Chapter 6 the cooling rate in our cold ion trap, namely, an average energy taken away from a hot ion per collision with a buffer gas molecule is assessed. We present the design of an experiment, results, and their interpretation.

Finally, in Chapter 7 the main results and possible applications of the current work are discussed.

References

1.   D. Voet and J. G. Voet, *Biochemistry, 4-th Edition*, John Wiley& Sons Inc, New York, 2011.

2.   M. Hong and Y. Su, *Protein Sci.*, 2011, **20**, 641-655.

3.   P. Nicolas, *FEBS Journal*, 2009, **276**, 6483-6496.

4.   J. M. Willey and W. A. van der Donk, *Annu. Rev. Microbiol.*, 2007, **61**, 477-501.

5.   S. Duquesne, V. Petit, J. Peduzzi and S. Rebuffat, *J. Mol. Microbiol. Biotechnol.*, 2007, **13**, 200-209.

6.   P. D. Cotter, C. Hill and R. P. Ross, *Nature Rev. Microb.*, 2005, **3**, 777-788.

7.   M. Tatar, A. Bartke and A. Antebi, *Science*, 2003, **299**, 1346-1351.

8.   C. Severini, G. Improta, G. Falconieri-Erspamer, S. Salvadori, V. Erspamer, G. Falconieri-Erspamer, S. Salvadori and V. Erspamer, *Pharmacol. Rev.*, 2002, **54**, 285-322.

9.   J. Axelrod and T. D. Reisine, *Science*, 1984, **224**, 452-459.

10.   K. J. Catt, J. P. Harwood, G. Aguilera and M. L. Dufau, *Nature*, 1979, **280**, 109-116.

11.   N. London, B. Raveh and O. Schueler-Furman, *Curr. Opin. Struct. Biol.*, 2013, **23**, 894-902.

12.   L. Yang and A. Schepartz, *Biochemistry*, 2005, **44**, 7469-7478.

13.   D. S. Dimitrov, *Nature Rev. Microb.*, 2004, **2**, 109-122.

14.   R. Eckel, R. Ros, A. Ros, S. D. Wilking, N. Sewald and D. Anselmetti, *Biophys. J.*, 2003, **85**, 1968-1973.

15.   S. L. Bernstein, N. F. Dupuis, N. D. Lazo, T. Wyttenbach, M. M. Condron, G. Bitan, D. B. Teplow, J.-E. Shea, B. T. Ruotolo, C. V. Robinson and M. T. Bowers, *Nature Chem.*, 2009, **1**, 326-331.

16.   C. A. E. Hauser, R. Deng, A. Mishra, Y. Loo, U. Khoe, F. Zhuang, D. W. Cheong, A. Accardo, M. B. Sullivan, C. Riekel, J. Y. Ying and U. A. Hauser, *PNAS*, 2011, **108**, 1361-1366.

17.   F. Chiti and C. M. Dobson, *Annu. Rev. Biochem*, 2006, **75**, 333-366.

18.   T. P. J. Knowles, M. Vendruscolo and C. M. Dobson, *Nature Rev. Mol. Cell Biol.*, 2014, **15**, 384-396.

19.   C. Tysoe, L. K. Williams, R. Keyzers, N. T. Nguyen, C. Tarling, J. Wicki, E. D. Goddard-Borger, A. H. Aguda, S. Perry, L. J. Foster, R. J. Andersen, G. D. Brayer and S. G. Withers, *ACS Cent. Sci.*, 2016, **2**, 154-161.

20.   K. V. R. Reddy, R. D. Yedery and C. Aranha, *Int. J. Antimicrob. Agents*, 2004, **24**, 536-547.

21.   C. D. Fjell, J. A. Hiss, R. E. W. Hancock and G. Schneider, *Nature Rev. Drug Disc.*, 2011, **11**, 37-51.

22.   R. Saxena and M. J. Nanjan, *Drug Deliv.*, 2015, **22**, 156-167.

23.   E. S. Khafagy and M. Morishita, *Adv. Drug Deliv. Rev.*, 2012, **64**, 531-539.

24.   S. Li, A. K. Mehta, A. N. Sidorov, T. M. Orlando, Z. Jiang, N. R. Anthony and D. G. Lynn, *J. Am. Chem. Soc.*, 2016, **138**, 3579-3586.

25.   J. D. Watson and F. H. C. Crick, *Nature*, 1953, **171**, 738.

26.   M. H. F. Wilkins, A. R. Stokes and H. R. Wilson, *Nature*, 1953, **171**, 740.

27.   R. E. Franklin and R. G. Gosling, *Nature*, 1953, **171**, 737.

28.   J. C. Kendrew, G. Bodo, H. M. Dintzis, R. G. Parrish, H. Wyckoff and D. C. Phillips, *Nature*, 1958, **181**, 662-666.

29.   M. F. Perutz, M. G. Rossmann, A. F. Cullis, H. Muirhead, G. Will and A. C. North, *Nature*, 1960, **185**, 416-422.

30.   http://www.rcsb.org/pdb/).

31.   H. M. Berman, J. Westbrook, Z. Feng, G. Gilliland, T. N. Bhat, H. Weissig and I. N. Shindyalov, *Nucleic Acids Res.*, 2000, **28**, 235-242.

32.   D. Sherwood and J. Coope, *Crystals, X-rays and Proteins: Comprehensive Protein Crystallography*, Oxford University Press, 2011.

33.   M. Benvenuti and S. Mangani, *Nature Prot.*, 2007, **2**, 1633-1651.

34.   M. Egli, in *Current Protocols in Nucleic Acid Chemistry*, 2010, vol. 41, pp. 7.13.11-17.13.35.

35.   C. J. Oldfield and A. K. Dunker, *Annu. Rev. Biochem*, 2014, **83**, 553-584.

36.   I. L. Karle, *Biopolymers*, 1996, **40**, 157-180.

37.   P. Paluch, T. Pawlak, A. Jeziorna, J. Trébosc, G. Hou, A. J. Vega, J.-P. Amoureux, M. Dracinsky, T. Polenova and M. J. Potrzebowski, *Phys. Chem. Chem. Phys.*, 2015, **17**, 28789-28801.

38. K. Henzler-Wildman and D. Kern, *Nature*, 2007, **450**, 7-9.

39. T. F. Havel, *Prog. Biophys. Molec. Biol.*, 1991, **56**, 43-78.

40. P. Güntert, *Quart. Rev. Biophys.*, 1998, **31**, 145-237.

41. D. S. Wishart and B. D. Sykes, *Methods Enzymol.*, 1994, **239**, 363-392.

42. A. M. Gronenborn and G. M. Clore, *Crit. Rev. Biochem. Mol. Biol.*, 1995, **30**, 351-385.

43. B. Bechinger, *Biochim. Biophys. Acta*, 1999, **1462**, 157-183.

44. J. Fiaux, E. B. Bertelsen, A. L. Horwich and K. Wüthrich, *Nature*, 2002, **418**, 207-211.

45. R. Sprangers and L. E. Kay, *Nature*, 2007, **445**, 618-622.

46. G. S. Rule and T. K. Hitchens, *Fundamentals of protein NMR spectroscopy*, pringer Science & Business Media, 2006.

47. I. C. Felli and R. Pierattelli, *Intrinsically Disordered Proteins Studied by NMR Spectroscopy*, Springer, 2015.

48. R. R. Hudgins and M. F. Jarrold, *J. Am. Chem. Soc.*, 1999, **121**, 3494-3501.

49. K. B. Shelimov, D. E. Clemmer, R. R. Hudgins and M. F. Jarrold, *J. Am. Chem. Soc.*, 1997, **119**, 2240-2248.

50. V. Kopysov and O. V. Boyarkin, *Angew. Chem. Int. Ed.*, 2016, **55**, 689-692.

51. S. W. Englander, *Annu. Rev. Biophys. Biomol. Struct.*, 2000, **29**, 213-238.

52. N. J. Greenfield, *Anal. Biochem.*, 1996, **235**, 1-10.

53. A. Micsonai, F. Wien, L. Kernya, Y.-H. Lee, Y. Goto, M. Réfrégiers and J. Kardos, *PNAS*, 2015, **112**, E3095-E3103.

54. N. J. Greenfield, *Nature Prot.*, 2007, **1**, 2876-2890.

55. T. R. Rizzo, Y. D. Park, L. Peteanu and D. H. Levy, *J. Chem. Phys.*, 1985, **83**, 4819.

56. T. R. Rizzo, Y. D. Park, L. A. Peteanu and D. H. Levy, *J. Chem. Phys.*, 1986, **84**, 2534.

57. Y. D. Park, T. R. Rizzo, L. A. Peteanu and D. H. Levy, *J. Chem. Phys.*, 1986, **84**, 6539-6549.

58. T. R. Rizzo, Y. D. Park and D. H. Levy, *J. Am. Chem. Soc.*, 1985, **107**, 277-278.

59. T. R. Rizzo, Y. D. Park and D. H. Levy, *J. Chem. Phys.*, 1986, **85**, 6945.

60. S. J. Martinez, J. C. Alfano and D. H. Levy, *J. Mol. Spectrosc.*, 1992, **156**, 421-430.

61. B. C. Dian, A. Longarte, S. Mercier, D. A. Evans, D. J. Wales and T. S. Zwier, *J. Chem. Phys.*, 2002, **117**, 10688-10702.

62. L. C. Snoek, R. T. Kroemer, M. R. Hockridge and J. P. Simons, *Phys. Chem. Chem. Phys.*, 2001, **3**, 1819-1826.

63. I. Hünig and K. Kleinermanns, *Phys. Chem. Chem. Phys.*, **6**, 2650-2658.

64. L. C. Snoek, E. G. Robertson, R. T. Kroemer and J. P. Simons, *Chem. Phys. Lett.*, 2000, **321**, 49-56.

65. C. Unterberg, A. Gerlach, T. Schrader and M. Gerhards, *J. Chem. Phys.*, 2003, **118**, 8296-8300.

66. G. M. Florio and T. S. Zwier, *J. Phys. Chem. A*, 2003, **107**, 974-983.

67. M. Gerhards, C. Unterberg, A. Gerlach and A. Jansen, *Phys. Chem. Chem. Phys.*, 2004, **6**, 2682-2690.

68. W. Chin, J. P. Dognon, C. Canuel, F. Piuzzi, I. Dimicoli, M. Mons, I. Compagnon, G. Von Helden and G. Meijer, *J. Chem. Phys.*, 2005, **122**, 054317.

69. J. M. Bakker, C. Plutzer, I. Hünig, T. Häber, I. Compagnon, G. Von Helden, G. Meijer and K. Kleinermanns, *ChemPhysChem*, 2005, **6**, 120-128.

70. W. Chin, J.-P. Dognon, F. Piuzzi, B. Tardivel, I. Dimicoli and M. Mons, *J. Am. Chem. Soc.*, 2005, **127**, 707-712.

71. A. Abo-Riziq, B. O. Crews, M. P. Callahan, L. Grace and M. S. De Vries, *Angew. Chem.*, 2006, **45**, 5166-5169.

72. M. S. De Vries and P. Hobza, *Annu. Rev. Phys. Chem.*, 2007, **58**, 585-612.

73. M. N. Blom, I. Compagnon, N. C. Polfer, G. von Helden, G. Meijer, S. Suhai, B. Paizs and J. Oomens, *J. Phys. Chem. A*, 2007, **111**, 7309-7316.

74. V. A. Shubert and T. S. Zwier, *J. Phys. Chem. A*, 2007, **111**, 13283-13286.

75. B. C. Dian, A. Longarte and T. S. Zwier, *J. Chem. Phys.*, 2003, **118**, 2696-2706.

76. T. Walther, H. Bitto, T. K. Minton and J. R. Huber, *Chem. Phys. Lett.*, 1994, **231**, 64-69.

77. B. C. Dian, A. Longarte and T. S. Zwier, *Science*, 2001, **296**, 2369-2373.

78. B. C. Dian, G. M. Florio, J. R. Clarkson, A. Longarte and T. S. Zwier, *J. Chem. Phys.*, 2004, **120**, 9033-9046.

79. B. C. Dian, J. R. Clarkson and T. S. Zwier, *Science*, 2004, **303**, 1169-1173.

80. B. C. Dian, A. Longarte, P. R. Winter and T. S. Zwier, *J. Chem. Phys.*, 2004, **120**, 133-147.

81. J. R. Clarkson, B. C. Dian, L. Moriggi, A. Defusco, V. McCarthy, K. D. Jordan and T. S. Zwier, *J. Chem. Phys.*, 2005, **122**, 214311.

82. K. Tanaka, *The Origin of Macromolecule Ionization by Laser Irradiation*, Nobel Lecture, 2002.

83. J. B. Fenn, *Electrospray Wings for Molecular Elephants*, Nobel Lecture, 2002.

84. J. B. Fenn, M. Mann, C. K. Meng, S. F. Wong and C. M. Whitehouse, *Mass Spectrom. Rev.*, 1990, **9**, 37-70.

85. L. H. Andersen, A. Lapierre, S. B. Nielsen, I. B. Nielsen, S. U. Pedersen, U. V. Pedersen and S. Tomita, *Eur. Phys. J. D*, 2002, **20**, 597-600.

86. H. Oh, K. Breuker, S. K. Sze, Y. Ge, B. K. Carpenter and F. W. McLafferty, *PNAS*, 2002, **99**, 15863-15868.

87. R. Prazeres, J. M. Berset, F. Glotin, D. Jaroszynski and J. M. Ortega, *Nucl. Instrum. Methods Phys. Res. A*, 1993, **331**, 15-19.

88. D. Oepts, A. F. G. van der Meer and P. W. Van Amersfoort, *Infrared Phys. Technol.*, 1995, **36**, 297-308.

89. J. Oomens, N. Polfer, D. T. Moore, L. van der Meer, A. G. Marshall, J. R. Eyler, G. Meijer and G. von Helden, *Phys. Chem. Chem. Phys.*, 2005, **7**, 1345.

90. L. M. Aleese, A. Simon, T. B. McMahon, J. M. Ortega, D. Scuderi, J. Lemaire and P. Maître, *Int. J. Mass spectrom.*, 2006, **249-250**, 14-20.

91. A. Kamariotis, O. V. Boyarkin, S. R. Mercier, R. Beck, D., M. F. Bush, E. R. Williams, T. R. Rizzo, R. Mercier and R. D. Beck, *J. Am. Chem. Soc.*, 2006, **128**, 905-916.

92. J. Lang, M. Gaffga, F. Menges and G. Niedner-Schatteburg, *Phys. Chem. Chem. Phys.*, 2014, **16**, 17417.

93. J. Oomens, B. G. Sartakov, G. Meijer and G. von Helden, *Int. J. Mass spectrom.*, 2006, **254**, 1-19.

94. O. V. Boyarkin, S. R. Mercier, A. Kamariotis and T. R. Rizzo, *J. Am. Chem. Soc.*, 2006, **128**, 2816-2817.

95. S. R. Mercier, O. V. Boyarkin, A. Kamariotis, M. Guglielmi, I. Tavernelli, M. Cascella, U. Rothlisberger and T. R. Rizzo, *J. Am. Chem. Soc.*, 2006, **128**, 16938-16943.

96. R. Mercier, PhD, EPFL, 2008.

97. J. A. Stearns, S. Mercier, C. Seaiby, M. Guidi, O. V. Boyarkin and T. R. Rizzo, *J. Am. Chem. Soc.*, 2007, **129**, 11814-11820.

98. J. A. Stearns, M. Guidi, O. V. Boyarkin and T. R. Rizzo, *J. Chem. Phys.*, 2007, **127**, 154322.

99. J. A. Stearns, C. Seaiby, O. V. Boyarkin and T. R. Rizzo, *Phys. Chem. Chem. Phys.*, 2009, **11**, 125-132.

100. J. A. Stearns, O. V. Boyarkin and T. R. Rizzo, *J. Am. Chem. Soc. Comm.*, 2007, **129**, 13820-13821.

101. N. S. Nagornova, M. Guglielmi, M. Doemer, I. Tavernelli, U. Rothlisberger, T. R. Rizzo and O. V. Boyarkin, *Angew. Chem.*, 2011, **50**, 5383-5386.

102. N. S. Nagornova, T. R. Rizzo and O. V. Boyarkin, *J. Am. Chem. Soc.*, 2010, **132**, 4040.

103. T. K. Roy, V. Kopysov, N. S. Nagornova, T. R. Rizzo, O. V. Boyarkin and R. B. Gerber, *ChemPhysChem*, 2015, **16**, 1374-1378.

104. N. S. Nagornova, T. R. Rizzo and O. V. Boyarkin, *Science*, 2012, **336**, 320-323.

105. M. Guidi, U. J. Lorenz, G. Papadopoulos, O. V. Boyarkin and T. R. Rizzo, *J. Phys. Chem. A*, 2009, **113**, 797-799.

106. V. Kopysov, A. Makarov and O. V. Boyarkin, *Anal. Chem.*, 2015, **87**, 4607-4611.

107. V. Kopysov, A. Makarov and O. V. Boyarkin, *Anal. Chem.*, 2017, **89**, 544-547.

108. V. Kopysov, A. Makarov and O. V. Boyarkin, *J. Phys. Chem. Lett.*, 2016, **7**, 1067-1071.

109. B. M. Elliott, R. A. Relph, J. R. Roscioli, J. C. Bopp, G. H. Gardenier, T. L. Guasco and M. A. Johnson, *J. Chem. Phys.*, 2008, **129**, 094303.

110. C. M. Leavitt, A. B. Wolk, J. A. Fournier, M. Z. Kamrath, E. Ganard, M. J. Van Stipdonk and M. A. Johnson, *J. Phys. Chem. Lett.*, 2012, **3**, 1099-1105.

111. A. Masson, M. Z. Kamrath, M. A. S. Perez, M. S. Glover, U. Rothlisberger, D. E. Clemmer and T. R. Rizzo, *J. Am. Soc. Mass. Spectrom.*, 2015, **26**, 1444-1454.

112. L. Voronina, A. Masson, M. Z. Kamrath, F. Schubert, D. Clemmer, C. Baldauf and T. R. Rizzo, *J. Am. Chem. Soc.*, 2016, **138**, 9224-9233.

113. A. Masson, E. R. Williams and T. R. Rizzo, *J. Chem. Phys.*, 2016, **143**, 104313.

Chapter 2

Experimental Approach

This chapter describes the experimental setup for recording spectra of cold biomolecular ions and the basic spectroscopic techniques, usually referred to as the double-resonance spectroscopy. It begins with a short overview of the tandem mass spectrometer, followed by a more detailed description of its constituent parts. Finally, we present a description of the double-resonance Cold Ion Spectroscopy methods that are commonly used for spectroscopic characterization of biomolecular ions in the gas phase.

2.1. Experimental Setup

2.1.1. General Description of the Tandem Mass-Spectrometer

A schematic view of the tandem mass spectrometer[1,2] combined with the cold octupole ion trap[3] is shown in figure 2.1. Protonated gas-phase ions are produced directly from solution using a nanoelectrospray ion source[4] (ESI) and enter a two-stage electrodynamic ion funnel[5] (IF) (Spectroglyph) through a 0.7-mm ID, 10-cm long metal capillary, orthogonal to the funnel axis. The funnel guides ions into a hexapole radio-frequency (RF) ion trap (HEX), where they are accumulated and thermalized for approximately 50 or 100 ms, depending on a repetition rate of experiment.

The ions are then released from the hexapole trap and mass-selected by a quadrupole mass filter (Q1) (Extrel), 90° steered by an electrostatic quadrupole bender (B1), decelerated by a stack of electrostatic lenses (EL), and, finally, guided into a cold octupole ion trap by an octupole ion guide (OIG).[3] The trap is mounted on a cold head (T = 6 K) of a two-stage closed-cycle refrigerator (RDK-408, Sumitomo). The ions are trapped and cooled in the octupole ion trap to vibrational

temperatures T ≈ 10 K by collisions with He buffer gas, which is pulsed into the trap 1 ms prior to the arrival of the ion packet.[3]

A UV and IR laser beams counter propagate into the vacuum chamber through two BaF_2 windows (BW) 100 μs before the release of the parent ions and UV-induced fragment ions from the trap. The beams are spatially overlapped on the axis of the trap. Laser pulses are typically separated by 200 ns delays. The released ions are bent 90° by a second electrostatic quadrupole bender (B2) and analyzed in a quadrupole mass spectrometer (Q2) (Extrel), equipped with a channeltron ion detector (DET). Ion signals from the channeltron are, finally, counted by a gated photon counter (CNT) (SR400, SRS Inc.), which transfers the data to a host PC, controlling the data acquisition via LabView software (DAC).
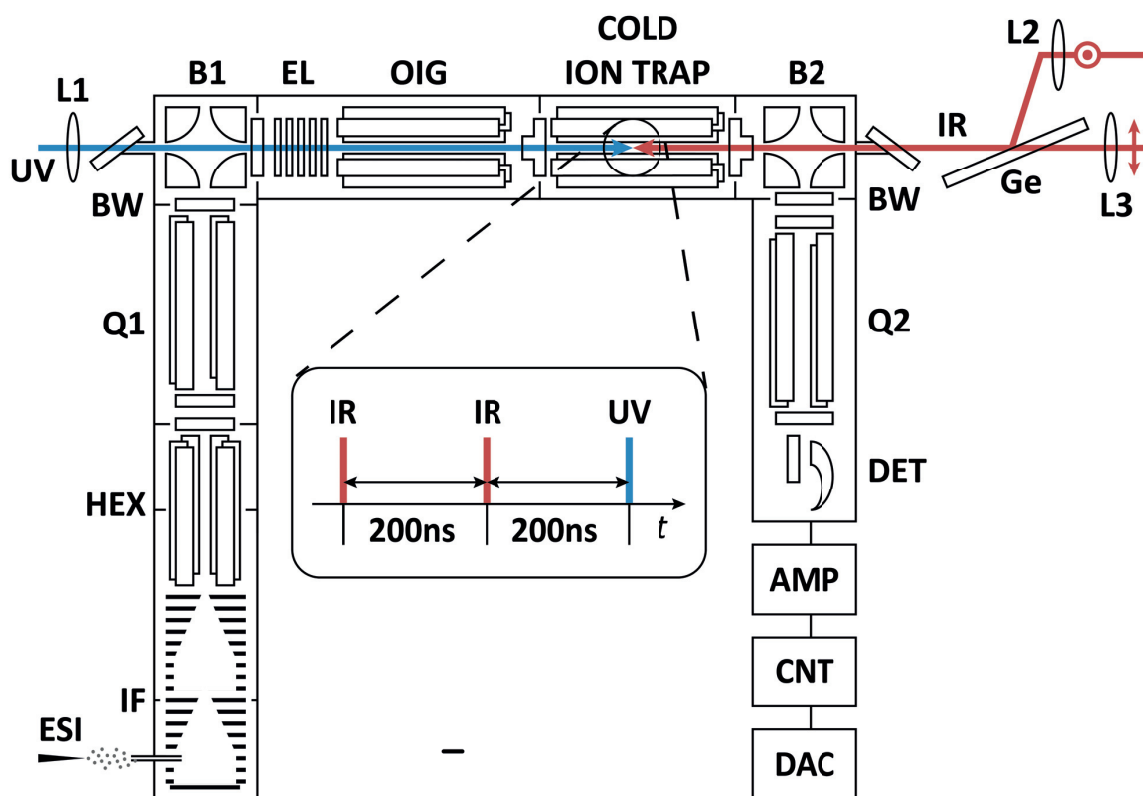
Figure 2.1. *Schematic view of the experimental setup for spectroscopy of cryogenically cooled ions. The inset shows the relative timing of laser pulses.*

The cold trap can be filled with ions and UV laser pulse can be shot in either 20 or 10 Hz cycles. IR OPO laser can be shot in either 10 or 5 Hz cycles. An average of typically 20 laser shots per data point is taken for spectral measurements. The UV laser, the OPOs, the release of ions from

the hexapole and from the cold octupole traps are synchronized with the data acquisition system using three multichannel pulse generators (BNC 575).

UV light is produced either by a (D)UV OPO (EKSPLA), tunable in a wide spectral range (typically, 192-280 nm spectral range, that covers absorption of His and peptide bond), or by doubling the output frequency of a dye laser (HD-500, Lumonics) in a KDP crystal of an Autotracker device (InRad) (typically, in the 280-310 nm spectral range, that covers absorption regions of Trp, Tyr, and Phe aromatic amino acids). The dye laser is pumped by 150 mJ of the 3rd harmonic of a Nd:YAG laser (GCR-200, Spectra-Physics). The beam is loosely focused by a F=70 cm fused silica lens (L1) 2-3 cm in front of the cold trap entrance. IR beams with orthogonal linear polarizations are generated by two tunable OPOs (Laser Vision), pumped by two different Nd:YAG lasers (Surelite III-Ex, Continuum; SpitLight 600, Innolas). The beams are combined on a germanium plate (Ge) placed at Brewstver's angle and focused in the centre of the trap by two F=70 cm CaF_2 lenses (L2, L3). In such configuration either IR OPO can be used for double-resonance spectroscopy or both of them can be used simultaneously for an IR-IR-UV hole-burning spectroscopy. Spectral resolution of the IR OPOs is about 1 cm^{-1} in the 3 μm region and around 2 cm^{-1} in the 6 μm region.

In the following sections the principles of operation of the key constituents of our experimental setup will be described in more details.

2.1.2. Electrospray Ionization of Biomolecular Ions

Large biological molecules have low vapor pressure and decompose upon heating. Gas phase studies of biomolecular ions require, therefore, soft ionization techniques that allow for transferring them from solution to vacuum without significant decomposition. In 2002 the Nobel Prize was awarded for two soft ionization techniques: electrospray ionization[6] (ESI) and matrix assisted laser desorbtion/ionization[7] (MALDI).

The first studies of electrospray phenomenon, i.e., the production of a spray of fine droplets by submitting a liquid surface to an intense electric field, were reported in the beginning of the 20th century.[8, 9] However, it was only at the end of the 1960s that Dole and coworkers started using it in the development of an ion source for mass spectrometry.[10] Major improvements by John Fenn's research group in the mid 1980s[11-13] made ESI a method of choice to bring large thermally labile molecules into the gas phase.[14, 15]

Figure 2.2 illustrates the mechanisms taking place in the atmospheric part of an electrospray ion source. A conductive needle is filled with an analyte dissolved in a polar solvent. A high voltage difference is applied between the needle and an entrance capillary of the vacuum system. Due to the strong electric field at the needle tip, positive charges (in the positive ion mode example of the figure) accumulate at the liquid surface and cause the formation of a cone-shaped liquid meniscus at the needle exit, a so-called «Taylor cone».[4, 16] When the charge density at the apex of this cone is high enough so that the charge repulsion overcomes the surface tension of the liquid, charged droplets are created and carried away by the electric field in a spray towards the counter-electrode. Due to a solvent evaporation these droplets shrink and their charge density increases until it reaches the «Rayleigh limit».[17] At this point, similarly to what happens at the Taylor cone, the surface tension is weaker than the charge repulsion and the droplet emits smaller droplets carrying away the excess charge. Several cycles of this evaporation/fission eventually lead to the formation of solvated ions.

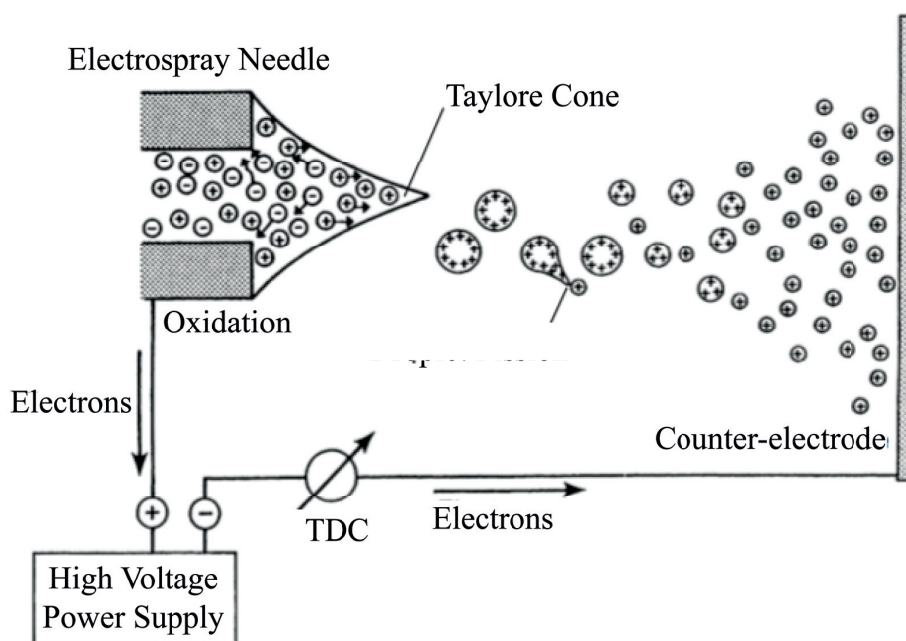***Figure 2.2.*** *Spray formation and droplet fission in the atmospheric part of an ESI source. (Adapted from Kebarle and Tang[18]).*

Depending on the spray conditions, different processes can lead to formation of the charged analyte ions. In the case of peptides and operation in positive ESI mode, protonation predominates. If metal ions are present in the sample the formation of adducts can also be observed. Two theories

are currently considered concerning the exact mechanism by which the solvated ions are produced. According to the «charge residue» model (CRM), the residual solvent in the smallest final droplets is simply evaporated to yield solvated ions.[10, 19] On the other hand, the «ion evaporation» model (IEM) states that it is the solvated ions that are, in fact, evaporated from the surface of charged nanodroplets.[20, 21] Recent contributions to this debate include references [22-28].

In our experimental setup we use nano-ESI (nESI) ion source, an ESI-variant that uses metalized borosilicate spray needles with smaller inner diameter (a few μm versus ~ 100 μm for electrospray). The principles of spray formation are identical for the two techniques. Nano-electrospray,[29] whose development started in the mid 1990s,[4, 30] has several benefits compared to conventional ESI. First of all, it allows much lower liquid flow rates (~ 1 nL·min⁻¹ to 1 μL·min⁻¹ for nESI compared with ~ 1 μL·min⁻¹ to 1 mL·min⁻¹ for ESI), which extends the running time of a given sample volume.[30, 31] Second, the onset voltage V_{on} [kV] needed to initiate a stable spray is reduced, as can be derived from the following equation:

$$V_{on} \approx 0.2\sqrt{r\gamma}\, ln\left(\frac{4000d}{r}\right)$$ (Eq. 2.1)

where r [μm] stands for the needle inner radius, γ [N·m⁻¹] is the surface tension of the liquid, and d [mm] denotes the distance of the needle tip to the counter-electrode.[32] A decrease of the needle diameter from 100 μm to 10 μm causes approximately a two-fold reduction of the onset potential for the typical values of d (1-10 mm). The equation also shows that smaller needle tips make it possible to use solvents with higher surface tension, such as pure water, while keeping the needle voltage low enough to prevent electric discharges to the counter-electrode.

This better ionization efficiency of nanospray is attributed to the smaller size of the initial droplets (typical 150 nm diameter as compared with 1.5 μm for conventional ESI). Consequently, fewer fission cycles are required to desolvate ions and the amount of «wasted» material that enters the vacuum and covers ion optics is also diminished, slowing down the contamination of the vacuum interface.

Comprehensive information about the mechanisms, instrumentation, and applications of the electrospray can be found in the aforementioned references, as well as in several textbooks (e.g., references[33, 34]).

A typical solution in our experiments has an analyte concentration of 50 μM in a 1:1 water/methanol mixture with 0.5% acetic acid added. The source head is mounted on a microtranslational xyz-manipulator and connected to a high-voltage power supply. Two cameras are used for a precise positioning of the needle with respect to the entrance capillary. The assembly

is also airtight, so that a very slight pressure of N_2 can be applied to the solution in order to facilitate the spray formation. In the positive ion mode the typical voltage applied to the needle is ~ 1.5 kV above the ground potential.

Gas-phase solvated ions formed at atmospheric pressure are entrained by viscous forces through the 10 cm long stainless-steel transfer capillary with an inner and outer diameters of 0.7 mm and 2 mm, respectively. The other end of the capillary is in the first vacuum stage of our differentially pumped mass spectrometer. Upon acceleration in this low vacuum region, the solvated ions undergo collisions with residual gas molecules. Internal heating due to high-energy collisions can induce final desolvation of the ions, destruction of the secondary structure, and even collision-induced dissociation. Thus, the conditions in first stages might have to be adjusted for each experiment.

2.1.3. Differential Pumping of the Tandem Mass Spectrometer

Specific regions of the mass spectrometer use controlled collisions of ions with neutral gas (for example, for Collision-Induced Dissociation[35] (CID) or to thermally stabilize ion packet in a hexapole trap). However, in general all mass analyzers function under low-pressure conditions. The vacuum in a tandem mass spectrometer serves several purposes. First of all, it allows ions to reach the detector without undergoing collisions with other gaseous molecules. Indeed, collisions may produce a deviation from the stable trajectory and an ion can lose its charge against the walls of the instrument. On the other hand, ion-molecule collisions can result in unwanted dissociation reactions and, hence, increase the complexity of the mass spectrum. Second, the high voltage used in RF devices (several kV in quadrupole mass filters, ion guides, and traps) causes electrical discharge in low vacuum conditions, causing crucial damage. Finally, cooling of the octupole ion trap down to cryogenic temperature of a few kelvins causes condensation of neutrals on the surface of the rods. The resulting dielectric cover can significantly influence the shape of the effective potential (see section 2.1.4) and the spatial distribution of the ion cloud, decreasing the effective volume overlapped with laser beams.

Figure 2.3 shows a schematic diagram of eight differentially pumped vacuum stages of our tandem mass spectrometer. The pumps that are used to create the vacuum as well as the typical pressures (with open inlet capillary and without He buffer gas being injected in the system) are listed in Table 2.1.
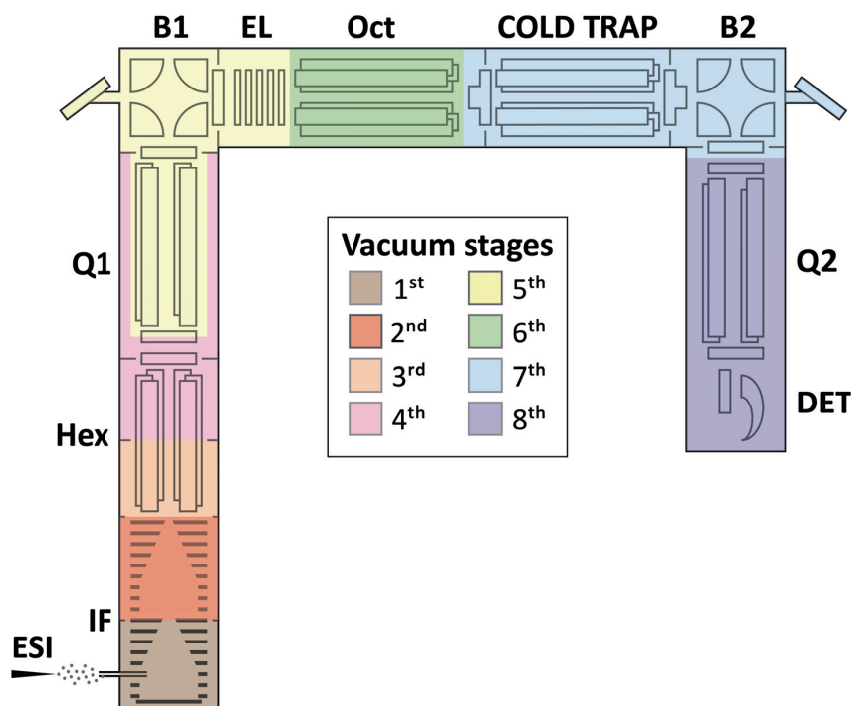
Figure 2.3. *Schematic view of the differential pumping stages of the tandem mass spectrometer.*

Table 2.1. Pressure in the vacuum chambers of the tandem mass spectrometer and their fore vacuum pressure (measured with the open inlet capillary and without He buffer gas injection). Letters in brackets denote specific type of the pump: O – oil pump; D – dry pump; M – membrane pump; T – turbomolecular pump.

Stage	Vacuum		Fore vacuum	
	Pump	Pressure, mbar	Pump	Pressure, mbar
1	[O] SV40 (Laybold vacuum)	5.4	NO	NO
2	[D] XDS 35 (Edwards)	$6.0 \cdot 10^{-1}$	NO	NO
3	[T] HiPace 300 (Pfeifer)	$1.5 \cdot 10^{-2}$	[O] DUO 35 (Pfeifer)	$4.8 \cdot 10^{-1}$
4	[T] TMU 521 (Pfeifer)	$1.4 \cdot 10^{-5}$	[M] MVP 055-3 (Pfeifer)	1.8
5	[T] TMU 521 Y P (Pfeifer)	$1.4 \cdot 10^{-8}$	[D] nXDS 10 (Edwards)	$3.4 \cdot 10^{-2}$
6	[T] TMU 071 P (Pfeifer)	$< 2 \cdot 10^{-9}$		$1.6 \cdot 10^{-2}$
7	[T] TMU 521 (Pfeifer)	$< 2 \cdot 10^{-9}$		
8	[T] TMU 261 (Pfeifer)	$< 2 \cdot 10^{-9}$		

2.1.4. RF Ion Funnel

An ion funnel (figure 2.4) was originally implemented in 1997 as a replacement for the ion transmission-limited skimmer because of its near lossless transmission of ions entering the first vacuum stage from an ESI source.[36] It is related to the stacked ring RF ion guide,[37] but consists of a series of cylindrical ring electrodes with progressively smaller inner diameters, which enables to efficiently focus the spatially dispersed ion cloud entering the funnel to a much smaller radial size for an efficient transfer through the conductance limiting orifice at the exit.
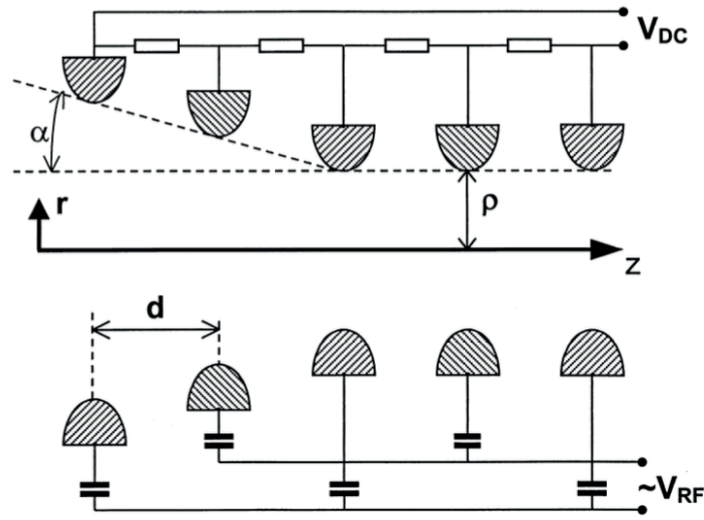
Figure 2.4. *Schematic view of the ion funnel (taken from Tolmachev et. al.[38]).*

The stacked ring arrangement with RF potentials of opposite polarity applied to adjacent electrodes creates an effective potential, V^*,[5, 37, 38] that corresponds to a steep potential gradient near the electrodes and a near field-free region over most of the internal volume:

$$V^*(r,z) = V_{trap} \left[I_1^2 \left(\frac{r}{\delta} \right) cos^2 \left(\frac{z}{\delta} \right) + I_0^2 \left(\frac{r}{\delta} \right) sin^2 \left(\frac{z}{\delta} \right) \right] \qquad \text{(Eq. 2.2)}$$

$$V_{trap} = \frac{V_{max}}{I_0^2(\rho/\delta)} \qquad \text{(Eq. 2.3)}$$

$$V_{max} = \frac{qV_0^2}{4m\omega^2\delta^2} \qquad \text{(Eq. 2.4)}$$

where V_{trap} is the axial effective potential well depth; V_{max} is the maximum value of the effective potential at $r = \rho$, $z = d(i + 1/2)$, $i = 0,1,...$; d is the spacing between the ring electrodes;

$\delta = d/\pi$; I_0 and I_1 are zero and 1st order modified Bessel functions, respectively; V_0 and ω are the amplitude and angular frequency of the RF potential; m and q are the mass and charge of an ion.

Another important feature of the RF ion funnel is the DC potential gradient applied to the ring electrodes to drive ions along the axis, which provided additional control relative to relying solely on gas dynamic effects.[39]

2.1.5. Multipole RF devices

Multipole RF ion traps and ion guides employ, typically, linear radiofrequency electrode geometries with discrete cylindrical symmetry. The time-dependent electric potential of an ideal two-dimensional multipole configuration of the order n with infinite extension along z-direction is given in cylindrical coordinates by:

$$V(r, \phi, t) = V_0 \, cos(n\phi) \left(\frac{r}{r_0}\right)^n sin(\omega t), \qquad\qquad \text{(Eq. 2.5)}$$

where V_0 is the RF amplitude, r_0 is the inscribed radius of the RF electrodes, and ω denotes the angular frequency.[40]

The motion of ion with mass m and charge q in an inhomogeneous RF field is described by the coupled differential equations, which have the exact analytical solution only for a quadrupole ($n = 2$) or Paul trap, because for $n > 2$ the equation of motion becomes nonlinear in the position coordinate. The best way to describe the ion dynamics is the use of the effective potential approximation, which was originally introduced for RF traps by Dehmelt.[41] If the oscillation frequency of the field is high, such that the amplitude of the ion periodic displacement (wiggles) is smaller than a typical scale of inhomogeneity of electrical field, the equation of motion can be treated within the adiabatic approximation.[42] According to the pioneering work of Teloy and Gerlich, the adiabatic approximation is valid if an adiabaticity parameter, μ, is smaller than 0.3.[37, 42, 43] The adiabaticity parameter is associated with a particular electrode configuration and is expressed by the equation:

$$\mu = \frac{n-1}{n} \frac{qV_0}{\varepsilon} \left(\frac{r}{r_0}\right)^{n-2} \qquad\qquad \text{(Eq. 2.6)}$$

The trajectory of an ion is then described in the adiabatic approximation as the superposition of a rapidly oscillating and a slow drift motion. The latter can be associated with a time-independent effective potential V^*, which, in the case of $2n$-multipoles, is expressed as a function of the radial position r by the following equation[40, 42]:

$$V^*(r) = \frac{1}{8} \frac{(qV_0)^2}{\varepsilon} \left(\frac{r}{r_0}\right)^{n-2} \qquad \text{(Eq. 2.7)}$$

where ε is the characteristic energy that is equal to:

$$\varepsilon = \left(\frac{1}{2n^2}\right) m\omega^2 r_0^2 \qquad \text{(Eq. 2.8)}$$

Thus, the $2n$-multipole is characterized by its inscribed radius r_0, as well as the amplitude V_0, and the frequency ω of the RF voltage applied to the electrodes. The form of the effective potential for three different $2n$-multipole geometries (quadrupole, hexapole and octupole) is represented in figure 2.5.
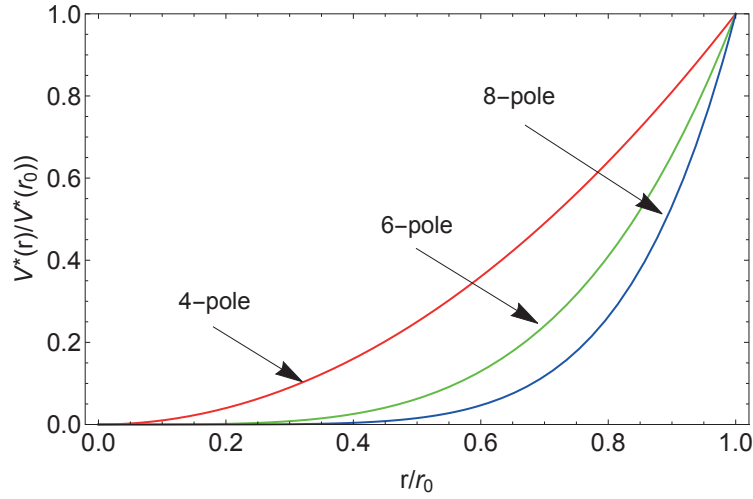
Figure 2.5. *Relative effective potentials as a function of the distance from the axis for a quadrupole (red line), hexapole (green line) and an octupole (blue line). The repulsive wall for the three cases rises as r^2, r^4, and r^6, respectively.*

2.1.6. Quadrupole Mass Filtering

Quadrupole mass filter was introduced by Paul and Steinwedel in the 1953,[44] who proposed to use electrodynamic, rather then magnetic field to separate charged particles of different mass-to-charge ratios.[45] This discovery became a milestone in the field of mass spectrometry and was followed by numerous studies devoted to the characterization of the device.[46-51]

Figure 2.6 shows a schematic view of a quadrupole mass filter which is made up of four circular or, ideally, hyperbolic rods aligned along the z axis and equally spaced on an inscribed circle of radius r_0, with a pair of opposite electrodes (on the x axis) set at a given potential Φ_0,

while the other pair (on the y axis) is set at a potential $-\Phi_0$. The potential applied to the rods is a sum of the DC component U and the RF potential V, oscillating with angular frequency ω. Φ_0 is thus expressed as:

$$\Phi_0 = U - V \cos(\omega t) \tag{Eq. 2.9}$$
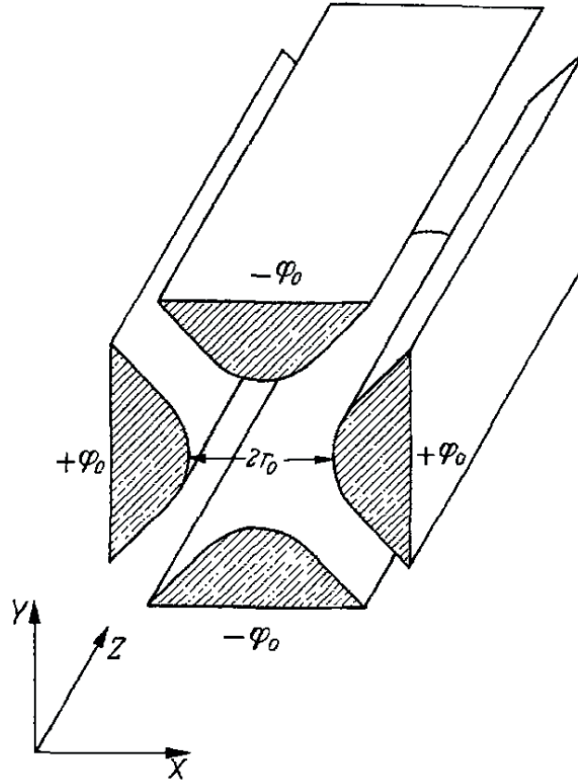
Figure 2.6. *Ideal quadrupole mass filter with hyperbolic electrodes that serve to create cylindrically symmetric field, being arranged at a distance r_0 from the z axis. (Adapted from Paul et al.[45])*

The saddle-shaped potential generated by two pairs of opposite electrodes is expressed by the following equation:

$$\Phi = \Phi_0 \frac{x^2 - y^2}{r_0^2} \tag{Eq. 2.10}$$

Since the potential is a periodic function of time the ion trajectory is alternately stable in one of the xz or yz planes, while diverging in the other. Using a high enough RF frequency, such that ion does not have enough time to escape in the xy plane, it is possible to confine an ion radially between the poles. This is the principle of operation of an RF-only multipole ion guide.[47]

Depending on the mass of the ion, the stability of its trajectory in the *x* and *y* directions differs substantially. Light ions have a tendency to follow the oscillatory field, while heavier ions are less influenced by it and, hence, show a relatively higher sensitivity to the DC voltage. Therefore, appropriate values of ω, *U,* and *V* should be chosen to stabilize the trajectories of ions within a particular mass range. The conditions of stability can be determined by solving the equations of motion for a singly charged ion in the quadrupole mass filter, which are obtained as follows. The force induced by an electric field is:

$$F_u = m\frac{d^2u}{dt^2} = -ze\frac{\partial\Phi}{\partial u}$$
(Eq. 2.11)

where *u* stands for either *x* or *y*. Substituting equations 2.9 and 2.10 to equation 2.11, differentiating, and rearrangement the terms leads to the Paul equation of movement, which has the form of the Mathieu equation. The solution is usually represented as a diagram (Figure 2.7), in which the stability regions are displayed as a function of the two Mathieu's dimensionless parameters, *a* and *q*, defined as:

$$a = \frac{8eU}{mr_0^2\omega^2}$$
(Eq. 2.12)

and

$$q = \frac{4eV}{mr_0^2\omega^2}$$
(Eq. 2.13)

In reality, the geometry (r_0) and frequency (ω) of a quadrupole are fixed, therefore the stability of ions is determined by the values of U/m and V/m, or by the proper selection of *U* and *V* for the ions of a particular mass-to-charge ratio (m/z). A mass spectrum is obtained by scanning simultaneously the values of *U* and *V* along a "mass scan line" of a fixed U/V ratio. From figure 2.7 it follows that only the ions in a narrow m/z range, where the mass scan line intersects the stability region, will have stable ion trajectories. Higher mass resolution is achieved by increasing the U/V ratio, which brings the mass scan line closer to the apex of the stability region.
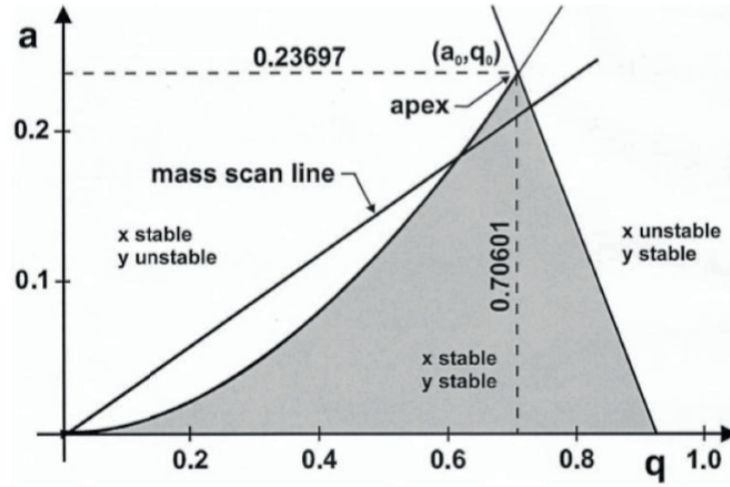
Figure 2.7. *Stability diagram showing the lower stability region in the (a,q) plane. (Taken from Blaum et al.[51])*

2.1.7. RF Ion Traps

As the number of poles increases, the effective potential (eq. 2.3) becomes steeper, and the field free region enlarges. The influence of the effective potential on the ion motion is depicted by the calculated ion trajectories in an octupole and a 32-pole ion traps (figures 2.8 a and b, respectively). The ions "see" electric field only in the vicinity of the rods and are, thus, confined in the radial direction of the device. The charged particles move undisturbed in the central part of the multipole, but, once they approach the electrodes, they undergo an oscillatory micromotion at the characteristic frequency of the RF field.[43]

From the figure 2.8 it follows that for higher-order multipoles, the wiggling motion occurs only in the close vicinity of the poles, leaving a large volume for non-accelerated trajectories. In the presence of a buffer gas collisions with the neutrals in the high electric field regions cause RF heating of the ions due to their fast oscillatory motion.[52, 53] On the other hand, the tighter confinement of ions in the lower order multipoles allows for a better intersection of the ion cloud with laser beams. Considering all the abovementioned factors, octupole ion trap has been shown to be extremely well suited for spectroscopic studies of cold ions.[3]
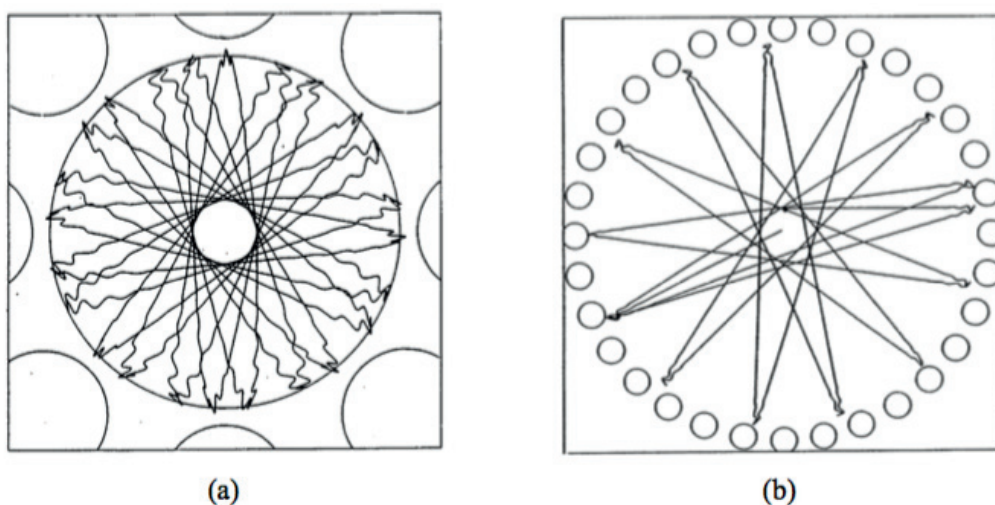
Figure 2.8. *Calculated trajectories of an ion in the potential of (a) an octupole and (b) a 32- pole RF traps (taken from Gerlich[37]).*

2.2. Spectroscopic Techniques

The experimental setup, described above, allows one to perform several types of measurements. The present chapter provides an overview of the most general techniques used in routine operations for UV and IR spectroscopy.

2.2.1. Photofragmentation Mass Spectrometry

Cold Ion Spectroscopy (CIS) records electronic and vibrational spectra of the mass-selected parent ions by monitoring the intensity of the light-induced photofragmentation signal as a function of the laser wavelength (so-called "action" spectroscopy). The choice for an "action" spectroscopy over photodetection techniques commonly used in condensed phase is determined by the low density of ions in the trap ($\sim 10^5$-10^6 cm^{-3}) compared to the one required for direct spectroscopic techniques ($\sim 10^8$-10^{10} cm^{-3}).

The resulting optical spectra depend, thus, not only on the absorption cross-section, but also on the fragmentation yield of the ion. The latter depends, in turn, on the photophysics following electronic excitation of the ion, energy of the UV photon, and an internal vibrational energy of the ion. The complex photophysics of biological ions makes an "action" spectroscopy essentially fragment-dependent.[54, 55] Therefore, prior to measuring optical spectra, one records photon-induced dissociation (PID) mass-spectra of parent ions.

The PID mass spectrum is recorded by fixing the UV laser wavelength in the spectral region with high absorption cross section, and scanning the analyzing quadrupole mass-spectrometer through the desires m/z range. The intensity of the resulting PID fragments and CID products are recorded in subsequent machine cycles to eliminate contribution of the undesired statistical fragmentation in an ion trap to the PID signal.

Typically, one chooses the most abundant fragment to record electronic spectra of ions. In the vibrational spectroscopy one often has to consider the influence of the vibrational pre-excitation by an IR photon prior to the electronic excitation on the branching ratios of different fragments and overall fragmentation yield. Recording UV and IR-UV PID signal at each m/z in a single scan allows choosing the fragment with the strongest response to the IR pre-excitation.

Figure 2.9 summarizes all UV and IR-UV double-resonance spectroscopic techniques that were developed for the conformational assignment of cold ions in the gas phase. In the following section they will be discussed in more details.

2.2.2. UV-photofragmentation Spectroscopy

UV photofragmentation spectra are recorded by monitoring the intensity of the selected fragment as a function of the UV photon wavelength. Once the fragment of interst has been chosen from the mass spectrum, one can proceed to measuring electronic photofragmentation spectrum of the parent ions by fixing the transmission of the quadrupole mass analyzer and scanning UV laser wavelength.

Figure 2.9a illustrates the principle of the UV photofragmentation spectroscopy. Collisionally cooled ions reside in their ground electronic state S_0. UV laser wavelength is scanned, and absorption of the UV photon by any conformer induces the photofragmentation signal, resulting in the conformer non-selective UV spectrum.

It is important to note, that action electronic spectroscopy is not identical to the direct absorption spectroscopy. Even if the UV PID spectrum is recorded by integrating the intensities of all fragments, it still does not take into account light emission, collisional energy dissipation, etc. However, the total absorption spectrum is beyond the scope of the CIS, and well-resolved electronic transitions are normally used only for the conformational assignment.
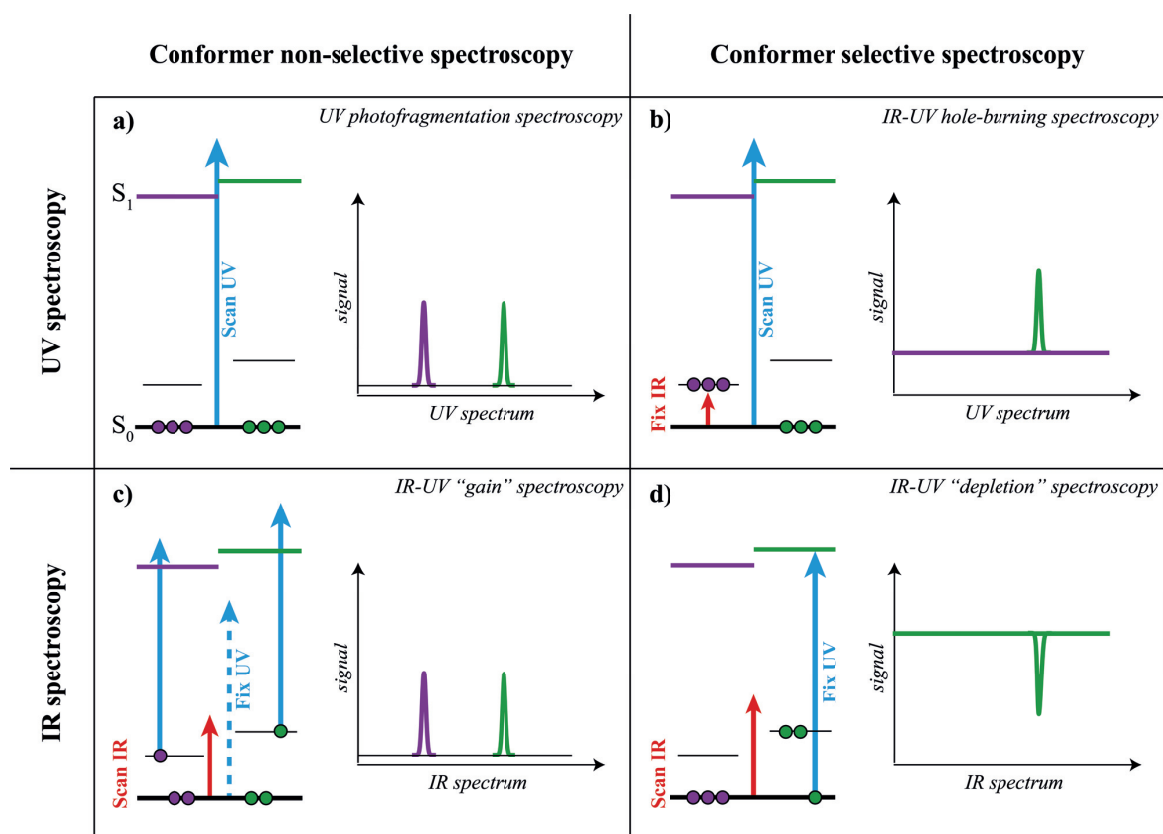
Figure 2.9. *Schematic description of the basic spectroscopic techniques for conformer-selective cold ion spectroscopy.*

2.2.3. Different Modes of IR-UV Spectroscopy

1. IR Pre-excitation of Cold Ions

Collisional cooling confines all ions in their ground vibrational state, thus elucidating thermal broadening. The vibronic transitions in the electronic spectrum are, thus, vibrationally resolved (not taking into account other possible sources of broadening) and unique for each conformer. In contrast, the electronic spectrum of ions at room temperature is unresolved because of the inhomogeneous broadening due to the internal vibrational energy.[56]

Excitation of the vibrational mode leads to the effect similar to the thermal broadening.[57] A pulse from an IR laser heats the ion internally, causing an inhomogeneous broadening and a redshift of electronic transitions, which are probed by a subsequent UV laser pulse. The IR-induced changes in UV absorption allow for measurements of three different types of spectra.

2. IR-UV Hole-Burning Spectroscopy

A UV "hole-burning" spectrum is measured by fixing the IR laser wavenumber at the conformer-specific vibrational transition, while the wavenumber of the UV laser is scanned (figure 2.9b). Absorption of an IR photon by a selected conformer converts all of its vibrationally resolved electronic transitions to a broad baseline. Since other conformers remain in their ground electronic state, their UV spectra remain unchanged. This allows for an assignment of the disappearing UV peaks to the selected conformer.[58-60]

Since electronic transitions are far more sensitive to even the slightest changes of the electronic configuration of the ion (the typical linewidth of the electronic transition is ~ 3 cm^{-1} while a UV photon wavenumber is $\sim 30\ 000$ cm^{-1}, thus the resolution power is $\sim 10^4$), the assignment of all of the electronic transition to one of the conformers allows a reliable identification of the number of conformers, present under the experimental condition.

3. IR-UV "Gain" Spectroscopy

An IR-UV "gain" spectrum is recorded by fixing the UV laser wavenumber to the red from the band origin, where absorption by cold ions is negligible, and scanning IR laser wavenumber (figure 2.9a). An IR pre-excitation of any conformer results in an increase in the UV fragmentation. An IR gain spectrum, thus, reflects the IR transitions of all abundant conformers of the ion in a single IR wavenumber scan.[2, 57, 60-62] Similar to the UV photofragmentation electronic spectrum, an IR-UV "gain" spectrum is non conformer-selective.

However, the assignment of all of the vibrational transitions to at least one of the conformers provides additional evidence that all of the conforms have been identified. Furthermore, an IR-UV "gain" spectrum is sometimes the only available vibrational spectroscopic technique.[62, 63] If the electronic transitions are lifetime-broadened and, thus, not vibrationally resolved, conformer-selective vibrational spectroscopy (see below) becomes impossible.

4. IR-UV "Depletion" Spectroscopy

An IR "depletion" spectrum is recorded by fixing the UV laser wavenumber at an electronic transition that is specific to one conformer of the studied ion (figure 2.9d). Absorption of a UV photon induces photofragmentation of this conformer. A preceding pulse from an IR laser, if absorbed by the same conformer, causes inhomogeneous broadening of the UV spectrum. Monitoring the resulting drop ("depletion") of the UV-induced photofragmentation as a function of IR wavelength generates the vibrational spectrum of this conformer.[1, 57, 60, 64-71]

For more than a decade the IR-UV "depletion" spectroscopy remained the only double-resonance spectroscopic technique that provided a benchmark conformer-selective vibrational spectra for validation of the theoretical calculations.[1, 66, 67, 70-75]

If another conformer absorbs an IR photon, its inhomogeneous broadening might cause an additional signal increase resulting in a "gain" spectrum. Most of the vibrational spectroscopic studies were reported for phenylalanine containing peptides because 1) the corresponding aromatic side chain has the longest excited state lifetime and, thus, the smallest linewidth of all aromatic amino acids[54, 56, 76] (Phe, Tyr, Trp); 2) it has twice less conformers, compared to a tyrosine containing peptides, because the latter can have two possible orientations of the OH group of the phenol ring; and 3) the fragmentation yield of this aromatic amino acid does not increase following the IR pre-excitation. The competing "gain" signal in the "depletion" spectrum is, thus, observed only in tyrosine containing peptides.

5. Strategy for the Full Conformational Assignment

Our strategy for finding all highly abundant conformers (families of conformers) of an ion is as follows. We first record conformer non-selective electronic and vibrational spectra of all conformers. Next, we measure the depletion spectrum, fixing UV laser at a well-resolved electronic transition (starting from the band origin). Choosing a single-standing vibrational transition in the resulting depletion spectrum that also appears in the conformer non-selective gain spectrum, allows for using an IR-UV hole-burning spectroscopy to assign all the resolved UV transitions to the selected conformer. We successively repeat such measurements until all of the prominent IR peaks in the gain spectrum and UV peaks in the electronic spectrum will be conformationally assigned.[60]

References

1. J. A. Stearns, S. Mercier, C. Seaiby, M. Guidi, O. V. Boyarkin and T. R. Rizzo, *J. Am. Chem. Soc.*, 2007, **129**, 11814-11820.

2. A. Y. Pereverzev, X. Cheng, N. S. Nagornova, D. L. Reese, R. P. Steele and O. V. Boyarkin, *J. Phys. Chem. A*, 2016, **120**, 5598-5608.

3. O. V. Boyarkin and V. Kopysov, *Rev. Sci. Instrum.*, 2014, **85**, 033105.

4. M. S. Wilm and M. Mann, *Int. J. Mass spectrom.*, 1994, **136**, 167-180.

5. R. T. Kelly, A. V. Tolmachev, J. S. Page, K. Tang and R. D. Smith, *Mass Spectrom. Rev.*, 2010, **29**, 294-312.

6. J. B. Fenn, *Electrospray Wings for Molecular Elephants*, Nobel Lecture, 2002.

7. K. Tanaka, *The Origin of Macromolecule Ionization by Laser Irradiation*, Nobel Lecture, 2002.

8.   J. Zeleny, *Phys. Rev.*, 1914, **3**, 69-91.

9.   J. Zeleny, *Phys. Rev.*, 1917, **10**, 1-6.

10.   M. Dole, L. L. Mack, R. L. Hines, R. C. Mobley, L. D. Ferguson and M. B. Alice, *J. Chem. Phys.*, 1968, **49**, 2240-2249.

11.   M. Yamashita and J. B. Fenn, *J. Phys. Chem.*, 1984, **88**, 4451-4459.

12.   M. Yamashita and J. B. Fenn, *J. Phys. Chem.*, 1984, **88**, 4671-4675.

13.   C. M. Whitehouse, R. N. Dreyer, M. Yamashita and J. B. Fenn, *Anal. Chem.*, 1985, **57**, 675-679.

14.   J. B. Fenn, M. Mann, C. K. Meng, S. F. Wong and C. M. Whitehouse, *Mass Spectrom. Rev.*, 1990, **9**, 37-70.

15.   M. Mann and M. Wilm, *Trends Biochem. Sci*, 1995, **20**, 219-224.

16.   G. Taylor, *Proc. R. Soc. London, Ser. A*, 1964, **280**, 383-387.

17.   L. Rayleigh, *Philos. Mag.*, 1982, **14**, 184-186.

18.   P. Kebarle and L. Tang, *Anal. Chem.*, 1993, **65**, 972A-986A.

19.   G. Schmelzeisen-Redeker, L. Bütfering and F. W. Röllgen, *Int. J. Mass Spectrom. Ion Processes*, 1989, **1989**.

20.   J. V. Iribarne and B. A. Thomson, *J. Chem. Phys.*, 1976, **64**, 2287-2294.

21.   B. A. Thomson and J. V. Iribarne, *J. Chem. Phys.*, 1979, **71**, 4451-4463.

22.   P. Kebarle and M. Peschke, *Anal. Chim. Acta*, 2000, **406**, 11-35.

23.   P. Kebarle, *J. Mass Spectrom.*, 2000, **35**, 804-817.

24.   A. T. Iavarone and E. R. Williams, *J. Am. Chem. Soc.*, 2003, **125**, 2319-2327.

25.   T. C. Rohner, N. Lion and H. H. Girault, *Phys. Chem. Chem. Phys.*, 2004, **6**, 3056-3068.

26.   S. Nguyen and J. B. Fenn, *PNAS*, 2007, **104**, 1111-1117.

27.   K. McQuinn, F. Hof and J. S. McIndoe, *Chem. Commun.*, 2007, 4099-4101.

28.   D. Touboul, M. C. Jecklin and R. Zenobi, *Rapid Commun. Mass Spectrom.*, 2008, **22**, 1062-1068.

29.   M. Karas, U. Bahr and T. Dülcks, *Fresenius J. Anal. Chem.*, 2000, **366**, 669-676.

30.   M. Wilm and M. Mann, *Anal. Chem.*, 1996, **68**, 1-8.

31.   S. Geromanos, G. Freckleton and P. Tempst, *Anal. Chem.*, 2000, **72**, 976-989.

32.   D. Smith, *IEEE Trans. Ind. App.*, 1986, **IA-22**, 527-535.

33.   R. B. Cole, *Cole Electrospray Ionization Mass Spectrometry: fundamentals, instrumentation and applications*, Willey, New York, 1997.

34.   B. N. Pramanik, A. K. Ganguly and M. L. Gross, *Applied electrospray mass spectrometry*, Marcel Dekker, New York, 2002.

35.   R. G. Cooks, *J. Mass Spectrom.*, 1995, **30**, 1215-1221.

36.   S. A. Shaffer, K. Tang, G. A. Anderson, D. C. Prior, H. R. Udseth and R. D. Smith, *Rapid Commun. Mass Spectrom.*, 1997, **11**, 1813-1817.

37. D. Gerlich, *Inhomogeneous RF Fields: a Versatile Tool for the Study of Processes with Slow Ions*, 1992.

38. A. V. Tolmachev, T. Kim, H. R. Udseth, R. D. Smith, T. H. Bailey and J. H. Futrell, *Int. J. Mass Spectrom. Ion Processes*, 2000, **203**, 31-47.

39. S. A. Shaffer, A. V. Tolmachev, D. C. Prior, G. A. Anderson, H. R. Udseth and R. D. Smith, *Anal. Chem.*, 1999, **71**, 2957-2964.

40. R. Wester, *J. Phys. B: At., Mol. Opt. Phys.*, 2009, **42**, 154001.

41. H. G. Dehmelt, *Adv. At. Mol. Opt. Phys.*, 1968, **3**, 53-72.

42. E. Teloy and D. Gerlich, *Chem. Phys.*, 1974, **4**, 417-427.

43. D. Gerlich, *Adv. Chem. Phys.*, 1992, **82**, 1.

44. W. Paul and H. Steinwedel, *Z. Naturforsch A*, 1953, **8**, 448.

45. W. Paul, H. P. Reinhard and U. von Zahn, *Zeitschrift für Physik*, 1958, **152**, 143-182.

46. W. M. Brubaker and J. Tuul, *Rev. Sci. Instrum.*, 1964, **35**, 1007-1010.

47. P. H. Dawson, *Quadrupole mass spectrometry and its applications*, Elsevier, Amsterdam, 1976.

48. P. H. Dawson, *Mass Spectrom. Rev.*, 1986, **5**, 1-37.

49. R. E. March, *J. Mass Spectrom.*, 1997, **32**, 351-369.

50. M. Nappi, C. Weil, C. D. Cleven, L. A. Horn, H. Wollnik and R. G. Cooks, *Int. J. Mass Spectrom. Ion Processes*, 1997, **161**, 77-85.

51. K. Blaum, C. Geppert, P. Müller, W. Nörtershäuser, E. W. Otten, A. Schmitt, N. Trautmann, K. Wendt and B. A. Bushaw, *Int. J. Mass Spectrom. Ion Processes*, 1998, **181**, 67-87.

52. D. Gerlich, 1994.

53. D. Gerlich, *Physica Scripta*, 1995, **T59**, 256-263.

54. G. Féraud, M. Broquier, C. Dedonder, C. Jouvet, G. Grégoire and S. Soorkia, *J. Phys. Chem. A*, 2015, **119**, 5914-5924.

55. F. O. Talbot, T. Tabarin, R. Antoine, M. Broyer and P. Dugourd, *J. Chem. Phys.*, 2005, **122**, 074310.

56. O. V. Boyarkin, S. R. Mercier, A. Kamariotis and T. R. Rizzo, *J. Am. Chem. Soc.*, 2006, **128**, 2816-2817.

57. N. S. Nagornova, T. R. Rizzo and O. V. Boyarkin, *Angew. Chem.*, 2013, **52**, 6002-6005.

58. V. A. Shubert and T. S. Zwier, *J. Phys. Chem. A*, 2007, **111**, 13283-13286.

59. P. M. Bialach, T. C. Martin and M. Gerhards, *Phys. Chem. Chem. Phys.*, 2012, **14**, 8185-8191.

60. A. Y. Pereverzev and O. V. Boyarkin, *PCCP*, 2017, **19**, 3468-3472.

61. Y. Inokuchi, O. V. Boyarkin, R. Kusaka, T. Haino, T. Ebata and T. R. Rizzo, *J. Am. Chem. Soc.*, 2011, **133**, 12256-12263.

62. N. L. Burke, J. G. Redwine, J. C. Dean, S. a. McLuckey and T. S. Zwier, *Int. J. Mass spectrom.*, 2015, **378**, 196-205.

63. N. S. Nagornova, PhD, ÉCOLE POLYTECHNIQUE FÉDÉRALE DE LAUSANNE, 2011.

64.   R. H. Page, Y. R. Shen and Y. T. Lee, *J. Chem. Phys.*, 1988, **88**, 5362-5376.

65.   J. R. Carney and T. S. Zwier, *J. Phys. Chem. A*, 2000, **104**, 8677-8688.

66.   J. A. Stearns, O. V. Boyarkin and T. R. Rizzo, *J. Am. Chem. Soc.*, 2007, **129**, 13820-13821.

67.   J. A. Stearns, M. Guidi, O. V. Boyarkin and T. R. Rizzo, *J. Chem. Phys.*, 2007, **127**, 154322.

68.   H. Fricke, A. Funk, T. Schrader and M. Gerhards, *J. Am. Chem. Soc.*, 2008, **130**, 4692-4698.

69.   H. Saigusa, S. Urashima and H. Asami, *J. Phys. Chem. A*, 2009, **113**, 3455-3462.

70.   T. R. Rizzo, J. A. Stearns and O. V. Boyarkin, *Int. Rev. Phys. Chem.*, 2009, **28**, 481 - 515.

71.   N. S. Nagornova, T. R. Rizzo and O. V. Boyarkin, *J. Am. Chem. Soc.*, 2010, **132**, 4040-+.

72.   T. R. Rizzo and O. V. Boyarkin, in *Gas-Phase IR Spectroscopy and Structure of Biological Molecules*, eds. A. M. Rijs and J. Oomens, Springer, 2015, vol. 364, pp. 43-98.

73.   T. K. Roy, V. Kopysov, N. S. Nagornova, T. R. Rizzo, O. V. Boyarkin and R. B. Gerber, *ChemPhysChem*, 2015, **16**, 1374-1378.

74.   N. S. Nagornova, M. Guglielmi, M. Doemer, I. Tavernelli, U. Rothlisberger, T. R. Rizzo and O. V. Boyarkin, *Angew. Chem.*, 2011, **50**, 5383-5386.

75.   M. Doermer, M. Guglielmi, P. Athri, N. S. Nagornova, T. R. Rizzo, O. V. Boyarkin, I. Tavernelli and U. Rothlisberger, *Int. J. Quantum Chem.*, 2013, **113**, 808-814.

76.   A. V. Zabuga, M. Z. Kamrath, O. V. Boyarkin and T. R. Rizzo, *J. Chem. Phys.*, 2014, **141**, 154309.

Chapter 3

IR-IR-UV Hole-Burning Spectroscopy

This chapter describes a novel experimental technique in cold ion vibrational spectroscopy, an IR-IR-UV Hole-Burning, which allows for recording conformer-selective vibrational spectra in cases when double-resonance technique fails to do so. We first describe the potential reasons precluding the use of the double resonance spectroscopy, alternative techniques that can overcome this obstacle as well as their drawbacks, and describe the IR-IR-UV Hole-Burning method. Next, we demonstrate the capabilities of this technique by solving structures of individual conformers of protonated amino acids Tryptophan and Histidine.

3.1. Introduction

3.1.1. Limitations of the Conformer-Selective IR-UV Spectroscopy

The IR-UV double-resonance cold ion spectroscopy (see Chapter 2) is a proven method for conformer-selective vibrational spectroscopy of neutral and protonated biomolecules.[1, 2] The conformer-specific spectra of neutral jet-cooled Trp,[3] trap-cooled protonated Tyr and Phe amino acids,[4] as well as many peptides with up to twelve residues[5-7] were recorded using this approach. The method relies on vibrational resolution in UV spectra, which, for large biomolecules, requires their cooling either in a supersonic expansion for neutrals[8] or in a cryogenic trap for ions.[9]

The vibrational resolution depends on the linewidth of the transition, which, in turn, depends on not only on the temperature, but also on the excited state lifetime. The UV spectrum of TrpH$^+$, for example, appeared unresolved even at $T = 10$ K[9] due to a significant lifetime broadening of the electronic transitions.[10] This fact prohibits the use of IR-UV double resonance for conformer-selective IR spectroscopy of protonated amino acids tryptophan and histidine.

The proposed mechanism of the inhomogeneous spectral broadening, on which the double resonance spectroscopy is based on,[11] assumes that the fragmentation yield of the electronically excited ions does not depend on their internal energy, and, thus, suggests that spectral broadening of cold ions caused by the absorption of an IR photon always leads to the depletion of the UV induced photofragmentation signal. This assumption is consistent with the reported behaviour of peptides with phenylalanine chromophore. [5-7] However, several peptides with tyrosine chromophore exhibit a dramatic increase of the fragmentation yield, which prohibits the use of double resonance spectroscopy.[12, 13]

In all such cases other conformer-specific features, rather than electronic transitions, have to be used as conformer labels. The next section gives an overview of the experimental techniques that use conformer-specific vibrational transitions for this purpose. In these cases one IR light source is required for conformer labelling, while the second is used for scanning.

3.1.2. Experimental Techniques for IR Transition Labelling

1. IR-IR Hole-Burning Spectroscopy of Tagged Ions

An alternative to the UV induced photodissociation of an ion is a tagging technique, in which absorption of an IR photon results in a dissociation of a weakly bound complex of an ion and a tag molecule.[14, 15] One apparent advantage of this method is that it does not require electronic excitation of ions and, hence, vibrational spectra can be recorded without UV laser. By monitoring the population depletion of the tagged species one measures a conformer non-specific vibrational spectrum of an ion. Recently, the group of Maier successfully used He tagging to measure near-IR conformers' non-specific spectrum of very cold, singly-ionized fullerene.[16] The conformers with noticeable differences in a collisional cross section (CCS) can be pre-selected by ion mobility to allow for conformer-selectivity.[15]

Alternatively, IR-IR hole-burning technique can be used for conformer-selective vibrational spectroscopy of cold ions.[17] It uses vibrational transitions, rather then electronic ones, to label conformers of an ion-tag complex. A pulse of a pump IR laser, fixed at a vibrational transition that is specific to one conformer, boils off the tag selectively from this conformer, such that the subsequent pulse of another tunable probe IR laser may add to this dissociation yield only if absorbed by other conformers. An IR spectrum of the targeted conformer is generated as the difference of the dissociation yields measured in alternative experimental cycles with the pump laser "on" and "off", as a function of IR wavelength.

The tagging technique relies on an assumption that the tag does not appreciably change the geometry and the vibrational frequencies of the bare ions. This aspect limits the possible tags to small, weakly bound molecules or rare gas atoms. However, in some cases even small tags may cause detectable shifts of vibrational frequencies.[18, 19] Weakly bound tags require very low temperatures to suppress thermal dissociation of metastable complexes and, hence, make the measurements of IR-induced dissociation background-free. In practice, this effect cannot be fully avoided, thereby limiting sensitivity of the measurements. In addition, small tags like H_2, D_2, or He require higher mass resolution to distinguish large bare ions from their complexes with a single tag. Leavitt *et. al.* demonstrated IR-IR hole-burning scheme with D_2-tagged biomolecular ions.[20] Later, Roithova *et. al.* have used the same technique with He and Ar tagged reactive ions.[18]

2. IR-IR-UV Triple Resonance Spectroscopy

A similar approach was previously demonstrated on neutral complexes, where UV light was used for non-selective photoionization of species in their vibrational ground state.[21] The use of an IR-UV depletion spectroscopy is prohibited in this case because of unresolved electronic transitions of the two conformers. Thus, the conformer-specific vibrational transitions were used for conformer labelling. Prior to the UV photoionization, two subsequent IR laser pulses were shot: the first laser wavelength was fixed at the conformer-specific transition of one conformer, while the other was scanned. Internal heating of cold complexes by a fixed-wavelength IR laser pulse removes a fraction of thermal population from the ground state, resulting in a constant depletion of the photoionization signal. Additional signal depletion, resulting from the internal heating of all other conformers by a second IR laser pulse, was recorded. The difference of the two spectral measurements reflects the vibrational transitions associated with the conformer, labelled by a first IR laser pulse.

This technique is only applicable for analytes with narrow electronic transitions, for which internal heating causes significant inhomogeneous broadening and a consecutive signal depletion. If transitions are, for example, lifetime-broadened the depletion induced by an IR pre-excitation cannot be detected. Another important disadvantage is a high background, making it difficult to record minor vibrational transitions with intensities comparable to the signal noise.

3.2. IR-IR-UV Hole Burning Technique

3.2.1. Description of the IR-IR-UV Hole-Burning Technique

IR-IR-UV hole burning technique combines the benefits of IR-IR tagging and IR-UV double-resonance gain techniques, enabling measurements of conformer-specific IR spectra with near-zero background. This combination does not require the tagging of the bare ion, as it employs UV photofragmentation, and relaxes the need for vibrational resolution in the UV spectrum of the ion because the conformational labelling employs IR transitions.

Figure 3.1 explains the principles of the IR-IR-UV Hole-Burning spectroscopy[22].   In opposite to the signal depletion approach,[21] in the IR-IR-UV hole-burning technique the UV laser is tuned to the red from a broad UV absorption band, so that the fragmentation signal of the initially prepared ensemble of cold ions with conformations **A** and **B** is negligible (fig. 3.1a). (NOTE: in the present analysis we assume for the sake of simplicity that the analyte has only two possible structures).

Absorption of the IR photon by any conformer results in an inhomogeneous spectral broadening,[11] which leads to a significant increase of UV-induced photofragmentation. Scanning the wavelength of a probe IR laser, while keeping the UV wavelength fixed, thus, generates an IR "gain" spectrum of all available conformers of an ion at once (fig. 3.1b). In contrast to the depletion spectroscopy, gain spectra are built on a near-zero baseline, drastically improving the signal-to-noise ratio in measurements of conformer-nonselective spectra.

To disentangle such a gain spectrum and generate vibrational spectra for each conformer, an additional pump IR laser is required. The pump IR OPO is tuned to a well-resolved vibrational band, specific to one conformer (conformer **B** in fig. 3.1c). A high-energy pulse of the pump IR OPO laser selectively saturates a chosen transition creating an ensemble of ions in new state, in which ions of a selected conformer **B** are internally pre-heated, while conformer **A** remains cold. Irradiation of this new ensemble with the UV laser pulse generates a constant non-zero fragmentation signal, which stems only from the conformer **B** tagged by the pump IR laser.

Figure 3.1d shows the IR-IR-UV hole-burning spectrum, which is essentially a "gain" spectrum of the selectively pre-heated ensemble. If the energy of the pump IR OPO pulse is enough to saturate the corresponding transition of the IR laser-tagged conformer **B,** its UV-induced photodissociation yield of the pump IR pre-heated ions does not change after absorption of the second photon from the probe IR OPO laser pulse. Therefore, all vibrational transitions associated

with the conformer **B** disappear in the IR-IR-UV hole-burning spectrum. Since the absorption of conformer **A** does not change after the pump IR OPO pulse was fired, its IR "gain" signal ads to the constant baseline from the conformer **B**. Thus, scanning the probe laser across the whole IR region, while simultaneously keeping the pump IR and UV lasers fixed, generates the IR-IR-UV gain spectrum that contains only the bands associated with all other conformers, except the selected one, on top of this baseline.
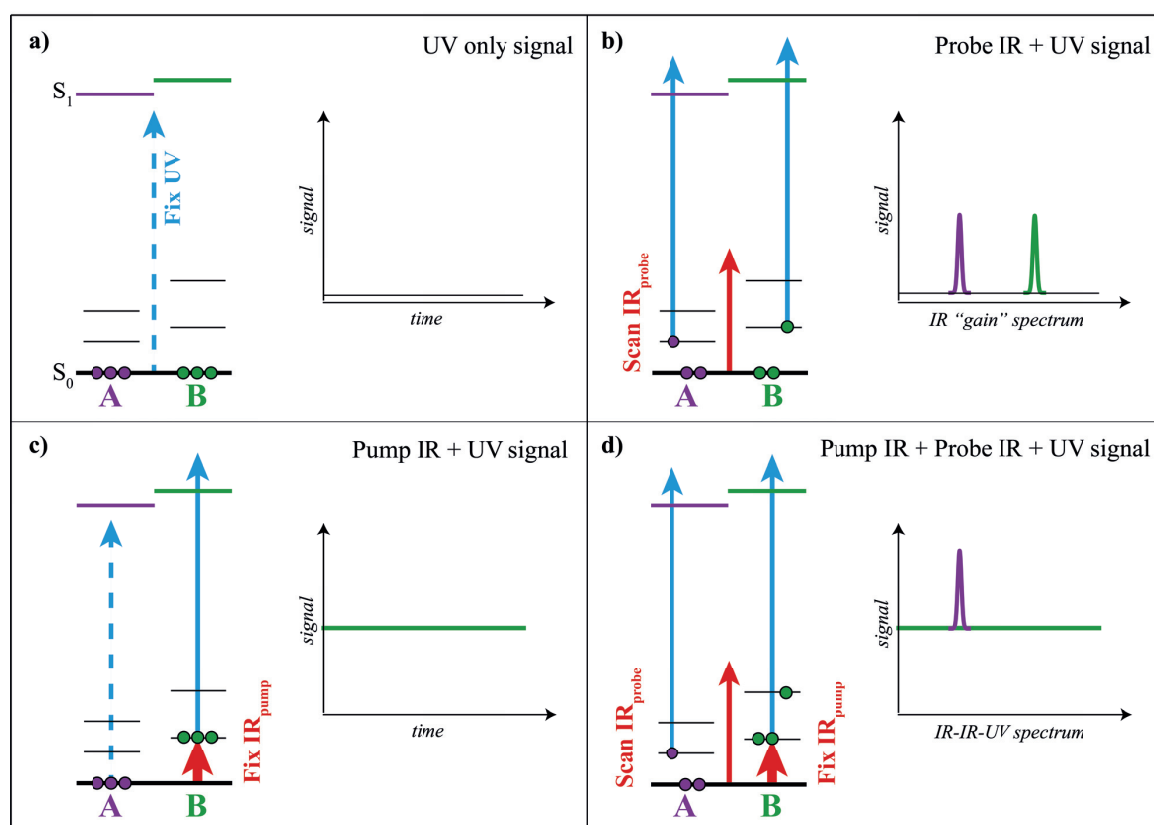

Figure 3.1. *Schematic explanation of the signal formation principles in the IR-IR-UV hole-burning spectroscopy: (a) UV-only signal; (b) probe IR-UV "gain" signal; (c) pump IR-UV signal; (d) pump + probe IR-IR-UV hole-burning signal.*

Similar to the IR-IR tagging technique, the vibrational spectrum of the targeted conformer, that is associated with the pump IR laser-tagged transition, is generated as the difference of the IR-UV "gain" and IR-IR-UV hole-burning spectra, measured as a function of probe IR OPO wavelength.

In some cases saturation of the vibrational transitions requires very high power of the pump IR laser pulse. This phenomenon can be observed when the bandwidth of UV absorption spectrum of cold ions is much broader compared with the spectral shift induced by the absorption of the first IR photon, which is a common feature for the peptide bond absorption spectrum (see Chapter 4) and was also observed in a protonated amino acid histidine (see Section 3.3). As a result, fragmentation yield of the pre-heated conformer may increase after absorbing another photon from a probe IR laser. This results in an additional weak signal gain from the labelled conformer in the IR-IR-UV spectrum. This gain is not identical to the spectrum of cold ions, since the vibrational transitions of "warm" ions broaden and shift to the red. Thus, assignment of the conformer-specific transitions might require more careful analysis in such complicated cases.

3.2.2. Different Measurement Modes

In the present section we discuss the possible measurement schemes for generating the conformer-specific spectra with the IR-IR-UV hole-burning spectroscopy. There are five possible types of measurements that can be done in one operation cycle of our tandem mass spectrometer, depending on the particular configuration of the one UV and two IR OPO laser pulses, which are summarized in Table 3.1.

Table 3.1. *Five possible types of signals that can be measured in a single machine cycle.*

Combination	Pump IR (fixed)	Probe IR (scanning)	UV (fixed)	
1	**OFF**	**OFF**	**OFF**	Parent ion signal
2	**OFF**	**OFF**	**ON**	Background signal from cold ions (ideally close to 0)
3	**ON**	**OFF**	**ON**	Constant fragmentation signal from the pumped conformer
4	**OFF**	**ON**	**ON**	All-conformer IR-UV gain signal
5	**ON**	**ON**	**ON**	IR-IR-UV hole-burning signal

The ion signal counting in our experimental setup scheme allows us to record any two types of signals in two consequent machine cycles. The combination 4/1 allows recording an all-conformer gain spectrum, normalized over the parent ion signal. Similarly, the combination 5/1 corresponds to the IR-IR-UV hole-burning signal, normalized over the parent ion signal, while the combination 5/3 allows to subtract the constant baseline from the IR-IR-UV hole-burning signal.

As was mentioned in the previous section, the vibrational spectrum of the targeted conformer is generated as the difference of the IR-UV "gain" and IR-IR-UV hole-burning spectra, measured as a function of the probe IR OPO wavelength. One of the possible solutions is to record them separately (combinations 4/1 and 5/1). However, due to the parent ion signal saturation in our channeltron ion detector, the parent ion signal and the resulting IR-UV or IR-IR-UV signals are not linearly dependent, thus the latter cannot be subtracted directly. Instead, one has to scale the intensities of some transitions, but the scaling coefficient might vary in time due to the long-term changes in the parent ion signal. Furthermore, such approach doubles the time required to generate one conformer-selective vibrational spectrum.

In the current analysis we generate the conformer-selective spectrum in a single scan by measuring the combination 4/5 in the two subsequent machine cycles. The corresponding laser pulses must be fired as shown in figure 3.2. The ion trap is filled in a 10 Hz cycle. The UV laser and the scanning probe IR laser run also at 10 Hz frequencies, while the pump IR laser runs at 5 Hz frequency. All laser pulses are separated by 200 ns time delays. In such configuration the signal is not normalized over the parent ion signal, however, the long term changes in nESI spray can be detected by watching for the background signal in the IR-IR-UV measurement.
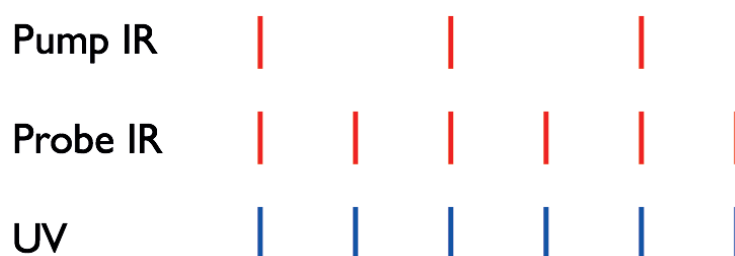

Figure 3.2. *Laser pulse sequence for generating conformer-selective vibrational spectra in the IR-IR-UV hole-burning spectroscopy.*

In the following sections we demonstrate the IR-IR-UV hole burning spectroscopy of the protonated amino acids tryptophan ($TrpH^+$) and histidine ($HisH^+$), for which the double resonance depletion spectroscopy is precluded due to the lack of vibrational resolution in their electronic spectra.

3.3. IR-IR-UV Hole-Burning Spectroscopy of TrpH$^+$

3.3.1. Introduction

Among all aromatic amino acids, tryptophan (Trp) exhibits the largest UV absorption cross section[23] and, in solution, exhibits the highest fluorescence quantum yield.[24] This residue, therefore, represents a benchmark photoactive building block of proteins. The local environment of Trp in biomolecules, including the local electrical field of neighbouring charges, strongly influences its fluorescence wavelength,[25] decay rate,[26] and quantum yield.[27] This property makes Trp a natural optical probe for studying protein structure and dynamics,[28, 29] interaction with membrane-mimicking environment,[30] as well as cancer diagnostics.[31]

The first spectroscopic investigations of the amino acids in the gas phase started in the mid 1980's in Levy's group with studies of neutral tryptophan.[32-36] A thermospray jet of tryptophan solution was injected into the throat of a pulsed nozzle producing a seeded supersonic free jet of neutral Trp in a carrier gas. In 1985 a resonantly enhanced two-photon ionization (R2PI) electronic spectrum of neutral Trp cooled in a supersonic expansion was reported.[33] R2PI process involves the absorption of two photons by a molecule, where the first photon excites the species to an intermediate electronic state and absorption of a second photon results in the ionization. Although ions are detected as a final product in a mass spectrometer, the ionization signal reflects the absorption spectrum of the resonant intermediate state.

A year later, six conformers of neutral Trp were identified based on the different response of spectral features of different conformers to power saturation[34] and confirmed by the dispersed fluorescence studies.[35] Different conformers were shown to not interconvert in the excited state during the fluorescence lifetime. The time-resolved spectroscopy of tryptophan conformers showed different lifetimes, in consistence with the multiexponential decay.[36] These observations supported the rotamer model, explaining the non-exponential fluorescence decay of Trp in aqueous solution. In 2001 Snoek *et al.* identified and structurally solved several conformers of neutral Trp in the gas phase.[3]

In contrast, protonated tryptophan (TrpH$^+$) has remained the last ionic aromatic amino acid for which the intrinsic structures of the low-energy conformers have not been unambiguously determined. The main challenge in validation of the predicted structures of TrpH$^+$ [37-41] has been a lack of measured conformer-specific molecular properties, such as vibrational spectra, which could be compared with calculated values.

In the present analysis, the vibrational spectra of TrpH$^+$ conformers are investigated with a combination of IR-IR-UV hole-burning photofragmentation spectroscopy and *ab initio* calculations of anharmonic vibrational spectra. The experimental half of this study provides conformer-resolved vibrational spectra using cold IR-IR-UV hole-burning spectroscopy. The computational half serves to identify these conformers, explain the source of their stability, and reveal the connection between this stability and the characteristic vibrational features. The main result of this analysis is that the intramolecular interactions within this biomolecule provide unique, conformer-specific vibrational signatures that allow for definitive assignment of the dominant structures. These signatures, in turn, illuminate the intramolecular interactions that are responsible for the dominant conformers' stability.

3.3.2. Computational Methods

The theoretical calculations of TrpH$^+$ were performed in the group of prof. Steele (University of Utah).[22] The computational analysis of TrpH$^+$ was divided into three components, which included (1) the search for — and benchmarking of — conformer structures and energies, (2) computation and assignment of anharmonic vibrational spectra of the resulting conformers, and (3) identification of the intramolecular interactions that are responsible for the strongly anharmonic vibrational signatures.

1. Conformer Structures and Energies

Because of the rigid indole ring contained in Trp, all of the relevant conformational flexibility originates from the 2-aminopropanoic acid (alanine-like) ligand. In this portion of the molecule, three dihedral angles exhibit conformational flexibility (figure 3.3), and each of these angles was found to exhibit two inequivalent structural minima. Therefore, eight possible low-energy conformers were generated from a manual search of this conformational space. Details of these conformers will be discussed below. A basin-hopping Monte Carlo search,[42] using a crude HF/3-21G potential surface, was also performed. The only additional stable isomer found through this more exhaustive search was a fused-ring species, which was originally reported in Ref[37]. The more accurate energy calculations in the present work confirm that this latter species is not energetically (or spectroscopically) relevant and will not be considered further in this analysis.

Relative energies of the resulting conformers were computed with a series of methods and basis sets. The more computationally economical methods included Hartree-Fock (HF) theory, second-order Møller-Plesset perturbation theory[43] within the resolution-of-the-identity

approximation[44-48] (RI-MP2), and a series of density functionals, including M05-2X,[49] B97M-V,[50] and B3LYP.[51, 52] The final benchmarks were computed using coupled-cluster theory[53, 54] with single, double, and perturbative triple excitations, within the frozen natural orbital approximation[55, 56] [FNO-CCSD(T)]. For the latter, a 99% natural orbital occupancy cutoff[57] and FNO-MP2 correction[58, 59] was employed, which was confirmed to be converged. Core orbitals were also frozen in all correlated calculations. Tested atom-centered Gaussian basis sets included 6-31++G**,[60-63] cc-pVDZ,[64] aug-cc-pVDZ,[65] and cc-pVTZ. Final benchmarks are reported as FNO-CCSD(T)/cc-pVTZ energies on CCSD/cc-pVDZ optimized structures. All quantum chemistry calculations in this work were performed with the Q-Chem quantum chemistry software package.[66]
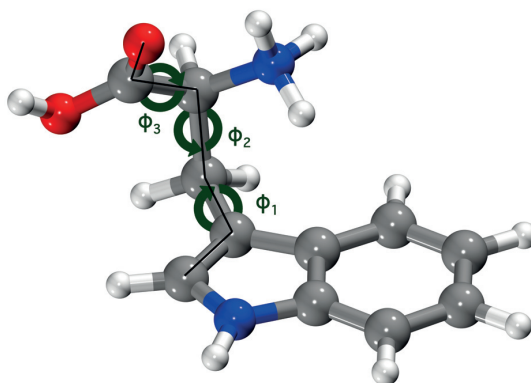

Figure 3.3. *Available conformational flexibility in TrpH$^+$. Indicated are dihedral angles about which structural searches were performed and the atoms to which these dihedral conventions are referenced. The same dihedral labeling is used throughout this study.*

2. Anharmonic Spectra

Preliminary harmonic analyses of the vibrational spectra of the eight conformers suggested that harmonic frequencies, using common density functionals, were insufficient to reproduce the experimental spectra, even when empirically scaled.[67, 68] The inhomogeneous nature of the anharmonicity in this complex is simply not amenable to a single scaling factor. Instead, anharmonicity was included via vibrational analogues of methods used in electronic structure theory. Mode correlation was included via vibrational second-order degenerate perturbation theory[69] (VDPT2), on top of vibrational self-consistent field[70-72] (VSCF) theory states and energies. Of the 78 total vibrational modes, only the 40 highest-frequency modes (above 1100 cm^{-1}) were included in the anharmonic simulations. The molecular potential was computed within the n-mode

expansion,[70] truncated in this work at 2-mode couplings. In each dimension, 11 Gauss-Hermite quadrature points of the potential were computed with dual-basis RI-MP2/cc-pVTZ,[73, 74] using equilibrium structures with the same level of theory. In order to refine the resulting spectra, CCSD(T)/cc-pVTZ corrections were applied to the one-mode scans of the bright transitions that will be discussed in Section 3.3.3.

Although normal coordinates were initially used to generate these spectra, the recently developed local-mode approach[75] was found to yield computed spectra closer to experiment and assist in interpretation of the resulting modes. Two bands were separately localized: one with frequency above 2800 cm^{-1} and one with frequency between 1390 cm^{-1} and 1520 cm^{-1}, corresponding to the same regions in which the IR-IR-UV hole-burning spectroscopy experiments were performed.

3.3.3. Experimental Results

1. In-source CID

Collisions with the residual gas in the first sections of a differentially pumped mass spectrometer cause internal heating of ions and may lead to their fragmentation. The Collisional Induced Dissociation[76] (CID) is widely used in mass spectrometry for sequencing of peptides and proteins. Additional thermal energy, acquired by the ion during a collision, is uniformly distributed between all of its vibrational modes, thus increase of the ion size decreases the average energy per mode and, hence, the dissociation probability. Normally, while working with relatively large ions (> 400 Da), the in-source CID is barely observed.

For small ions like, single amino acids, the collisional heating, however, leads to the extensive in-source fragmentation and, potentially, to the gas phase conformational rearrangement. The relation between the cold gas-phase and the room-temperature solution structures is still under debate, although it is generally believed, that ion desolvation in gentle conditions followed by a rapid cooling leads to a kinetic trapping of the liquid phase structures, because the internal energy of an ion is not enough to overcome energy barriers separating local minima on potential energy surface[77, 78] (PES).

Figure 3.4 shows the CID mass spectrum recorded on the 1st detector at typical source conditions: pressure in the high-pressure ion funnel (HPIF) 5 mbar, 0.8 mbar in low-pressure ion funnel (LPIF), and 0.01 mbar in hexapole ion trap; RF amplitudes are ∼ 100 V in HPIF and LPIF

and 200 V in hexapole. Each data point was averaged over 10 measurements, mass increment was 0.5 Da, and resolution on Q1 was set to 4.7.
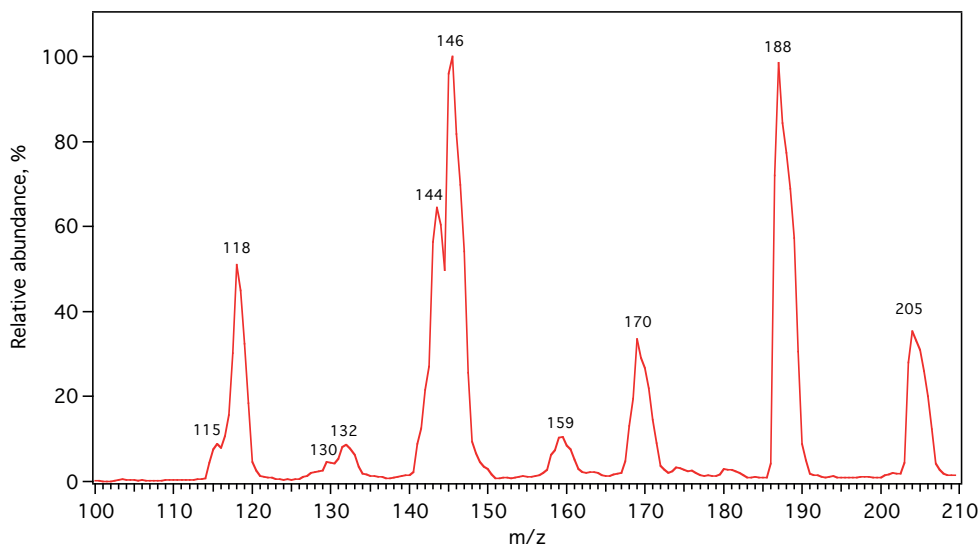

Figure 3.4. *CID mass spectrum of TrpH$^+$ measured on 1st detector at low pressure and high RF voltages in the ion funnels.*

The CID mass spetrum in figure 3.4 is similar to ones reported previously for protonated tryptophan. The low energy CID experiments showed that the most favourable statistical dissociation channel of TrpH$^+$ is ammonia loss, resulting in a [Trp + H - NH$_3$]$^{1+}$ ion with m/z = 188 Da.[79, 80] In 2004 Lioe *et al.*[38] showed that the lowest energy structure of this ion is a spirocyclopropane derivative formed by a nucleophilic attack from the C$_3$ position of the indole ring, which was later confirmed with IRMPD experiments.[81] Another abundant ion with m/z = 146 Da is a secondary fragmentation product corresponding to the ketene (CH$_2$CO) loss following the elimination of ammonia [Trp + H – NH$_3$ – CH$_2$CO]$^{1+}$. El Aribi *et al.*[82] have done more profound analysis of the fragmentation patterns of aromatic amino acids at high collisional energies. Table 3.2 summarizes the origin and relative abundance of the fragmentation products based on previous MS studies of tryptophan.[38, 79-82]

The presence of secondary fragmentation products in the CID mass spectrum indicates that the internal energy, accumulated by an ion during collisional heating, is above the dissociation threshold. Collisional energy depends on 1) the axial acceleration of ions by an electrostatic field, 2) the oscillatory motion in RF fields, and 3) the pressure in the first stages of a differentially pumped mass spectrometer, i.e., the average time between collisions. In order to reduce the

collisional heating, the influence of these parameters on the fragmentation yield of TrpH$^+$ was investigated. First of all, the RF heating in a hexapole trap was examined, because the accumulation time of ions is approximately 100 ms, therefore, if the conditions are harsh an extensive dissociation may occur. At no conditions, however, do hexapole RF frequency and amplitude affect the relative abundance of the secondary fragment with m/z = 146 Da, thus they were chosen so that to increase the ion signal: ν_{HEX} = 1.67 MHz and A_{HEX} = 230 V. Similarly, variation of the axial electric field gradient does not result in any visible changes in the fragmentation mass spectrum.

Table 3.2. Neutral Fragments Loss in CID of Protonated Tryptophan.[38, 79-82]

Fragment mass, Da	Neutrals lost	Relative abundance, %
188	NH_3	98.7
170	(NH_3+H_2O)	33.6
159	(H_2O+CO)	10.4
146	(NH_3+CH_2CO)	100
144	(NH_3+CO_2)	64.4
132	$(H_2O+CO+HCN)$	8.6
130	$(H_2O+CO+HCN+H_2)$	4.4
118	(NH_3+CH_2CO+CO)	51.1
115	$(NH_3+CH_2CO+CO+H_2+H)$	8.9

In contrast, the influence of the RF fields in HPIF and LPIF is crucial. In order to decrease the RF heating, the amplitudes in HPIF and LPIF were decreased to the limit, where the total ion current measured on the rods of the hexapole trap begins to drop, which correspond to the RF voltage 40 – 50 V both in HPIF and LPIF.

The mass spectrum measured with the low RF voltages and the maximum pumping speed in the ion funnels is shown in figure 3.5. As can be seen from the CID mass spectrum, the collisional energy is reduced and only energetically the most fragile fragmentation channel (ammonia loss, m/z = 188 Da) is observed. The destabilization of the lower mass ion trajectories and their escape from the ion funnels due to decreased RF amplitudes is unlikely, because the total ion current on the hexapole rods does not decrease. At the final step, the pressure in both sections of the ion funnel was increased in order to decrease the average time between collisions, and, hence, the collisional speed, induced by axial acceleration in the source. The pressure increase in HPIF up to P_{HPIF} = 10

mbar significantly decreases the fragmentation efficiency. In LPIF the pressure was increased to P_{LPIF} = 2.14 mbar - the maximum allowed pressure, limited by the turbomolecular pump in the following hexapole section. The corresponding mass spectrum (figure 3.6) shows that the in-source CID is effectively suppressed and, hence, the collisional heating is at least below the dissociation threshold. This does not necessarily imply the absence of the structural deformations upon heating, however the in-source CID is the best available measure of the "gentleness" of our ion source conditions. All the data for TrpH$^+$, described below, were obtained under these conditions.
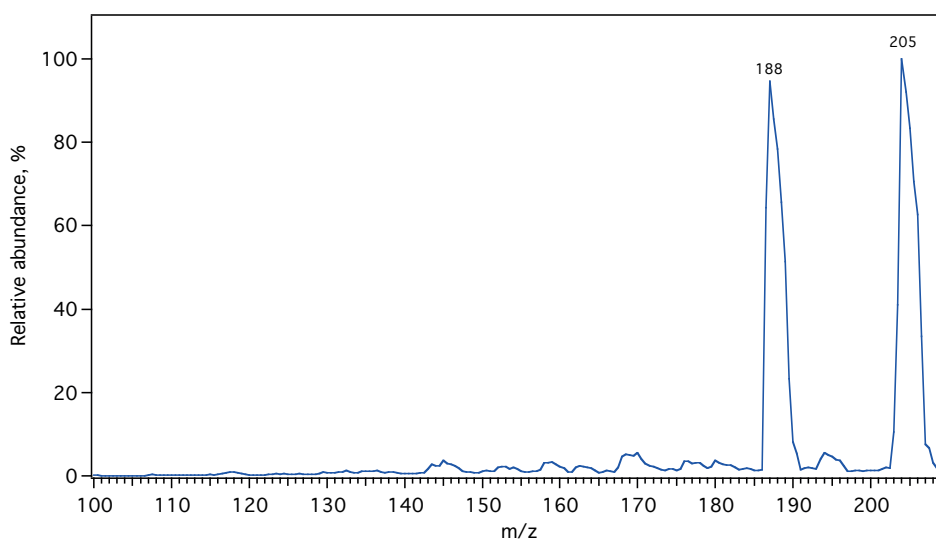

Figure 3.5. *CID mass spectrum of TrpH$^+$ measured on 1st detector with low pressure and low RF voltages in the ion funnels.*
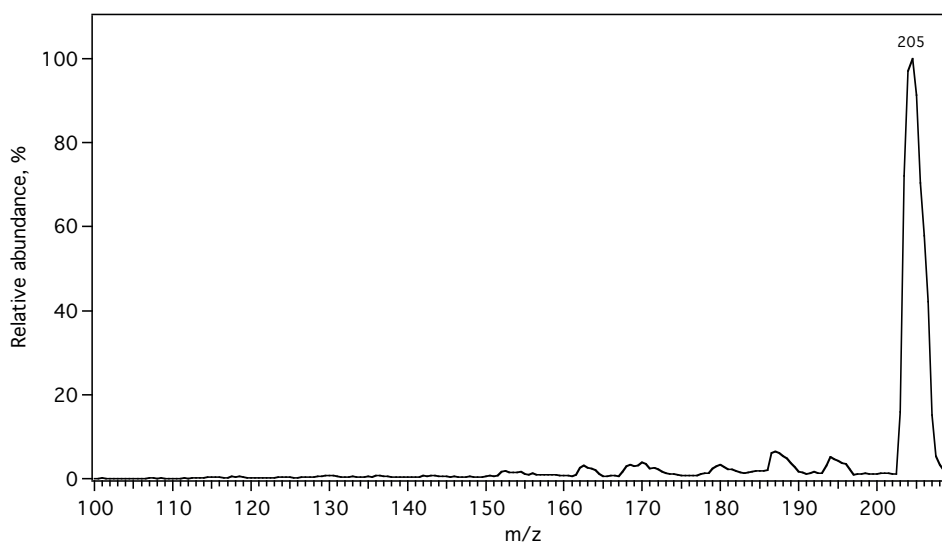

Figure 3.6. *CID mass spectrum measured on 1st detector with high pressure and low RF voltages of the ion funnels.*

48

2. *Internal Energy Dependence of TrpH$^+$ Photodissociation*

IR and UV spectra are recorded by monitoring the intensity of some fragment(s) while scanning the laser wavelength. In order to choose the best fragment for spectroscopic measurements, UV PID mass spectra of TrpH$^+$ were recorded 1) at T = 6 K and 2) 200 ns after IR pre-excitation (figure 3.7, blue and red lines, respectively). The photofragmentation pathways of TrpH$^+$ were studied in much detail.[83-88] These studies have confirmed that the ammonia loss fragment (m/z = 188 Da) is, indeed, a statistical dissociation product following an internal conversion of energy to the ground state, and that the fragment with m/z = 146 Da corresponds to the subsequent ketene loss from the m/z = 188 Da fragment.

Vibrational preheating of cold ions by an IR OPO laser pulse increases the UV fragmentation yield of the fragment $[Trp + H - NH_3 - CH_2CO]^{1+}$ with m/z = 146 Da by more than a factor of five, which makes it the best signature of IR photon absorption by the parent ions. All the following spectra were taken by monitoring m/z = 146 Da fragment, with resolution Q3 = 4.5.

One can also compare PID MS of TrpH$^+$, excited by IR photons in 6 and 3 μm regions. The resulting mass spectra are shown in figure 3.8.
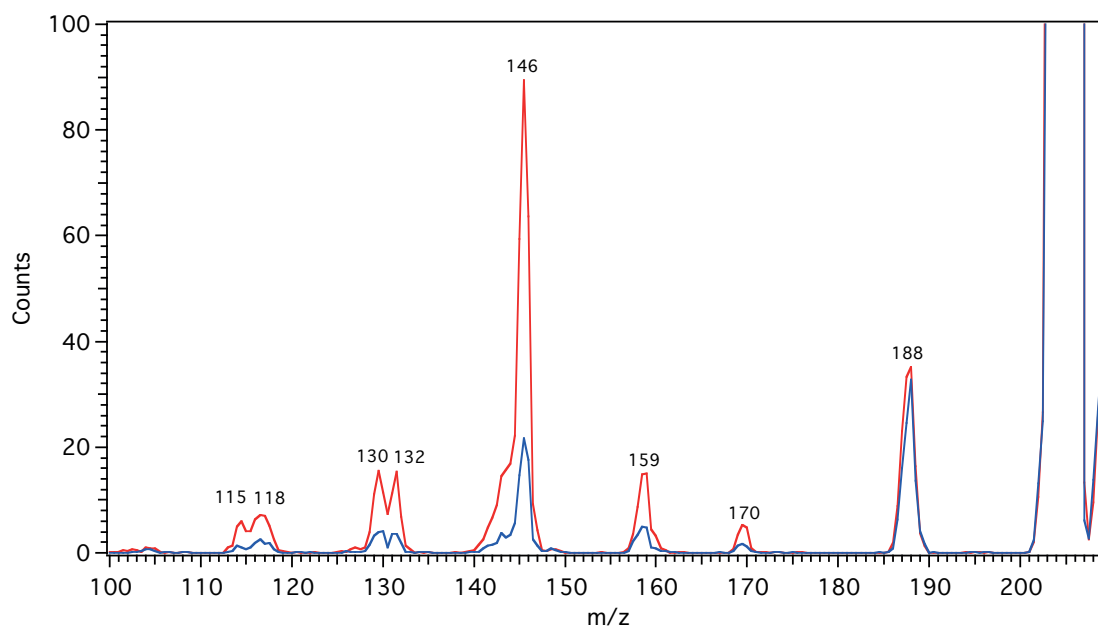

Figure 3.7. *UV photofragmentation mass spectra of cold (black) and IR preheated (red) TrpH$^+$ ions. UV wavenumber was fixed at 34400 cm^{-1}; IR wavenumber was fixed at 3338.6 cm^{-1}.*
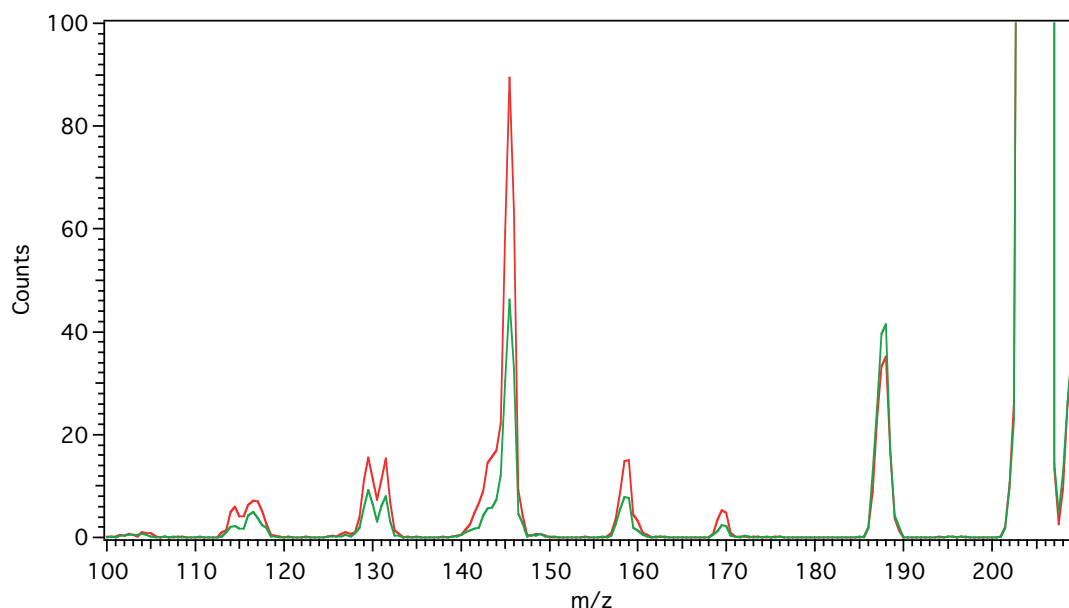
Figure 3.8. *Photofragmentation mass spectra of TrpH$^+$ pre-heated by an IR photon either in 3 (3356 cm^{-1}, red trace) or 6 (1450.5 cm^{-1}, green trace) μm regions.*

The absolute intensity of these spectra cannot be compared directly because of different fluencies of IR beams and absorption cross sections. However, the relative abundances of the fragment corresponding to the ammonia loss and its secondary fragmentation product corresponding to an additional loss of ketene vary significantly. In case of higher photon energy pre-excitation, the secondary fragmentation increases by a factor of two in accordance with the assumption that the efficiency of this fragmentation channel depends on the amount of the internal energy of the parent ion.

3. IR Spectroscopy of TrpH$^+$ in 3- and 6-μm Regions

Figure 3.9a shows the IR gain spectrum of cold TrpH$^+$, measured in the 3-μm spectral region with the UV wavenumber fixed at 34400 cm^{-1} (700 cm^{-1} to the red from the absorption maximum) by monitoring the photodissociation fragment with m/z = 146 Da (black trace). TrpH$^+$ is protonated on the N-terminus[89] and has five characteristic vibrations in the 3-μm region: a carboxylic acid O-H stretch, an indole N-H stretch, and three N-H stretches of the amine NH$_3$ group. The benefit of CIS over IRMPD spectroscopy is evident from the comparison of the vibrational spectra reported herein and the ones obtained via IRMPD.[81] In the latter, vibrational bands are significantly broadened and overlapped, so that vibrational resolution is partially lost. In

contrast, the presence of at least seven intense well-resolved bands in the experimental vibrational spectrum of cold TrpH$^+$ suggests the presence of more than one conformer.
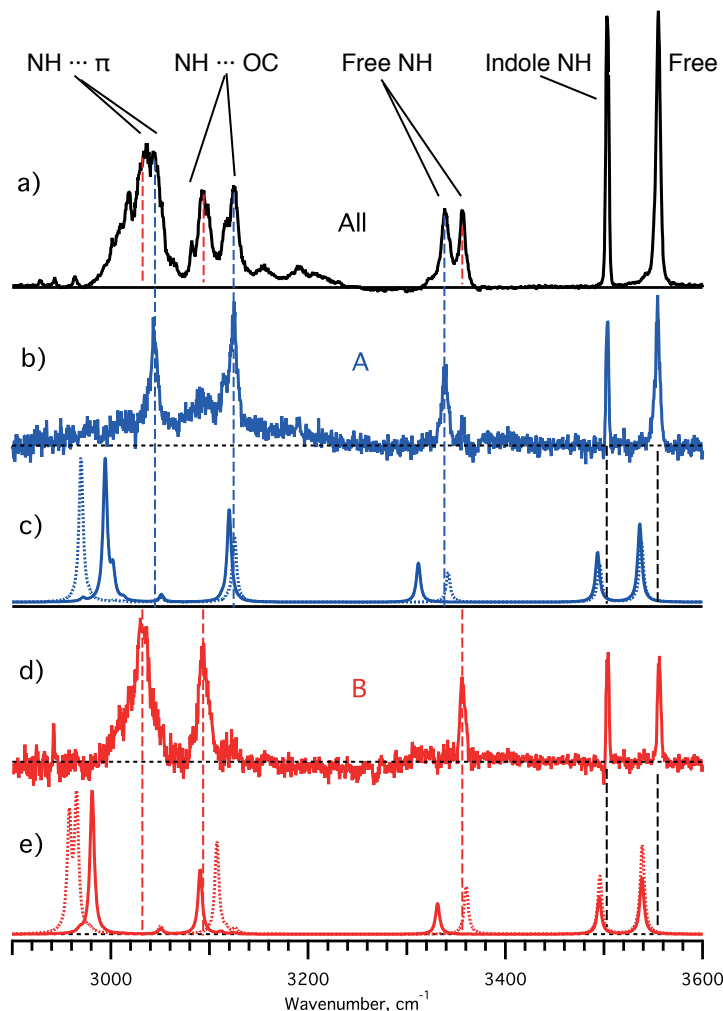

Figure 3.9. *IR spectra of TrpH$^+$ in 3-µm region: (a) the IR-UV gain spectrum of all available conformers; (b) and (d): conformer-specific IR spectra of conformers **A** and **B** generated with the pump OPO wavenumber fixed at 3339 cm^{-1} and 3356.7 cm^{-1}, respectively; (c) and (e): calculated anharmonic vibrational spectra for computed conformers **A** and **B**; solid and dashed lines correspond to CSSD(T) and MP2 levels of theory, respectively. Vertical dashed lines correspond to conformer-specific, experimentally measured transitions. All the spectra are normalized by the intensity of the peak centred at 3032.8 cm^{-1} in (a).*

Figures 3.9b and 3.9d show two generated conformer-specific IR spectra, associated with the pump OPO fixed at 3339 cm^{-1} and 3356.7 cm^{-1}, respectively. The two spectra, together, contain

all the intense bands of the gain spectrum, implying that only two highly abundant conformers are observed, which are named as **A** and **B** in this analysis.

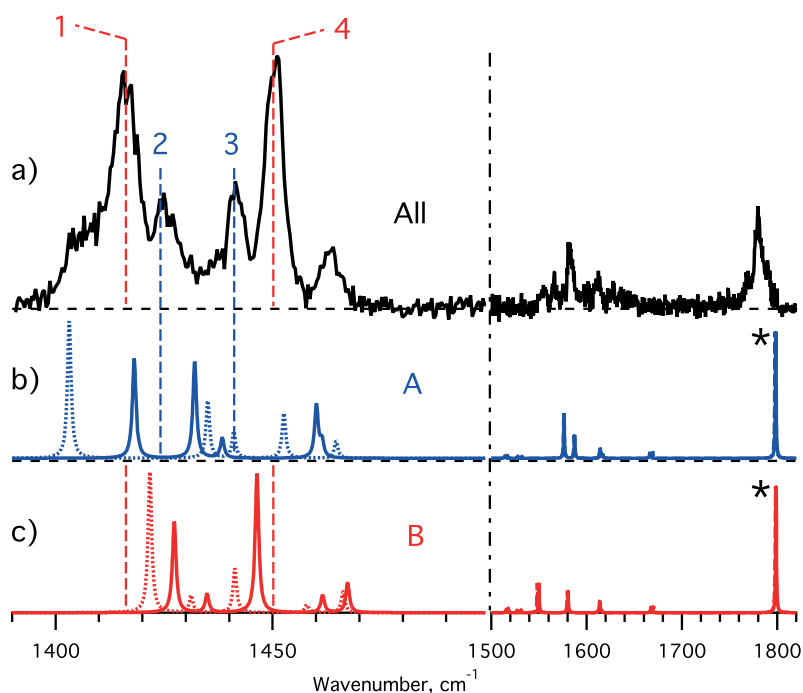Figure 3.10a shows the recorded TrpH$^+$ IR gain spectrum, measured in the 6-μm region.

Figure 3.10. *IR spectra of TrpH$^+$ in 6-μm spectral region: (a) the IR-UV gain spectrum of all available conformers; (b) and (c) calculated anharmonic vibrational spectra for computed conformers **A** and **B**, respectively; solid and dashed lines correspond to CSSD(T) and MP2 levels of theory; intensity of the asterisk-marked transitions has been reduced by the factor of 2 for graphical clarity. Vertical blue and red dashed lines correspond to the experimentally assigned transitions in the conformers **A** and **B**, respectively. Note the difference in horizontal scales to the left and to the right from the black dashed line.*

One could assign the peaks in this spectrum to conformers **A** and **B** in the same manner as described above for the 3 μm region: fixing the pump IR laser wavelength at the peak in the 3-μm region, previously assigned to one of the conformers, while scanning the frequency of the probe IR laser through the 6-μm region. However, because of the limited energy of the probe OPO, the intensity of the peaks in the IR-IR-UV spectrum in the 6-μm region appeared to be insufficient to distinguish them reliably from the noise in the baseline, induced by the pump OPO. Instead, each

transition in the 6-µm region, labelled 1 to 4 in figure 3.10a, was assigned separately. The pump OPO was fixed each time at one of the unassigned transitions, while the probe OPO monitored changes in the intensity of the assigned characteristic peaks between 3305 and 3375 cm^{-1} (figure 3.11). A comparison of the generated conformer-specific traces in the 3-µm region with the spectra in figures 3.9b and 3.9d allows for conformational assignment of the low-intensity bands in the 6-µm region.

The limited energy of the pump IR OPO in the 6-µm region (ca. 1 mJ) did not allow for saturation of even strong transitions in this spectral region. Nevertheless, on the basis of the comparison of the benchmark peaks in the 3-µm region, the transitions 2 and 3 in figure3.10a (1424.9 cm^{-1} and 1441.4 cm^{-1}) have been assigned to conformer **A**, while the transitions 1 and 4 (1415.8 cm^{-1} and 1451 cm^{-1}) have been assigned to conformer **B**. The trace 3, recorded by excitation of conformer **A**, also shows a minor peak corresponding to conformer **B**. This is, most likely, due to an overlap of the two peaks belonging to both conformers.
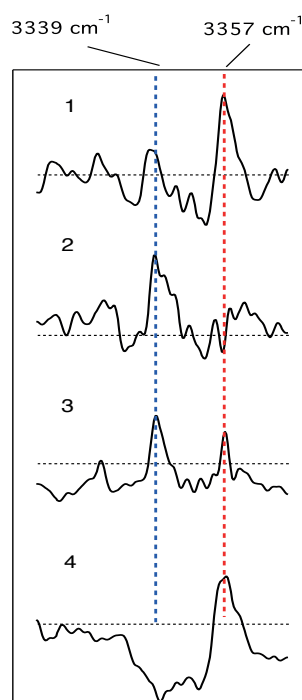

Figure 3.11. *Conformational assignment of peaks labeled 1-4 in figure. 3.3.7a. Each trace shows conformer-specific spectra between 3305 and 3375 cm^{-1}, generated with pump OPO fixed at the corresponding transition in 6-µm region. Assignment is based on comparison of the maximum intensity peak in each trace and the characteristic transitions of conformers **A** and **B** (blue and red vertical dashed lines, respectively).*

3.3.4. Calculations

The eight low-energy conformers of TrpH$^+$, obtained from the *ab initio* optimizations, are shown in figure 3.12. The corresponding dihedral angles, using the labelling convention defined above, and relative energies of all conformers are listed in table 3.3.
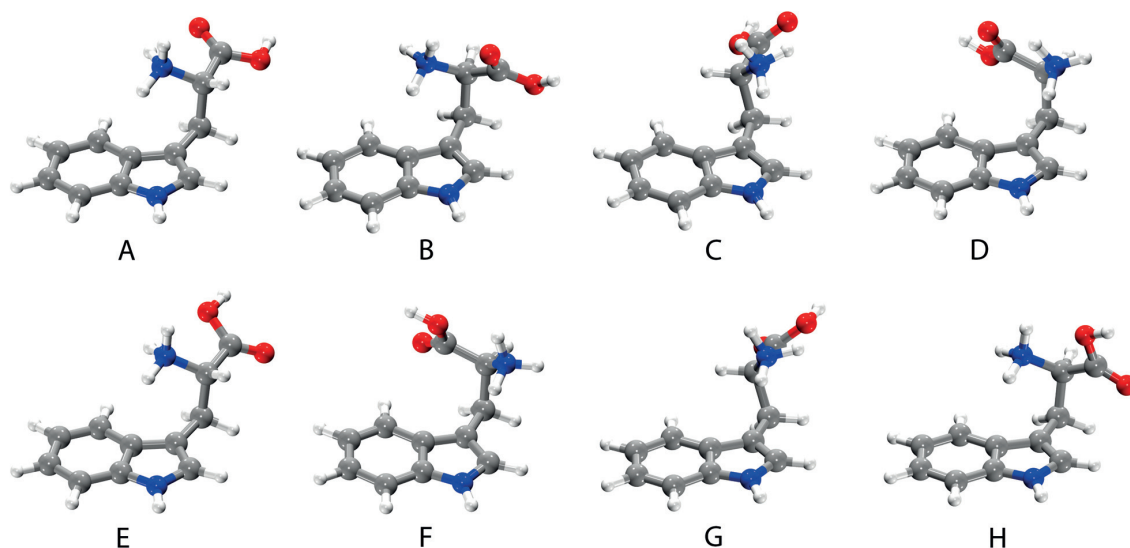

Figure 3.12. *Equilibrium structures of TrpH$^+$ conformers, calculated at the CCSD/cc-pVDZ level of theory (silver=C, red=O, blue=N, white=H). In order to provide a structural reference point, the indole ring orientation is chosen to be qualitatively consistent in these plots, which means that the L- (structures **A**, **D**, **E**, **F**) and D- (structures **B**, **C**, **G**, **H**) forms of Trp are mixed. Only L- forms are relevant to natural Trp used in the experiments; these stereoisomers can be viewed as mirror images of the shown D-forms of the structures B, C, G and H.*

The common structural motifs of the two lowest-energy conformers **A** and **B** are (1) alignment of an amine N-H bond toward the acid group's C=O bond, rather than the O-H bond, and (2) positioning of the protonated-amine N-H$^+$ toward the middle of the π face of the indole moiety, rather than toward the end of the pyrrole ring. All other, higher-energy conformers lack one or both of these interactions, suggesting that these two unique factors are the source of the stability of the dominant isomers. The main structural difference between the two low-energy isomers is the position of carboxyl/amine moieties, relative to the remainder of the molecule, and the isomer with the acid group pointing toward the indole ring is the more stable of the two. Little energetic penalty for this latter rotation is observed, however.

Table 3.3. Relative electronic energies and structural parameters of TrpH$^+$ conformers.

Conformer	ΔE^a	$\Delta E_{ZPE}{}^b$	$\phi_1{}^d$	$\phi_2{}^d$	$\phi_3{}^d$
A	0.51	0.50 (0.49^c)	-91	-168	106
B	0.00	0.00 (0.00^c)	90	-65	133
C	0.95	0.83 (0.84^c)	116	-166	106
D	1.64	1.50 (1.47^c)	-104	-76	127
E	4.64	4.49	-91	-176	-58
F	5.26	5.05	-102	-75	-53
G	5.13	4.84	116	-174	-74
H	3.42	3.33	91	-68	-38

^{a}FNO(99%)-CCSD(T)/cc-pVTZ relative energies (kcal/mol) on CCSD/cc-pVDZ structures.

^{b}Relative FNO(99%)-CCSD(T)/cc-pVTZ energies (kcal/mol), with harmonic zero-point energy corrections computed with RI-MP2/cc-pVTZ frequencies.

^{c}Relative energies (kcal/mol) with RI-MP2/cc-pVTZ anharmonic zero-point energy corrections for the 40 highest-frequency modes and harmonic corrections for the remaining modes. [The CCSD(T) 1-mode corrections, which were only applied to isomers **A** and **B**, change the relative energy of isomer **A** to 0.45 kcal/mol.]

^{d}Dihedral angles (degrees), defined in Fig. 3.3. In this table, the L- form of Trp is used throughout.

The two lowest-energy isomers are separated by only 0.51 kcal/mol, using FNO-CCSD(T)/cc-pVTZ electronic energies. The energy gap between these very similar species was found to be surprisingly sensitive to the level of electronic structure theory, which necessitated the use of reasonably large basis sets and a high degree of electron correlation. Harmonic zero-point energy corrections do not change the qualitative ordering of the isomers and only make small changes to the quantitative relative energies.

The presence of two conformers in the experimental spectrum is consistent with the two dominant low-energy conformers obtained from the *ab initio* computations. With an energy gap of 0.51 kcal/mol, however, appreciable population of isomer **A** should not be observed at 10 K. Whether this result stems from remnant error in the electronic structure calculations or from trapping of the isomer ensemble in local minima (due to the fast non-adiabatic collisional cooling)

remains unclear. Anharmonic zero-point corrections do not appreciably change this relative energy ordering since the intramolecular interactions—and, therefore, the inherent frequencies—of these conformers are very similar. Nonetheless, the calculations do predict two nearly degenerate isomers, each containing the same qualitative intramolecular interactions. The next-lowest conformer (**C**) sits another 0.44 kcal/mol above **A**, due to the shifted position of its NH^+-π interaction. Although this third isomer may contribute to some of the minor peaks in the spectrum, the relative energies suggest that isomers **A** and **B** should dominantly contribute to the ensemble.

The qualitative vibrational motions of $TrpH^+$ in the 3-μm region were also observed in the computational results for all isomers. The remaining task of the vibrational simulations, therefore, was to identify the conformer-specific anharmonic shifts induced by the variety of intramolecular interactions. This task places strict requirements on the vibrational simulations, which necessitated the use of accurate anharmonic methods with accurate underlying potential surfaces. The computed spectra in this frequency window are shown in figures 3.9c,e. The spectra from the DB-RI-MP2/cc-pVTZ surface are shown as dashed lines, whereas the spectra containing modes corrected by one-mode FNO-CCSD(T)/cc-pVTZ scans are shown as solid lines. Frequencies discussed in the following section will refer to the latter data, unless otherwise noted.

3.3.5. Discussion

The experimental spectra suggest the presence of two dominant isomers with similar, yet resolvable, spectral signatures. In this subsection, the computed structures, frequencies, and properties are used to uniquely identify these isomers and connect the structures to the defining spectral transitions.

1. *Analysis of the Spectra in 3-μm Region*

The carboxyl O-H stretch and indole N-H stretch are both "free" stretches, and their calculated vibrational frequencies are nearly independent of conformer. This result is consistent with the experimental spectra, which exhibit peaks at 3555.0 cm^{-1} and 3503.3 cm^{-1} in both the conformer-agnostic IR-UV and conformer-resolved IR-IR-UV spectra. While these two vibrational modes do not present any information toward identifying the conformers, they do provide a preliminary calibration of the computational approach. The local-mode VSCF+VDPT2 anharmonic frequencies for these two fundamental transitions are 3536/3539 cm^{-1} (**A/B**) and 3494/3495 cm^{-1}, respectively. Importantly, this fidelity (≤ 19 cm^{-1}) with experimental results has been obtained *without* empirical scaling factors.[67, 68]

The free N-H stretch of the protonated amine exhibits conformer-specific behaviour (3338.6 and 3356.7 cm^{-1}) in the experimental spectrum, which is resolved well enough in this cold spectrum to be used as the pump IR for conformer selection. The computed spectra of isomers **A** and **B** are in good agreement with these measured quantities, yielding a spacing between the two conformers' N-H stretches of 19.5 cm^{-1} (18.1 cm^{-1} experimental) and an absolute accuracy of 26 cm^{-1} in each conformer. (The MP2 frequencies actually show better absolute fidelity with the experiment for these bands, exhibiting errors of only 3 cm^{-1} in each conformer.) This agreement is the first evidence that the computed structures of these two lowest-energy isomers correspond to the experimentally observed species. Based on the computed structures and vibrational coupling strengths (data not shown) for these two isomers, the frequency of the conformer-specific amine stretch transition is ascribed to two sources: it is strongly coupled to the other amine N-H stretches, which are, in turn, sensitive to their surrounding structure, and it is also perpendicular to the indole plane in conformer **A** yet parallel to the plane in **B**.

The second of the three amine N-H stretch frequencies is red-shifted more than 200 cm^{-1}, relative its free-NH counterpart. This motion involves an N-H bond interacting with the neighbouring carbonyl oxygen in a form akin to hydrogen bonding (or, possibly, dipole-dipole alignment), albeit at an atypical H-bonding angle. This motion is also found to be unique to the two conformers, which is observed in both the experiment (**A**: 3123.3 cm^{-1}, **B**: 3093.8 cm^{-1}) and in the computations (**A**: 3120 cm^{-1}, **B**: 3090 cm^{-1}).

The proton in the last amine NH stretch is directed toward the π face of the indole group in all of the low-energy isomers. This interaction, resembling an intramolecular cation-π interaction,[90] leads to the largest red-shift of the amine stretches, indicating a rather strong cation-π effect. Two closely spaced peaks are observed experimentally for conformers **A** and **B**, and together they become a broad, unresolved peak in the IR-UV gain spectrum. The clearly resolved peaks (**A**: 3044.2 cm^{-1}, **B**: 3032.8 cm^{-1}) in the IR-IR-UV difference spectra highlight the utility of this experimental approach. The calculated frequencies for this mode are also similar in the **A** (2994 cm^{-1}) and **B** (2981 cm^{-1}) conformers, and the ordering of these conformers' transitions is consistent with those observed in the experiment. The frequencies are found to be about 60 cm^{-1} to the red from the experimental transitions, however. At present, the source of this computationally overemphasized red-shift remains unclear. The inclusion of targeted three-mode couplings involving this mode, as well as the inclusion of low-frequency motions, were both unable to recover the proper red-shifts.[22] The remnant discrepancy is, therefore, tentatively assigned either to the inherent accuracy of the potential energy surface—higher levels of theory are currently cost-

prohibitive since the present two-mode approach required more than 94,000 quantum chemistry calculations—or the need for FNO-CCSD(T)-quality 2-mode couplings. The MP2-only spectra were actually further red-shifted, indicating that the quality of the underlying potential does play a significant role in the position of these proton-stretch transitions. Strong hydrogen bonds are typically the most challenging motions to recover in computed spectra, and this remnant error does not detract from the overall consistency of the computed absorption patterns.

2. Analysis of the Spectra in 6-μm Region

The lower-frequency (6-μm) region also provides conformer-specific structural information, with the technical IR-IR-UV caveats discussed above. Near 1785 cm^{-1}, two conformer-nonspecific carbonyl stretches dominate the intensity of this region, as shown in figure 3.10a. The calculations predict that both isomers exhibit a transition at 1799 cm^{-1}, which is roughly 15-20 cm^{-1} to the blue of the (somewhat surprisingly) broad experimental peak. The weak pattern observed in the 1550-1650 cm^{-1} window, consisting mainly of amine bending modes, is reproduced by the combined, computed spectra for these two conformers.

The 1400-1475 cm^{-1} region, on which the IR-IR-UV conformer-selective experiments were focused, once again suggests the presence of two dominant isomers, although the characteristic signatures in the 3-μm region (figure 3.11) exhibit appreciable noise. Based on the computational analyses, the experimentally observed transitions, labelled 3 (1441.4 cm^{-1}) and 4 (1451 cm^{-1}) in figure 3.10a, can be assigned to the amine umbrella motion in conformers **A** and **B**, respectively. Because this mode involves motion of the excess proton, including the making/breaking of the cation-π interaction, it would be expected to carry appreciable intensity. The computed frequencies of these two transitions occur at 1432.0 cm^{-1} and 1446.4 cm^{-1}, and the ordering of the two isomers' frequencies is consistent with the experimental assignment. The fact that isomer **B** exhibits a higher frequency is consistent with the slightly stronger, stabilizing interaction between the protonated amine and the indole ring in this conformer, which was suggested by the red-shift of the N-H stretch in the high-frequency region.

Experimental transitions 1 (1415.8 cm^{-1}, isomer **B**) and 2 (1424.9 cm^{-1}, isomer **A**) are more difficult to assign, mainly due to the delocalized nature of the mode. In both conformers, this motion includes an in-plane, fused-ring C=C stretch, in-plane C-H wags, and a motion that would nominally be ascribed to the carboxyl O-H wag (although the latter contains additional heavy-atom motion in the remainder of the carboxyl group). In the normal-mode representation, this composite motion is also strongly mixed with the amine umbrella, as well as additional in-plane wagging

motions. This mixing leads to non-trivial displacement of almost every atom in the complex. The local-mode representation separates these motions into the qualitative 'regional' motions described above, and the VDPT2 mixing coefficients subsequently allow for assignment of the modes. The computed 1418.1 cm^{-1} transition for conformer **A** is consistent with the experimental assignment to transition 2. The computed frequency for transition 1 (1427.3 cm^{-1}) in conformer **B** is enough in error that the ordering of the conformer's transitions is, unfortunately, reversed. Based upon the close fidelity of the remaining peaks, we suspect that this lone transition in **B**—which could reasonably involve higher-order anharmonic couplings among the nearly degenerate modes—is the problematic mode. An 11-cm^{-1} error is almost certainly within the error bars of this computational approach, and such small experimental splittings severely challenge *ab initio* vibrational machinery. Even with this error, however, the spacing between these qualitatively similar transitions in the two conformers exhibits the correct trend. Experimentally, the gap between peaks 2 and 3 (16.5 cm^{-1}) in **A** is reduced, compared to peaks 1 and 4 (35.2 cm^{-1}) in **B**. The computed 2-3 gap (13.9 cm^{-1}) in **A** is also reduced, compared to the 1-4 gap (19.1 cm^{-1}) in **B**.

Based on the computational results, additional interpretation of the experimental spectrum is also available. A weak transition in conformer **B** at 1438.4 cm^{-1} happens to land close to transition 3, which was assigned to conformer **A**. This overlap may explain the presence of response in *both* conformers' high-frequency regions upon excitation of this transition. The smaller peak at 1462.7 cm^{-1} is assigned to the carboxyl O-H wag (without mixing ring motions) in both conformers. This mode appears at 1460 cm^{-1} in **A** and 1467 cm^{-1} in **B**. This mode was a key assignment in the fingerprint spectrum of neutral Trp[91] because the carboxyl group forms a hydrogen bond with the amine. In TrpH^{+}, no such interaction is available, and the intensity is reduced. The ability of the experiments to resolve this band is noteworthy, however, since this band was not resolvable in non-H-bonded conformers of neutral Trp.

Aside from a slight shift of one peak, the fidelity between the experimental and computational results in the 6 μm region reaffirms the assignment of the two observed spectra to the low-energy conformers computed herein. The position of the computed vibrational bands is generally within 10-20 cm^{-1} of the experimental values, and relative conformer ordering/splitting is consistent with this assignment. Worth noting is the relative intensity of the transitions in the two regions, however. In the high-frequency (3 μm) region, the observed intensity of the free NH stretches is roughly equal. Since the computed intensities of these two isolated isomers are also roughly equal, this portion of the spectrum suggests approximately equal population of the conformers in the trap. The low-frequency (6 μm) region, however, suggests that conformer **B** is

more prevalent at the experimental conditions, which is more consistent with the computed conformer relative energies (although the computed 0.5 kcal/mol spacing would still yield almost exclusively isomer **B**). Whether this effect stems from error in the computed intensities or from non-uniform intensity response in the IR-UV technique remains an open question that requires future investigation and cannot be disentangled in the present analysis.

3. *Intramolecular Interactions*

On the basis of the computed low-energy conformers, the stability of these structures was hypothesized to stem from strong interactions between the protonated amine group and both the carbonyl of the carboxylic acid (H-bond) and the delocalized π face of the indole ring (cation-π).[90] Indeed, the isomer energy trends are consistent with this assessment, and red-shifts in the vibrational spectrum suggest strong interactions. This energetic effect is difficult to quantify, however, since most energy decomposition schemes[92-99] require distinct molecular fragments. In lieu of these quantitative approaches, a qualitative analysis of the electron density rearrangements, due to protonation of the amine, was performed. Specifically, the total electron density difference $\Delta\rho = \rho(TrpH^+) - \rho(Trp)$ was computed at the TrpH$^+$-optimized structure. This quantity does *not* depict the electrostatic interaction between the groups—an effect that can be large for cation-π interactions[90]—but it does serve to visualize the strong polarization induced in the remainder of the molecule by the protonated amine. The separate magnitudes of these constituent effects were, instead, assessed quantitatively with a related $NH_4^+\cdots$indole model.

The eight potential conformers of TrpH$^+$ differ in subtle backbone orientations, leading to the characteristic spectral signatures discussed above. Quantifying the effect of each of these intramolecular interactions is challenging since most energy decomposition schemes require distinct molecular fragments. By comparing the energies of similar conformers with only a particular interaction active/inactive, however, a bracketing of the *relative* energetic contributions can at least be made. For example, the H-bond-like interaction between the amine N-H and the carboxyl C=O provides 3.6-4.2 kcal/mol of relative stabilization over the alternative NH$\cdots$OH interaction. Similarly, the NH$^+\cdots$π interaction toward the middle of the indole moiety provides 0.6-1.7 kcal/mol of relative stabilization over the alternative interaction at the end of the ring. The fact that the cation-π interaction red-shifts the N-H$^+$ stretch frequency most strongly suggests that this relative assessment does not capture the absolute magnitude of the effect, which is typically large in reference complexes.[90] It does, however, provide a comparative trend for the favoured biomolecular interactions in this complex.

60

In order to provide more direct insight into the nature of the cation-π interaction, density difference plots were generated for TrpH$^+$. The plots for isomers **A**, **B**, **D**, and **F** are shown in figure 3.13. An increase in electron density, relative to Trp, is shown as a blue isosurface; depletion in electron density is similarly shown in red. For all isomers, significant differences are observed near the amine nitrogen, as expected. The formation of the N-H$^+$ bond leads to appreciable gain in electron density on, and near, the excess proton. This electron density is dominantly drawn from the opposite side of the nitrogen atom. Most interesting is the behaviour near the π face of the indole ring, however. In conformers **A** and **B**, for example, the interaction between the protonated amine and the ring below is quite local, rather than a roughly uniform polarization of the π electrons, as is typically found in face-bound cation-π interactions. In fact, the dominant interaction appears to be between the protonated amine and the C=C π bond of the pyrrole-like portion of the complex. This effect is at least partially driven by the structural constraints of the molecule. The "tether" is short enough that the amine cannot fully access the π face, and a strong polarization of the closest π density region results. Isomers **D** and **F** sit higher in energy than **A** and **B**, and the magnitude of the π polarization is clearly lessened for these (and related) isomers in figure 3.13.

Based on this somewhat unexpected result, one final examination of the cation-π effect was performed, in order to clarify the relative contributions of electrostatic interactions and polarization effects. Using the optimized structure of conformer **B**, an analogous N-H_4^+···indole complex was created; the backbone connection of **B** was replaced by capping hydrogen atoms. Only these two hydrogens were allowed to relax, while the rest of the complex remained fixed at the coordinates of **B**. In this structure, the RI-MP2/aug-cc-pVDZ binding energy is 17.2 kcal/mol. This magnitude is consistent with energies of known reference complexes.[100, 101] Because this model complex now exhibits distinct fragments, modern energy decomposition analyses[92-95, 97] (EDA) may also be employed. Using the same structure, a HF/aug-cc-pVDZ EDA calculation shows that only 6% of the interaction stems from electrostatic (frozen-density) contributions, whereas 84% comes from polarization effects. A non-trivial intramolecular charge-transfer fraction (10%, including basis set superposition error) was also observed. Therefore, in spite of precedent that suggests a large electrostatic component to cation-π interactions,[90] both the EDA and $\Delta\rho$ analyses confirm that local, yet strong, polarization of the indole ring accounts for the dominant stabilization of these conformers. This result is consistent with a recent report[101] that suggests that non-facebound cation-π interactions can be both favorable and dominated by induced electronic (polarization) effects. This result for the present complex also suggests that this polarization-based cation-π effect is the source of the strongly red-shifted and anharmonic spectral signatures.
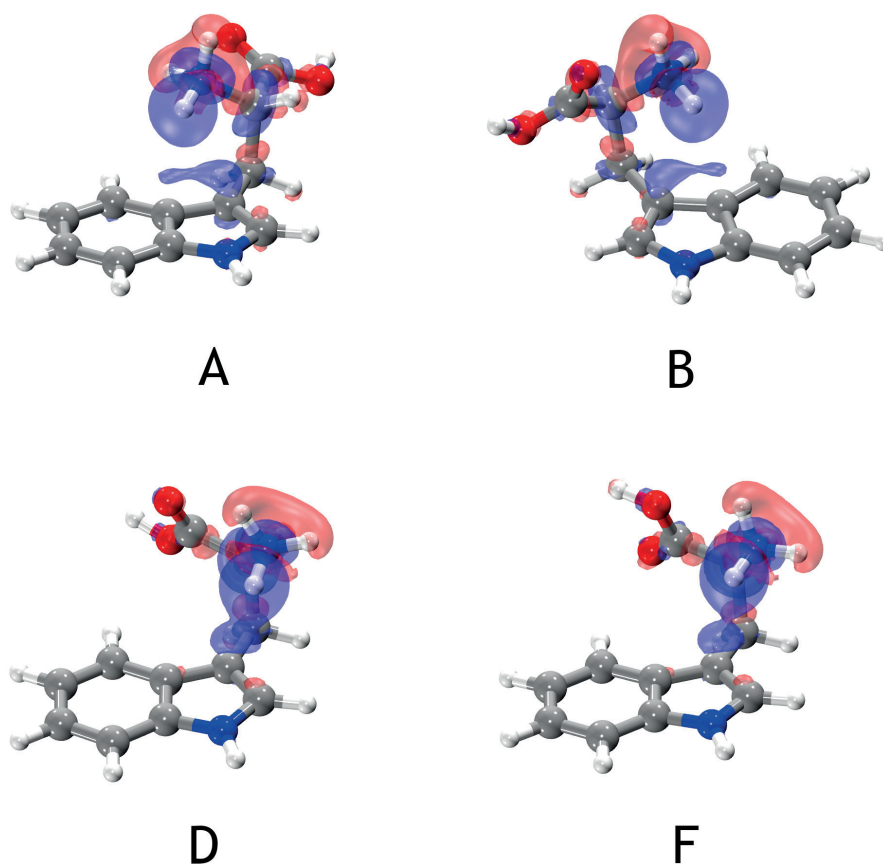
Figure 3.13. *Density difference plots for four representative computed conformers (L-stereoisomers). Shown are total electron density differences between TrpH$^+$ and Trp, fixed in the optimized TrpH$^+$ geometry. Blue surfaces depict relative increases in electron density in TrpH$^+$; red surfaces depict electron depletion.*

3.4. IR-IR-UV Spectroscopy of HisH$^+$

3.4.1. Introduction

Histidine (figure 3.14) is one of the most versatile amino acids. It can serve as both a hydrogen-bond donor and an acceptor.[102, 103] Histidine is, thus, a competent proton-transfer mediator in many proteins[102, 104-106] and is an important constituent of the catalytic sites of protein enzymes.[103, 107, 108] Several metal ions bind to histidine in metalloproteins, such as hemoglobin, ferritin, or the antioxidant super oxide dismutase.[109-111] Regarding this wide range of biological functionalities, histidine was extensively studied in solution phase both theoretically and experimentally.[112-114] His owns the unique ability to adopt five different protonation forms in

aqueous solution.[113, 114] In particular, at neutral pH His adopts a zwitterionic structure deprotonated on the C-terminus and protonated on the N-terminus. Upon increasing the acidity, a second proton binds to histidine imidazole ring. Despite this firm protonation hierarchy, the calculations predict that in the gas phase the most stable conformer of HisH$^+$ is protonated on the imidazole ring, rather than on the amino group.[115, 116]
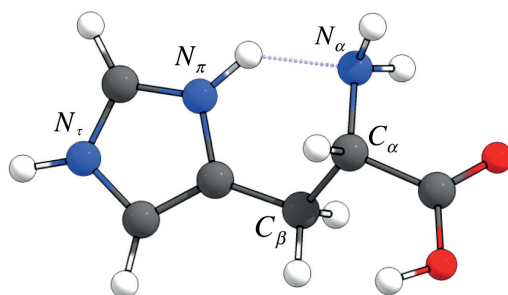

Figure 3.14. *Schematic representation of HisH$^+$, protonated on the imidazole ring. Histidine atoms are named here according to the IUPAC Compendium of Chemical Terminology (Gold Book), in which positions of the nitrogen atoms of the imidazole ring relative to the side chain are denoted by pros ('near', abbreviated π) and tele ('far', abbreviated τ).*[117]

UV absorption of histidine in aqueous solution exhibits a strong unstructured band with the maximum at 211 nm.[118] Nevertheless, histidine remained the last aromatic amino acid for which the intrinsic structure and photophysical properties in the gas phase, where it is isolated from interactions with solvent molecules, have not been explicitly characterised.

Room temperature IRMPD spectroscopy of HisH$^+$, performed in the 6-10 μm spectral region, suggested the presence of only one major conformer with a likely small contribution from another one.[116] The lowest-energy intrinsic structures of HisH$^+$, calculated in harmonic oscillator approximation of theory, correspond, indeed, to the protonation site on the imidazole ring.[115, 116, 119] Such geometry, however, does not exist in solution at all, which explains a great interest in studying properties of this amino acid in the gas phase.

A few factors greatly reduce confidence in the use of IRMPD for a strict validation of the calculated structures. First, although simple and convenient, this technique lacks conformational selectivity; therefore, the number of conformers and their relative contributions to the spectrum cannot be measured. Moreover, IRMPD technique may drastically distort relative intensities and widths of vibrational transitions because its fragmentation yield is a non-linear function of IR laser power and absorption cross-section. Together with thermal congestion at room temperature, these

effects drastically limit spectral resolution of the technique, complicating a comparison of IRMPD and calculated linear absorption spectra. Furthermore, IRMPD spectra of HisH$^+$ in the gas phase have not been measured for the most decongested and characteristic spectral region of N-H and O-H stretching vibrations (3.7 - 2.7 µm). Finally, calculated harmonic frequencies employ empirical scaling coefficients in order to account for the intramode anharmonicity of vibrations. Ideally, one should use different coefficients for different types of vibrations. Although this approach is proven to work properly for large polyatomics with many vibrations, a use of the empirical coefficients reduces the confidence in validating structures of small molecules. This adds more ambiguity to the previous validation of HisH$^+$ structures.

Herein we present the first electronic photofragmentation spectrum of cold, protonated histidine (HisH$^+$) in the gas phase. We employ IR-UV double-resonance and IR-IR-UV hole-burning spectroscopic techniques to record vibrational all-conformer gain spectra of HisH$^+$ and its isotopically labelled analogue in 3 and 6 µm spectral regions and conformer-specific vibrational spectra of individual conformers of this aromatic amino acid. A combination of UV/IR cold ion spectroscopy and high-level anharmonic *ab initio* quantum chemistry calculations allows for an unambiguous assignment of the previously calculated (and rectified herein) structures of HisH$^+$ to the experimentally observed conformers of HisH$^+$ ion. We also compare the gas phase and solution structures of HisH$^+$ and assess the presence of "kinetic" trapping in our experiments. Finally, we propose an additional experimental constrain, which may significantly simplify the conformational search in structural calculations.

3.4.2. Experimental Results

1. *Photodissociation Mass Spectra of HisH+*

Figure 3.15 shows CID (black trace) and photofragmentation mass spectra of HisH$^+$, recorded with UV OPO fixed at two wavelengths: close to the band origin at 231.5 nm (blue trace) and at 215.6 nm, i.e., 231.5 nm shifted by the typical IR photon energy (3400 cm^{-1}) to the blue from the band origin (red trace). The branching ratios of photodissociation channels of UV-excited protonated biomolecular ions depend crucially on the UV photon wavelength as well as the internal energy of the ion; therefore one has to carefully choose specific fragments and UV laser wavelength in multilaser experiments to improve the signal-to-noise ratio.

The photodissociation fragments can be assigned as follows:[79, 80, 82] 1) m/z = 81 and 83 Da correspond to the protonated side-chain of histidine after the C_α-C_β bond cleavage with hydrogen

atom transfer either from C_α to C_β or vice-versa; 2) m/z = 110 Da fragment corresponds to the iminium ion, produced by hydrogen atom transfer to the C-terminus and a consecutive loss of H_2O and CO; 3) m/z = 93 Da fragment corresponds to the additional loss of NH_3 from the fragment with m/z = 110 Da.
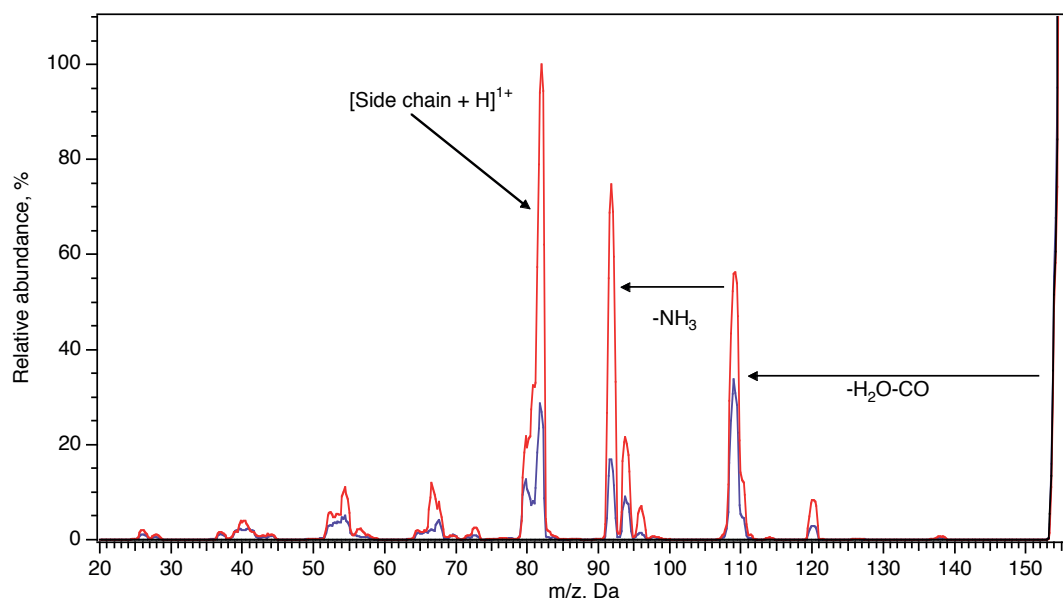

Figure 3.15. *CID (black trace) and photofragmentation mass spectra of HisH$^+$, recorded with UV OPO fixed at 231.5 nm (blue trace) and at 215.6 nm (red trace). UV OPO pulse energy is 3.3 mJ, each data point is averaged over 10 measurements, mass-increment is 0.2 Da. The rising signal on the right side corresponds to the parent ion, m/z = 156 Da.*

2. *Electronic Spectroscopy of HisH$^+$*

Figure 3.16 shows the UV photofragmentation spectra of HisH$^+$, cooled in an octupole ion trap to $T \sim 10$ K, recorded by monitoring separately the most abundant photofragmentation fragments with m/z = 81-83 Da (red trace), m/z = 110 Da (blue trace), and m/z = 93 Da (violet trace), or by collecting all fragments with low resolution of the analyzing mass filter (black trace). Compared with water solutions, the absorption band of cold gas phase HisH$^+$ is red-shifted and exhibits much sharper rising edge with the onset around 234 nm and maximum at 221 nm (232 nm and 211 nm for a solution spectrum, respectively) with no resolved vibrational structure. Regarding the latter observation and the small size of His, one may suggest certain contribution of a lifetime broadening in the gas phase spectrum of this ion. In overall, the shape of the spectrum resembles the first absorption band of cold TrpH$^+$, which is fully lifetime broadened.
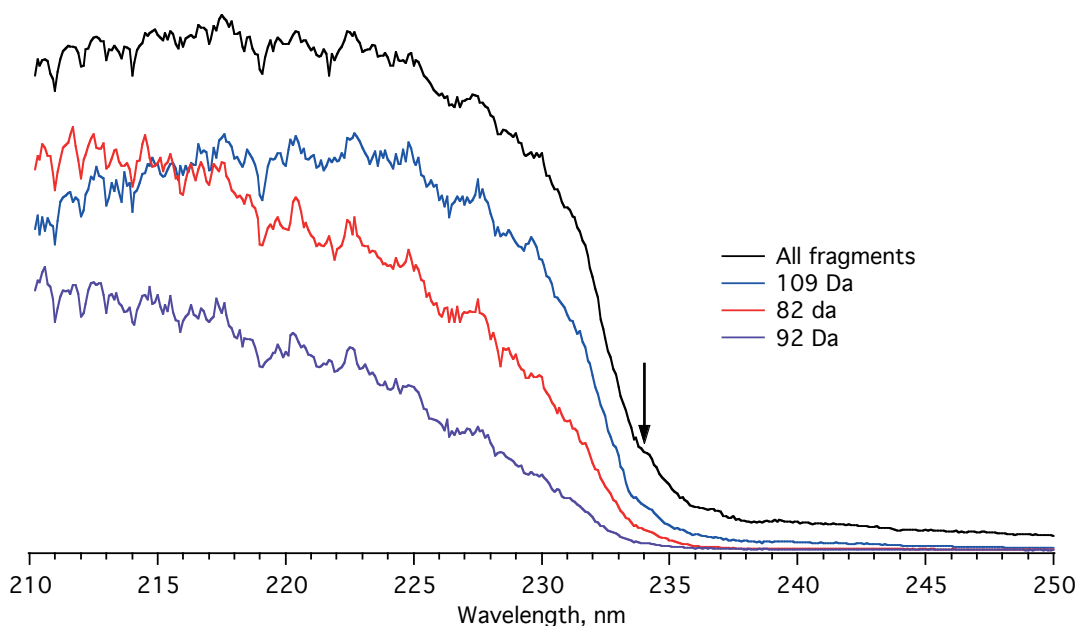
Figure 3.16. *Electronic photofragmentation spectra of HisH$^+$, recorded by detecting the fragment with m/z = 93 Da (violet trace), m/z = 81-83 Da (red trace), and m/z = 110 Da (blue trace), as well as all major charged fragments (black trace).*

3. IR Photon-Induced Fragmentation Enhancement of HisH$^+$

The spectra, recorded by monitoring different fragments, exhibit different behaviour in the blue side of the spectrum. The increased UV photon energy changes the branching ratios of the fragmentation channels, making their relative intensity an energy-dependent value. The fragmentation signal increase and changes in relative abundance are also observed for IR-preheated ions. Figure 3.17 shows UV photofragmentation mass spectra of cold (blue line) and IR preheated (red line) HisH$^+$. UV OPO was tuned to the red from the absorption band (236 nm), while IR OPO wavenumber was fixed at the imidazole N‑H stretch vibration (3480.9 cm^{-1}), which is approximately the same for all conformers (see below).

As can be seen from the figure 3.17, the relative increase of the fragments with m/z = 81-83 Da is the highest, therefore all further spectral measurements were recorded by monitoring the intensity of these fragments only. Figure 3.18 shows UV photofragmentation spectra of cold (blue trace) and IR pre-heated (red trace) HisH$^+$. The red shift of the absorption upon increasing an internal energy of the ions is used to record its vibrational spectra. In these experiments the UV OPO wavenumber was fixed on the rising edge of the UV absorption band of HisH$^+$ at 42735 cm^{-1} (234 nm) (figure 3.18), where the fragmentation increase is the highest.
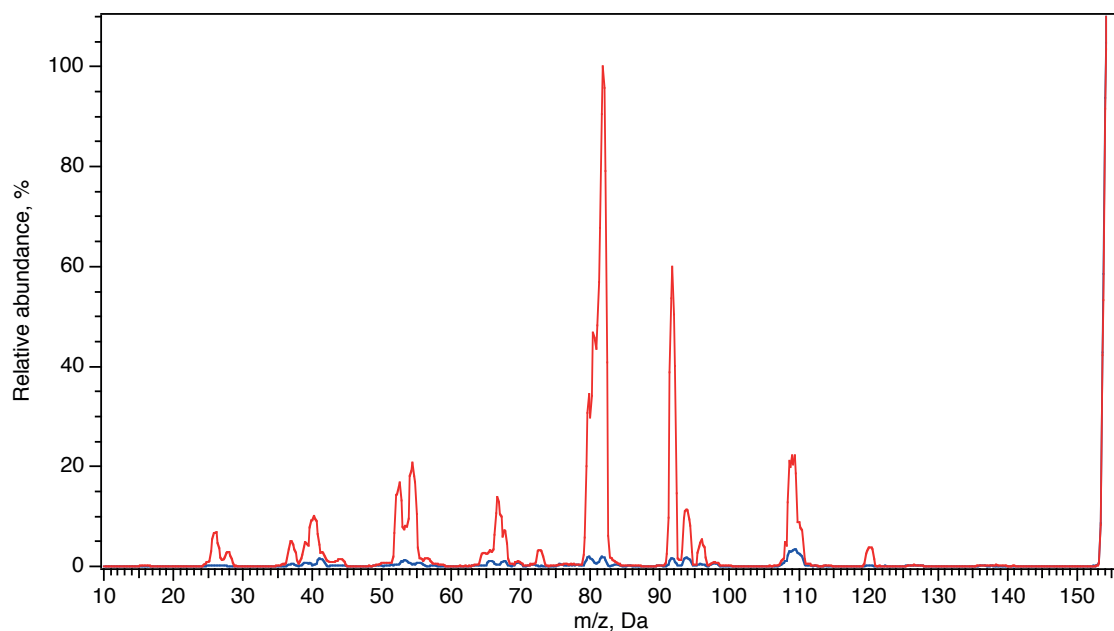
Figure 3.17. *Photofragmentation mass spectra of cold (blue trace) and IR-preheated (red trace) HisH$^+$, recorded with UV OPO wavelength fixed at 236 nm and IR OPO wavenumber fixed at 3480.9 cm^{-1}. UV OPO energy is 3.3 mJ per pulse; each data point is averaged over 10 measurements; mass-increment is 0.2 Da.*
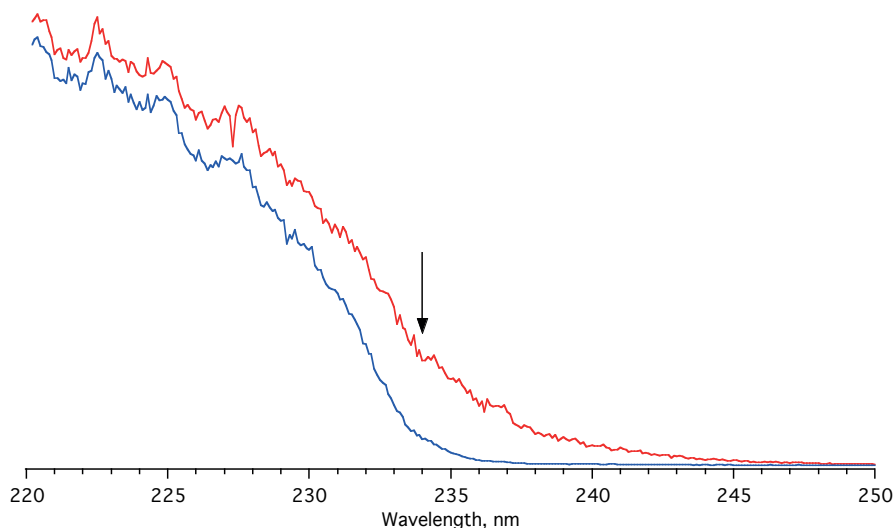

Figure 3.18. *Electronic photofragmentation spectra of cold (blue trace) and IR pre-heated (red trace) HisH$^+$, recorded by detecting the fragment with m/z = 81-83 Da. IR OPO wavenumber was fixed at 3480.9 cm^{-1}. The arrow points to where the UV OPO was tuned in the IR-UV and IR-IR-UV measurements.*

The choice of the fragment with the highest increase of the fragmentation yield upon IR pre-excitation and the UV OPO wavelength corresponding to the highest fragmentation yield allows for achieving the best available signal-to-noise ratio.

4. Vibrational Spectroscopy of HisH$^+$ in 3 µm Spectral Region

We applied an IR-UV double-resonance spectroscopy[7] to measure an all-conformer IR-UV gain spectrum in 3 µm spectral region of cold HisH$^+$ (figure 3.19a) and an IR-IR-UV hole-burning spectroscopy[22] to separate the vibrational transitions of individual conformers (figures 3.19b and 3.19c).
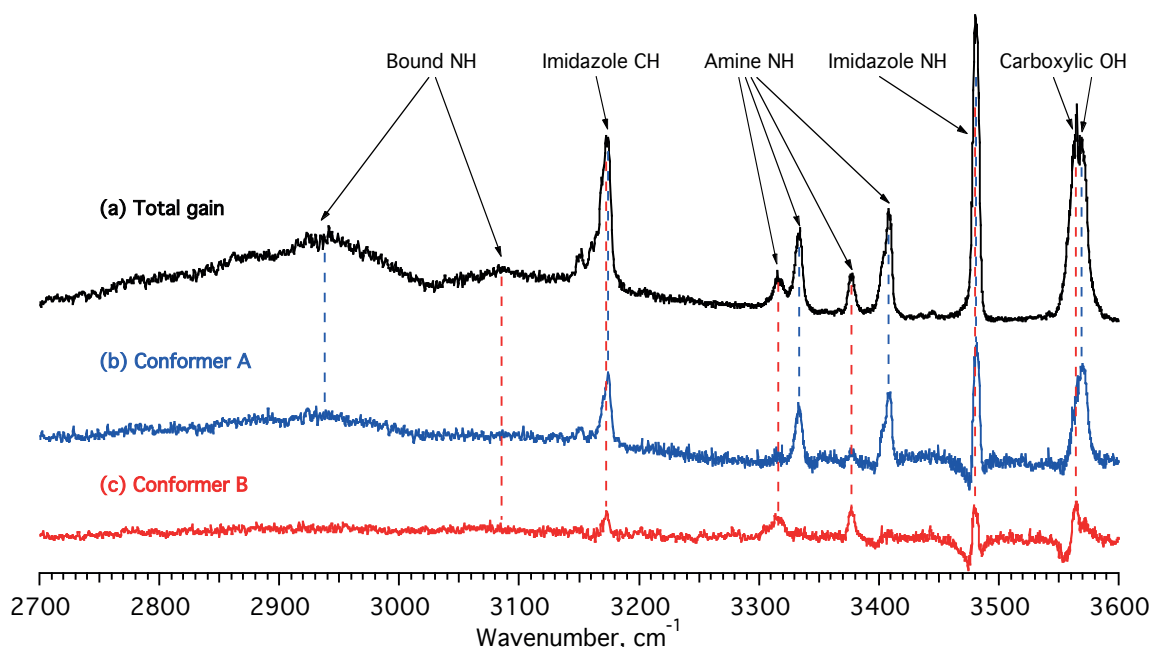

Figure 3.19 *IR spectra of HisH$^+$ in 3-µm region: (a) the IR-UV gain spectrum of all available conformers; (b and c) conformer-specific IR spectra of conformers **A** and **B** generated with the pump OPO wavenumber fixed at 3408.2 and 3377.1 cm^{-1}, respectively.*

In previous studies it was suggested that the lowest energy structures of the HisH$^+$ correspond to the protonation site residing on the imidazole ring.[115, 116] Therefore, HisH$^+$ should have five characteristic vibrations in the 3 µm spectral region: a carboxylic acid O-H stretch, symmetric and anti-symmetric amine N$_\alpha$-H stretches, and imidazole N$_\pi$-H and N$_\tau$-H stretches. The number of well resolved transitions in the experimental IR-UV gain spectrum in figure 3.19a suggests the presence of more then one conformer under our experimental conditions. Figures

3.19b and c show the conformer-specific spectra of HisH$^+$, measured with the pump IR OPO wavenumber fixed at 3408.3 and 3377.3 cm^{-1}, respectively. All of the observed transitions in the gain spectrum are present in either one or both conformer-selective spectra, which are assigned to conformers named **A** (figure 3.19b) and **B** (figure 3.19c) in this analysis.

The signal dips on the lower-energy sides of the two blue-most vibrations in conformer-selective spectra of conformers **A** and **B** (figures 3.19b and c) are explained as follows. An IR photon absorption by cold ions results in an inhomogeneous broadening and red shift of the electronic spectrum.[11] Since electronic absorption band of HisH$^+$ is much broader compared to this shift, vibrational transition cannot be fully saturated by a pump IR OPO laser in IR-IR-UV hole-burning spectroscopy. Following internal heating due to the pump IR OPO laser, an absorption of an additional IR photon from a scanning probe IR OPO laser pulse results in an additional gain from the "hot" conformer. Since vibrational transitions of hot ions shift to the red due to intramode anharmonicity, this additional gain appears to the red from the vibrational transition and results in a signal dip after it is subtracted from the all-conformer gain spectrum.

Vibrational transitions reflect structural preferences of ions and molecules. Tables 3.4-6 show experimentally measured conformer-specific vibrational transition energies for all protonated aromatic amino acids, neutral amino acids Phe and Trp, and two charge states of imidazole ring, respectively.

Careful analysis of these data allows determination of certain patterns in vibrational spectra, related to the structural features. For example, in protonated aromatic amino acids conformers Phe$^+$ **A**, Trp$^+$ **A** and Tyr$^+$ **A** and **B** (highlighted with grey color in Table 3.4) exhibit higher frequency of the free NH stretch, compared to the second half of conformers.

Figure 3.20 shows the comparison of previously reported vibrational spectra of protonated and neutral amino acids and peptides in the gas phase,[3, 4, 22, 120] as well as different charge states of imidazole ring,[121, 122] with the ones of HisH$^+$. The analysis allows to assign vibrational transitions and qualitatively predict the protonation cite in histidine.

The blue-most transitions at 3569.8 and 3563.2 cm^{-1} are the carboxylic acid O-H stretch vibrations of conformers **A** and **B**, respectively. The presence of this transition in the spectra of both conformers eliminates existence of zwitterion charge state, though the position of these bands is approximately between the ones of neutral and protonated amino acids (figures 3.20a-d) and does not allow for an identification of the protonation site.

Table 3.4. Conformer specific energies of vibrational transitions (in cm^{-1}) of protonated aromatic amino acids Phe, Tyr and Trp. Highlighted are conformers of aromatic amino acids with higher frequency of the free amine N-H stretch vibration.

	Phenol OH	Carboxylic acid OH	Indole NH	Amine NH	Amine NH…OC	Amine NH…π
Phe$^+$ A	-	3553.9	-	3356.8	3083.4	3056.8
Phe$^+$ B	-	3552.6	-	3338.9	3126.7	3091.5
Tyr$^+$ A	3643.4	3554.3	-	3354.6	3083.8	3058.8
Tyr$^+$ B	3645.2	3554.9	-	3358.3	3077.8	3055.4
Tyr$^+$ C	3643.9	3553.4	-	3338.6	3128.3	3087.4
Tyr$^+$D	3642.2	3553.2	-	3341.1	3127.3	3087.5
Trp$^+$ A	-	3556.2	3504.3	3355.9	3093.7	3029.9
Trp$^+$ B	-	3554.4	3503.7	3339.9	3124.9	3042.9

Table 3.5. Conformer specific energies of vibrational transitions (in cm^{-1}) of neutral aromatic amino acids Phe and Trp.

	Carboxylic acid OH	Indole NH	Amine NH$_s$	Amine NH$_a$
Phe I	3235	-	3428	3341
Phe II	3579	-	3402	3342
Phe III	3280	-	3411	3351
Phe V	3581	-	3420	3342
Phe VI	3567	-	3405	3370
Trp A	3223	3521	3426	3337
Trp B	3577	3522	3423	3337
Trp C	3576	3524	3398	3337
Trp D	3579	3524	3412	3337
Trp E	3578	3523	3401	3337
Trp F	3276	3523	3405	3337

Table 3.6. Energies of vibrational transitions (in cm^{-1}) of neutral and protonated imidazole.

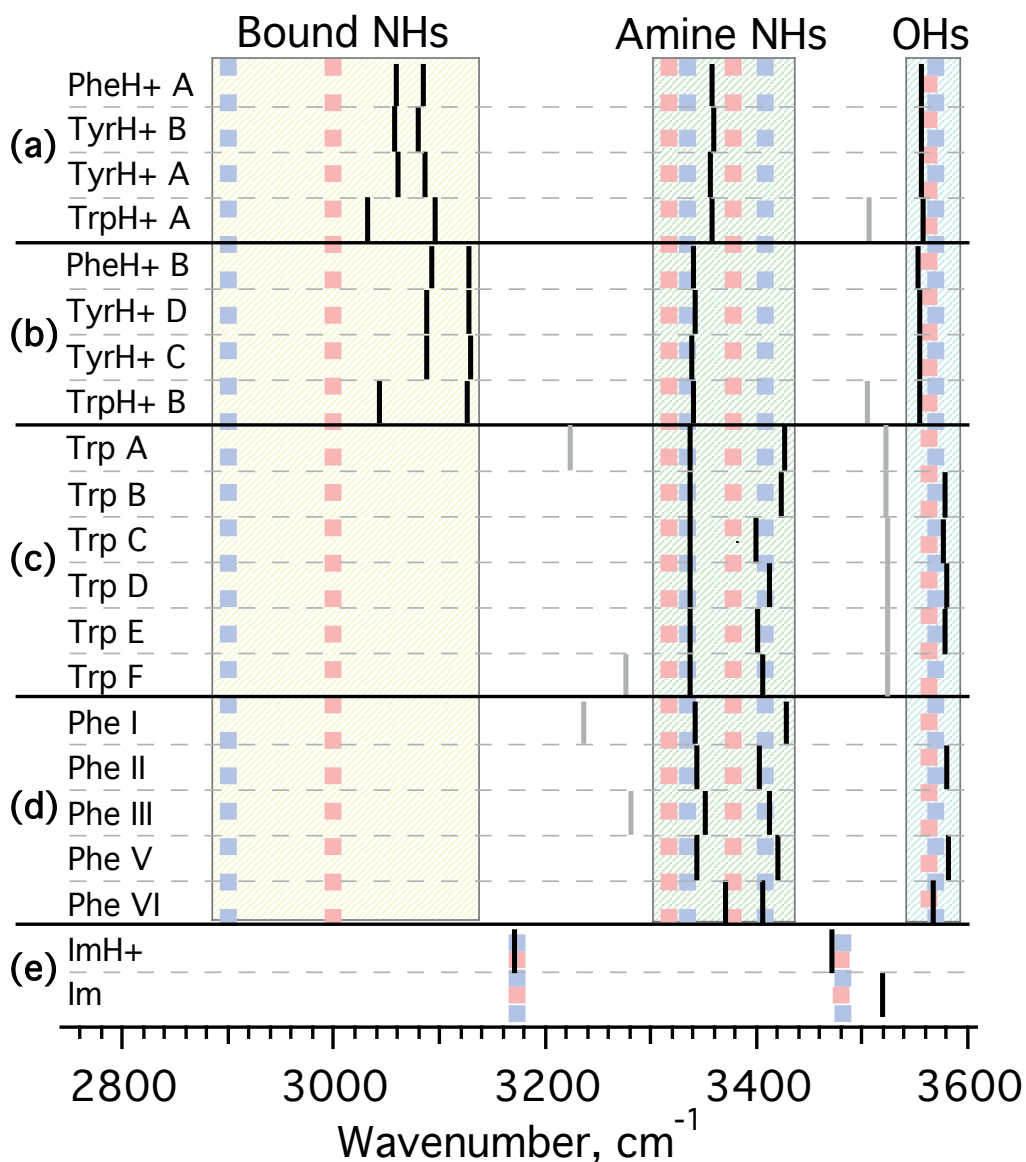|	Imidazole NH	Imidazole CH$_s$	Imidazole CH$_a$
ImH$^+$	3470	3170	3170
Im	3517.9	-	-

Figure 3.20. *Comparison of IR spectra of protonated and neutral aromatic amino acids and imidazole. (a) and (b) two groups of conformers of protonated aromatic amino acids TrpH⁺, TyrH⁺ and PheH⁺; (c) and (d) neutral amino acids Trp and Phe, respectively; (e) protonated and neutral imidazole, compared to vibrational transitions frequencies of HisH⁺ conformers **A** and **B** (blue and red dashed vertical lines, respectively). NOTE: C-H and N$_\tau$-H stretch vibrations are present only in 3.20e. Coloured areas denote the ranges of vibrational wavenumbers for specific vibration types, containing the frequencies of all species. Grey lines denote transitions, irrelevant for the current analysis, namely indole N-H transitions in Trp and O-H stretch vibrations involved in strong hydrogen bonds.*

In contrast, the N_τ-H stretch vibrations in protonated[121] and neutral[122] imidazole are centred at 3470 and 3517.9 cm^{-1}, respectively (figure 3.20e). The peaks of HisH$^+$ conformers at 3481.5 (**A**) and 3480.3 (**B**) cm^{-1} are very close in both conformers, and correspond to the N_τ-H stretch of ImH$^+$. The sharp transition at 3173.3 cm^{-1} also appears in spectra of both conformers and matches the C-H stretch vibration of the protonated imidazole ring.[121] The coincidence of N_τ-H and C-H vibrational transitions (nearly identical for conformers **A** and **B**) of ImH$^+$ and of HisH$^+$ indicates that both lowest energy structures are protonated on the imidazole ring.

The transitions at 3408.3 and 3333.5 cm^{-1} for conformer **A** and 3377.3 and 3317.2 cm^{-1} for conformer **B** correspond to the free amine N_α-H stretch vibrations. These vibrational transitions are conformer-specific and, hence, can be used as benchmarks for structural identification.

As was already mentioned above, vibrational transitions reflect structural features of molecules. For example, the spectra of protonated aromatic amino acids TrpH$^+$, TyrH$^+$, and PheH$^+$ exhibit common patterns, consistent with the similar intramoleculecular interactions in these ions (Table 3.4 and figures 3.20a and b). Two out of three characteristic amine N_α-H vibrations are involved in $N_\alpha H...\pi$ and $N_\alpha H...OC$ interactions, which shift their vibrational energies below 3130 cm^{-1}, while the third N_α-H vibration remains relatively "free" and its frequency changes in each group only within ~2-3 cm^{-1} interval. Such narrow distribution stems from the strong stabilizing effect of the charge. The NH groups, involved in intramolecular interactions, have wider range of values for different amino acids, which is due to the different electron density of the aromatic rings.

In contrast, only one N-H stretch in HisH$^+$ is involved in a strong interaction that shifts the vibrational transition to the red, while the other two remain free. Furthermore, the vibrational energies of the blue-most N-H transition in both conformers of HisH$^+$ are higher then 3370 cm^{-1}, while for all conformers of other aromatic amino acids vibrational transition frequencies reside below 3360 cm^{-1}.

Neutral amino acids exhibit much broader conformational space compared to their protonated counterparts due to the lack of strong stabilizing interactions of the protonated NH$_3^+$ moiety. Nevertheless, figures 3.20c and d clearly demonstrate, that in neutral amino acids Trp[3] and Phe[120] the frequencies of the N_α-H bands are similar with those of HisH$^+$ conformer **A**. In conformer **B** the "free" N_α-H and O-H vibrations are shifted to the red with respect to the ones in conformer **A**.

These considerations confirm again the protonation site on the imidazole ring, and allow assigning the broad bands centered at approximately 3000 and 2900 cm^{-1} (figure 3.19a) to the strongly bound N$_\pi$-H stretching vibration. The band at 2915 cm^{-1} belongs to the conformer **A** (figure 3.19b). We thus suggest that the band at 3000 cm^{-1} corresponds to the conformer **B**. However, the conformer-selective spectrum in figure 3.19c cannot confirm this assumption because this low-intensity band overlaps with the band of conformer **A**.

The peak at 3408.3 cm^{-1} in both gain (figure 3.19a) and the conformer-selective spectrum of conformer **A** (figure 3.19b) consists of two overlapping transitions, which might occur due to the presence of a third conformer, **A***, whose structure and spectrum resemble the ones of conformer **A**, although their spectra cannot be separated. Figure 3.21 shows the fitting of this transition with a double-Gaussian function. It is only due to the low temperature that these transitions are resolved.
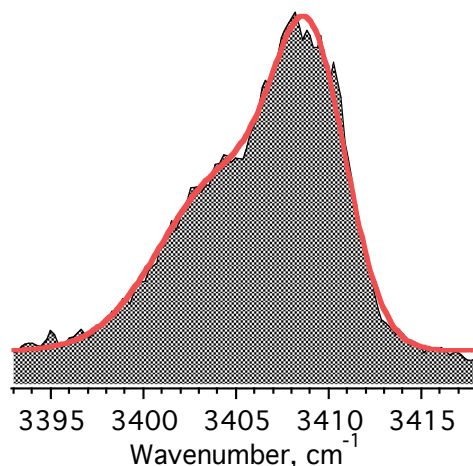

Figure 3.21. *Expanded view of the "doubled" peak at 3408.5 cm^{-1} and its fit by a double Gaussian function.*

5. Isotopically Substituted HisH$^+$ in 3 µm Spectral Region

The comparative analysis, provided above, demonstrates that even an all-conformer vibrational gain spectrum can provide certain information to derive some conclusions regarding the structural motifs of the studied ion. Alternatively, measuring spectra of isotopically labeled analogues of an ion can provide an experimental verification of the assignment.

Figure 3.22 shows the comparison of the IR gain spectra of HisH$^+$ (black trace) and [^{15}N$_\alpha$]HisH$^+$, an ion whose N-terminal nitrogen atom was substituted by ^{15}N$_\alpha$ (mirrored green trace). The shift of the amine N$_\alpha$-H stretch vibrations with frequencies higher than 3300 cm^{-1} is in the full

agreement with the harmonic oscillator approximation and is $\sim$5-8 cm^{-1}. The sharp transition at 3173.3 cm^{-1} exhibits no shift, which does not contradict to its assignment to the imidazole C-H stretch vibration. The broad transitions at 3000 and 2915 cm^{-1} do not exhibit any visible shift, in accordance with the assumption that they belong to the N$_\pi$-H stretching vibrations of the imidazole ring, rather than of the amine group. However, this observation cannot be used as a strict validation of the assumption regarding the protonation site on the imidazole ring, because isotopic shifts ($\sim$5 cm^{-1}) are much smaller compared with the width of these transitions.
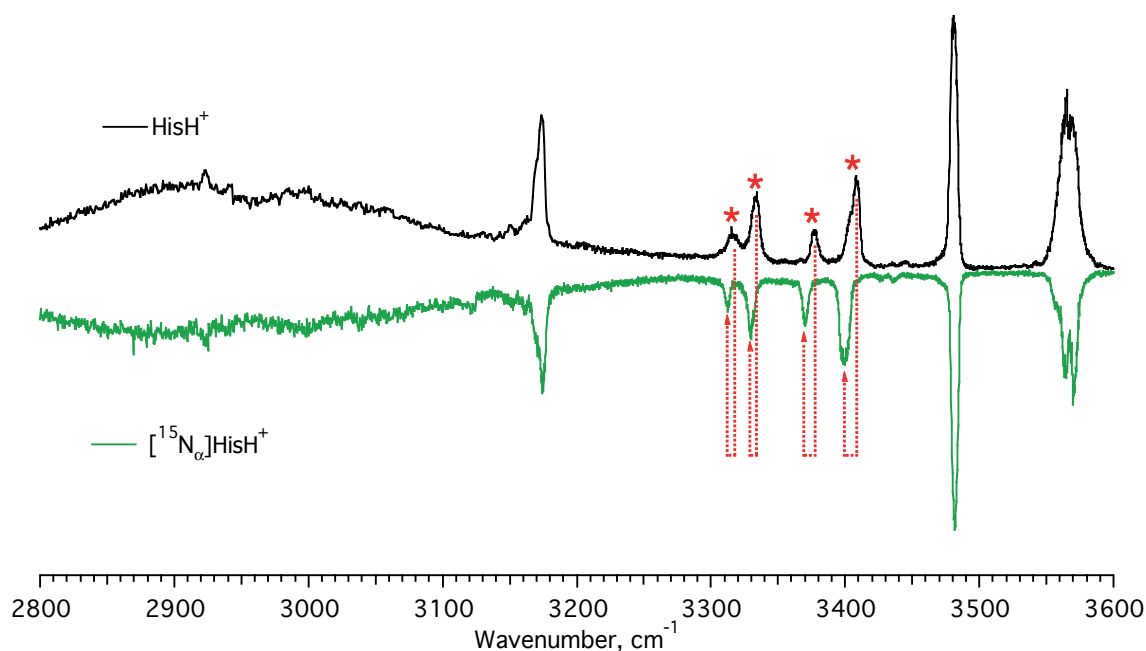

Figure 3.21. *All-conformer IR-UV gain spectra of natural (black trace) and isotopically labelled (^{15}N in the amine group; mirrored green trace) HisH$^+$ in the 3 μm spectral region. The transitions labelled by red asterisks exhibit isotopic redshifts of $\sim$4-8 cm^{-1}.*

6. *Vibrational Spectroscopy of HisH$^+$ and [^{15}N$_\alpha$]HisH$^+$ in 6 μm Spectral Region*

Figure 3.22 shows the gain spectra of natural HisH$^+$ and its analogue, isotopically labelled by N^{15} on the N-terminus. It is worth to notice, that the recorded linear IR spectra do not resemble the previously reported IRMPD spectra HisH$^+$ at room temperature in 9-5.5 μm spectral range. However, the spectrum of the [^{15}N$_\alpha$]HisH$^+$ in the 6 μm spectral range clearly shows, that only two transitions exhibit isotopic shifts. These transitions correspond to the amine scissoring vibrations. If the protonation would occur on the N-terminus, ammonia group would exhibit two scissoring

vibrations for each conformer. Therefore, this observation can be used as a direct evidence for the protonation of HisH$^+$ on its imidazole ring.
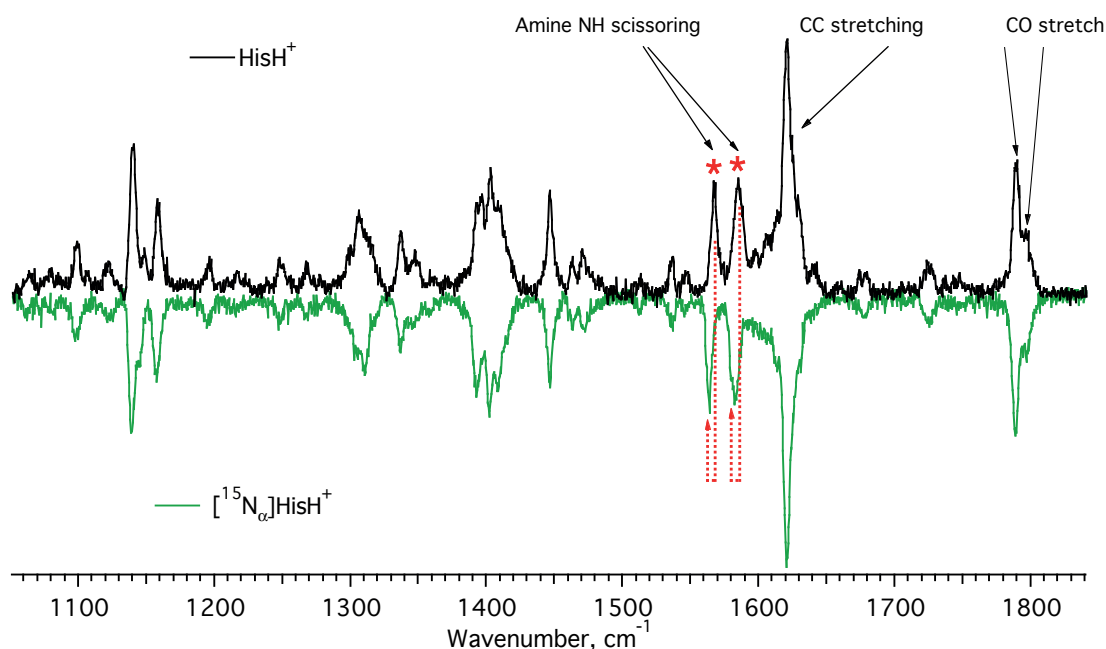

Figure 3.22. *All-conformer IR-UV gain spectra of natural (black trace) and isotopically labelled (^{15}N in the amine group; mirrored green trace) HisH$^+$ in the 6 µm spectral region. The transitions labelled by red asterisks exhibit isotopic redshifts of ~3 cm^{-1}.*

3.4.3. Theoretical Calculations

The initial set of the 3D structures of the thirty nine lowest energy conformers of protonated histidine were gracefully provided by professor Lin.[115] Twelve of these conformers have a protonation site at the N-terminal amine group, while the other twenty-seven conformers are protonated on the imidazole ring. Given the spectral analysis and speculations, described above in details, there is sufficient evidence in favor of side chain protonated histidine, therefore any other structures were excluded from the present analysis.

1. Structure Optimization

The geometries of all the conformers were re-optimized (with tight convergence criteria) using the B3LYP functional (with VWN functional III for local correlation)[123-126] with the

Grimme's empirical dispersion correction (GD3BJ)[127] and the 6-311+G(d,p) basis set. Table 3.7 shows the relative energies of these conformers.

Table 3.7. Electronic energies of HisH$^+$[N$_\pi$] structures with respect to the lowest energy structure.

Structure	Δε, kcal/mol		Structure	Δε, kcal/mol		Structure	Δε, kcal/mol
1	0		10	4.25		19	10.20
2	0.78		11	6.95		20	10.20
3	0.90		12	7.79		21	10.81
4	2.06		13	8.25		22	10.54
5	1.98		14	8.47		23	11.16
6	1.41		15	8.83		24	11.80
7	2.03		16	9.00		25	12.02
8	2.78		17	8.25		26	16.59
9	3.31		18	9.90		27	17.15

2. Harmonic Calculations

The optimized structures were subsequently subjected to harmonic frequency calculations. The calculated harmonic frequencies were scaled by a factor α = 0.9538 to account for the intramode anharmonicity (in the 3 μm region) and compared with experimental IR spectra. The empirical scaling coefficient α was chosen so that to minimize the Root Mean Square Deviation (RMSD) between the experimental and scaled theoretical frequencies for the two best matching structures (structure 1 for conformer **A** and structure 3 for conformer **B**), whose spectra are drawn with the same color as their corresponding conformers. α was calculated as follows[67, 68]:

$$\alpha = \frac{\sum_{i,j}\left(\nu_{i,j}^{exp}\nu_{i,j}^{calc}\right)}{\sum_{i,j}\left(\nu_{i,j}^{calc}\right)^2} \tag{Eq. 3.1}$$

where ν^{exp} and ν^{calc} are the experimental and calculated vibrational frequencies, respectively, $i =$ A, B is the conformer identification, $j =$ O-H, N$_\alpha$-H$_{sym}$ and N$_\alpha$-H$_{antisym}$ vibrational modes, used for the calculation. The imidazole N$_\tau$-H vibration is very similar in all calculated structures and is consistently red-shifted from the experimental value. We assume that this miscalculation is intrinsic to the B3LYP level of theory. Figure 3.23 shows the resulting spectra of the candidate structures.

Calculated harmonic frequencies employ empirical scaling coefficients in order to account for the intramode anharmonicity of vibrations. Ideally, one should use different coefficients for different types of vibrations. Although this approach is proven to work properly for large

polyatomics with many vibrations, a use of the empirical coefficients reduces the confidence in validating structures of small molecules. This adds more ambiguity to the previous validation of HisH$^+$ structures. We, therefore, use harmonic calculations to pre-select the best-matching candidate structures in order to perform more time-costly anharmonic calculations.
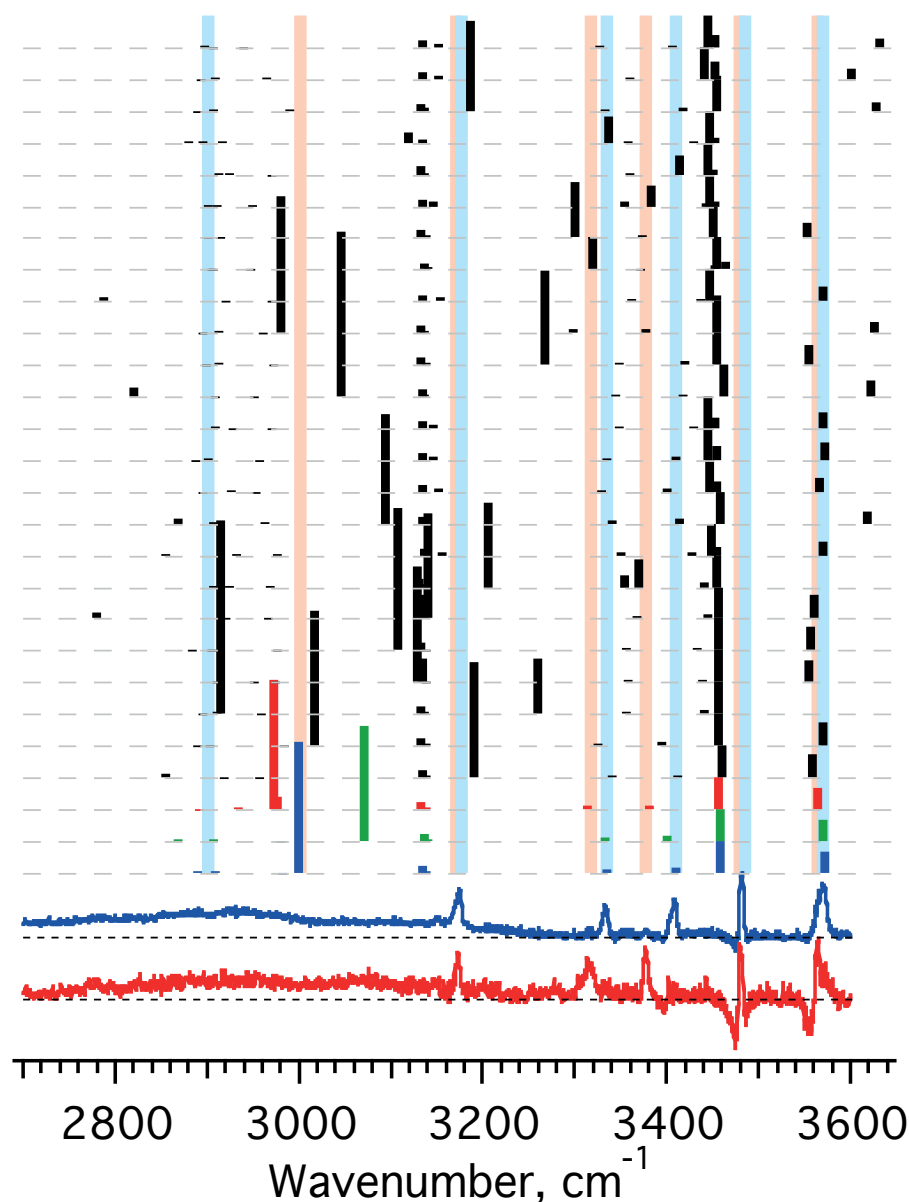

Figure 3.23. *Comparison of the calculated harmonic spectra of the 27 lowest energy structures of HisH$^+$[N$_\pi$] (numbering of the structures starts from the lowest row) with conformer-selective spectra of HisH$^+$ (blue and red traces correspond to conformers **A** and **B**, respectively). Vertical light-blue and light-red lines denote frequencies of corresponding conformers. The best-matching spectra (three lowest energy structures) are color-coded as the corresponding conformers.*

The three lowest-energy structures show a good match of the calculated O-H and amine N_α-H stretch vibrations with experimentally measures values. The vibrational transitions, associated with the imidazole ring are similar in all conformers, which is in a full agreement with the experiment. Strangely, N_τ-H stretching vibration seems to be miscalculated in all structures.

The spectra of the structures 1 and 3 match best the experimentally measured spectra of conformers **A** and **B**, respectively. The spectrum of the structure 2 (figure 3.23, green trace) is similar to the one of structure 1 and differs only in the slightly red-shifted symmetric N_α-H vibration. This is in a full agreement with experimentally observed splitting of this transition in the gain spectrum (figure 3.21).

Figure 3.24 shows the geometries of the structures 1, 2 and 3, corresponding to the conformers **A**, **A***, and **B**, respectively. The structures differ, mainly, in the position of the C-terminal group. All low energy conformers of HisH$^+$, protonated on the imidazole ring, are stabilized by the strong non-covalent interaction of the proton, shared between N_π atom of the imidazole ring and the amide group. In this respect, the intrinsic structures of HisH$^+$ fundamentally differ from all known solution-phase geometries at any pH.[112-114] Protonation on the imidazole ring in solution occurs only in at pH<2.5 for doubly protonated form of histidine.[113] Only the most stable structure **A** was correctly identified in the previous studies.[116]
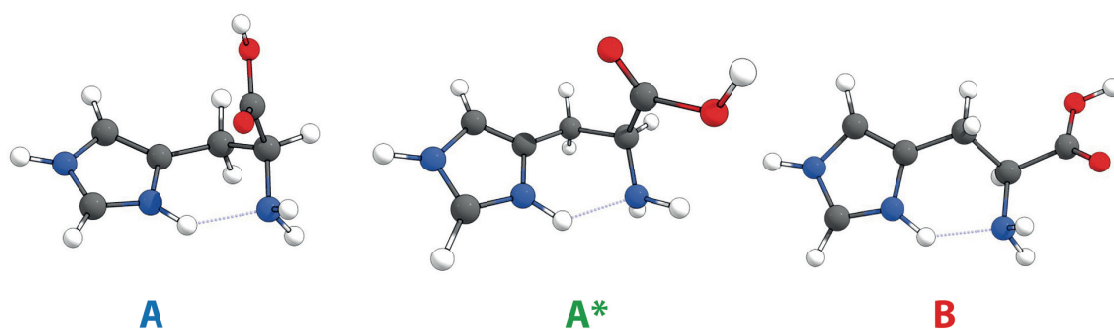

Figure 3.24. *Calculated lowest-energy intrinsic structures of HisH$^+$ **A**, **A*** and **B**.*

3. Anharmonic Calculations

Finally, for the pre-selected lowest energy conformers within a 2 kcal/mol window the anharmonic frequencies were calculated by means of the VPT2 approach[128] with four displacements for each degree of freedom and a step size of 0.025 Å. All the DFT calculations were carried out with the Gaussian 09 program[129] using the UltraFine integration grid. The comparison of

anharmonic calculations for structures **A**, **A***, and **B** (blue, green, and red traces, respectively) with the experimentally measured conformer-selective spectra in the 3 μm spectral region is shown in figure 3.25. A good match of the calculated and experimental vibrational frequencies is achieved without the use of any empirical scaling coefficient.
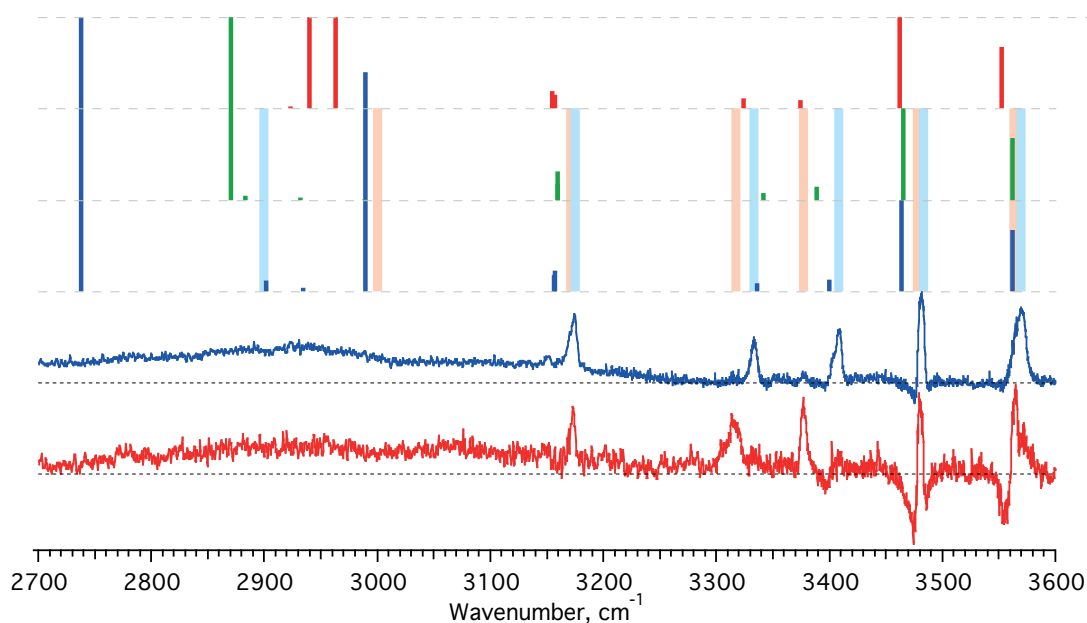

Figure 3.25. *Comparison of the anharmonic calculations for structures **A**, **A*** and **B** (blue, green and red traces, respectively) with conformer-selective vibrational spectra of HisH$^+$ in 3 μm spectral region.*

In the analysis of the calculated harmonic spectra the scaling coefficient was calculated such as to minimize the RMSD for the three conformer-specific vibtational transitions. The resulting scaled spectra, therefore, might seem a better match for the experimental ones (at least for the transitions, that were accounted for in the calculation of the scaling coefficient). Are the anharmonic calculations, indeed, more reliable compared with the scaled harmonic ones? In order to answer this question quantitatively, the scaling coefficient was recalculated taking into account all five well-resolved transitions in the 3 μm spectral region of the conformer **A**. The corresponding $RMSD_{harm}$ for the scaled, harmonic spectrum is 37.5 cm^{-1}, while the $RMSD_{anh}$ for the anharmonic calculated spectrum, without any artificial scaling coefficient, is 30.0 cm^{-1} for the same conformer **A**, that is, 20% lower! This quantitative difference supports the suggestion, that the use of anharmonic calculations for small molecules provides more confidence in their structural validation.

The anharmonic spectra are also compared with all-conformer gain spectrum of HisH$^+$ in 6 μm spectral region (figure 3.26). The calculated carboxylic acid C=O and and imidazole C=C stretching vibrations show a good match with experiment. The calculated amine N$_\alpha$-H scissoring modes are blue-shifted with respect to the experiment. Nevertheless, the overall agreement between experiment and theory is extremely good.
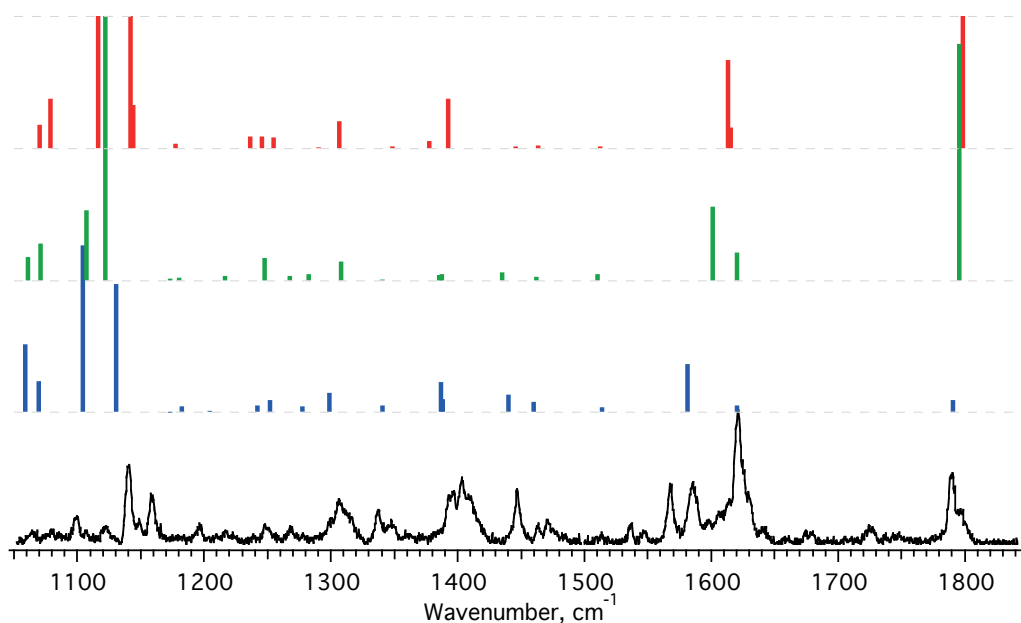

Figure 3.26. *Comparison of the anharmonic calculations for structures* **A**, **A*** *and* **B** *(blue, green and red traces, respectively) with all-conformer vibrational gain spectrum of HisH$^+$ in 6 μm spectral region.*

4. *Experimental Constraints for Theoretical Calculations*

The conformer-selective multilaser cold ion spectroscopy combined with high-level *ab initio* calculations has proven the existence of three highly abundant conformers of HisH$^+$ in the gas-phase. The electronic energies of conformers **A*** and **B** are ~0.8-0.9 kcal/mol higher with respect to the one of the conformer **A**. Assuming Boltzman distribution of conformers' populations in the trap at $T = 10$ K, the relative populations of the conformers **A*** and **B** should be negligible ($1.1 \cdot 10^{-19}$ for the second lowest energy structure)! Observation of these conformers in experiment may originate from two processes:

(i) a fast non-adiabatic collisional cooling of ions, which traps them in the local minima of the gas-phase potential energy surface;

(ii) "kinetic" trapping of ions in their solution-like local minima of the potential energy surface.

The fact that all three conformers of HisH$^+$ do not even exist in solution phase[113] points to the non-adiabatic cooling and rules out the presence of "kinetic" trapping in our experiments. Therefore, only the gas-phase conformers that are populated at high temperatures (presumably, in the ion source) can be observed in the gas-phase.

In section 3.3.3 it was demonstrated that the in-source CID of the protonated tryptophan can be used to decrease the internal heating of ions. The settings (pressure and RF amplitudes) were chosen so that to suppress the most fragile fragment of TrpH$^+$, namely, the ammonia loss. The energetics of this dissociation reaction[38] ($\sim$25 kcal/mol, or $\sim$8500 cm^{-1}) allows us to estimate the maximum "effective" internal temperature of the ions in the source. The average internal energy of an ion at any temperature T can be calculated as follows:

$$\overline{E(T)} = \sum_{i=1}^{k} \nu_i \frac{e^{-\frac{\nu_i}{kT}}}{1-e^{-\frac{\nu_i}{kT}}} \qquad \text{(Eq. 3.2)}$$

where ν_i are the vibrational mode energies, $k=3N$-6 is a number of vibrational modes in the molecule, $N-$ is the number of atoms. According to the eq. 3.2 the internal vibrational energy of protonated tryptophan is $\sim$8500 cm^{-1} at $T \approx 600$ K. In reality, the width of the Boltzman distribution suggests that a considerable fraction of ions would have internal energies exceeding the dissociation threshold, and some fragmentation would be inevitably detected. Therefore, $T = 600$ K is, indeed, an upper limit for the internal vibrational temperature of ions. A practical limit of the relative population of conformers that can be reliably detected using cold ion spectroscopy is about 10%. This implies that at $T = 600$ K only the conformer with the relative potential energies below $\Delta E \leq -ln(0.1) \cdot kT \approx 2.7$ kcal/mol can be detected in our experiment. Here we assume a prompt nonadiabatic cooling in the cold trap that conserves the initial relative populations of the conformers. A partial collisional relaxation of higher-energy conformer to the lower-energy structures may only lower the 2.7 kcal/mol cutoff energy.

These considerations imply that there is no sense in calculating vibrational spectra for structures with relative potential energies more than $\sim$ 3 kcal/mol. This constrain should only be applied, when the subsequent structural optimizations do not change the energetics of the structures for more than $\sim$ 0.5 kcal/mol. As can be seen from table 3.7, an application of this rough criterion

in calculations of IR spectra of $HisH^+$ would immediately eliminate 70% (19 out of 27) of initial structures, protonated on the imidazole ring. If such constrained calculations do not identify an experimentally detected conformer, it might correspond, indeed, to a "kinetically" trapped geometry, for which the potential minimum is higher than the cutoff, in which case other physical constraints (e.g. collisional cross section) have to be applied.

3.4.4. Conformer-Specific Photofragmentation Mass Spectra

Previous studies have shown, that intrinsic structure affects the relative efficiency of different fragmentation channels; therefore different conformers can have different photofragmentation mass spectra. This effect is observed not only in small molecules, such as single amino acids[4] or dipeptides, but also for large, rigid peptide gramicidin S.[130] There the selective excitation of the vibrationally resolved conformer-specific electronic transitions resulted in different photofragmentation mass spectra. Whenever UV spectrum lacks vibrational resolution, excitation of an ion ensemble at any wavelength results in photofragmentation of all available conformers, as in the cases of protonated aromatic amino acids tryptophan and histidine.

In contrast to UV, IR spectra of these ions remain vibrationally resolved. Excitation of ions with an IR pulse results in the increased fragmentation yield. This increase results from the higher fragmentation yield of the IR pre-heated ions and is conformer-specific depending of the IR frequency. Because of the small energy of IR photon that is distributed equally among all vibrational modes of an ion, the IR-induced differences in photofragmentation mass spectra are not expected to be striking. Nevertheless, this experiment results still in a very interesting observation.

Figure 3.27 compares the IR-induced additional photofragmentation signal, generated as the difference between photofragmentation mass spectra of IR pre-heated and cold ions, recorded with IR OPO fixed at the carboxylic acid O-H stretch vibrations of conformers **A** (3569.8 cm^{-1}, blue trace) and **B** (3563.2 cm^{-1}, red trace). Given the above assignment of the fragments, m/z = 110 Da corresponds to the concomitant loss of (H_2O+CO) following hydrogen atom transfer to the carboxylic group.[79, 80, 82] The efficiency of this transfer should depend crucially on the distance between the proton and the carboxylic group in $HisH^+$ conformers. Hence, it was suggested that the relative abundances of this fragment and the competing process of C_α-C_β bond cleavage that does not imply hydrogen transfer differ in conformers **A** and **B**. Indeed, the decrease of the relative abundance of the iminium ion fragment with m/z = 110 Da in conformer **B** agrees well with the increased distance between the proton and the C-terminus in this conformer, which leads to the less efficient hydrogen atom transfer. The distances between the geometrical center of the imidazole

ring and the oxygen atom of the OH group are 4.21 Å for conformer **A**, 4.76 Å for conformer **A***, and 5.44 Å for conformer **B**. Therefore, increasing the distance between the ring and the C-terminus 1.3 times causes 1.5 times decrease in relative abundance of the associated fragment. This observation, thus, qualitatively agrees with our assignment of the structures observed in the gas-phase.
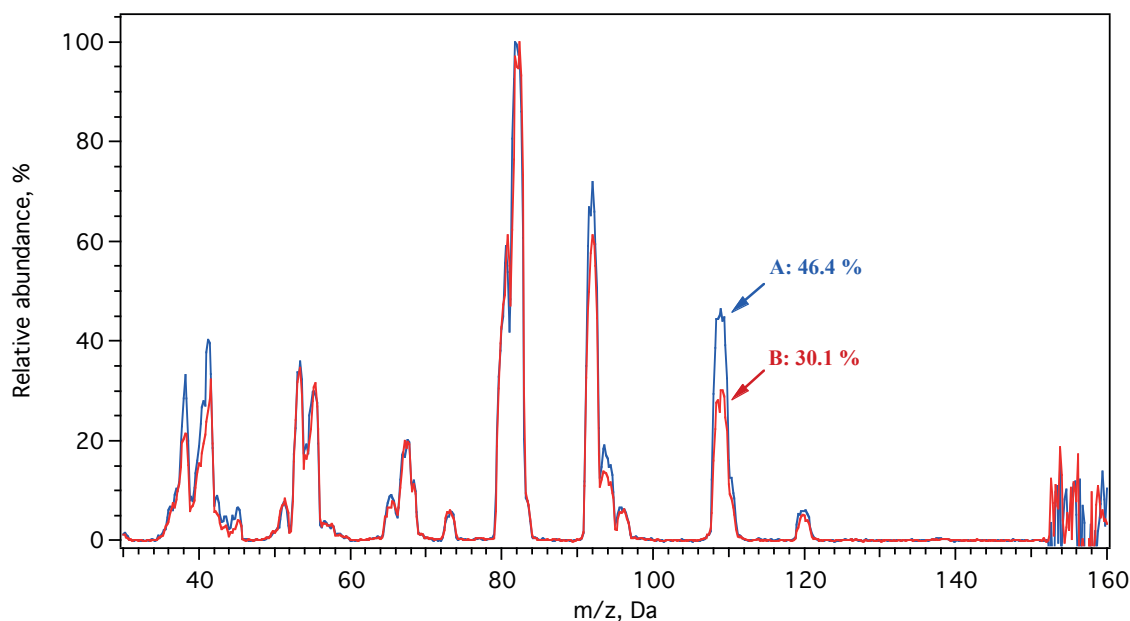

Figure 3.27. *IR-induced additional fragmentation signals, generated as the difference between photofragmentation mass spectra of IR pre-heated and cold ions, recorded with IR OPO fixed at the carboxylic acid O-H stretch vibrations of conformers **A** (3569.8 cm^{-1}, blue trace) and **B** (3563.2 cm^{-1}, red trace).*

3.5. Conclusions

An ancillary aim of this work has been to devise and demonstrate a novel conformer selective spectroscopic technique, IR-IR-UV hole-burning, which allows extending the applicability of cold ion spectroscopy to species with broad UV photofragmentation spectra. Herein this technique was applied to record conformer-specific vibrational spectra of the protonated aromatic amino acids tryptophan and histidine. Provided that a UV-active chromophore is present in a molecule, this technique holds significant promise for the conformer-specific assessment of structures in larger biomolecules, where UV absorptions are often broad and unresolved.

A combined experiment-theory approach has definitively assigned the lowest-energy conformers of the protonated aromatic amino acids tryptophan and histidine, whose structures have remained elusive. These biomolecular ions challenge existing spectroscopic and computational protocols.

Two nearly degenerate isomers were found to dominate the contributions to the cold, gas-phase vibrational spectrum of protonated tryptophan. These vibrational signatures, some of which exhibited significant anharmonicities, were found to be sensitive probes of the intramolecular interactions that dictate the low-energy structures. Finally, the intramolecular interactions within TrpH$^+$ were investigated with a variety of computational approaches. Both an H-bonding/dipole-dipole interaction and a strong cation-π interaction were found to be the source of both the stability of the low-energy isomers and the strong redshifts in the vibrational spectrum. These stabilizing interactions are expected to be transferable effects to larger biomolecular complexes, at the N-terminus of Trp-containing systems. Whether these short-range interactions *within* TrpH$^+$ outcompete related interactions *between* amino acid subunits (or solvent) requires future investigation. The techniques employed in the present study should be transferable to these larger complexes, however, and provide necessary experimental and computational tools to access such structural information in biologically relevant molecules.

UV photo fragmentation spectrum cold protonated histidine isolated in the gas phase has been recorded for the first time in a wide spectral range. Despite the observed broadband UV absorption, an application of the IR-IR-UV technique revealed three abundant conformers of this ion. A detailed comparison of structure-specific vibrational frequencies in neutral and protonated species together with experimental investigation of isotopically substituted histidine and high-level anharmonic calculations point to the protonation of the imidazole ring in all three experimentally observed conformers of HisH$^+$. The stepwise conformational search within the calculated geometries of the ion was constrained by a comparison of the measured IR spectra with those, calculated at a harmonic level of theory and, finally, with the anharmonic spectra, computed from the first principles. It was suggested that such search can be simplified if only the structures with potential energy ≤ 3 kcal/mol will be retained for spectral calculations.

In overall, this work demonstrates feasibility for the extension of conformer-selective vibrational cold ion spectroscopy to the peptides with broad electronic spectra and, in particular, the ones that contain histidine as a chromophore.

References

1.   T. R. Rizzo, J. A. Stearns and O. V. Boyarkin, *Int. Rev. Phys. Chem.*, 2009, **28**, 481-515.

2.   T. R. Rizzo and O. V. Boyarkin, in *Gas-Phase IR Spectroscopy and Structure of Biological Molecules*, eds. A. M. Rijs and J. Oomens, Springer, 2015, vol. 364, pp. 43-98.

3.   L. C. Snoek, R. T. Kroemer, M. R. Hockridge and J. P. Simons, *Phys. Chem. Chem. Phys.*, 2001, **3**, 1819-1826.

4.   J. A. Stearns, S. Mercier, C. Seaiby, M. Guidi, O. V. Boyarkin and T. R. Rizzo, *J. Am. Chem. Soc.*, 2007, **129**, 11814-11820.

5.   J. A. Stearns, C. Seaiby, O. V. Boyarkin and T. R. Rizzo, *Phys. Chem. Chem. Phys.*, 2009, **11**, 125-132.

6.   N. S. Nagornova, T. R. Rizzo and O. V. Boyarkin, *J. Am. Chem. Soc.*, 2010, **132**, 4040-+.

7.   A. Y. Pereverzev and O. V. Boyarkin, *Phys. Chem. Chem. Phys.*, 2017, **19**, 3468-3472.

8.   D. H. Levy, *Science*, 1981, **214**, 263-269.

9.   O. V. Boyarkin, S. R. Mercier, A. Kamariotis and T. R. Rizzo, *J. Am. Chem. Soc.*, 2006, **128**, 2816-2817.

10.   H. Kang, C. Jouvet, C. Dedonder-Lardeux, S. Martenchard, G. Grégoire, C. Desfrancois, J.-P. Schermann, M. Barat and J. A. Fayeton, *Phys. Chem. Chem. Phys.*, 2005, **7**, 394-398.

11.   N. S. Nagornova, T. R. Rizzo and O. V. Boyarkin, *Angew. Chem.*, 2013, **52**, 6002-6005.

12.   N. L. Burke, J. G. Redwine, J. C. Dean, S. a. McLuckey and T. S. Zwier, *Int. J. Mass spectrom.*, 2015, **378**, 196-205.

13.   N. S. Nagornova, PhD, ÉCOLE POLYTECHNIQUE FÉDÉRALE DE LAUSANNE, 2011.

14.   J. Jašík and J. Roithová, *Int. J. Mass spectrom.*, 2015, **377**, 109-115.

15.   A. Masson, M. Z. Kamrath, M. A. S. Perez, M. S. Glover, U. Rothlisberger, D. E. Clemmer and T. R. Rizzo, *J. Am. Soc. Mass. Spectrom.*, 2015, **26**, 1444-1454.

16.   E. K. Campbell, M. Holz, D. Gerlich and J. P. Maier, *Nature*, 2015, **523**, 322-323.

17.   B. M. Elliott, R. A. Relph, J. R. Roscioli, J. C. Bopp, G. H. Gardenier, T. L. Guasco and M. A. Johnson, *J. Chem. Phys.*, 2008, **129**, 094303.

18.   J. Roithova, A. Gray, E. Andris, J. Jas and D. Gerlich, *Acc. Chem. Res.*, 2015, **49**, 223-230.

19.   A. Masson, E. R. Williams and T. R. Rizzo, *J. Chem. Phys.*, 2016, **143**, 104313.

20.   C. M. Leavitt, A. B. Wolk, J. A. Fournier, M. Z. Kamrath, E. Ganard, M. J. Van Stipdonk and M. A. Johnson, *J. Phys. Chem. Lett.*, 2012, **3**, 1099-1105.

21.   V. A. Shubert and T. S. Zwier, *J. Phys. Chem. A*, 2007, **111**, 13283-13286.

22.   A. Y. Pereverzev, X. Cheng, N. S. Nagornova, D. L. Reese, R. P. Steele and O. V. Boyarkin, *J. Phys. Chem. A*, 2016, **120**, 5598-5608.

23.   Y. P. Meshalkin, E. E. Alfimov, D. E. Groshev and V. K. Makukha, *J. Appl. Spectrosc.*, 1996, **63**, 357-360.

24.   R. F. Chen, *Anal. Lett.*, 1967, **1**, 35-42.

25.   J. T. Vivian and P. R. Callis, *Biophys. J.*, 2001, **80**, 2093-2109.

26.   J. R. Lakowicz, *Photochem. Photobiol.*, 2000, **72**, 421-437.

27.   P. L. Muino and P. R. Callis, *J. Phys. Chem. B*, 2009, **113**, 2572-2577.

28.   J. S. Anderson, G. S. Bowitch and R. L. Brewster, *Biopolym.*, 1983, **22**, 2459-2476.

29.   I. Munro, I. Pecht and L. Stryer, *PNAS*, 1979, **76**, 56-60.

30.   A. P. Romani, C. A. Marquezin and A. S. Ito, *Int. J. Pharm.*, 2010, **383**, 154-156.

31.   G. M. Palmer, P. J. Keely, T. M. Breslin and N. Ramanujam, *Photochem. Photobiol.*, 2003, **78**, 462-469.

32.   T. R. Rizzo, Y. D. Park and D. H. Levy, *J. Am. Chem. Soc.*, 1985, **107**, 277-278.

33.   T. R. Rizzo, Y. D. Park, L. Peteanu and D. H. Levy, *J. Chem. Phys.*, 1985, **83**, 4819.

34.   T. R. Rizzo, Y. D. Park, L. A. Peteanu and D. H. Levy, *J. Chem. Phys.*, 1986, **84**, 2534.

35.   T. R. Rizzo, Y. D. Park and D. H. Levy, *J. Chem. Phys.*, 1986, **85**, 6945.

36.   L. A. Philips, S. P. Webb, S. J. Martinez, G. R. Fleming and D. H. Levy, *J. Am. Chem. Soc.*, 1988, **110**, 1352-1355.

37.   D. Nolting, C. Marian and R. Weinkauf, *Phys. Chem. Chem. Phys.*, 2004, **6**, 2633-2640.

38.   H. Lioe, R. A. J. O'Hair and G. E. Reid, *J. Am. Soc. Mass. Spectrom.*, 2004, **15**, 65-76.

39.   J. Mino, Warren K., K. Gulyuz, D. Wang, C. N. Stedwell and N. C. Polfer, *J. Phys. Chem. Lett.*, 2011, **2**, 299-304.

40.   V. Riffet, S. Bourcier and G. Bouchoux, *Int. J. Mass spectrom.*, 2012, **316-318**, 47-56.

41.   U. Purushotham and G. N. Sastry, *J. Comput. Chem.*, 2014, **35**, 595-610.

42.   D. J. Wales and J. P. K. Doye, *J. Phys. Chem. A*, 1997, **101**, 5111-5116.

43.   C. Møller and M. S. Plesset, *Phys. Rev.*, 1934, **46**, 618-622.

44.   M. Feyereisen, G. Fitzgerald and A. Komornicki, *Chem. Phys. Lett.*, 1993, **208**, 359-363.

45.   O. Vahtras, J. Almlöf and M. W. Feyereisen, *Chem. Phys. Lett.*, 1993, **213**, 514-518.

46.   F. Weigend, M. Häser, H. Patzelt and R. Ahlrichs, *Chem. Phys. Lett.*, 1998, **294**, 143-152.

47.   Y. Jung, A. Sodt, P. M. W. Gill and M. Head-Gordon, *PNAS*, 2005, **102**, 6692-6697.

48.   R. A. Distasio, R. P. Steele, Y. M. Rhee, Y. Shao and M. Head-Gordon, *J. Comput. Chem.*, 2007, **28**, 839-856.

49.   Y. Zhao, N. E. Schultz and D. G. Truhlar, *J. Chem. Theor. Comput.*, 2006, **2**, 364-382.

50.   N. Mardirossian and M. Head-Gordon, *J. Chem. Phys.*, 2015, **142**, 074111.

51.   A. D. Becke, *J. Chem. Phys.*, 1993, **98**, 5648-5652.

52.   P. J. Stephens, F. J. Devlin, C. F. Chabalowski and M. J. Frisch, *J. Phys. Chem.*, 1994, **98**, 11623-11627.

53.   J. Cizek, *J. Chem. Phys.*, 1966, **45**, 4256-4266.

54.   R. J. Bartlett and M. Musiał, *Rev. Mod. Phys.*, 2007, **79**, 291-352.

55.   C. Sosa, J. Geertsen, G. W. Trucks, R. J. Bartlett and J. A. Franz, *Chem. Phys. Lett.*, 1989, **159**, 148-154.

56.   A. G. Taube and R. J. Bartlett, *J. Chem. Phys.*, 2008, **128**, 164101.

57. A. Landau, K. Khistyaev, S. Dolgikh and A. I. Krylov, *J. Chem. Phys.*, 2010, **132**, 014109.

58. A. E. DePrince and C. D. Sherrill, *J. Chem. Theor. Comput.*, 2013, **9**, 2687-2696.

59. A. E. DePrince and C. D. Sherrill, *J. Chem. Theor. Comput.*, 2013, **9**, 293-299.

60. W. J. Hehre, R. Ditchfield and J. A. Pople, *J. Chem. Phys.*, 1972, **56**, 2257-2261.

61. P. C. Hariharan and J. A. Pople, *Theoret. Chim. Acta*, 1973, **28**, 213-222.

62. R. Krishnan, J. S. Binkley, R. Seeger and J. A. Pople, *J. Chem. Phys.*, 1980, **72**, 650-654.

63. T. Clark, J. Chandrasekhar, G. W. Spitznagel and P. V. R. Schleyer, *J. Comput. Chem.*, 1983, **4**, 294-301.

64. T. H. Dunning, *J. Chem. Phys.*, 1989, **90**, 1007-1023.

65. R. A. Kendall, T. H. Dunning and R. J. Harrison, *J. Chem. Phys.*, 1992, **96**, 6796-6806.

66. Y. Shao, Z. Gan, E. Epifanovsky, A. T. B. Gilbert, M. Wormit, J. Kussmann, A. W. Lange, A. Behn, J. Deng, X. Feng, D. Ghosh, M. Goldey, P. R. Horn, L. D. Jacobson, I. Kaliman, R. Z. Khaliullin, T. Kuś, A. Landau, J. Liu, E. I. Proynov, Y. M. Rhee, R. M. Richard, M. A. Rohrdanz, R. P. Steele, E. J. Sundstrom, H. L. Woodcock, P. M. Zimmerman, D. Zuev, B. Albrecht, E. Alguire, B. Austin, G. J. O. Beran, Y. A. Bernard, E. Berquist, K. Brandhorst, K. B. Bravaya, S. T. Brown, D. Casanova, C.-M. Chang, Y. Chen, S. H. Chien, K. D. Closser, D. L. Crittenden, M. Diedenhofen, R. A. DiStasio, H. Do, A. D. Dutoi, R. G. Edgar, S. Fatehi, L. Fusti-Molnar, A. Ghysels, A. Golubeva-Zadorozhnaya, J. Gomes, M. W. D. Hanson-Heine, P. H. P. Harbach, A. W. Hauser, E. G. Hohenstein, Z. C. Holden, T.-C. Jagau, H. Ji, B. Kaduk, K. Khistyaev, J. Kim, J. Kim, R. A. King, P. Klunzinger, D. Kosenkov, T. Kowalczyk, C. M. Krauter, K. U. Lao, A. D. Laurent, K. V. Lawler, S. V. Levchenko, C. Y. Lin, F. Liu, E. Livshits, R. C. Lochan, A. Luenser, P. Manohar, S. F. Manzer, S.-P. Mao, N. Mardirossian, A. V. Marenich, S. A. Maurer, N. J. Mayhall, E. Neuscamman, C. M. Oana, R. Olivares-Amaya, D. P. O'Neill, J. A. Parkhill, T. M. Perrine, R. Peverati, A. Prociuk, D. R. Rehn, E. Rosta, N. J. Russ, S. M. Sharada, S. Sharma, D. W. Small, A. Sodt, T. Stein, D. Stück, Y.-C. Su, A. J. W. Thom, T. Tsuchimochi, V. Vanovschi, L. Vogt, O. Vydrov, T. Wang, M. A. Watson, J. Wenzel, A. White, C. F. Williams, J. Yang, S. Yeganeh, S. R. Yost, Z.-Q. You, I. Y. Zhang, X. Zhang, Y. Zhao, B. R. Brooks, G. K. L. Chan, D. M. Chipman, C. J. Cramer, W. A. Goddard, M. S. Gordon, W. J. Hehre, A. Klamt, H. F. Schaefer, M. W. Schmidt, C. D. Sherrill, D. G. Truhlar, A. Warshel, X. Xu, A. Aspuru-Guzik, R. Baer, A. T. Bell, N. A. Besley, J.-D. Chai, A. Dreuw, B. D. Dunietz, T. R. Furlani, S. R. Gwaltney, C.-P. Hsu, Y. Jung, J. Kong, D. S. Lambrecht, W. Liang, C. Ochsenfeld, V. A. Rassolov, L. V. Slipchenko, J. E. Subotnik, T. Van Voorhis, J. M. Herbert, A. I. Krylov, P. M. W. Gill and M. Head-Gordon, *Mol. Phys.*, 2015, **113**, 184-215.

67. A. P. Scott and L. Radom, *J. Phys. Chem.*, 1996, **100**, 16502-16513.

68. P. Sinha, S. E. Boesch, C. Gu, R. A. Wheeler and A. K. Wilson, *J. Phys. Chem. A*, 2004, **108**, 9213-9217.

69. N. Matsunaga, G. M. Chaban and R. B. Gerber, *J. Chem. Phys.*, 2002, **117**, 3541-3547.

70. S. Carter, S. J. Culik and J. M. Bowman, *J. Chem. Phys.*, 1997, **107**, 10458-10469.

71. S. Carter, J. M. Bowman and N. C. Handy, *Theor. Chem. Acc.*, 1998, **100**, 191-198.

72. O. Christiansen, *Phys. Chem. Chem. Phys.*, 2012, **14**, 6672-6687.

73. R. A. Distasio, R. P. Steele and M. Head-Gordon, *Mol. Phys.*, 2007, **105**, 2731-2742.

74.   R. P. Steele, R. A. DiStasio, Y. Shao, J. Kong and M. Head-Gordon, *J. Chem. Phys.*, 2006, **125**, 074108.

75.   X. Cheng and R. P. Steele, *J. Chem. Phys.*, 2014, **141**, 104105.

76.   R. G. Cooks, *J. Mass Spectrom.*, 1995, **30**, 1215-1221.

77.   K. L. Fort, J. A. Silveira, N. A. Pierson, K. A. Servage, D. E. Clemmer and D. H. Russell, *J. Phys. Chem. B*, 2014, **118**, 14336-14344.

78.   J. A. Silveira, K. L. Fort, D. Kim, K. A. Servage, N. A. Pierson, D. E. Clemmer and D. H. Russell, *J. Am. Chem. Soc.*, 2013, **135**, 19147-19153.

79.   N. N. Dookeran, T. Yalcin and A. G. Harrison, *J. Mass Spectrom.*, 1996, **31**, 500-508.

80.   F. Rogalewicz, Y. Hoppilliard and G. Ohanessian, *Int. J. Mass spectrom.*, 2000, **195/196**, 565-590.

81.   W. K. J. Mino, K. Gulyuz, D. Wang, C. N. Stedwell and N. C. Polfer, *J. Phys. Chem. Lett.*, 2011, **2**, 299-304.

82.   H. El Aribi, G. Orlova, A. C. Hopkinson and K. W. M. Siu, *J. Phys. Chem. A*, 2004, **108**, 3844-3853.

83.   H. Kang, C. Dedonder-Lardeux, C. Jouvet, S. Martrenchard, G. Grégoire, C. Desfrancois, J.-P. Schermann, M. Barat and J. A. Fayeton, *Phys. Chem. Chem. Phys.*, 2004, **6**, 2628-2632.

84.   H. Kang, C. Dedonder-Lardeux, C. Jouvet, G. Grégoire, C. Desfrançois, J. P. Schermann, M. Barat and J. A. Fayeton, *J. Phys. Chem. A*, 2005, **109**, 2417-2420.

85.   F. O. Talbot, T. Tabarin, R. Antoine, M. Broyer and P. Dugourd, *J. Chem. Phys.*, 2005, **122**, 074310.

86.   V. Lepère, B. Lucas, M. Barat, J. A. Fayeton, V. J. Picard, C. Jouvet, P. Carcabal, I. Nielsen, C. Dedonder-Lardeux, G. Grégoire and A. Fujii, *J. Chem. Phys.*, 2007, **127**, 134313.

87.   U. Kadhane, J. U. Andersen, A. Ehlerding, P. Hvelplund, M.-b. S. Kirketerp and M. Kœcks, *J. Chem. Phys.*, 2008, **129**, 184304.

88.   B. Lucas, M. Barat, J. A. Fayeton, M. Perot, C. Jouvet, G. Grégoire and S. B. Nielsen, *J. Chem. Phys.*, 2008, **128**, 164302.

89.   Z. B. Maksic and B. Kovacevic, *Chem. Phys. Lett.*, 1999, **307**, 497-504.

90.   J. C. Ma and D. A. Dougherty, *Chem. Rev.*, 1997, **97**, 1303-1324.

91.   J. M. Bakker, L. M. Aleese, G. Meijer and G. von Helden, *Phys. Rev. Lett.*, 2003, **91**, 203003.

92.   E. A. Cobar, R. Z. Khaliullin, R. G. Bergman and M. Head-Gordon, *PNAS*, 2007, **104**, 6963-6968.

93.   R. Z. Khaliullin, E. A. Cobar, R. C. Lochan, A. T. Bell and M. Head-Gordon, *J. Phys. Chem. A*, 2007, **111**, 8753-8765.

94.   R. Z. Khaliullin, A. T. Bell and M. Head-Gordon, *J. Chem. Phys.*, 2008, **128**, 184112.

95.   R. C. Lochan, R. Z. Khaliullin and M. Head-Gordon, *Inorganic Chemistry*, 2008, **47**, 4032-4044.

96.   B. Jeziorski, R. Moszynski and K. Szalewicz, *Chem. Rev.*, 1994, **94**, 1887-1930.

97.   R. Z. Khaliullin, A. T. Bell and M. Head-Gordon, *Chem. Eur. J.*, 2009, **15**, 851-855.

98.   R. Moszynski, T. Heijmen and B. Jeziorski, *Mol. Phys.*, 1996, **88**, 741-758.

99.   K. Kitaura and K. Morokuma, *Int. J. Quantum Chem*, 1976, **10**, 325-340.

100.   C. A. Deakyne and M. Meot-Ner, *J. Am. Chem. Soc.*, 1985, **107**, 474-479.

101.   M. S. Marshall, R. P. Steele, K. S. Thanthiriwatte and C. D. Sherrill, *J. Phys. Chem. A*, 2009, **113**, 13628-13632.

102.   P. A. Frey, S. A. Whitt and J. B. Tobin, *Science*, 1994, **264**, 1927-1930.

103.   S. Hashimoto and H. Takeuchi, *J. Am. Chem. Soc.*, 1998, **120**, 11012-11013.

104.   A.-M. A. Hays, I. R. Vassiliev, J. H. Golbeck and R. J. Debus, *Biochemistry*, 1998, **37**, 11352-11365.

105.   C. Tu, D. N. Silverman, C. Forsman, B.-H. Jonsson and S. Lindskog, *Biochemistry*, 1989, **28**, 7913-7918.

106.   A. Warshel and S. Russell, *J. Am. Chem. Soc.*, 1986, **108**, 6569-6579.

107.   D. Wang, X. Zhao, M. Vargek and T. G. Spiro, *J. Am. Chem. Soc.*, 2000, **122**, 2193-2199.

108.   N. Wellner and G. Zundel, *J. Mol. Struct.*, 1994, **317**, 249-259.

109.   T. E. Hofstetter, C. Howder, G. Berden, J. Oomens and P. B. Armentrout, *J. Phys. Chem. B*, 2011, **115**, 12648-12661.

110.   R. C. Dunbar, A. C. Hopkinson, J. Oomens, C.-K. Siu, K. W. M. Siu, J. D. Steill, U. H. Verkerk and J. Zhao, *J. Phys. Chem. B*, 2009, **113**, 10403-10408.

111.   E. Mateo Marti, C. Méthivier, P. Dubot and C.-M. Pradier, *J. Phys. Chem. B*, 2003, **107**, 10785-10792.

112.   S. Kumar, A. K. Rai, S. B. Rai and D. K. Rai, *Ind. J. Phys.*, 2010, **84**, 563-573.

113.   E. Deplazes, W. Van Bronswijk, F. Zhu, L. D. Barron, S. Ma, L. A. Nafie and K. J. Jalkanen, *Theor. Chem. Acc.*, 2008, **119**, 155-176.

114.   J. G. Mesu, T. Visser, F. Soulimani and B. M. Weckhuysen, *Vib. Spectrosc*, 2005, **39**, 114-125.

115.   Zhijian Huang, Zijing Lin and C. Song, *J. Phys. Chem. A*, 2007, **111**, 4340-4352.

116.   M. Citir, C. S. Hinton, J. Oomens, J. D. Steill and P. B. Armentrout, *Int. J. Mass spectrom.*, 2012, **330-332**, 6-15.

117.   A. D. McNaught and A. Wilkinson, *IUPAC, Compendium of Chemical Terminology (the Gold Book), 2nd ed.*, Blackwell Scientific Publications, Oxford, 1997.

118.   L. Saidel, J., A. R. Goldfarb and S. Waldman, *J. Biol. Chem.*, 1952, **197**, 285-291.

119.   B. Kovačević, M. Rožman, L. Klasinc, D. Srzić, Z. B. Maksić and M. Yáñez, *J. Phys. Chem. A*, 2005, **109**, 8329-8335.

120.   L. C. Snoek, E. G. Robertson, R. T. Kroemer and J. P. Simons, *Chem. Phys. Lett.*, 2000, **321**, 49-56.

121.   H.-S. Andrei, N. Solcà and O. Dopfer, *ChemPhysChem*, 2006, **7**, 107-110.

122.   M. Y. Choi and R. E. Miller, *J. Phys. Chem. A*, 2006, **110**, 9344-9351.

123.   A. D. Becke, *J. Chem. Phys.*, 1993, **98**, 5648-5652.

124.   C. Lee, W. Yang and R. G. Parr, *Phys. Rev. B: Condens. Matter*, 1988, **37**, 785-789.

125.   B. Miehlich, A. Savin, H. Stoll and H. Preuss, *Chem. Phys. Lett.*, 1989, **157**, 200-206.

126.   S. H. Vosko, L. Wilk and M. Nusair, *Can. J. Phys.*, 1980, **58**, 1200-1211.

127.   S. Grimme, S. Ehrlich and L. Goerigk, *J. Comput. Chem.*, 2011, **32**, 1456-1465.

128.   V. Barone, *J. Chem. Phys.*, 2005, **122**, 14108.

129.   M. J. Frisch, G. W. Trucks, H. B. Schlegel, G. E. Scuseria, M. A. Robb, J. R. Cheeseman, G. Scalmani, V. Barone, G. A. Petersson, H. Nakatsuji, X. Li, M. Caricato, A. Marenich, J. Bloino, B. G. Janesko, R. Gomperts, B. Mennucci, H. P. Hratchian, J. V. Ort and D. J. Fox, *Journal*, 2016.

130.   V. Kopysov, A. Makarov and O. V. Boyarkin, *J. Phys. Chem. Lett.*, 2016, **7**, 1067-1071.

The Use of Peptide Bonds for
Cold Ion Spectroscopy

In the present chapter we explore an alternative agent for an electronic excitation of biomolecular ions instead of the aromatic side chains of Phe, Tyr, Trp, and His amino acids, namely the peptide bond. Following an Introduction section, the first electronic photofragmentation spectrum of the peptide bond in AlaAlaH$^+$ protonated dipeptide is reported. Next, several IR-DUV gain spectra of peptides that do not contain aromatic chromophore are presented and experimental challenges of the method are discussed. Finally, the ability of the IR-IR-DUV hole-burning spectroscopy to resolve conformer-specific vibrational spectra of a cyclic peptide drug is demonstrated. The results, presented below, indicate that the intrinsic limitation of CIS, related to the amino acid composition of studied peptides, is now off the table.

4.1. Introduction

1. Intrinsic Limitation of Cold Ion Spectroscopy

Vibrational spectroscopy of cold ions is a proven tool for unambiguous conformational assignment of intrinsic structures of biological molecules and ions. IR-UV double-resonance depletion spectroscopy allows recording conformer-specific IR spectra of biomolecular ions as large as ten amino acids,[1, 2] provided their UV spectra are vibrationally resolved.

This approach is most effective for peptides containing only phenylalanine of all aromatic amino acids (tryptophan, tyrosine, phenylalanine and histidine), because the electronic spectrum of this chromophore is likely to remain vibrationally resolved even in large enough species. Since the fragmentation yield of this amino acid is the lowest among all aromatics, it is almost suppressed in

cases when other aromatic amino acids are present in the peptide sequence. Electronic spectrum of protonated amino acid tyrosine is also well-resolved,[3, 4] however electronic spectra of larger peptides with this chromophore may be congested and the depletion spectroscopy is, therefore, prohibited.[5, 6] Furthermore, even in cases when conformer-specific, well-resolved electronic transitions can be found, the absorption of an IR photon by cold ions can increase an overall fragmentation yield so that the depletion cannot be observed.[7] UV spectra of other aromatic amino acids, tryptophan and histidine, were shown to be broad and indistinguishable for different conformers (see Chapter 3).[3] Their photophysics in more complex molecules is difficult to predict but, most likely, vibrational resolution might not be observed.

The recently reported IR-IR-UV hole-burning spectroscopy has removed the need for vibrational resolution of electronic spectra to employ conformer-selective vibrational spectroscopy.[8] However, CIS has remained essentially applicable only to peptides that contain any aromatic amino acids in their sequence. But what if a peptide does not contain any aromatic amino acids? Does this preclude the use of gas-phase action spectroscopy?

2. Vibrational Spectroscopy Without UV Absorption

The alternative approaches for vibrational spectroscopy that do not employ UV-induced dissociation were discussed previously with respect to the IR-IR-UV hole-burning spectroscopy (see Chapter 3). Briefly, one could use either IRMPD spectroscopy at room temperature, or tagging IR spectroscopy. Both techniques have important limitations. IRMPD approach lacks conformer-selectivity and suffers from thermal broadening and nonlinear yield to IR laser power. IR-IR hole-burning of species tagged with light atoms requires elevated temperatures in the trap to prevent freezing of the tagging gas, has low signal stability, and sample-specific conditions, at which the most efficient complexation occurs. Finally, addition of the tag might alter the observed vibrational frequencies[9].

3. The Use of Deep UV Excitation for Photofragmentation Mass Spectrometry

An alternative approach to peptide photodissociation is to use chromophore common for all peptides – peptide bond. This enables the electronic excitation of any peptide, even without aromatic amino acids in its sequence. The spectrum of poly-alanine in dry films, originally measured by Robin in 1975 in dry films,[10] exhibits three major absorption bands: one centred near 190 nm, another near 160 nm, and a third at approximately 130 nm. These bands have been associated with the peptide backbone amides.[11-13]

Available laser sources matched two of the three bands: the ArF excimer laser at 193 nm and the F2 laser at 157 nm. ArF laser has higher pulse energies and fused silica optics efficiently transmits 193 nm light. The first photodissociation experiments by using ArF excimer laser were reported in 1984 for several short oligopeptides.[14] Several years later, Hunt and co-workers successfully applied this technique to analyse 15 amino acid peptide, extracted from the beef liver.[15] The main advantage of using DUV PID is a rich mass spectrum; in contrast to CID, almost all ion fragment types are present (*a, b, c, x, y,* and *z*), as well as iminium ions, and v/w ions corresponding to the side chain losses. Many groups adopted this approach in combination with various mass spectrometers.[16-20] Currently, many labs around the world employ the photofragmentation approach in modern proteomics.[21-24] More about the development of VUV photodissociation for mass spectrometry can be found in reference [25].

The scope of the present study is to explore the possibility to apply a UV OPO (EKSPLA), tunable in a wide spectral range (192-2600 nm), to perform cold ion action spectroscopy of peptides using peptide bond as a universal chromophore.

4.2. Electronic Spectrum of a Single Peptide Bond

A dipeptide is the simplest model system that contains peptide bond. Although glycine is the easiest amino acid in terms of chemical composition (it has only a single hydrogen atom as a side chain), it is also the only achiral of all amino acids. Therefore, protonated alanine dipeptide (AlaAlaH$^+$, figure 4.1a) was chosen as a benchmark ion to study the absorption of the peptide bond. In this section we compare electronic spectrum of the AlaAlaH$^+$ (m/z = 161.2 Da) with a single peptide bond and the one of protonated amino acid AlaH$^+$ (m/z = 90.0 Da, figure 4.1b). Comparison of these spectra allows to eliminate absorption by N- and C-terminal groups and single out the absorption spectrum of the single pair peptide bond + backbone C=O group.

4.2.1. DUV Spectroscopy of AlaAlaH$^+$

1. *Photo-Induced Dissociation Mass Spectrum of AlaAlaH$^+$*

Figure 4.2 shows the PID (red trace) mass spectrum of protonated AlaAlaH$^+$, recorded with UV OPO wavelength fixed at 196 nm. The blue trace in figure 4.2 corresponds to the statistical dissociation of ions in the trap in the absence of laser excitation. The statistical dissociation (referred to as "CID" further on) is recorded to estimate the background signal. For most analytes, studied herein, the statistical "in-trap" fragmentation is negligible. The most abundant fragment in

the PID mass spectrum is a_1 fragment (m/z = 45 Da). All optical spectra of AlaAlaH$^+$ reported below were recorded by monitoring the intensity of this fragment.
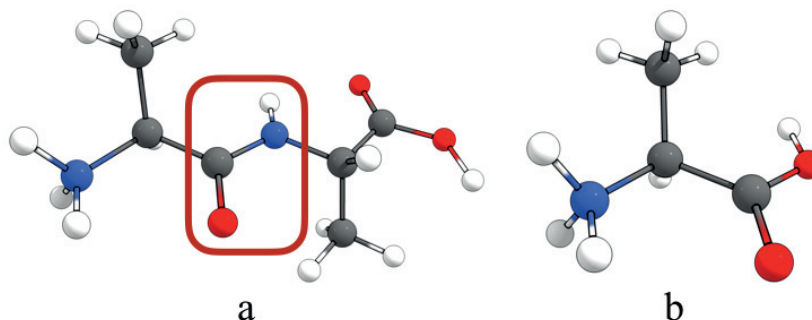

Figure 4.1. *Schematic structures of a) AlaAlaH$^+$, and b) AlaH$^+$. The light-absorbing peptide bond is enclosed in a red rectangle.*
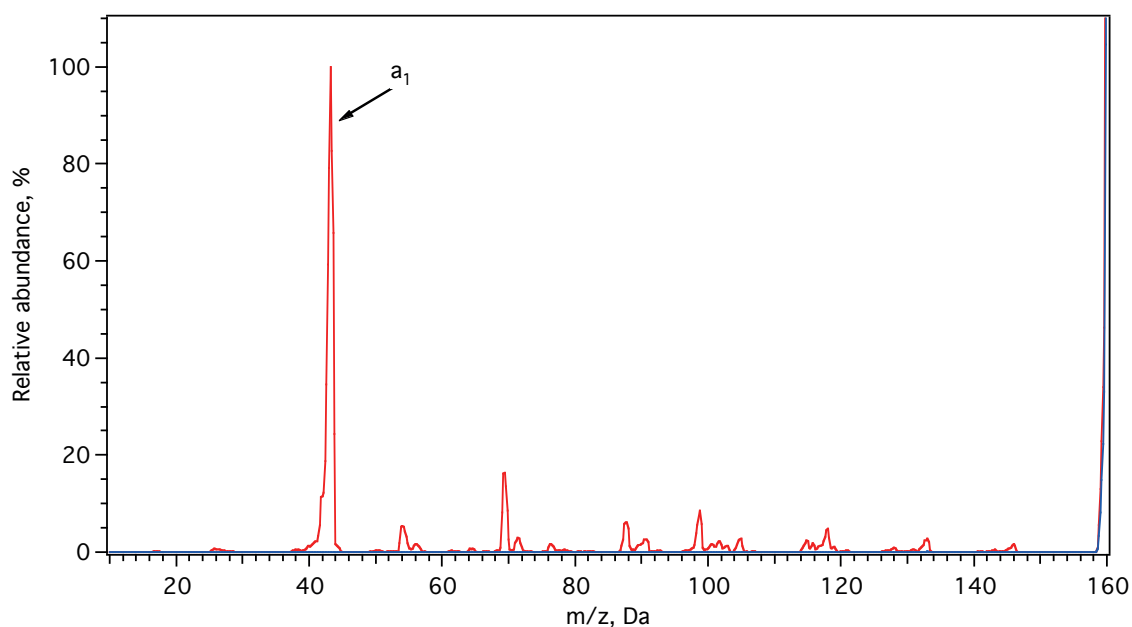

Figure 4.2. *Photo-induced dissociation mass spectrum of AlaAlaH$^+$. The red trace corresponds to the DUV OPO wavelength fixed at 196 nm. The blue trace corresponds to the CID mass spectrum. The rising edge on the right side of the graph corresponds to the parent ion. Each data point was averaged over 20 measurements and mass increment was 0.2 Da.*

2. Electronic Photodissociation Spectrum of AlaAlaH$^+$

Figure 4.3 shows the electronic photodissociation spectrum of AlaAlaH$^+$ measured by monitoring the intensity of the a_1 fragment. The spectrum was normalized on parent ion signal and DUV OPO power. Since generation of OPO radiation in 210 – 192 nm spectral region requires an additional nonlinear crystal, the beam in this region is spatially separated from the one in the 250 – 210 nm spectral region and is less intense. Therefore, the intensity in short-wavelength region was scaled to match the signal intensity in the 250 – 210 nm region. The relatively high signal instability in the blue side of the spectrum appears due to strong wavelength dependence of laser power in the DUV region, rather than partially resolved vibrational transitions.
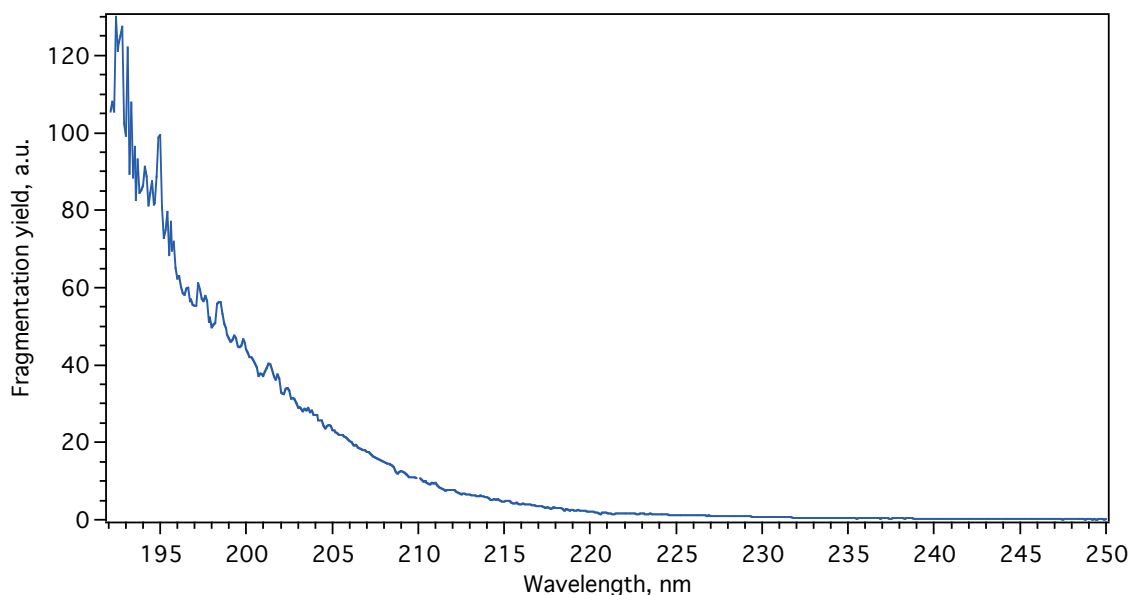
Figure 4.3. *Electronic spectrum of AlaAlaH$^+$ recorded by monitoring intensity of the a_1 fragment ion with m/z = 45 Da. The spectrum was normalized over the parent ion signal and laser power. Each data point was averaged over 20 measurements.*

4.2.2. DUV Spectroscopy of AlaH$^+$

1. Photo-Induced Dissociation Mass Spectrum of AlaH$^+$

Figure 4.4 shows the CID (blue trace) and PID (red trace) mass spectra of AlaH$^+$. UV OPO wavelength was fixed at 211 nm. The most abundant fragment corresponds, likely, to the

95

immonium ion with m/z = 44.1 Da, although, given the low resolution and possible miscalibration of the quadrupole mass-analyser in low m/z region, the assignment of this fragment is ambiguous.
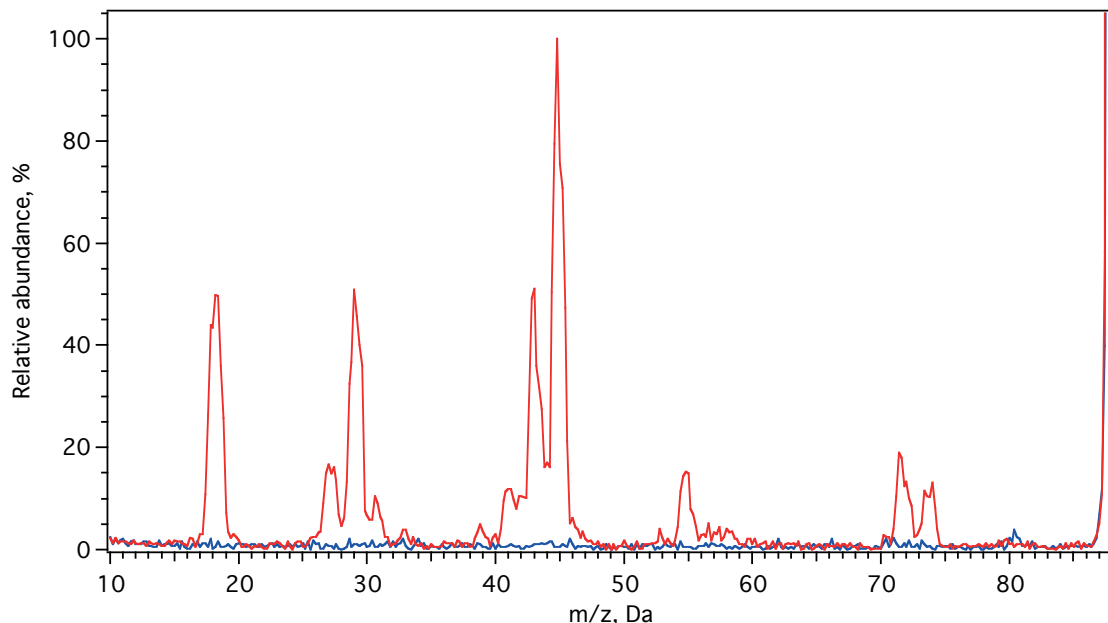
Figure 4.4. *CID (blue trace) and DUV PID (red trace) mass spectra of AlaH$^+$. UV OPO wavelength fixed at 211 nm. The rising edge on the right side of the graph corresponds to the parent ion. Each data point is averaged over 20 measurements and mass increment was 0.2 Da.*

2. Electronic Photodissociation Spectrum of AlaH$^+$

Figure 4.5 shows the electronic photofragmentation spectrum of AlaH$^+$ normalized on parent signal and UV OPO power. Since the photofragmentation signal is very low, DUV spectra were measured with quadrupole mass filter transmittance set to 41 Da and resolution lowered to 2.0 to collect more fragments. The spectrum in 210 – 192 nm region is scaled to match the signal intensity in the 250 – 210 nm spectral region.

Note, that both spectra of AlaAlaH$^+$ and AlaH$^+$ are plotted in the same arbitrary units. The difference is striking – the presence of a peptide bond increases fragmentation signal more that 100 times! The absorption maximum is not observed, indicating that the spectrum of a dipeptide in the gas-phase is blue-shifted with respect to the one of poly-alanine in dry films.
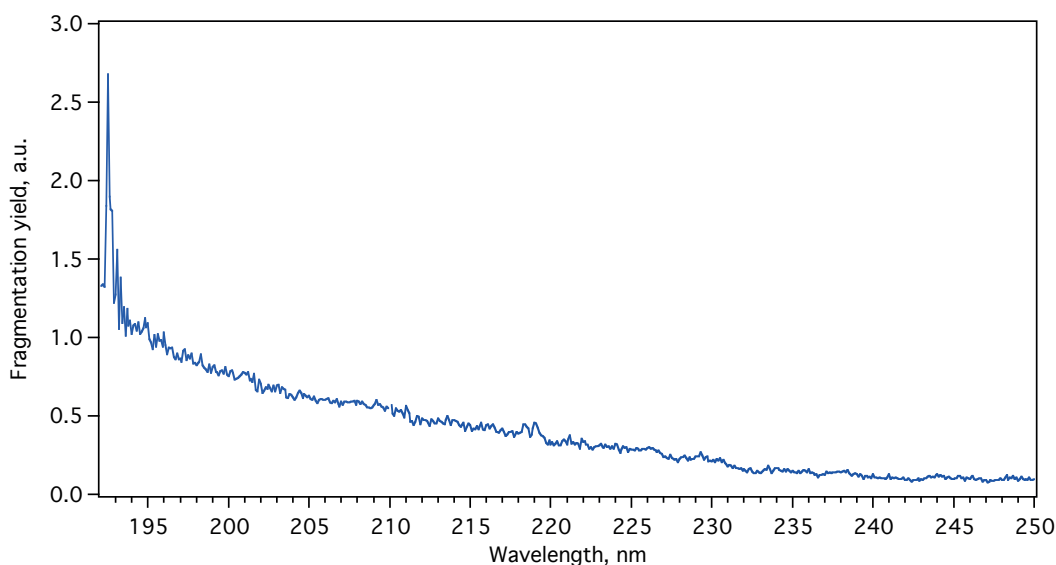
Figure 4.5. *Electronic spectrum of AlaH$^+$ recorded with a quadrupole mass analyser set to 41 Da and resolution lowered to 2.0. The spectrum was normalized over the parent ion signal and laser power. Each data point was averaged over 20 measurements; the final spectrum is an average of two scans.*

4.3. IR-DUV Gain Spectroscopy

The main principle of double-resonance cold ion spectroscopy is based on the drastic difference between spectra of cold and IR-preheated ions, provided that cold ions have a vibrationally resolved electronic spectrum.[2] Absorption of an IR photon causes inhomogeneous spectral broadening and a red shift of the absorption spectrum.[26] In cases, when electronic spectra of ions are already lifetime-broadened, only the red shift of the absorption, resulting in a signal gain, can be detected.[8] However, the electronic spectrum of a dipeptide in the gas-phase (figure 4.3) is significantly broader ($\sim$6700 cm^{-1} between the onset at 220 nm and the blue-most available wavelength 192 nm), compared to spectra of protonated tryptophan[3] ($\sim$1000 cm^{-1}) and even histidine ($\sim$2500 cm^{-1}), see Section 3.3). The width of the UV spectrum, therefore, is at least twice higher compared to the typical energy of an IR photon in 3 μm spectral region.

The question is whether it is possible to measure, at least, the IR-DUV gain spectra of ions and, if so, how should one choose appropriate UV OPO wavelength, fragmentation channels to be monitored, and other parameters that can potentially affect the signal-to-noise ratio of the vibrational gain spectrum to achieve the best signal quality? In the following section we discuss

these parameters and suggest an analytical procedure to choose them. The approach is applied to record vibrational gain spectrum of AlaAlaH$^+$.

4.3.1. Quality Optimization for IR-DUV Gain Spectroscopy

1. Numerical Measure of the S/N Ratio in IR-DUV Gain Spectroscopy

Figure 4.6 shows the electronic spectra of cold (blue trace) and IR pre-heated (red trace) AlaAlaH$^+$ in the 192-210 nm region, recorded by monitoring the intensity of the a$_1$ fragment as a function of UV OPO wavelength. IR-induced changes in the UV absorption are clearly visible, which allows using them for recording IR-DUV vibrational gain spectra of biomolecular ions. The increase of the fragmentation yield is wavelength dependent, hence one may improve the S/N ratio by choosing the most suitable wavelength of the UV light source.
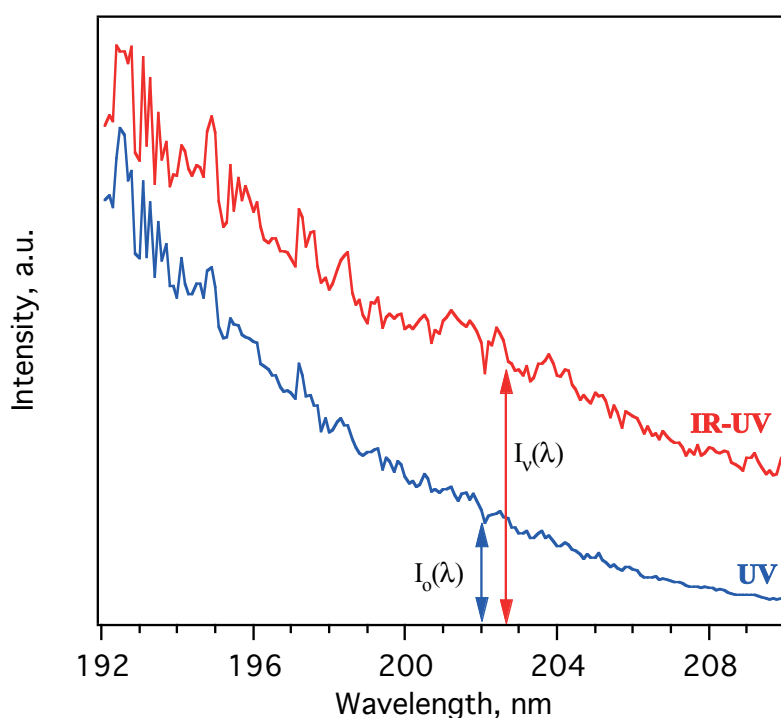
Figure 4.6. *Electronic spectra of cold (blue trace) and IR-preheated (red trace) AlaAlaH$^+$. IR OPO was tuned to the OH stretching vibration of AlaAlaH$^+$ (3567.2 cm^{-1}).*

The gain in the following experiments is defined as follows (see notations in figure 4.6):

$$S = \frac{I_v(\lambda) - I_0(\lambda)}{I_0(\lambda)} = \frac{I_v(\lambda)}{I_0(\lambda)} - 1 \qquad \text{(Eq. 4.1)}$$

where $I_0(\lambda)$ is the photofragmentation signal of cold ions and $I_v(\lambda)$ is the photofragmentation signal of IR-preheated ions. The difference $I_v(\lambda) - I_0(\lambda)$ is the photofragmentation signal increase following an IR photon absorption.

The noise N of the function, defined in Eq. 4.1, is calculated as follows:

$$N = \frac{\sqrt{\sigma^2(I_v)I_0^2 + \sigma^2(I_0)I_v^2}}{I_0^2} \tag{Eq. 4.2}$$

where the wavelength dependence is omitted for the sake of clarity. Since $\sigma \sim \sqrt{I}$, eq. 4.2 can be rewritten as follows:

$$N \sim \frac{\sqrt{I_v I_0^2 + I_0 I_v^2}}{I_0^2} = \frac{\sqrt{\frac{I_v}{I_0}}\sqrt{\frac{I_v}{I_0}+1}}{\sqrt{I_0}} \tag{Eq. 4.3}$$

If we define the relative signal increase as $\alpha = \frac{I_v}{I_0}$, the signal-to-noise ratio is determined as follows:

$$\frac{S}{N} = \frac{(\alpha-1)}{\sqrt{\alpha(\alpha+1)}}\sqrt{I_0} = f(\alpha)\sqrt{I_0} \tag{Eq. 4.4}$$

The signal-to-noise ratio increases as the square root of the signal and is proportional to the function of the relative signal increase $f(\alpha)$. When $\alpha \gg 1$ (near-zero background), this function asymptotically approaches unity, whereas when $\alpha = 1$, which corresponds to the lack of the signal gain, $f(\alpha) = 0$. The dependence of the function $f(\alpha)$ on α is shown in figure 4.7. The function increases rapidly until $\alpha \approx 5$, which is a typical signal gain for some of the fragments (figure 4.7).
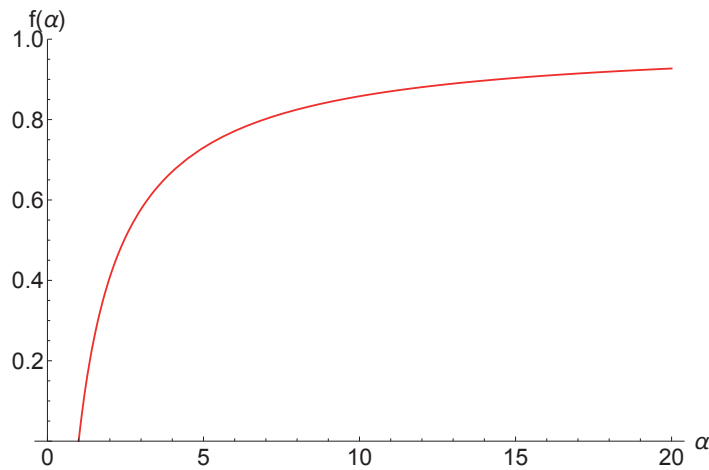
Figure 4.7. *Analytical dependence of $f(\alpha)$ on α.*

By plotting the S/N function measured experimentally for each promising fragment in a wide spectral range one will be able to determine the optimum combination of UV OPO excitation wavelength and fragment to be monitored.

2. Effect of the IR Pre-excitation on Photodissociation Pathways of AlaAlaH$^+$

As was already shown in Chapter 3, the relative abundances of various fragmentation channels of a peptide change with the excitation wavelength. Even though the excited state photophysics of biological molecules is beyond the scope of this investigation, from the practical point of view the choice of the fragment can play a crucial role in the quality of spectral measurements.

Figure 4.8 shows PID mass spectra of cold (blue trace) and IR-preheated (red trace) AlaAlaH$^+$ recorded with UV OPO wavelength fixed at 210 nm and IR OPO laser tuned to the O–H stretching vibration of AlaAlaH$^+$ (3567.2 cm^{-1}).
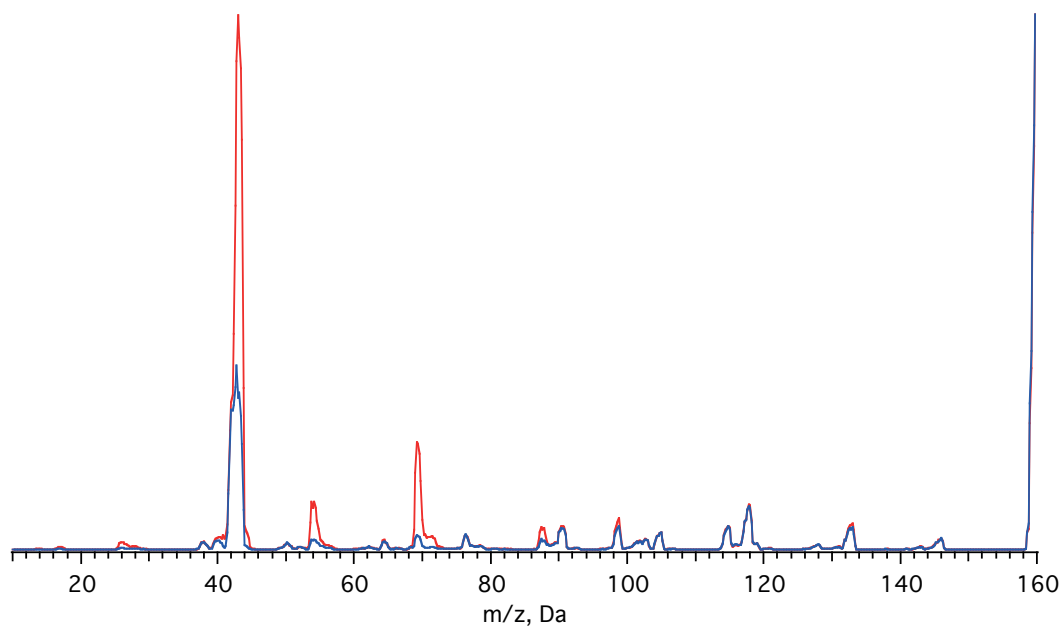
Figure 4.8. DUV (blue trace) and IR-DUV (red trace) mass spectra of AlaAlaH$^+$. Each data point was averaged over 20 measurements, mass increment was 0.2 Da.

The immonium ion (m/z=44.1 Da) remains the most abundant fragment. Absorption of the IR photon results in an increase of the fragmentation yield by a factor of 3. The fragment with m/z = 69.2 Da (likely corresponding to the [x$_1$-H$_2$O-CO]$^{1+}$ fragment with m/z = 70 Da), though, exhibits

the highest increase (7.5 times), but is ∼5 times less abundant, compared to the immonium ion. Both relative abundance and fragmentation efficiency might affect the S/N ratio.

The S/N ratio is calculated from the measured electronic spectra of cold and IR-preheated ions (figure 4.6) for each potential fragment. Figure 4.9 shows the function f(α), plotted for two fragments of AlaAlaH$^+$. As can be seen, the best S/N ratio is achieved for more intense fragment a$_1$ with m/z = 45 Da at UV OPO wavelength 210 nm.
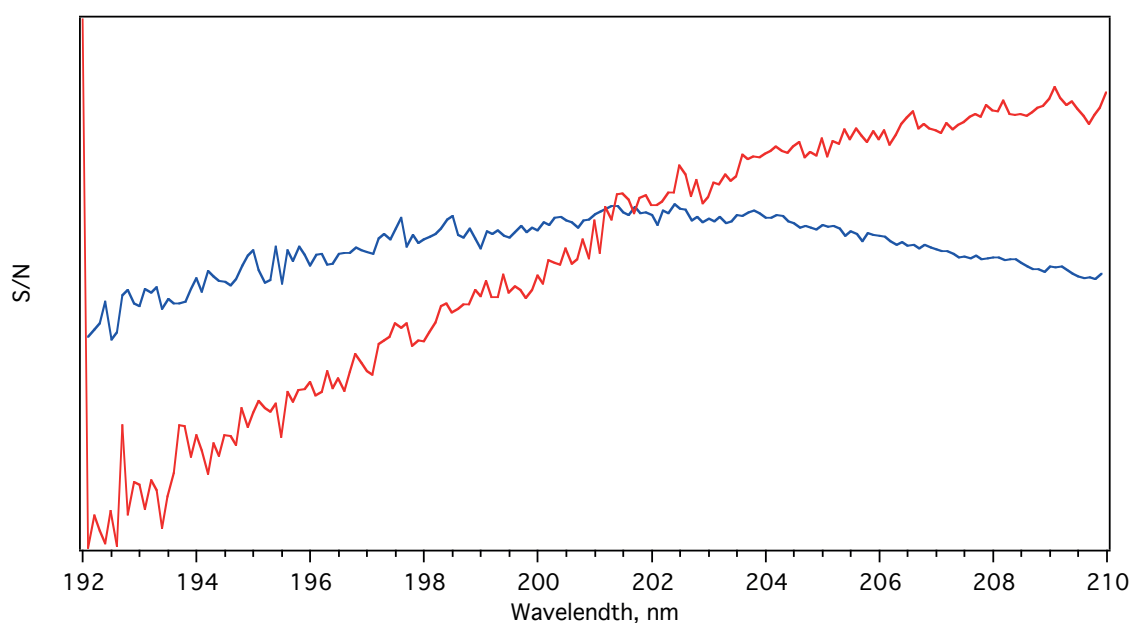
Figure 4.9. *S/N ratio calculated as in eq. 4.4 for fragment ion with m/z = 44.1 Da (red trace) and m/z = 69.2 Da (blue trace).*

3. *IR-DUV Gain Spectrum of AlaAlaH$^+$*

Figure 4.10 shows the IR-DUV gain spectrum of AlaAlaH$^+$. The assignment of the vibrational transitions is as follows: the transition at 3567.2 cm^{-1} corresponds to the O-H stretch vibration, transitions at 3402.1, 3380.2, 3363.3 and 3323.3 cm^{-1} belong to the three amine N-H and one amide N-H stretching vibration, while the weak transitions below 3030 cm^{-1} correspond to the C-H stretches. Since the number of the recorded IR transitions matches the number of vibrations in the molecule, likely only one conformer of AlaAlaH$^+$ is populated under experimental conditions. This assumption will be confirmed in section 4.4 by IR-IR-DUV hole-burning spectroscopy.
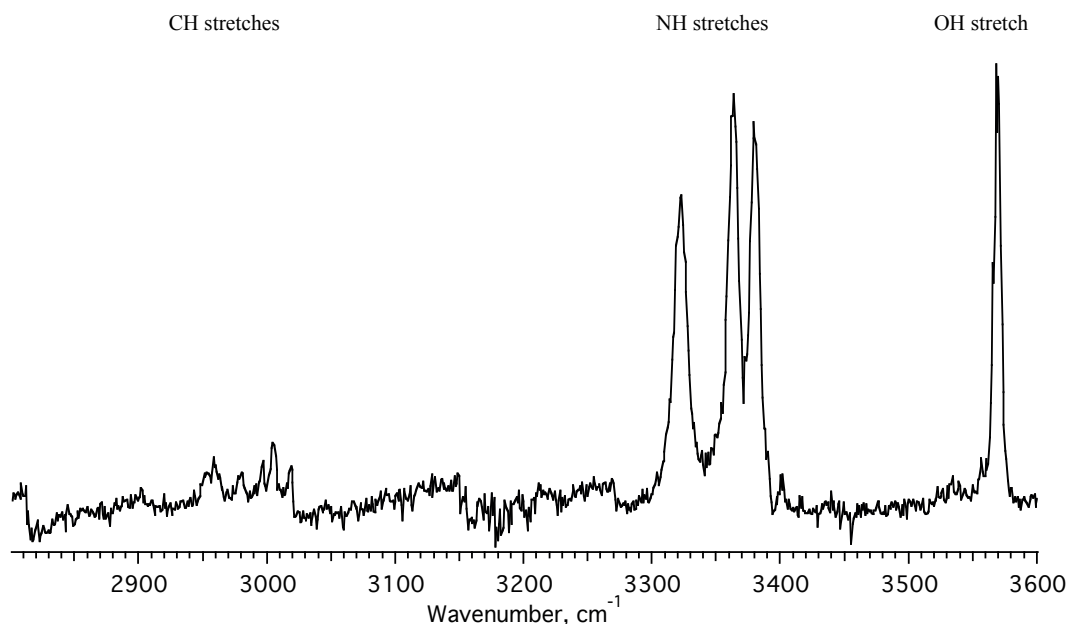
Figure 4.10. *IR-DUV gain spectrum of AlaAlaH$^+$.*

The background noise if figure 4.10 is due to the poor parent ion stability. However, the vibrational transitions are well resolved. In the following sections IR-DUV gain spectra of several peptides are presented. In each case, the same workflow as described above was used. The aim of these measurements was to compare IR-DUV gain spectroscopy with other techniques, explore the possibility to measure vibrational spectra of larger peptides, and finding possible bottlenecks of the technique.

4.3.2. IR-DUV Gain Spectroscopy of GlyProGlyGlyH$^+$

In order to compare the proposed method for measuring the vibrational spectra of cold biomolecular ions that do not have a chromophore containing amino acids in their sequence with tagging IR spectroscopy, we chose a protonated peptide GlyProGlyGlyH$^+$ (GPGG^{1+}, m/z = 287 Da, figure 4.11), for which the vibrational spectrum was reported previously.[27] Figure 4.12 shows its CID (blue trace) and DUV PID (red trace) mass spectra of GPGG^{1+}. UV OPO wavelength was fixed at 212.8 nm. The low resolution of the quadrupole mass-analyzer does not allow for an unambiguous assignment of the observed fragments. Regardless of their origin, the fragments are only used for spectral measurements, therefore the precise assignment is not necessary.
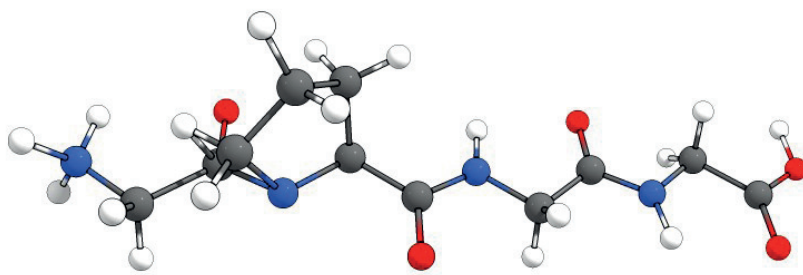
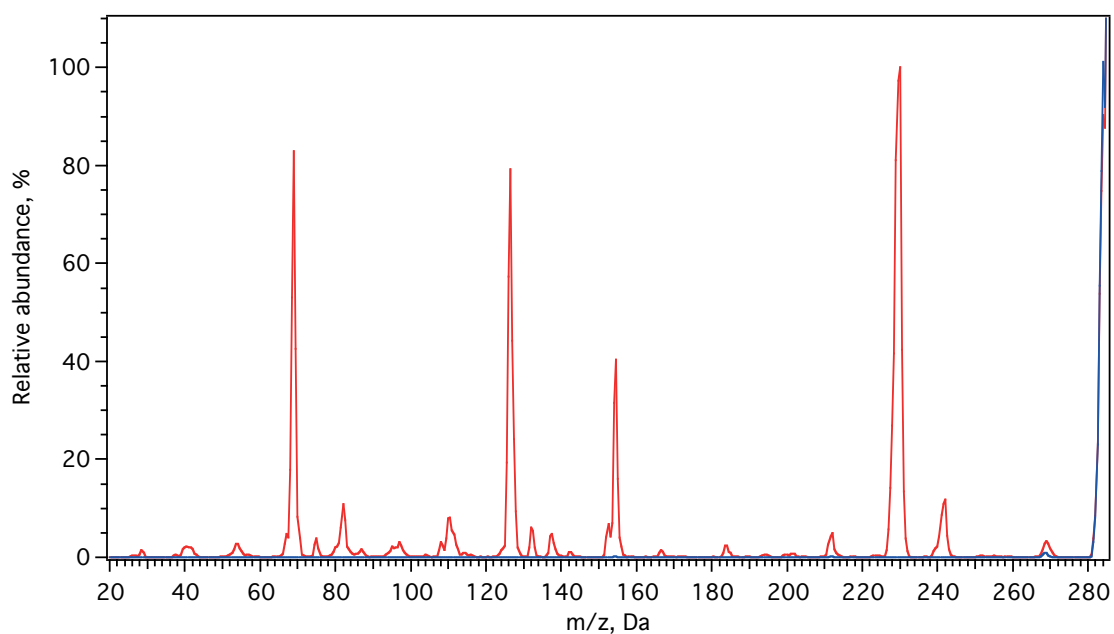**Figure 4.11.** *Schematic structure of GlyProGlyGlyH[+].*

Figure 4.12. *CID (blue trace) and DUV PID (red trace) mass spectra of GPGG[1+]. Each data point was averaged over 20 measurements; mass increment was 0.5 Da.*

Figure 4.13 shows the photofragmentation spectrum of GPGGH[1+] normalized on parent signal and UV OPO power, measured with analysing quadrupole mass filter tuned to each of the most abundant fragments with m/z equal to 69, 126, 154, and 229 Da, as well as with low mass resolution, collecting the maximum number of fragments (see colour coding on the graph).
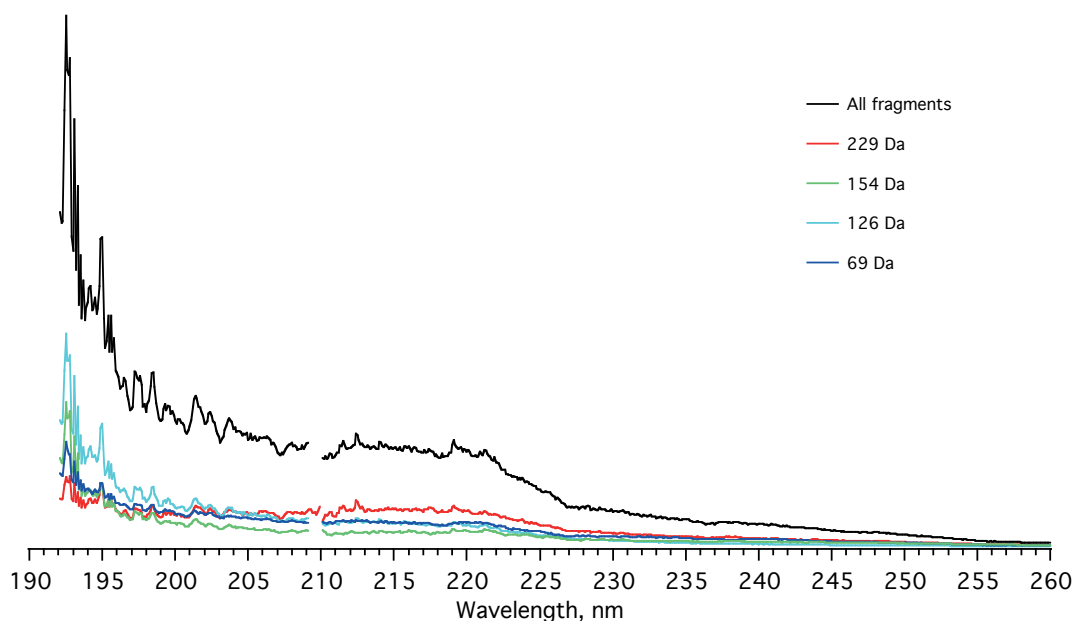
Figure 4.13. *Electronic spectra of GPGG[1+] measured by monitoring different fragments (see colour coding). Each data point is averaged over 20 measurements.*

Figure 4.14 shows the PID mass spectra of cold (blue trace) and IR-preheated (red trace) GPGG[1+]. The fragments with m/z = 69 and 123 Da exhibit the two-fold increase of the fragmentation yield following an IR pre-excitation. Since the relative abundance of the fragment with m/z = 69 Da is higher, it was chosen for the IR-DUV gain spectrum measurement.

Analysis of the signal-to-noise ratio recorded in broad spectral range (not shown here) showed that the highest value of S/N ratio corresponds to the UV OPO excitation wavelength equal to 240 nm. The corresponding IR-DUV gain spectrum is shown in figure 4.15. Note, that despite the need for accurate preliminary measurements to determine the most suitable fragmentation channel and UV wavelength, this approach is universal for every peptide, while the conditions in tagging spectroscopy have to be adjusted in each case.

Two highly abundant conformers were previously identified.[27] Full assignment of the transitions in figure 4.15 requires comparison with calculation and is beyond the scope of the current study. Briefly, vibrational transition at 3575.4 cm^{-1} belongs to O–H stretching vibration of one of the conformers (the analogous vibration in the other conformer is red shifted by ~550 cm^{-1} due to the strong hydrogen-bonding interaction, according to ref. 27), sharp transitions below 3000 cm^{-1} are the C–H stretches, while other transitions are, likely, N–H stretches. Vibrational spectrum

of GPGG^{1+} recorded with IR-DUV gain spectroscopy shows better S/N ratio compared to one obtained with the IR tagging technique,[27] and is recorded in wider spectral range.
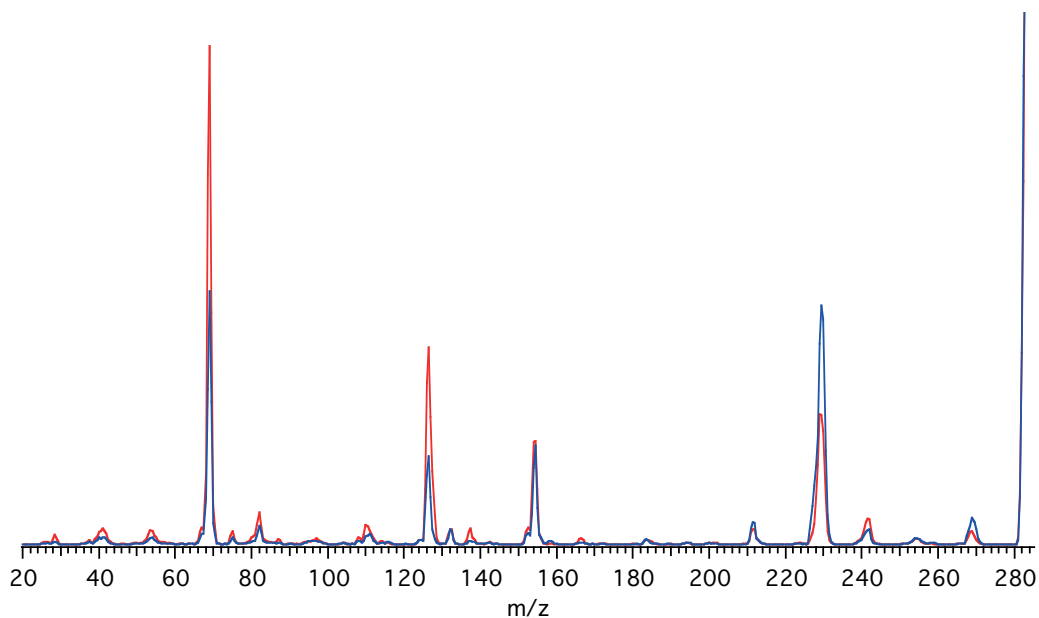

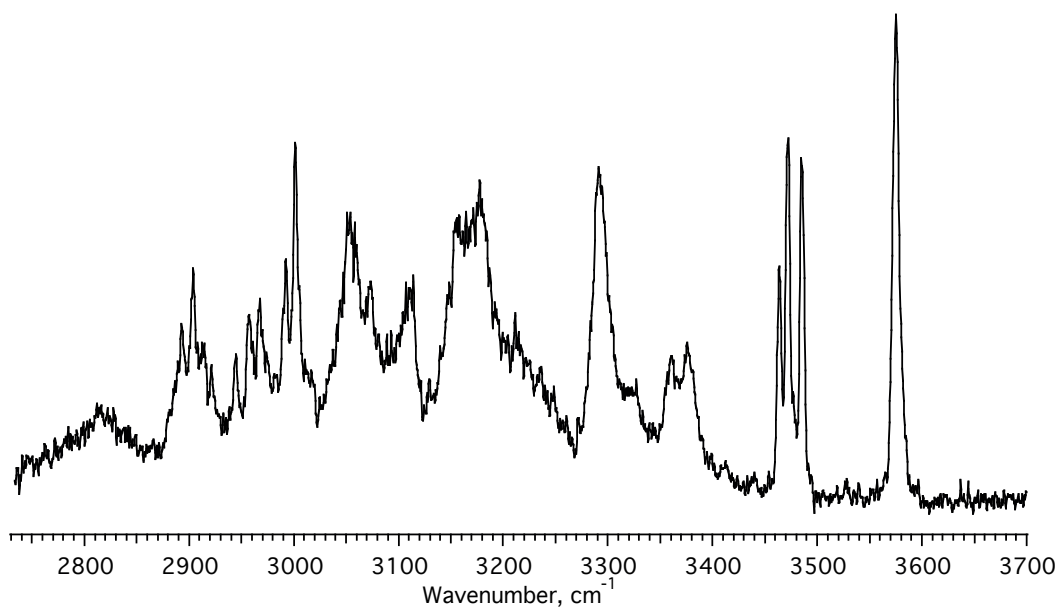*Figure 4.14. DUV (blue trace) and IR-DUV (red trace) mass spectra of GPGG^{1+}.*

Figure 4.15. IR-DUV vibrational gain spectrum of GPGG^{1+}, recorded by monitoring the intensity of the fragment with m/z = 69 Da.

4.3.3. IR-DUV Gain Spectroscopy of Ac-Ala$_6$LysH$^+$

Poly-alanine peptides were extensively studied previously in our laboratory.[28-30] Their structural preferences and secondary structure formation were investigated by a combination of conformer-selective cold ion spectroscopy and theoretical calculations. All studied peptides contain phenylalanine amino acid, therefore their spectra at cryogenic temperatures exhibit sharp, vibrationally resolved electronic transitions in the near-UV spectral region.

Herein the analog of such peptide, Ac-Ala$_6$LysH$^+$ (figure 4.16), in which Phe residue was replaced by Ala, is studied. Replacing the N-terminal amino acid should not significantly change the overall structure of a lysine-capped poly-alanine peptide, which was shown to adopt a well-defined helical structure stabilized by several hydrogen bonds. One might, therefore, expect certain similarities between the vibrational spectra of Ac-Ala$_6$LysH$^+$ and its Phe containing analogue.
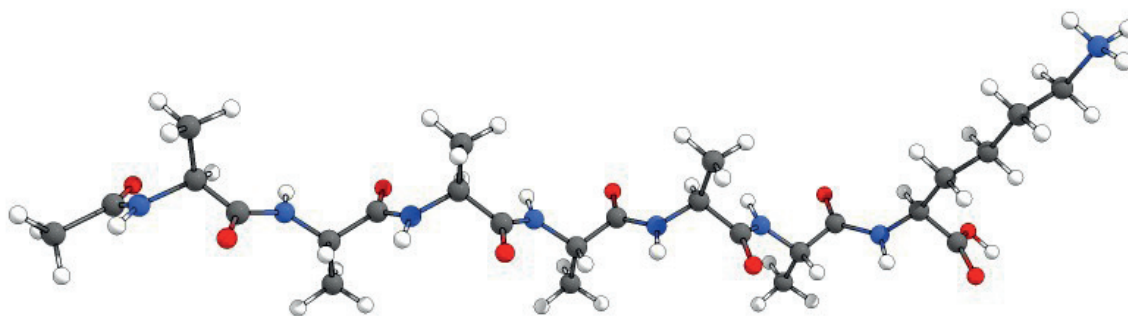

Figure 4.16. *Schematic structure of Ac-Ala$_6$LysH$^+$.*

Figure 4.17 shows CID (blue trace) and PID (red trace) mass spectra of protonated Ac-Ala$_6$LysH$^+$, recorded with UV OPO wavelength fixed at 227 nm. Here, again, we omit the assignment of the observed fragments. Since the photofragmentation mass spectrum of Ac-Ala$_6$LysH$^+$ shows a wide distribution of photofragments, its electronic spectrum was recorded by fixing the mass analyser transmission at m/z = 325 Da and lowering its resolution to the minimum, thus integrating the fragment intensity over the whole mass spectral range (figure 4.18).
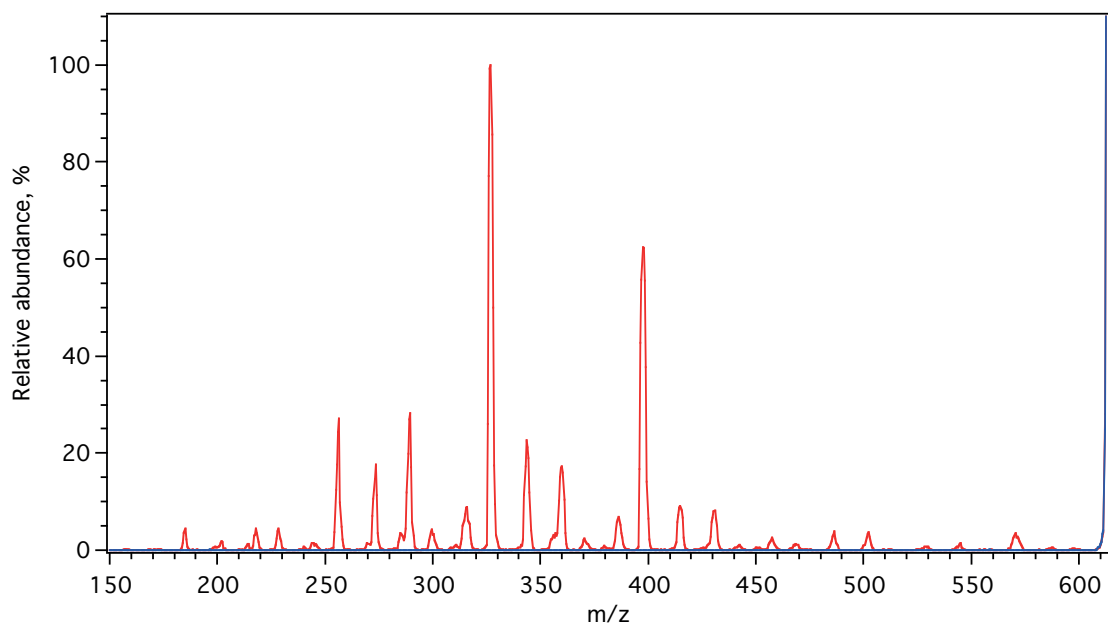
Figure 4.17. *PID (red trace) and CID (blue trace) mass spectra of Ac-Ala$_6$LysH$^+$ with UV OPO wavelength fixed at 227 nm. Each data point was averaged over 10 measurements; mass increment was 0.5 Da.*

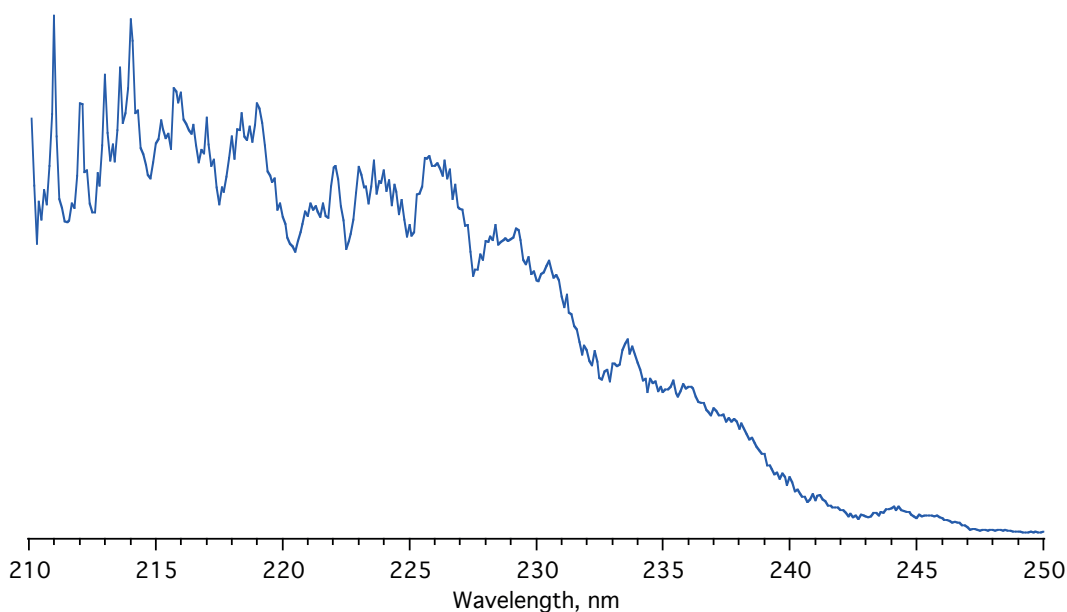**Figure 4.18.** *DUV spectrum of Ac-Ala$_6$LysH$^+$ measured by integrating the intensity of all fragments.*

Figure 4.19 shows the DUV (blue trace) and IR-DUV (red trace) mass spectra of Ac-Ala$_6$LysH$^+$, recorded with UV OPO wavelength fixed at 246 nm and IR OPO wavenumber fixed at 3572 cm^{-1}. All major fragments exhibit approximately the same increase in the fragmentation yield upon IR pre-excitation, therefore the IR spectral measurements were performed similarly to the UV spectral measurement, i.e., by integrating the intensities of all fragments.
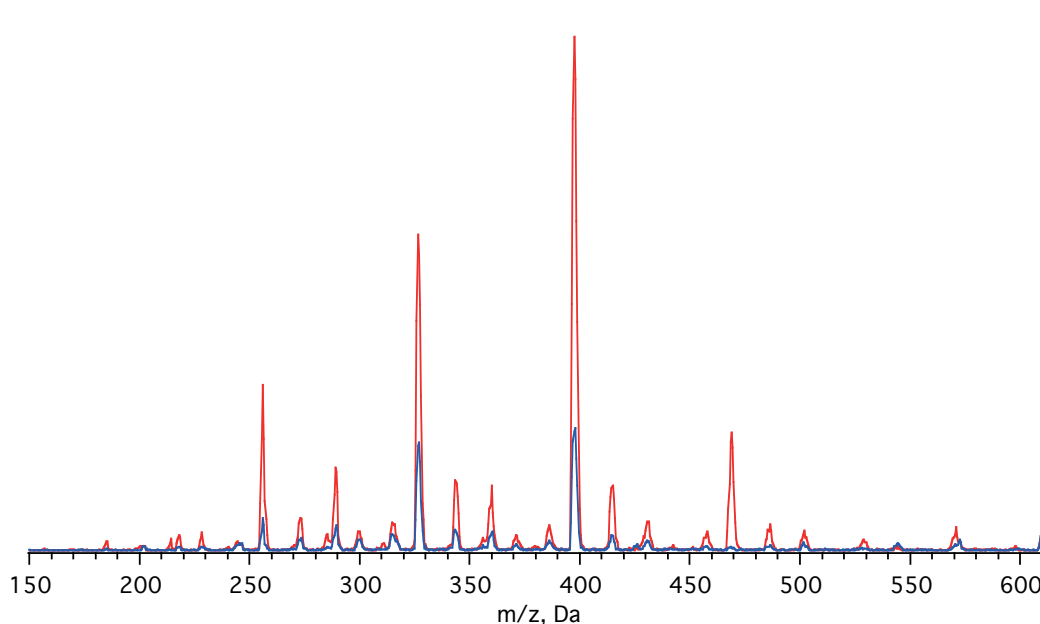

Figure 4.19. *DUV (blue trace) and IR-DUV (red trace) mass spectra of Ac-Ala$_6$LysH$^+$.*

In order to choose the best UV OPO wavelength for recording an IR-DUV gain spectrum wavelength dependence of the S/N ratio (Eq. 4.4) for Ac-Ala$_6$LysH$^+$ was measured. The resulting S/N curve is shown in figure 4.20. Negative contrast corresponds to signal depletion. Based on this curve UV OPO wavelength was fixed at 246 nm.

The IR-DUV of Ac-Ala$_6$LysH$^+$ measured with UV OPO laser wavelength fixed at 246 nm, which corresponds to the best signal-to-noise ratio is shown in figure 4.21. As can be seen, even though some transitions are partially resolved, the all-conformer IR gain spectrum is very congested. The reason for this is that its analogue, studies previously, was shown to have four distinct conformers. [28] Frequencies of the vibrational transitions in these conformers are localized in a narrow spectral region. In contrast to the depletion spectroscopy, an IR-UV gain spectrum reflects the transitions of all conformers, resulting in the overlapped spectra that are difficult to assign.
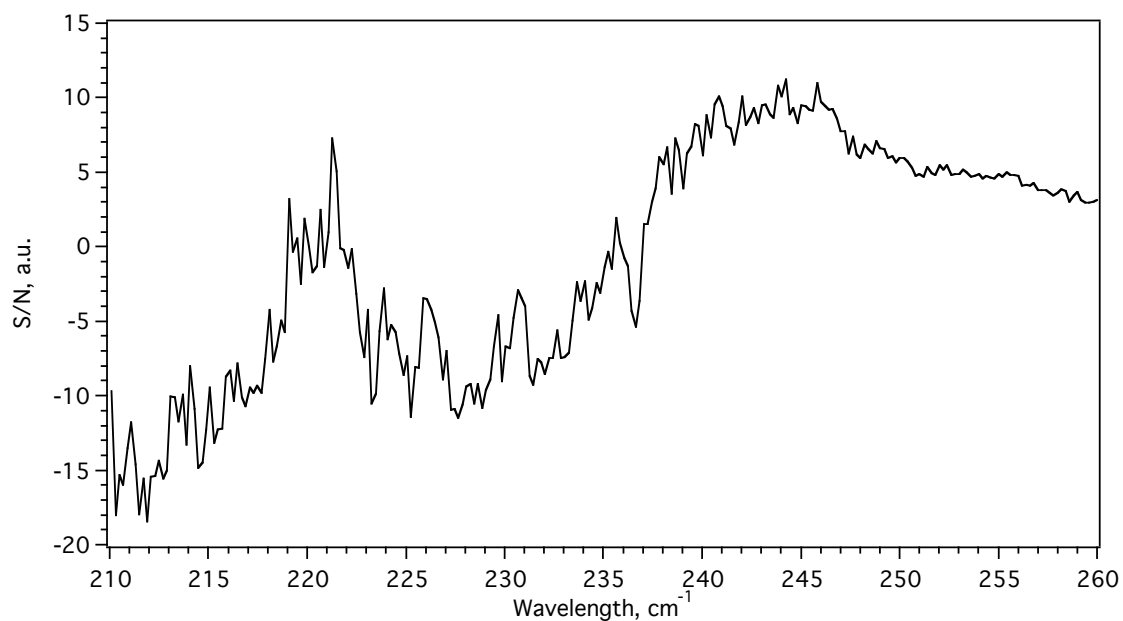
Figure 4.20. *S/N ratio of Ac-Ala$_6$LysH$^+$ calculated as in eq. 4.4 and measured by integrating the intensity of all ions.*

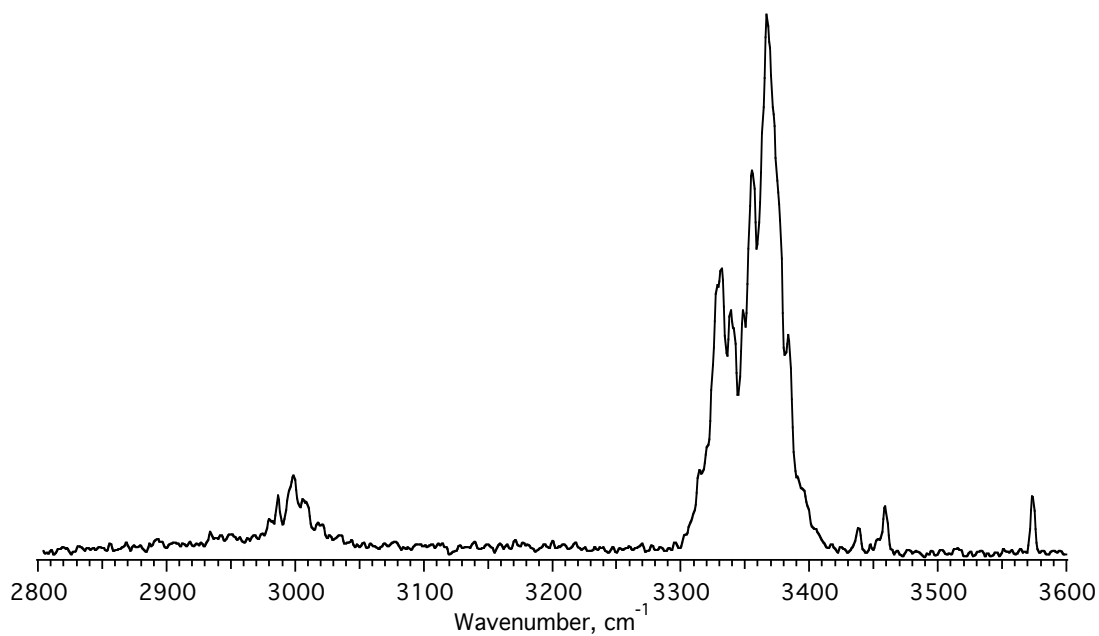***Figure 4.21.*** *IR-DUV gain spectrum of Ac-Ala$_6$LysH$^+$.*

The spectral congestion is, probably, one of the most crucial limitations of the IR-IR-UV hole-burning technique – when both UV and IR spectra exhibit no well-resolved conformer-specific spectral features the acquisition of the vibrational spectra of individual conformers becomes impossible. Vibrational transitions appearing between 3400 and 3500 cm^{-1} belong, presumably, to the N–H stretches of the lysine side chain and are resolved. However, given their weak intensity, they require high power of the pump IR OPO in order to reach saturation.

4.3.5. IR-DUV Gain Spectroscopy of cyclo-GlyArgGlyAspSerProH$^+$

In this section we demonstrate the application of the IR-DUV gain spectroscopy to a native peptide cyclo-GlyArgGlyAspSerProH$^+$ (cGRGDSP^{1+}, m/z = 570.6 Da, figure 4.22). This cyclic peptide is a potent vasodilator.[31-35] Figure 4.23 shows the CID (blue trace) and PID (red trace) mass spectra of cGRGDSP^{1+} measured with the UV OPO wavelength fixed at 220 nm.
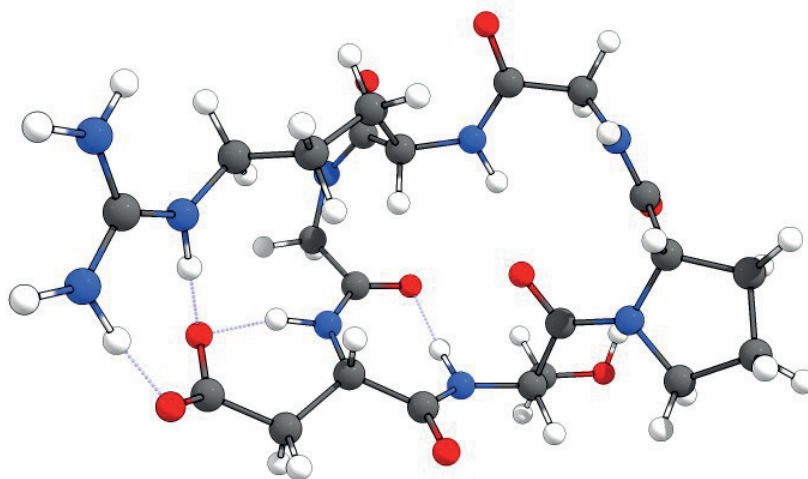

Figure 4.22. *Schematic structure of cGRGDSP^{1+}.*

PID mass spectrum reveals numerous fragmentation channels and results in a very rich photofragmentation spectrum. In order to record an electronic photofragmentation spectrum, the quadrupole mass analyser transmission was fixed at m/z = 445 Da and its resolution was lowered in order to collect the maximum number of fragments. The resulting electronic photofragmentation spectrum is shown in figure 4.24. Each point is averaged over 20 measurements, UV wavelength step is 0.1 nm.
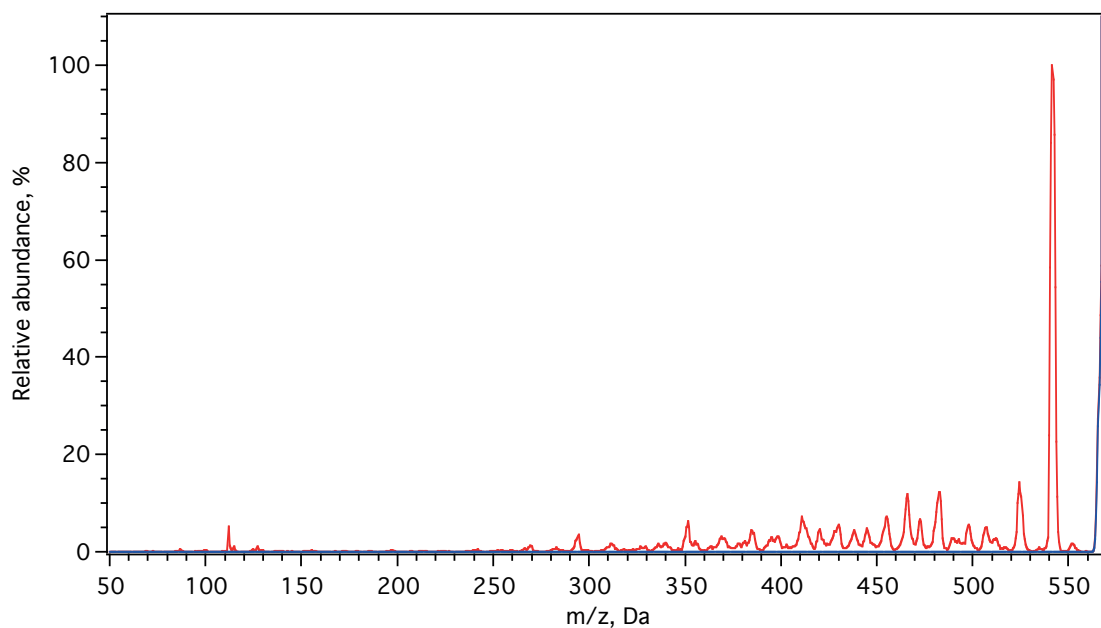
Figure 4.23. *CID (blue trace) PID (red trace) mass spectra of cGRGDSP^{1+}, recorded with UV OPO wavelength fixed at 220 nm. Each data point was averaged over 20 measurements; mass increment was 0.5 Da.*
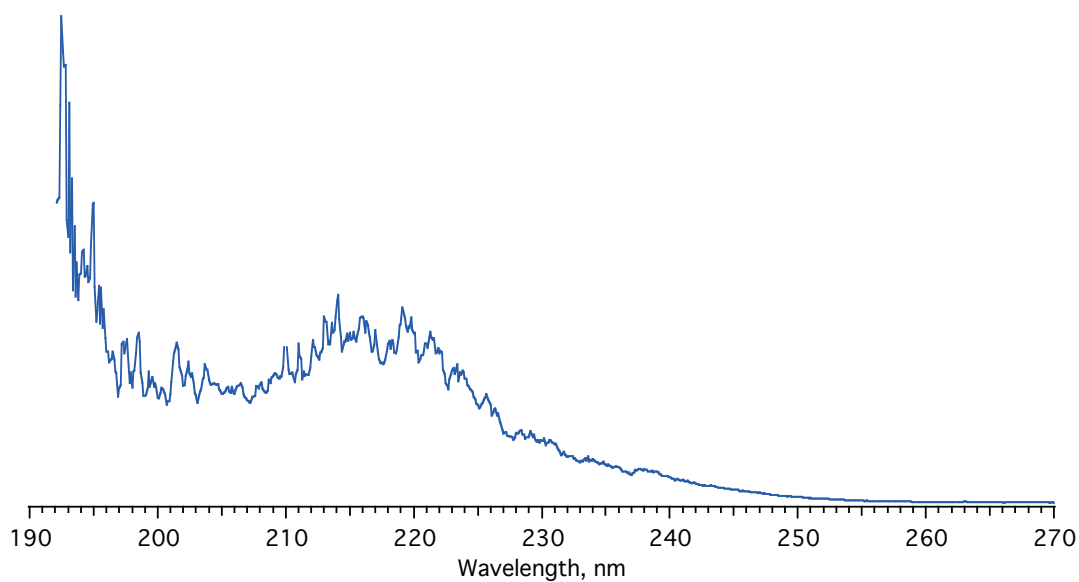

Figure 4.24. *Electronic photodissociation spectrum of cGRGDSP^{1+}, recorded by integrating intensities of all fragments.*

111

Figure 4.25 shows the PID mass spectra of cold (blue trace) and IR-preheated (red trace) cGRGDSP[1+] recorded with UV OPO wavelength fixed at 196 nm and IR OPO wavenumber fixed at O-H stretching vibration at 3573.7 cm^{-1}. The only fragment that increases significantly due to the absorption of an IR photon and is, thus, suitable for the "gain" spectrum measurement is the water loss, presumably from the Ser residue. Other fragments either exhibit only a small increase of the fragmentation yield, or have low signal intensity. Given that the peptide is cyclic, the most abundant fragments correspond to the neutral losses from the side chains, because other fragments require cleavage of two peptide bonds, and an additional energy from an IR photon does not significantly change the fragmentation efficiency.
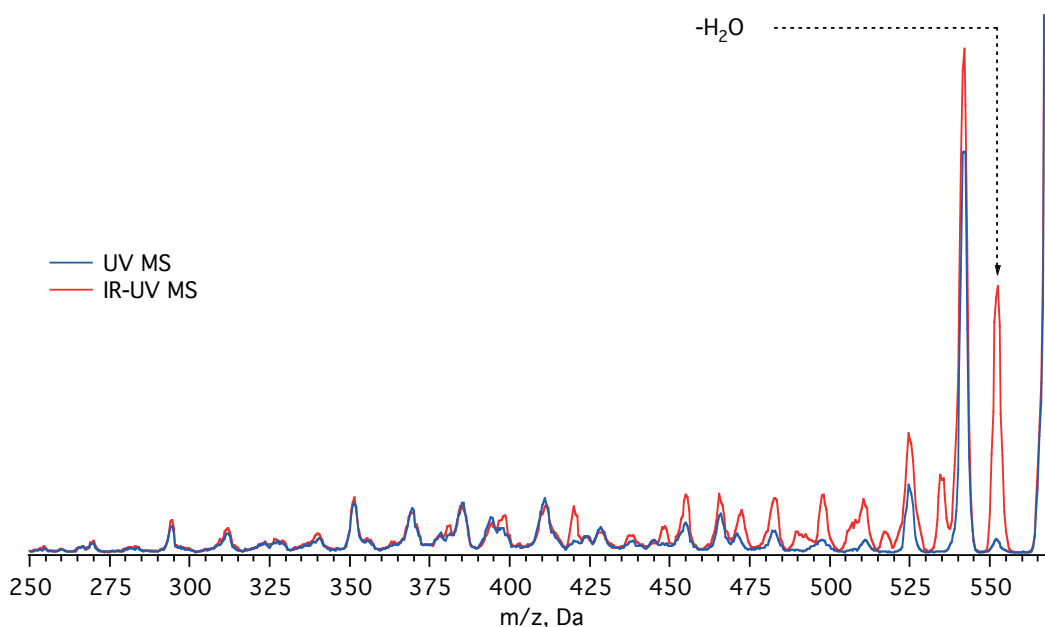

Figure 4.25. *Photofragmentation mass spectra of cold (blue trace) and IR-preheated (red trace) cGRGDSP[1+].*

The water loss fragment was not initially observed in the PID mass spectrum (figure 4.23), therefore its electronic spectrum was recorded separately (figure 4.26). The S/N ration was measured for this fragment and is shown in figure 4.27. Figure 4.28 shows the IR-DUV gain spectrum of cGRGDSP[1+] measured with UV OPO laser wavelength fixed at 194 nm. The highly congested vibrational spectrum suggests the presence of more than one conformer. The lower S/N ratio in the gain spectrum of cGRGDSP[1+] with the spectra of other peptides, reported herein, is due to the low intensity of the fragment being recorded. However, this result clearly demonstrates the

applicability of the IR-DUV gain spectroscopy for natural peptides even in complicated cases. The precise assignment of the transitions requires comparison with calculations, and is beyond the scope of this report.
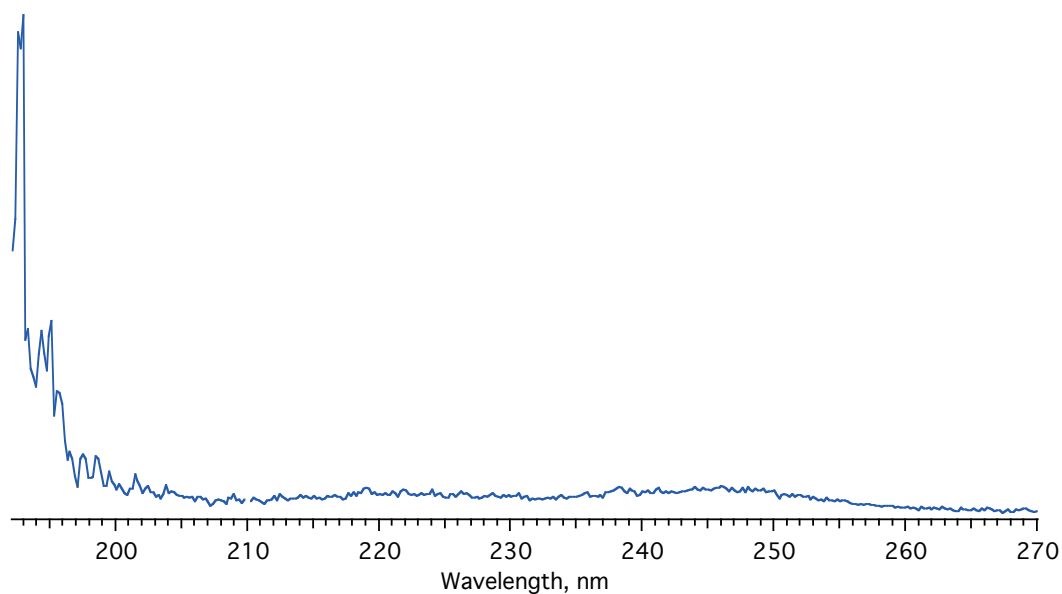

Figure 4.26. *PID electronic spectrum of cGRGDSP^{1+} recorded by monitoring the H$_2$O neutral loss fragment.*
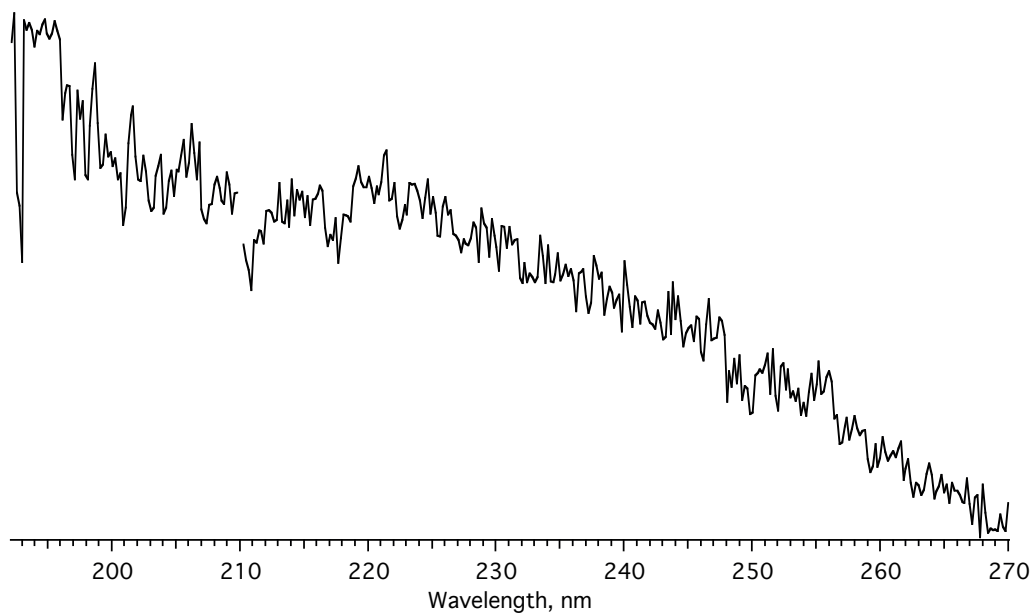

Figure 4.27. *S/N ratio of cGRGDSP^{1+} calculated as in eq. 4.4 and measured by monitoring the intensity the fragment with m/z = 552 Da corresponding to the water loss.*
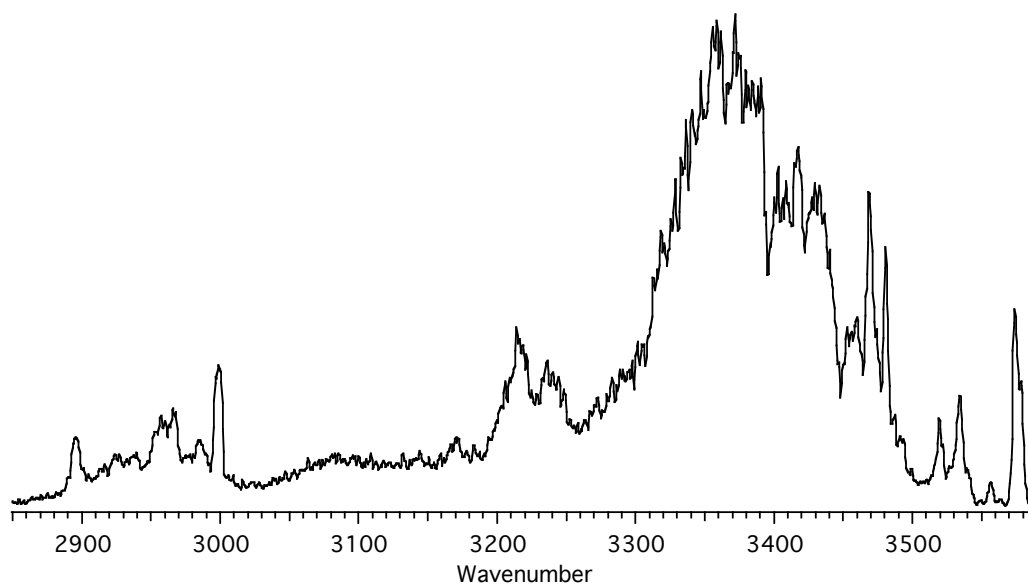
Figure 4.28. *IR-DUV "gain" spectrum of cGRGDSP[1+].*

4.4. IR-IR-DUV hole-burning spectroscopy

The possibility to record linear vibrational IR-DUV gain spectra of cold protonated peptides of any primary structure opens new horizons to cold ion spectroscopy, mainly because it can now successfully compete with other techniques, such as IRMPD. Nevertheless, the obtained gain spectra remain non-conformer selective, which limits their use in validation of calculated structures. The ultimate goal for this study is to demonstrate the ability to record conformer-selective vibrational spectra of peptides that do not contain aromatic amino acids. For this purpose well-resolved conformer-specific vibrational transitions are required. In this section the ability of the IR-IR-UV hole-burning spectroscopy (Chapter 3) in the DUV region to record conformer-specific vibrational spectra is demonstrated.

4.4.1. IR-IR-DUV Hole-Burning Spectroscopy of AlaAlaH[+]

The IR-DUV gain spectrum of AlaAlaH[+] shown in figure 4.10 suggests the presence of only one abundant conformer. In order to verify this suggestion the IR-IR-DUV hole-burning technique was applied. The pump IR OPO wavenumber was tuned to 3323.5 cm^{-1}. Figure 4.29 shows the probe IR-DUV gain spectrum (blue trace), IR-IR-DUV hole-burning spectrum (red trace) and their difference (black trace).
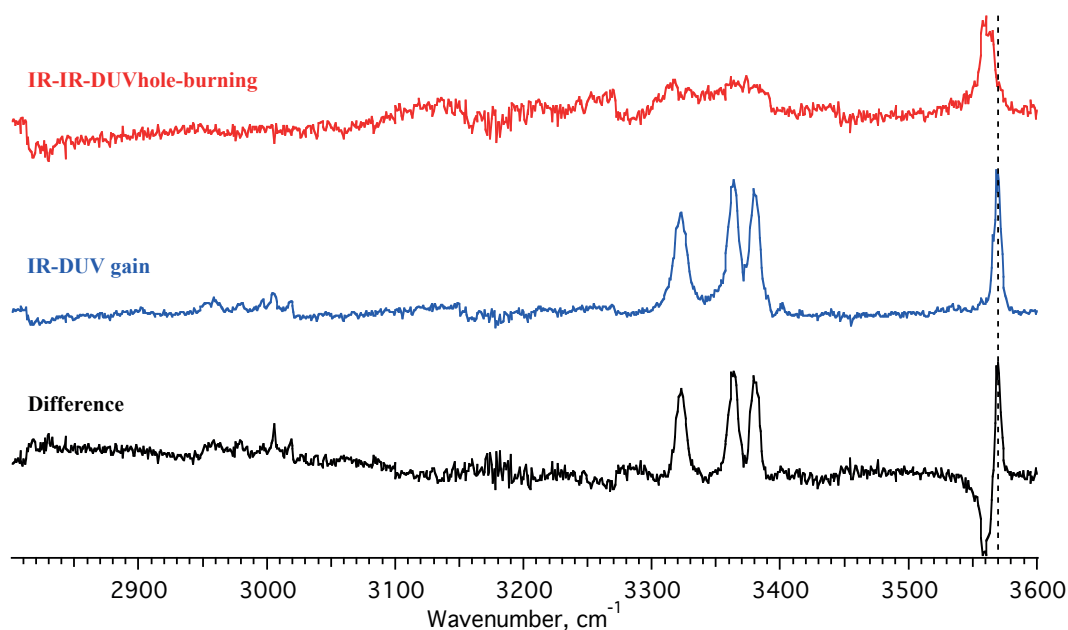
Figure 4.29. *IR spectra of AlaAlaH⁺ in the 3 μm spectral region. The blue trace corresponds to the IR-DUV "gain" spectrum; the red trace corresponds to the IR-IR-DUV hole-burning spectrum, measured with the pump IR OPO laser wavenumber fixed at 3323.5 cm⁻¹; the black trace corresponds to their difference. Vertical dashed line denotes the O-H stretching vibration.*

As can be seen from figure 4.29, all of the C-H and N-H stretching vibrational transitions from the gain spectrum are associated with the same conformer. The additional gain near the O–H vibration is not present in the IR-DUV gain spectrum. It is broadened and shifted to the red from the O–H band by ~8 cm⁻¹. The likely explanation is that it stems from the increased fragmentation yield of the pumped ions due absorption of an additional photon from the probe IR OPO laser. The IR-IR-DUV hole-burning spectroscopy allows thus to verify the presence of only one major conformer of AlaAlaH⁺ under the experimental conditions of our setup, although previous theoretical calculations have predicted four lowest-energy conformers,[36-38] of which one corresponds to *cis* form, and one is protonated on the C=O group on the backbone. The two remaining conformers are of the *trans* form and protonated on the N-terminus, separated by 0.5 kcal/mole energy gap[36] (trans, cis refers to the orientation between carbonyl and amino group in the peptide bond). IRMPD spectroscopy of AlaAlaH⁺ at room temperature confirmed the presence of two *trans* conformers[37]. The fact that only one conformer is present at our experimental conditions suggests that either calculations failed to predict correct relative energetics of the conformers, or that during the collisional cooling higher-energy conformer fully relaxes into the lowest-energy one.

The discrepancy between theory and experiment for even a small dipeptide highlights the importance of the experimental validation of the calculations.

4.4.2. IR-IR-DUV Hole-Burning Spectroscopy of cGRGDSP[1+]

Figure 4.30 shows the IR-IR-DUV hole-burning spectroscopy of cGRGDSP[1+] measured with the pump IR OPO laser wavenumber fixed at 3535.2 cm^{-1}. The blue trace corresponds to the IR-DUV gain spectrum, red trace corresponds to the IR-IR-DUV hole-burning spectrum, and the black trace represents their difference, corresponding to the conformer named **A**. When the pump IR OPO laser wavenumber was fixed at the vibrational transition of another conformer, at 3519.5 cm^{-1}, the signal-to-noise ratio did not allow reliable identification of conformer-specific transitions of the minor conformer. This is mainly due to the fact that only a minor fragment is collected, and the fragmentation signal is low. Since the presence of only two conformers is assumed due to the *cis*- and *trans*- isomers of proline, the IR-IR-DUV hole-burning spectrum automatically reflects the gain spectrum of conformer **B**. Vertical blue and red dashed lines denote conformer-specific vibrational transitions of conformers **A** and **B**, respectively.

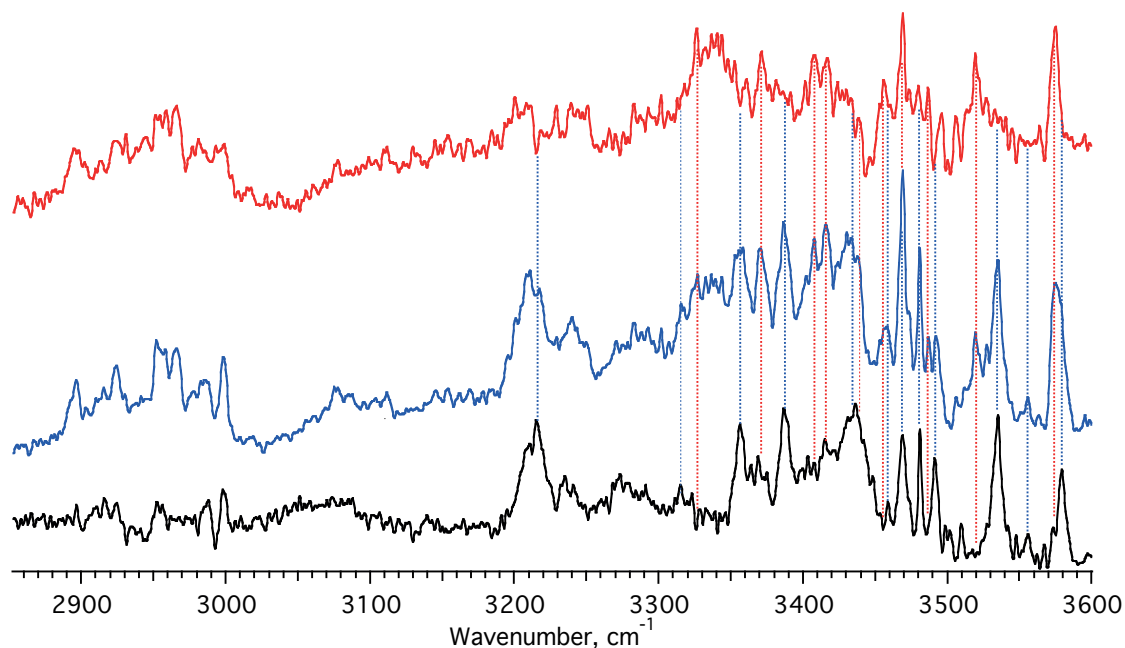**Figure 4.30.** *IR-IR-DUV hole-burning spectroscopy of cGRGDSP[1+], recorded with the pump IR OPO wavenumber fixed at 3535.2 cm^{-1}. Color-coding denotes the three traces as follows: blue trace – IR-DUV gain spectrum; red trace – IR-IR-DUV hole-burning spectrum; black trace – their difference. Vertical dashed lines denote vibrational transitions, that belong to the pump IR laser-labelled conformer.*

4.5. Conclusions

In this chapter the extension of the available techniques in Cold Ion Spectroscopy to peptides that do not contain aromatic side chains was explored. First of all, electronic spectrum of a single peptide bond in AlaAlaH$^+$ dipeptide in the gas phase was measured in the spectral region above 192 nm. A closer analysis of electronic spectra of different peptides revealed that they are all shifted to red with respect to the absorption of a single peptide bond. Furthermore, the two peptides that are not expected to adopt any particular secondary structure, GPGG[1+] and cGRGDSP[1+], reveal a weak band near 220 nm, while the peptide Ac-A$_6$K[1+], which is suggested to be helical, has no distinct maximum. Whether this band is a characteristic feature for peptides with random relative orientation of the peptide bonds' dipole moments and, thus, the peptides with the ordered orientation of peptide bonds can be identified with cold ion DUV spectroscopy based solely on their electronic spectra – is a question for further investigation.

It was demonstrated that despite the width of the peptide bond absorption spectrum, the IR-DUV gain spectroscopy can be applied to record all-conformer gain spectra of peptides as large as six amino acids even when their dissociation yield is low. The quality of such spectra exceeds the ones obtained with tagging IR technique and the resolving power is much better, compared to the IRMPD spectroscopy. Furthermore, various parameters, that can potentially affect the quality of the gain spectra, were discussed and the procedure for the S/N optimization was proposed.

Finally, the ability to disentangle the non-conformer-selective gain spectra into the spectra of individual conformers by applying IR-IR-DUV hole-burning spectroscopy was demonstrated for a dipeptide and a natural cyclic six amino acid peptide.

The results, presented herein, indicate that conformer-selective cold ion spectroscopy can now be applied to peptides of virtually any chemical composition. Given other advantages of this technique over the alternative experimental approaches (resolution of vibrational spectra, linear power-dependence of the signal, etc.) cold ion spectroscopy is now a method of choice to study structures of peptides in the gas phase.

References

1.   N. S. Nagornova, T. R. Rizzo and O. V. Boyarkin, *J. Am. Chem. Soc.*, 2010, **132**, 4040-+.

2.   A. Y. Pereverzev and O. V. Boyarkin, *PCCP*, 2017, **19**, 3468-3472.

3.   O. V. Boyarkin, S. R. Mercier, A. Kamariotis and T. R. Rizzo, *J. Am. Chem. Soc.*, 2006, **128**, 2816-2817.

4.   J. A. Stearns, S. Mercier, C. Seaiby, M. Guidi, O. V. Boyarkin and T. R. Rizzo, *J. Am. Chem. Soc.*, 2007, **129**, 11814-11820.

5.   N. L. Burke, J. G. Redwine, J. C. Dean, S. a. McLuckey and T. S. Zwier, *Int. J. Mass spectrom.*, 2015, **378**, 196-205.

6.   V. Kopysov and O. V. Boyarkin, *Angew. Chem. Int. Ed.*, 2016, **55**, 689-692.

7.   N. S. Nagornova, PhD, ÉCOLE POLYTECHNIQUE FÉDÉRALE DE LAUSANNE, 2011.

8.   A. Y. Pereverzev, X. Cheng, N. S. Nagornova, D. L. Reese, R. P. Steele and O. V. Boyarkin, *J. Phys. Chem. A*, 2016, **120**, 5598-5608.

9.   A. Masson, E. R. Williams and T. R. Rizzo, *J. Chem. Phys.*, 2016, **143**, 104313.

10.   M. B. Robin, *Higher Excited States of Polyatomic Molecules*, New York, 1975.

11.   D. L. Peterson and W. T. Simpson, *J. Am. Chem. Soc.*, 1957, **79**, 2375-2382.

12.   L. B. Clark, *J. Am. Chem. Soc.*, 1995, **117**, 7974-7986.

13.   R. W. Woody and A. Koslowski, *Biophys. Chem.*, 2002, **101-102**, 535-551.

14.   W. D. Bowers, S.-S. Delbert, R. L. Hunter and R. T. J. McIver, *J. Am. Chem. Soc.*, 1984, **106**, 7288-7289.

15.   D. F. Hunt, J. Shabanowitz and J. R. I. Yates, *J. Chem. Soc., Chem. Commun.*, 1987, **1**, 548-550.

16.   S. A. Martin, J. A. Hill, C. Kittrell and K. Biemann, *J. Am. Soc. Mass. Spectrom.*, 1990, **1**, 107-109.

17.   E. R. Williams, K. D. Henry, F. W. McLafferty, J. Shabanowitz and D. F. Hunt, *J. Am. Soc. Mass. Spectrom.*, 1990, **1**, 413-416.

18.   D. C. Barbacci and D. H. Russell, *J. Am. Soc. Mass. Spectrom.*, 1999, **10**, 1038-1040.

19.   M. S. Thompson, W. Cui and J. P. Reilly, *Angew. Chem. Int. Ed.*, 2004, **43**, 4791-4794.

20.   H. M. Jeong, H. Y. So and S. K. Myung, *Rapid Commun. Mass Spectrom.*, 2005, **19**, 3248-3252.

21.   K. M. Choi, S. H. Yoon, M. Sun, J. Y. Oh, J. H. Moon and M. S. Kim, *J. Am. Soc. Mass. Spectrom.*, 2006, **17**, 1643-1653.

22.   W. Cui, M. S. Thompson and J. P. Reilly, *J. Am. Soc. Mass. Spectrom.*, 2005, **16**, 1384-1398.

23.   Y. M. E. Fung, F. Kjeldsen, O. A. Silivra, T. W. D. Chan and R. A. Zubarev, *Angew. Chem. Int. Ed.*, 2005, **44**, 6399-6403.

24.   L. Joly, R. Antoine, M. Broyer, P. Dugourd and J. Lemoine, *J. Mass Spectrom.*, 2007, **42**, 818-824.

25.   J. P. Reilly, *Mass Spectrom. Rev.*, 2009, **28**, 425-447.

26.   N. S. Nagornova, T. R. Rizzo and O. V. Boyarkin, *Angew. Chem. Int. Ed.*, 2013, **52**, 6002-6005.

27.   A. Masson, M. Z. Kamrath, M. A. S. Perez, M. S. Glover, U. Rothlisberger, D. E. Clemmer and T. R. Rizzo, *J. Am. Soc. Mass. Spectrom.*, 2015, **26**, 1444-1454.

28.   J. A. Stearns, C. Seaiby, O. V. Boyarkin and T. R. Rizzo, *PCCP*, 2009, **11**, 125-132.

118

29. J. A. Stearns, O. V. Boyarkin and T. R. Rizzo, *J. Am. Chem. Soc. Comm.*, 2007, **129**, 13820-13821.

30. T. R. Rizzo, J. A. Stearns and O. V. Boyarkin, *Int. Rev. Phys. Chem.*, 2009, **28**, 481-515.

31. M. L. Burch, R. Getachew, N. Osman, M. A. Febbraio and P. J. Little, *J. Biol. Chem.*, 2013, **288**, 7410-7419.

32. V. J. Mukhatyar, M. Salmerón-Sánchez, S. Rudra, S. Mukhopadaya, T. H. Barker, A. J. García and R. V. Bellamkonda, *Biomaterials*, 2011, **32**, 3958-3968.

33. F. Kong, A. J. García, A. P. Mould, M. J. Humphries and C. Zhu, *J. Cell Biol.*, 2009, **185**, 1275-1284.

34. N. D. Kirkpatrick, S. Andreou, J. B. Hoying and U. Utzinger, *AJP: Heart and Circulatory Physiology*, 2007, **292**, H3198-H3206.

35. S. Nadanaka, C. Sato, K. Kitajima, K. Katagiri, S. Irie and T. Yamagata, *J. Biol. Chem.*, 2001, **276**, 33657-33664.

36. W. Y. Sohn and J. S. Lee, *J. Phys. Chem. A*, 2010, **114**, 7537-7543.

37. B. Lucas, G. Grégoire, J. Lemaire, P. Ma*itre*, J.-M. Ortega, A. Rupenyan, B. Reimann, J. P. Schermann and C. Desfrancois, *PCCP*, 2004, **6**, 2659-2663.

38. D. C. Marinica, G. Grégoire, C. Desfrancois, J. P. Schermann, D. Borgis and M. P. Gaigeot, *J. Phys. Chem. A*, 2006, **110**, 8802-8810.

Chapter 5

Exploring the Relevance of the Gas-Phase Studies to Biology

In the present chapter we address one of the key questions in Cold Ion Spectroscopy - are the structures of biomolecular ions in the gas phase similar in any sense to their native geometries *in vivo*? Following an introduction, sections 5.2 and 5.3 present experimental results for stereoisomers of an opioid peptide [Ala^2, Leu^5]-Enkephalin and an intrinsically disordered peptide neurokinine A, respectively. The goal of these studies was to check for a correlation between the gas-phase structures and native geometries for peptides that are biologically active in a hydrophobic environment.

5.1. Introduction

Over the last decade cold ion spectroscopy has demonstrated its ability to provide detailed spectroscopic fingerprints for stringent validation of the three-dimensional (3D) structures of small to mid-size biomolecules (e.g., peptides) that are isolated from interactions with solvents in the gas phase.[1, 2] For example, the calculated intrinsic geometries of the two lowest-energy gas-phase conformers of a doubly protonated decapeptide gramicidin S (176 atoms) were validated by conformer-selective cold ion spectroscopy[3, 4] (CIS). Although from the point of view of "classical" gas-phase spectroscopy the size of this peptide is very large, it remains "small" on the scale of biological species (e.g., proteins and their complexes). High spectral density of optical transitions forbids, however, vibrational resolution in IR and UV spectra even for a small protein, e.g., cytochrome C.[5] The use of CIS for validating calculated structures is thus limited to peptides with less than 10-15 amino acids; gramicidin S remains the largest protonated molecule for which conformer selective spectra are available and the accurate intrinsic structure has been solved.

A fundamental question that still remains open for peptides of this size is to what extent the gas-phase structures of these biomolecules resemble their native structures *in vivo*? It is, for instance, well established that non-cyclic peptides with unprotected N- and C-terminus are typically zwitterions at physiological pH in aqueous solutions, but not in the gas phase.[6] This fact alone seems to limit the practical relevance of CIS to biological problems because, for example, gas-phase structures of relatively small biomolecules, such as amino acids, differ completely from their structures in solution, as was shown in Chapter 3.

Electrospray ionization[7-9] (ESI) is the most widely used technique to transfer biological molecules from solution to the gas phase. Although ESI is believed to be a soft method and has the potential to preserve structural features of large complexes and biomolecules in native-like conditions,[10-16] whether the structures of small to mid-size peptides survive the transfer to the gas phase – remains unclear. Numerous experimental studies (ion mobility measurement of CCS,[17-19] IR spectroscopy,[20, 21] solvent dependence,[22-26] collisional activation,[27, 28] etc.) suggest that one can produce and preserve metastable species that are significantly different from the lowest energy gas-phase structures and are kinetically trapped, with barriers on the potential energy surface that inhibit them from isomerizing. Ion mobility experiments have demonstrated that in certain conditions some higher-energy conformations might be present in the gas phase.[29-34] These experiments, however, considered mainly the cis-/trans- isomerization of proline residue, the process with an extremely high energy barrier (20-50 kJ/mole),[30] that preserves ion from breaking native-state intramolecular hydrogen bonds.

In addition to the different charge state, the lack of solvent shell is another obvious difference between the gas phase and solution. In condensed phase a subtle balance between intramolecular bonds and intermolecular interactions with the solvent determine the structure of a hydrophilic peptide in solution.[35] Isolating molecules in the gas phase eliminates strong intermolecular hydrophilic interactions with solvent, thus changing the 3D structure of a peptide. Hence, in the absence of strong energetic barrier, the structure of an ion in the gas phase rearranges and the new intramolecular hydrogen-bonding network determines the intrinsic geometry. Therefore, the chances that the intrinsic structure of a midsize peptide resembles the one in solution are low.

But what if the native structure was formed in the absence of the hydrophilic environment? Wouldn't the most favorable structure be determined by intramolecular hydrogen bonding pattern, similarly to the gas phase? Indeed, there are cases, when the gas-phase structure of peptides might be a good reflection of their biologically active geometry. Many peptide ligands adopt this

geometry only when they bind to the hydrophobic lipid bilayer of the cell membrane or into hydrophobic pockets of receptor proteins.[36, 37] It is the tertiary structure of such peptides in a hydrophobic environment, not in aqueous solution, that determines their biological activity and, therefore, must be understood in detail.

Enkephalins, for instance, dock into hydrophobic pockets of opioid receptor proteins. It was recently revealed that the pharmacological activity of these peptide drugs correlates with their gas-phase geometries, but not with the condense-phase structures determined by X-ray crystallography.[38] It was suggested that, perhaps, the gas phase and not the crystal or aqueous solution structures best reflect the biologically active geometry of peptide ligands in hydrophobic environment. Another example is an interaction of neuropeptides with their target receptors. Their flexibility and the lack of definite structural motif in the aqueous environment allow low receptor-type specificity. However, when interacting with a specific receptor, their structure undergoes vast conformational changes.

The aim of the present chapter is to assess the hypothesis, that a solvent-free vacuum mimics to some extent the native hydrophobic environment (e.g., binding pockets of receptors). Intrinsic structures are, by definition, determined only by the intramolecular bonds and, therefore, may resemble native ones for peptides that *in vivo* reside in a hydrophobic environment at least by their backbone orientation (secondary structure). A verification of this suggestion requires a comparison of the gas-phase 3D structure of ligands with their biologically active structures in hydrophobic pockets of receptors and will allow linking the intrinsic tertiary structures of biomolecules to their native geometries, which is a central prerequisite for making gas-phase studies directly relevant to biology. Spectroscopic data, presented below, provide necessary information for structural characterization of several ligands in the gas phase and provide some evidence to support the positive answer to the aforementioned question: are the structures of biomolecular ions in the gas phase similar in any sense to their native geometries *in vivo*?

5.2. Intrinsic Structures of [Ala^2, Leu^5]-Enkephalin Stereoisomers

5.2.1. Introduction

Enkephalins belong to the family of opioid peptides that bind to the transmembrane opioid receptors and have been used as efficient drugs for pain treatment for decades.[39-41] Opioid peptides contain two aromatic rings of their Tyr and Phe residues, the spacing between which is considered

one of the key structural parameters that determine the pharmacology of these drugs[36, 42, 43] and is typically determined from condensed-phase structures.

Leu-enkephalin (Tyr-Gly-Gly-Phe-Leu) is a benchmark peptide for many gas-phase studies. Substitution of a Gly^2 by an Ala residue allows studying three stereoisomers of the peptide [Ala^2, Leu^5]-Enkephalin (figure 5.1) with different chirality of the Ala^2 and Leu^5 amino acids. Three isomers, corresponding to the L-L, D-L, and D-D chirality combinations of Ala^2 and Leu^5 residues, have different structures and pharmacological activity. For the sake of clarity, they are addressed in the present analysis as LALLE, DALLE, and DADLE, respectively.
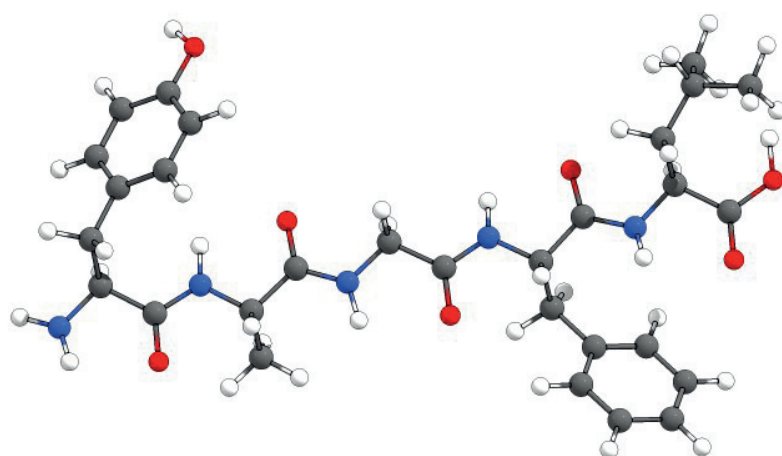

Figure 5.1. *Schematic view of [L-Ala^2, L-Leu^5]-Enkephalin, m/z = 556.3 Da.*

Among these three peptides examined herein, DADLE isomer is by far the most potent and selective δ-opioid receptor agonist.[41, 44, 45] Question remains whether the efficiencies of DADLE and other isomers correlate with their Phe–Tyr spacing. The available X-ray diffraction data suggest 5 to 13.9 Å (depending on the conformer) and 9.3 Å for this spacing in crystallized Leu-enkephalin and DADLE, respectively,[42] and exhibit no apparent correlation with the drug efficiencies. Similar uncertainty remains in correlating structures and pharmacological activity for many other opioid peptides.[36, 43]

Resonance Energy Transfer (RET) in solution is another proven technique that allows for an estimation of the interchromophore distances in biomolecules.[46, 47] Several groups have recently demonstrated the use of fluorescence[48-50] and photodissociation mass spectrometry[51-53] for measuring RET in the gas-phase ions labeled with large chromophores. The Phe-Tyr spacing in [Ala^2, Leu^5]-Enkephalin stereoisomers, isolated in the gas phase, were estimated by the resonance

energy transfer, detected by a combination of cold ion spectroscopy and high-resolution mass spectrometry. The distances between the centers of the chromophore rings, calculated as the average coordinates of their atoms and averaged over all calculated structures that satisfy the limitations set by FRET experiments, have the following distribution[38]: LALLE structures exhibit two families with $R \approx 9.9$ and 11.2 Å, which yield the overall average distance $R_{LL} = 10.6 \pm 0.7$ Å. The distribution of the calculated DADLE structures exhibits three distinct conformational families with $R = 5$, 6 and 7.5 Å. Averaging over all of the DADLE structures yields $R_{DD} = 5.7 \pm 1$ Å. The DALLE isomer has an intermediate distribution[54]: it is more heterogeneous, compared with LALLE and exhibits three distinct conformational families with $R = 9.6$, 10.4 and 11.2 Å.

In contrast to the condensed-phase structures, these distances differ substantially in stereoisomers with different pharmacological efficiencies, suggesting that gas-phase structures might be a better pharmacophoric metrics for ligand peptides. However, the inter-chromophore distance is not the only important structural parameter. Peptides *in vivo* are, likely, zwitterions. Furthermore, Leu–Enk exhibits different conformational preferences in water and in a hydrophobic solvent,[55] suggesting that charge solvation affects the structures of peptides. It would be naive to suggest the complete coincidence of the structures in liquid and vacuum environments. But the overall secondary structure (and, consequently, the inter-chromophore spacing) can be preserved, making intrinsic structures of these ligands directly relevant for biology.

This assumption has to be validated by strict comparison of the gas-phase and native structures. First of all, all gas-phase conformers of all isomers have to be identified by comparing the conformer-specific experimental spectra with theoretical calculations. Then, one has to compare the interchromophore distances for in validated structures with the predictions from the gas-phase FRET studies, as the latter are supposed to be correlated with the native structures. Finally, the gas-phase structures have to be compared with the native ones, measured by NMR.

As the first step towards achieving this goal, the conformer-specific vibrational spectra of all major conformers of three stereoisomers of [Ala^2, Leu^5]-enkephalin (one, two, and three conformers for LALLE, DALLE and DADLE, respectively) are presented herein. Though the all-conformer UV and IR-UV gain spectra of three isomers of [Ala^2, Leu^5]-enkephalin^{1+} were reported previously,[54] the high spectral density and drastic increase of the fragmentation yield following IR pre-excitation of cold ions preclude the use of IR-UV depletion spectroscopy for most conformers of this tyrosine-containing pentapeptides. We apply a combination of all double-resonance and IR-IR-UV hole-burning spectroscopic approaches to identify conformer-specific vibrational transitions that can be used for strict validation of the calculated structures. The results, presented below,

allow for structural elucidation of the lowest-energy structures and provide hints for improving further calculations.

5.2.2. Experimental Results

Each conformer of all stereoisomers of [Ala^2, Leu^5]-Enkephalin^{1+} (figure 5.1) has the following vibrational transitions in the 3 μm spectral region: tyrosine O-H, carboxylic acid O-H, seven N-H and thirty-one C-H stretching vibrations, though the latter type of vibrations is rarely involved in the structural assignment because a typical peptide has a relatively high number of C-H groups with approximately similar vibrational energies and weak absorption cross-sections. Thus, only O-H and N-H stretches are relevant for structure elucidation.

1. [L-Ala^2, L-Leu^5]-Enkephalin^{1+}

Electronic spectra of singly protonated LALLE and Leu-Enkephalin in the gas-phase are nearly identical.[38, 56] Given the high sensitivity of the electronic transitions to structural changes, one can assume that conformations of these two peptides are also similar. Leu-Enkephalin was shown to have only one backbone orientation in the gas phase.[56]

Figure 5.2 shows the IR-UV gain spectrum of LALLE isomer, measured previously in our laboratory.[54] The exact number of the O-H transitions in the spectrum is difficult to assess because the IR OPO power in the spectral region of interest has sharp dips due to the symmetric stretching vibration absorption of atmospheric water at 3657.1 cm^{-1},[57] as well its corresponding ro-vibrational transitions.[58] The spectrum contains, though, five intensive vibrational transitions in the free N-H region and two broad N-H transitions, overlapped with narrow C-H transitions. Together with the similarity of this peptide with Leu-Enk, the low number of vibrational transitions in the gain spectrum of LALLE suggests that only one major conformer is populated under our experimental conditions. In order to verify this conclusion, an IR-UV hole-burning spectroscopy was employed.

Figure 5.3 shows electronic spectra of cold and IR pre-heated LALLE (black and the red traces, respectively), measured between 35600 and 36000 cm^{-1} with IR OPO wavenumber fixed at 3405.7 cm^{-1} (transition marked with red asterisk in figure 5.2). As can be seen from figure 5.3, all intense electronic transitions are hole-burned simultaneously following the excitation of the vibrational transition at 3405.7 cm^{-1}. Given its extremely small width, this vibration is unlikely to be identical in all possible conformers of LALLE; thus all electronic transitions indeed belong to one major conformer in the gas phase, named LL-**A** in the further analysis.
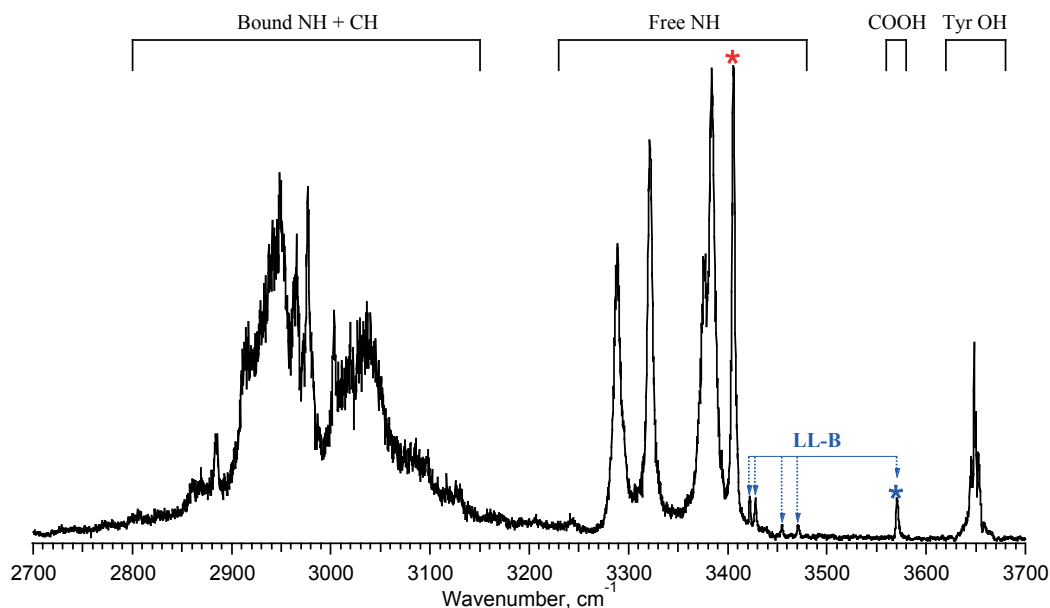
126

Figure 5.2. *IR-UV gain spectrum of LALLE, adopted from Kopysov[54]. Blue arrows mark vibrational transitions of the minor conformer LL-**B**. Red and blue asterisks denote transitions used in IR-UV hole-burning experiments (figures 5.3 and 5.4, respectively).*
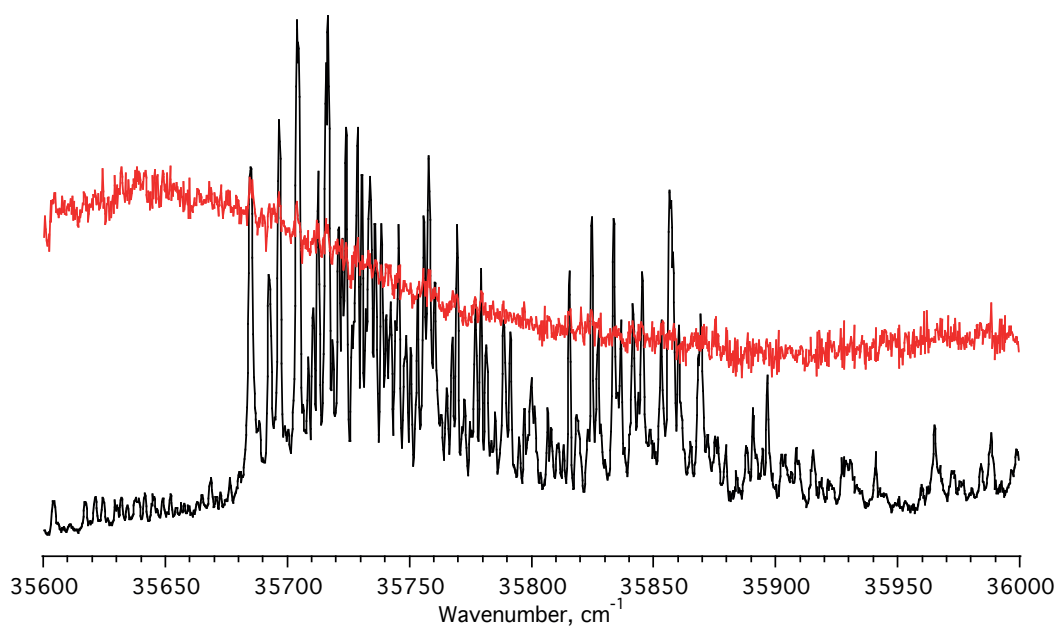

Figure 5.3. *IR-UV hole-burning spectroscopy of LALLE. The black and the red traces correspond to UV spectra of cold and IR pre-heated LALLE, respectively. UV laser energy was 2 mJ per pulse, step rate was 0.2 cm^{-1}, each data point was averaged over 10 measurements, and the resulting spectra were averaged over 3 scans. IR OPO wavenumber was fixed at 3405.7 cm^{-1}(transition, marked with red asterisk in figure 5.2), energy was 8 mJ per pulse.*

However, the data in figure 5.3 do not allow to unambiguously determine whether the small UV transitions between 35600 and 35680 cm^{-1} also belong to the conformer LL-**A** (hot bands) because of the low signal-to-noise ratio in this region. Furthermore, the weak vibrational transitions in figure 5.2 can correspond either to the combination bands of the conformer LL-**A**, or they belong to some minor conformer LL-**B**. In order to determine the origin of these transitions an IR-UV hole-burning spectroscopy between 35600 and 35700 cm^{-1} was employed (figure 5.4). IR OPO wavenumber was fixed at the isolated peak centered at 3571.0 cm^{-1} (marked with blue asterisk in figure 5.2). Excitation of this vibration does not deplete intense electronic transitions, thus it belongs to a different conformer with a band origin at 35603 cm^{-1}. All the electronic transitions of the conformer LL-**B** are labeled with vertical dashed blue lines in figure 5.4. The weak transitions at 35663, 35669, 35677 and 35681 cm^{-1}, marked by red asterisks are probably hot bands of the main conformer LL-**A**.
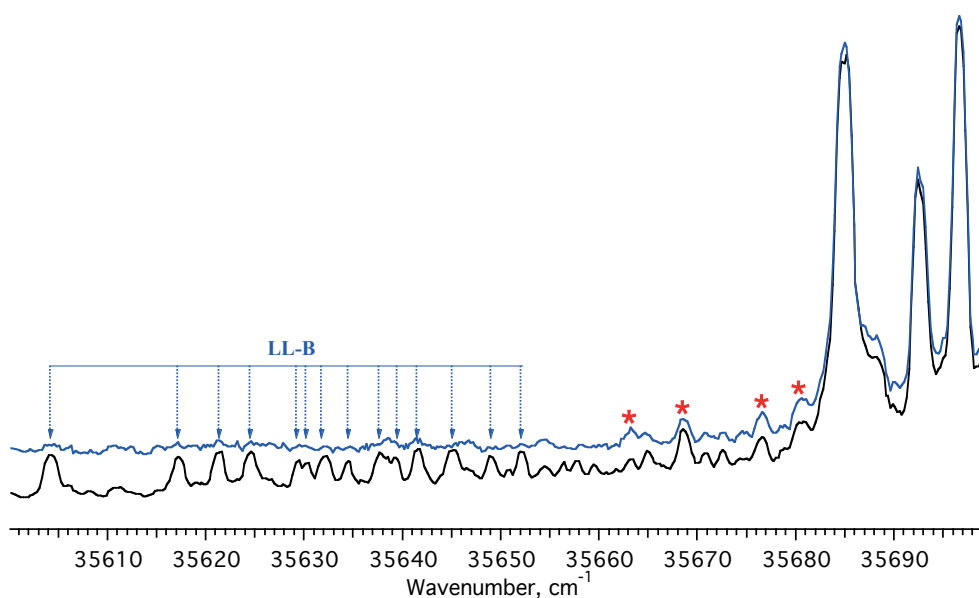

Figure 5.4. *IR-UV hole-burning spectroscopy of LALLE. The black and the blue traces correspond to the UV spectra of cold and IR pre-heated LALLE, respectively. IR laser wavenumber was fixed at 3571.0 cm^{-1} (transition marked with blue asterisk in figure 5.2). Vertical dashed blue lines denote transitions that belong to conformer LL-**B**. Hot bands of conformer LL-**A** are marked with red asterisks*

Unfortunately, small intensities of both electronic and vibrational transitions of the conformer LL-**B** do not allow measuring its conformer-specific spectrum. Nevertheless, the fact that the vibrational transition at 3571 cm^{-1}, corresponding to the carboxylic acid O-H stretch

vibration, is observed only in the conformer LL-**B** suggests that the structures of these conformers differ significantly. The relative intensities of the UV and IR transitions of the two conformers suggest that the relative population of the minor conformer LL-**B** is negligible and the conformer LL-**A** is dominant under our experimental conditions.

2. [D-Ala^2, L-Leu^5]-Enkephalin^{1+}

Figure 5.5 shows an IR-UV gain spectrum of DALLE. The number of peaks clearly indicates the presence of at least two conformers under our experimental conditions, although, based on the relative intensities of the vibrational transitions, the second conformer is less populated (as in the case of LALLE). The two conformers are referred to as DL-**A** and DL-**B** in the following analysis.
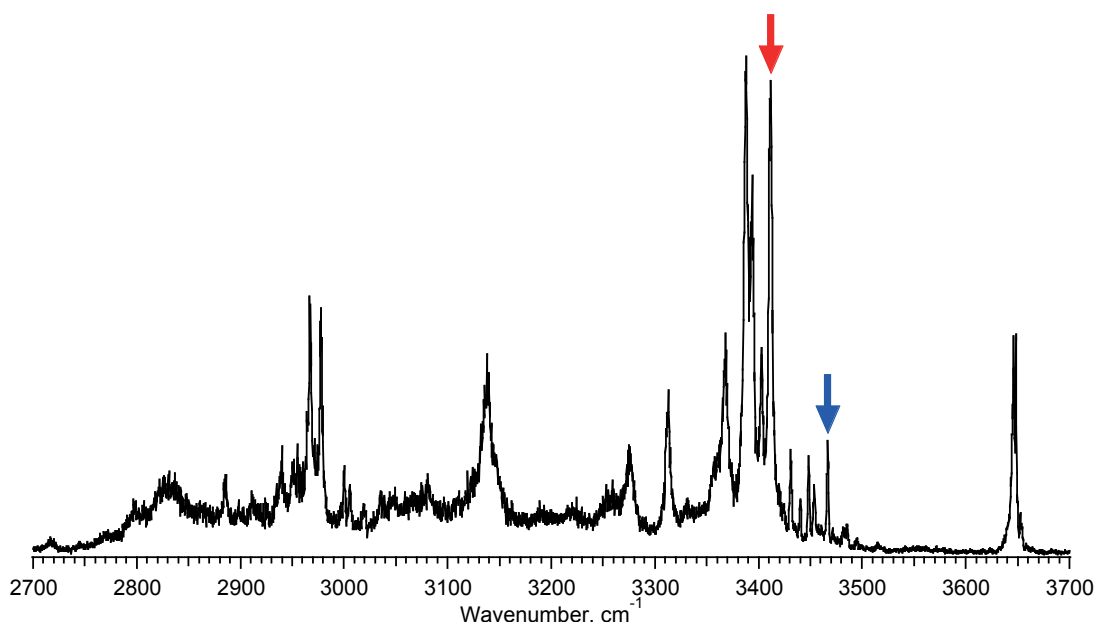

Figure 5.5. *IR-UV gain spectrum of DALLE, adopted from Kopysov[54]. Red and blue arrows mark vibrational transitions used in IR-UV hole-burning experiments (figures 5.6 a and b, respectively).*

Figures 5.6 a and b show electronic spectra of DALLE at $T = 6$ K (black traces) and IR-UV hole-burning spectra recorded with IR OPO wavenumber fixed at 3411.2 cm^{-1} and 3466.5 cm^{-1} (red and blue traces, respectively).

Comparison of these IR-UV hole-burning spectra indicates the presence of two different conformational families. The band origin of conformer DL-**B** is centered at 35486 cm^{-1} and is blue-shifted by $\sim$ 250 cm^{-1} with respect to the band origin of conformer DL-**A** (35238 cm^{-1}). All sharp

129

vibronic transitions in the electronic spectrum of DALLE are associated with one of the conformational families. The band origin of DL-**A** exhibits almost 50% depletion after absorption of an IR photon.
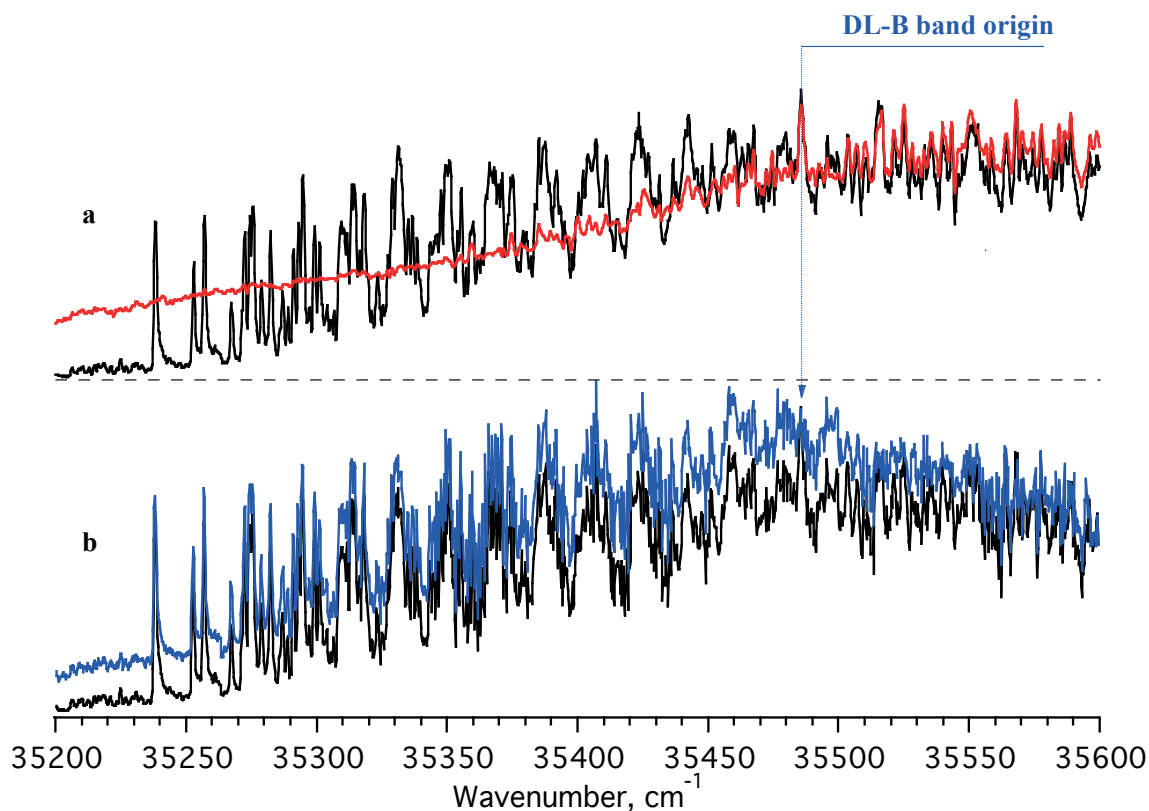

Figure 5.6. *IR-UV hole-burning spectroscopy of DALLE. Black traces correspond to electronic spectra of cold ions, while red and blue traces correspond to the UV spectra of DALLE following IR excitation. IR OPO wavenumber fixed at transitions marked with arrows of the corresponding color in figure 5.5: a) 3411.2 cm^{-1} and b) 3466.5 cm^{-1}.*

Figures 5.7 and 5.8 show IR-UV depletion spectra of DL-**A** in 3 and 6 μm spectral regions, respectively, each averaged over two scans. Depletion spectra allow identifying all vibrational transitions in the all-conformer gain spectrum (figure 5.5) that belong to the main conformer DL-**A**. Signal gain, observed in depletion spectrum of this conformer in 3 μm spectral region (figure 5.7), stems from the conformer DL-**B** (and from all other conformers, if any are present). Both spectra were recorded with UV laser wavenumber fixed at 35238.6 cm^{-1}, IR laser power was 1 mJ.

Figure 5.7. *Comparison of IR-UV gain (black trace) and depletion (red trace) spectra of the DALLE conformer DL-**A** in 3 μm spectral region.*

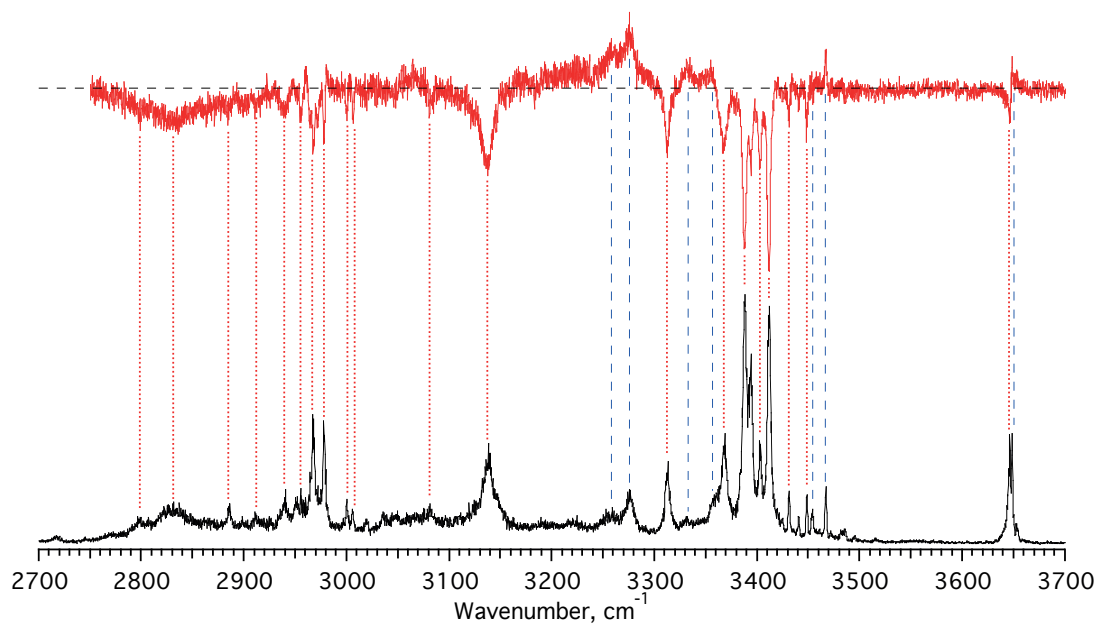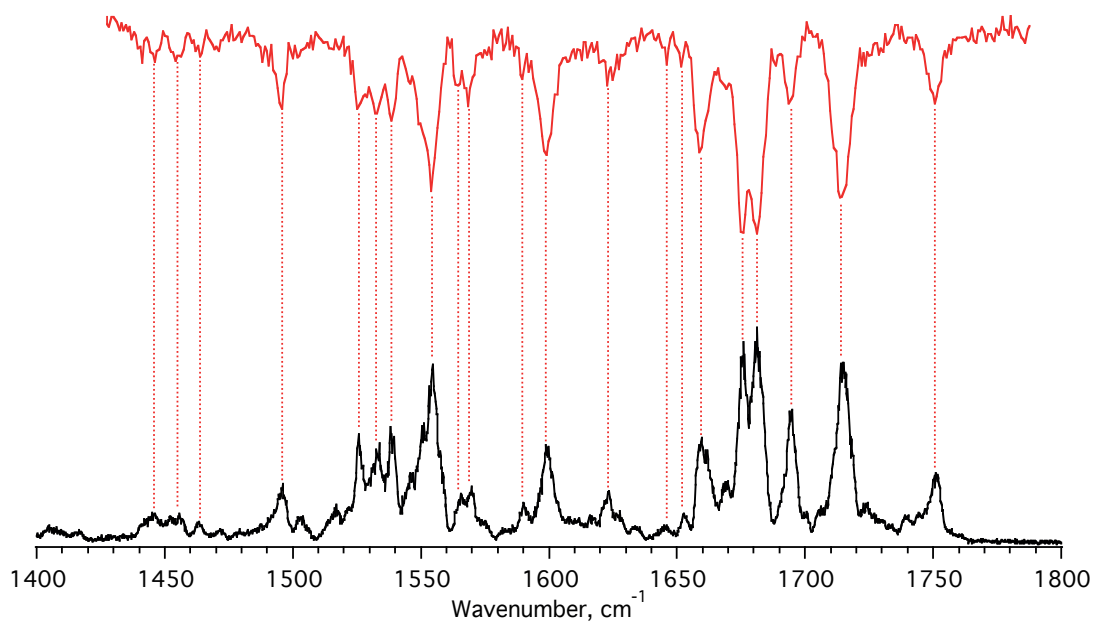***Figure 5.8.*** *Comparison of IR-UV gain (black trace) and depletion (red trace) spectra of the DALLE conformer DL-**A** in 6 μm spectral region.*

Transitions in all-conformer gain spectrum that do not appear in depletion spectrum of conformer DL-**A** (marked with red vertical dashed lines in figure 5.7) might belong to more than one conformer. Since the band origin of the conformer DL-**B** is not vibrationally resolved, it is impossible to apply IR-UV depletion spectroscopy to record conformer-specific vibrational spectrum of this conformer. As was discussed in Chapters 3 and 4, IR-IR-UV hole-burning spectroscopy can be used instead (figure 5.9). The blue and the red traces correspond to IR-UV gain and IR-IR-UV hole-burning spectra, recorded by monitoring the intensity of the tyrosine side-chain loss fragment (m/z = 449.3 Da). The black trace is generated as their difference and reflects all the vibrational transitions associated with the conformer DL-**B** (denoted by dashed vertical lines).
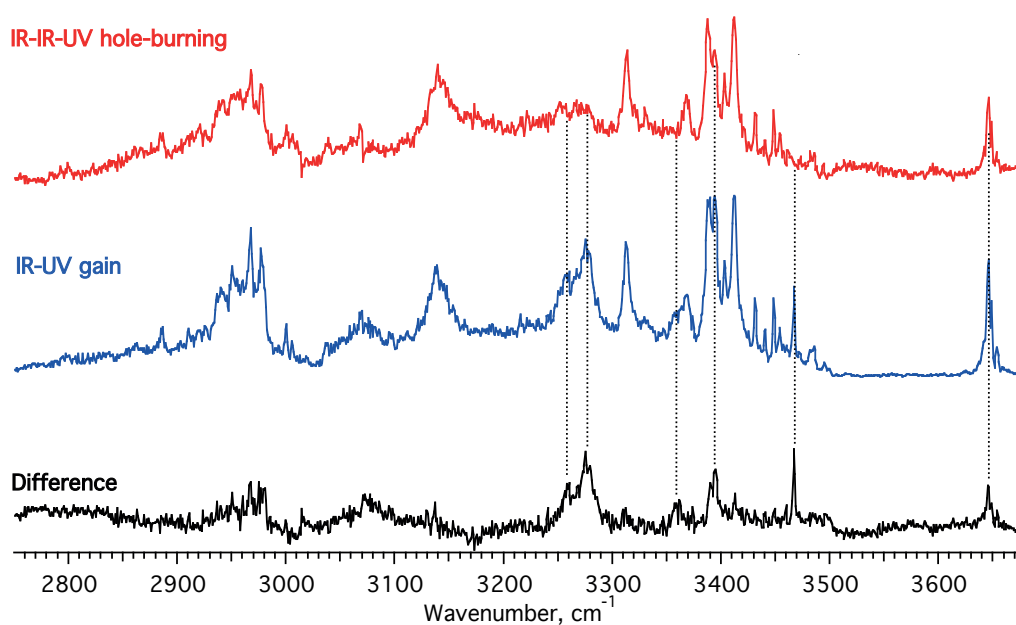

Figure 5.9. *IR-IR-UV hole-burning spectroscopy of DALLE. The blue and the red traces correspond to the IR-UV gain and IR-IR-UV hole-burning spectra of DALLE, measured with UV OPO wavenumber tuned to 35140 cm^{-1} and the Pump IR OPO wavenumber fixed at 3466.5 cm^{-1}. The Probe IR OPO scanning rate was 0.05 cm^{-1} per step, each data point is averaged over 40 measurements. The black trace is generated as their difference and corresponds to the conformer-specific vibrational spectrum of conformer DL-**B**. Vertical dashed lines denote conformer-specific vibrational transitions of this conformer.*

The vibrations that are unique for the conformer labeled by the pump IR laser can now be unambiguously assigned. All transitions in the gain spectrum belong to at least one of the

conformers identified previously with IR-UV hole-burning spectroscopy. It still remains challenging to identify transitions that belong to both conformers provided the small relative intensity of the conformers. However, the IR-IR-UV hole-burning spectroscopy is the only technique for unambiguous assignment of conformer-specific transitions of the conformer DL-**B**.

3. *Protonated [D-Ala², D-Leu⁵]-Enkephalin*

Figure 5.10 shows an IR-UV gain spectrum of DADLE. In contrast to the previous two isomers, LALLE and DALLE, the number of vibrational transitions observed for DADLE clearly indicates the presence of at least three highly abundant conformers in the gas-phase under the conditions of our experiment. Given the highly congested electronic spectrum of this stereoisomer[38] (black traces in figure 5.11), the use of IR-UV depletion spectroscopy is precluded and the IR-IR-UV hole-burning spectroscopy remains the only option for decomposing the all-conformer gain spectrum into separate conformer-specific ones.
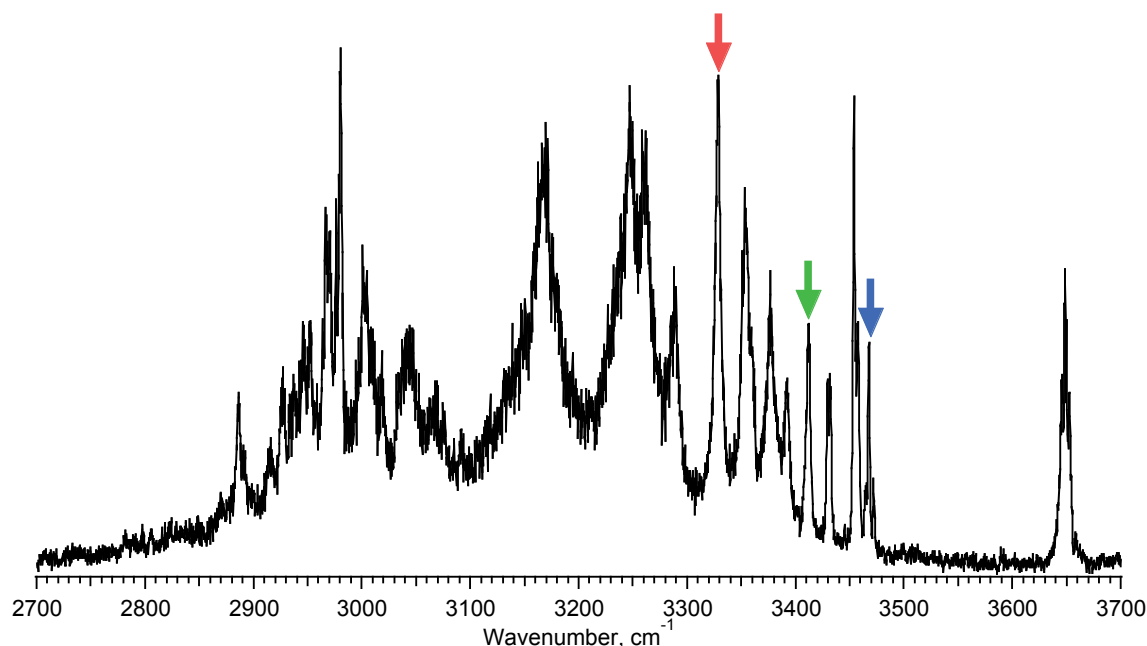
Figure 5.10. *IR-UV gain spectrum of DADLE, adopted from Kopysov.[54] Colored arrows mark transitions, used for IR-UV hole-burning experiments (see below).*

In order to apply IR-IR-UV hole-burning spectroscopy a well resolved and intense conformer-specific vibrational transitions are required. Figure 5.11 shows IR-UV hole-burning spectra recorded with IR OPO wavenumber subsequently tuned to several vibrational transitions (marked with colored arrows in figure 5.10), centered at 3329.2, 3412, and 3468.1 cm⁻¹. The IR-

133

UV hole-burning spectrum recorded with IR OPO wavelength fixed at 3329.2 cm^{-1} is clearly different from the ones two analogous spectra, whereas excitation of the other two transitions results in similar spectra of pre-heated ions because the band origins of the corresponding conformers are blue-shifted and overlap with the intense background. Nevertheless, a close analysis reveals certain differences. Conformer-specific electronic transitions, associated with 3412 and 3468.1 cm^{-1} excitation are marked with asterisks in the corresponding spectra. Therefore, at least three abundant conformers of DADLE are present in our experimental conditions. In the following analysis we adopt the following notation of DADLE conformers: the conformers associated with vibrational transitions at 3329.2, 3413, and 3468.1 cm^{-1} are called DD-**A**, DD-**B**, and DD-**C**, respectively. These transitions are conformer-specific, and can be used for an IR-IR-UV hole-burning spectroscopy.
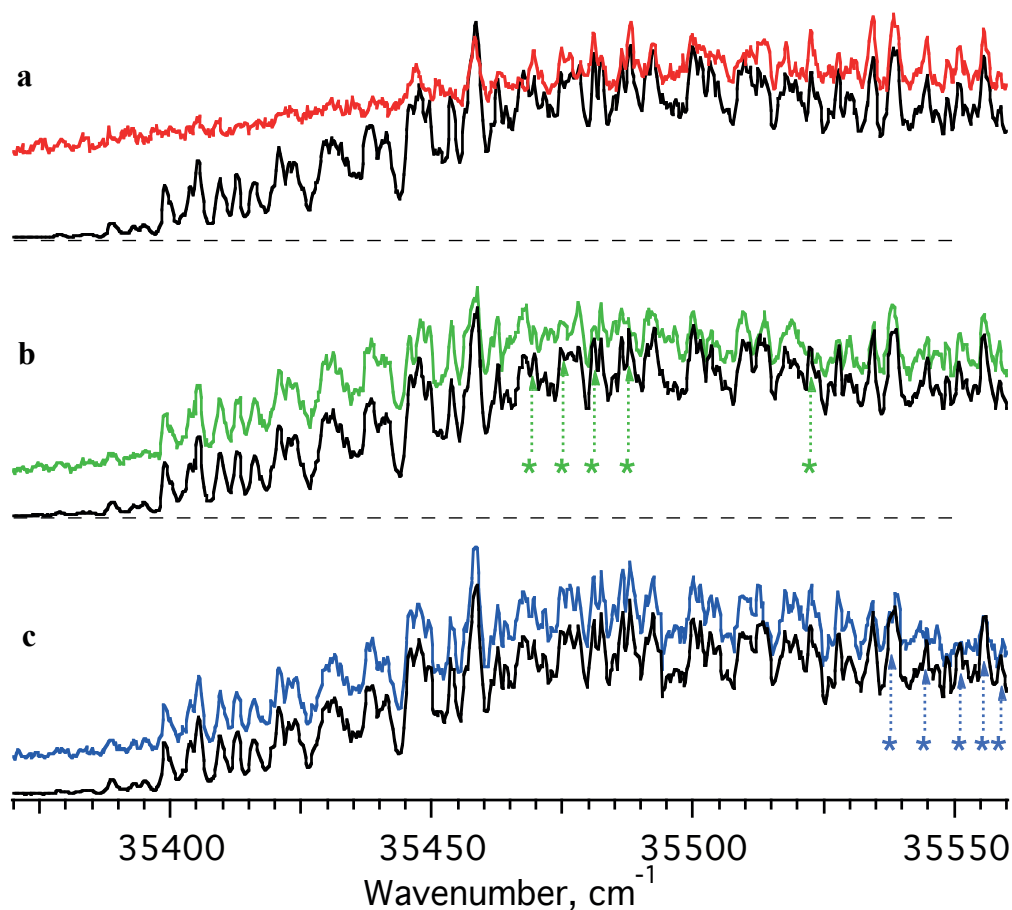

Figure 5.11. *IR-UV hole-burning spectroscopy of DADLE. Black traces are electronic spectra of cold DADLE, colored traces correspond to electronic spectra of IR pre-heated DADLE with IR OPO wavenumber fixed at a) 3329.2 cm^{-1}, b) 3413 cm^{-1}, and c) 3689.1 cm^{-1}. Asterisks mark conformer-specific electronic transitions for each conformer.*

Figures 5.12-14 show the IR-IR-UV hole-burning spectra of DADLE conformers DD-**A**, DD-**B**, and DD-**C**, respectively. The blue and the red traces correspond to the IR-UV gain and IR-IR-UV hole-burning spectra, respectively, while the black trace is generated as their difference. The UV laser wavenumber in all experiments was fixed at 35370 cm^{-1}.

In contrast to the conformer-selective spectroscopy of the protonated amino acids tryptophan[59] and histidine, the IR-UV gain spectrum of DADLE is far more congested. It is thus important to keep the probe IR laser power constant. The 3 μm spectral region was split into several parts and probe IR laser power was manually adjusted in each of them. The spectra were recorded separately in each part and were combined as follows: the probe IR – UV gain signal was scaled to match different parts: $S'_{IR-UV} = \alpha * S_{IR-UV}$. The IR-IR-UV hole-burning signal consists of the constant background, S_{BG}, independent of the probe IR laser power, and gain from all other conformers, S_{gain}: $S_{HB} = S_{BG} + S_{gain}$. Thus, the IR-IR-UV signal was scaled according to the following procedure: $S'_{HB} = \alpha * S_{HB} + S_{BG} \cdot (1 - \alpha)$.

Figure 5.12. *IR-IR-UV hole-burning spectroscopy of DADLE, measured with the pump IR OPO wavenumber fixed at 3329.2 cm^{-1} (DD-**A**). Vertical dashed lines denote conformer-specific vibrational transitions of this conformer.*

Figure 5.13. *IR-IR-UV hole-burning spectroscopy of DADLE, measured with the pump IR OPO wavenumber fixed at 3413 cm^{-1} (DD-**B**). Vertical dashed lines denote conformer-specific vibrational transitions of this conformer.*

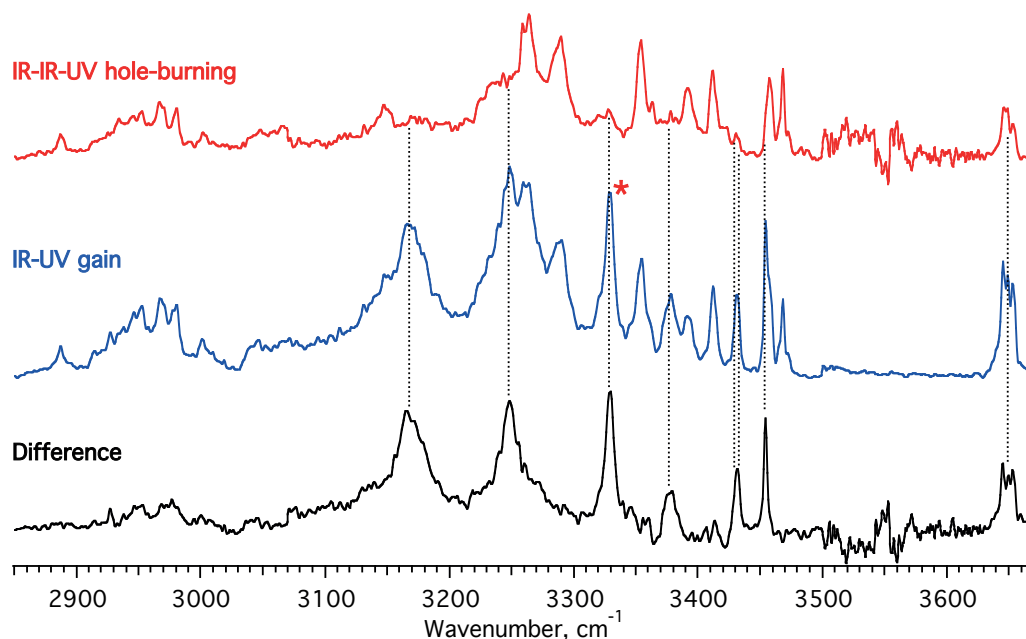***Figure 5.14.*** *IR-IR-UV hole-burning spectroscopy of DADLE, measured with the pump IR OPO wavenumber fixed at 3468.1 cm^{-1} (DD-**C**). Vertical dashed lines denote conformer-specific vibrational transitions of this conformer.*
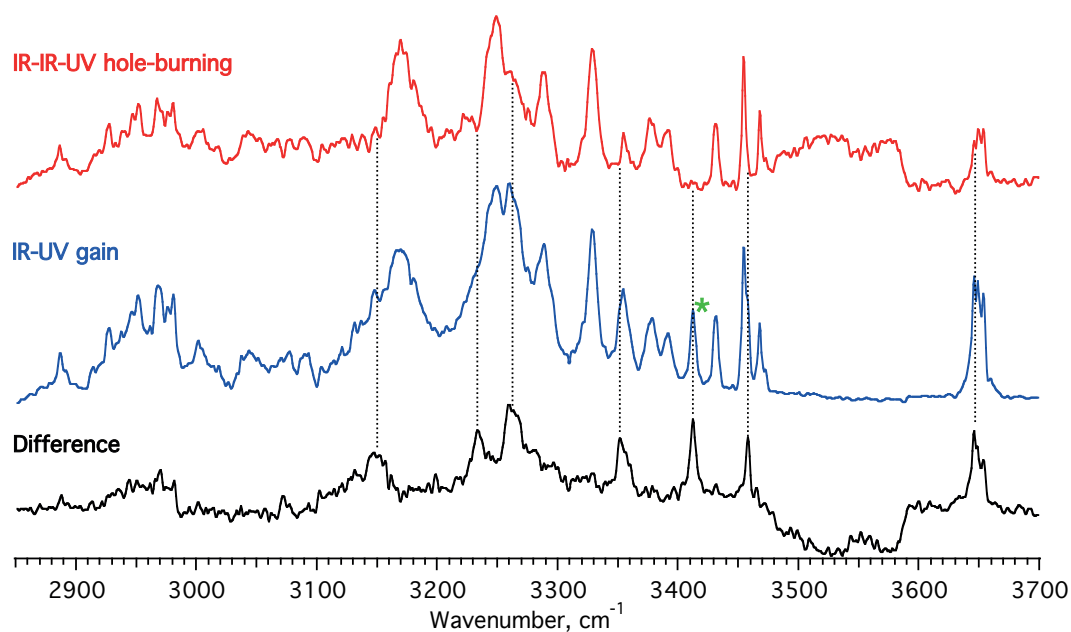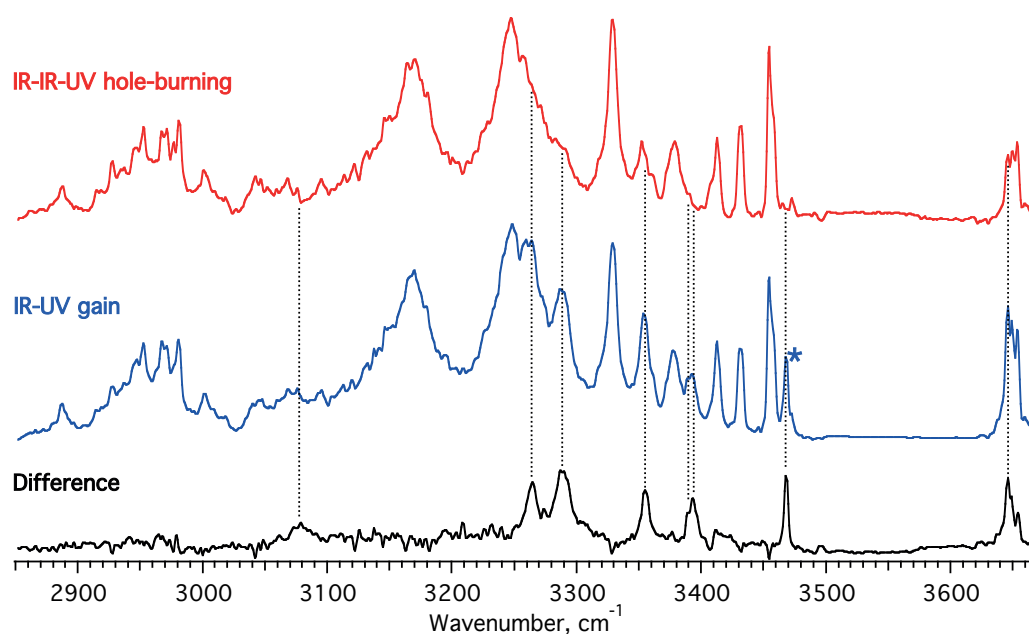
136

Figure 5.15 shows all three conformer-specific spectra and the total IR-UV gain spectrum of DADLE. All the main transitions in the IR-UV gain spectrum of DADLE do appear in one of the conformer-specific spectra, thus the presence of any other abundant conformer is unlikely. Based on the conformational assignment, eight conformer-specific transitions were identified for both conformers DD-**A** and DD-**C**, and only seven for conformer DD-**B**. Some of the transitions may belong to more than one conformer or might be difficult to assign due to their high width or low intensity and for more detailed assignment the comparison with calculations is required.
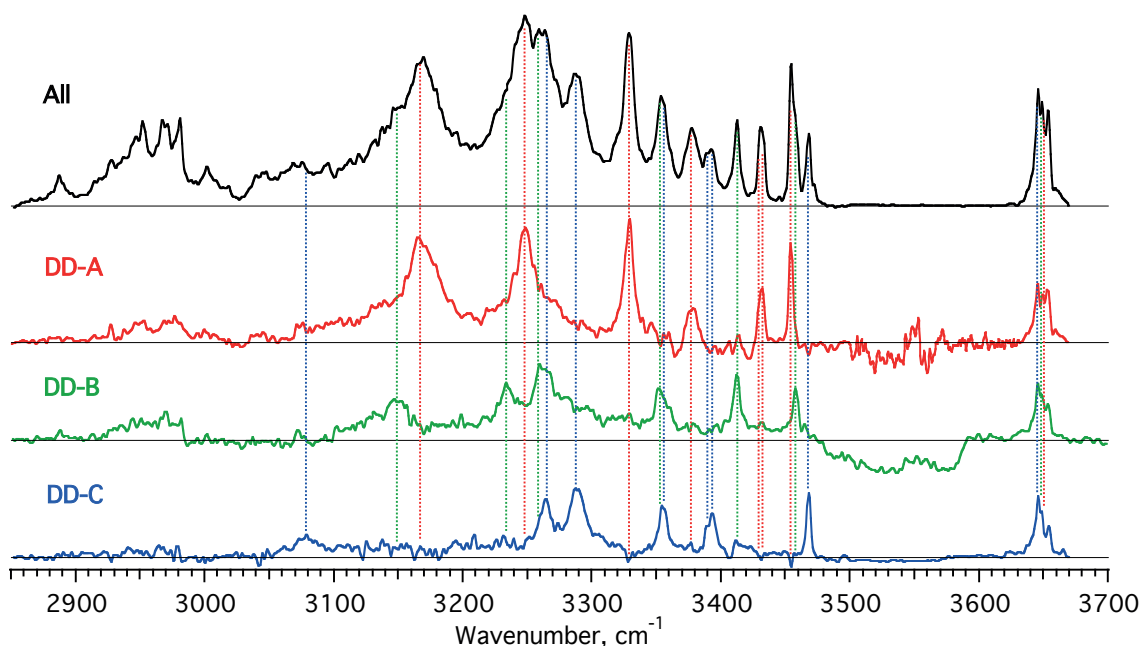
Figure 5.15. *Comparison of the IR-UV gain spectrum of DADLE (black trace) with conformer-specific vibrational spectra of its conformers DD-**A** (red trace), DD-**B** (green trace) and DD-**C** (blue trace). Color-coded vertical dashed lines denote the conformer, to which different transitions belong.*

To conclude the experimental part, one, two, and three conformers were identified and their conformer-specific vibrational spectra were recorded for LALLE, DALLE and DADLE, respectively. These spectra now can be used for validation of their structures and comparison of the distance between the two chromophores predicted from FRET and calculated in the validated structures.

5.2.3. Calculations

1. Methods

The structural calculations have been reported previously.[38, 54] Herein the main steps are briefly described and the calculated spectra are compared to the experimental ones obtained in the present work. A conformational search for the low-energy structures of singly protonated LALLE, DALLE, and DADLE peptides has been performed within the TINKER molecular modeling package[60] using the OPLS-AA/L force field.[61, 62] The search starts from the local minimization of an initial structure, which becomes the first local minimum in the search list. The normal mode activation step is performed for each structure from the search list and, whenever a previously unknown minimum is located, it is added to the search list, if its energy falls within a 10 kcal/mol window with respect to the lowest-energy structure. The convergence criterion for the local geometry minimization was set to 10^{-4} kcal/mol/Å.

Quantum chemical calculations were performed in three steps. First, all of the conformers of LALLE, DALLE, and DADLE within a 7.5 kcal/mol energy window (to sample structures from al conformational families) were optimized at the B3LYP/3-21G level with a convergence criterion 10^{-3} a.u. for the largest component of the nuclear gradient. Thus, after the first step one obtains more or less reliable geometries of 123, 781 and 873 conformers of LALLE, DALLE and DADLE, respectively, and their relative energies, which are, however, still not accurate enough. At the next step a portion of these structures within a 7.5 kcal/mol energy window was re-optimized at the B3LYP-D/6-31G* level with a convergence criterion of 10^{-4} a.u., which resulted in 70, 44 and 62 final structures of LALLE, DALLE and DADLE, respectively. This level of theory should be sufficient to adequately describe peptide geometries and predict the relative energies of conformers with an error not exceeding 1 kcal/mol.[63-66] Therefore, only the conformers within a 1 kcal/mol energy window were finally optimized at the B3LYP-D/6-31+G** level of theory with a convergence criterion of 10^{-5} a.u. All the quantum chemical calculations were performed using the Firefly software package[67].

2. General Notes Before Validating the Structures

The basic assumptions that justify the interest in the present study are summarized below:

- for short peptides without proline amino acid the kinetic trapping is unlikely, therefore intrinsic structures do not resemble the ones in solution;

- all conformers, observed in the gas phase, result from the quick, non-adiabatic cooling of an ion ensemble at initial temperature below 600 K, therefore their energies are within 3 kcal/mol window (see section 3.4.3);

- the intrinsic structure of peptides, biologically active in hydrophobic environment, are likely to be similar to their native geometries.

Therefore, the lowest-energy intrinsic structures should correspond to the major conformer in the gas phase. Note, that the terms "major" and "minor" referred to a conformer are used to account for relative intensity of either electronic or vibrational transitions, specific for the particular structure, rather than the actual relative population of ions. Intensities of optical transitions in action spectroscopy and relative populations, though, are not directly related for several possible reasons, e.g., conformer-specific fragmentation yield. Furthermore, because electronic spectra are congested, the intensities of vibrational transitions in the gain spectra are used to assess the relative populations. However, intensity of the UV spectrum of IR-preheated ions is a non-uniform function of UV wavelength (see, for example, figures 5.3, 5.6 and 5.11). Therefore, UV wavelength-dependence of IR-UV gain spectroscopy (namely, the offset from the band origins) may not allow for an unambiguous assignment of the most intense vibrational transitions to the most populated lowest-energy conformer.

3. *Validation of the Calculated Intrinsic Structures*

Figure 5.16 shows the lowest-energy conformers of LALLE, DALLE, and DADLE, respectively. These structures are suggested to have the highest population in the gas-phase and their structures are determined by intramolecular interactions without the influence of the solvent, similarly to the hydrophobic environment.

Figure 5.17 shows the vibrational spectra of all conformers, found herein. The calculated vibrational spectra of the lowest energy structures are shown as vertical red lines and are overlapped with the best-matching experimental spectrum of the corresponding stereoisomer.

As can be seen from figure 5.17, the calculated vibrational spectra match well one of the conformer-specific spectra for each stereoisomer. Only one conformer of LALLE was detected and its structure has been assigned. In cases DALLE and DADLE the lowest-energy geometries correspond to the conformers, which electronic spectra are the most blue-shifted, therefore the relative input of these conformers in the IR-UV gain spectra might be underestimated.

139

LL, R_{FY}=11.62 Å

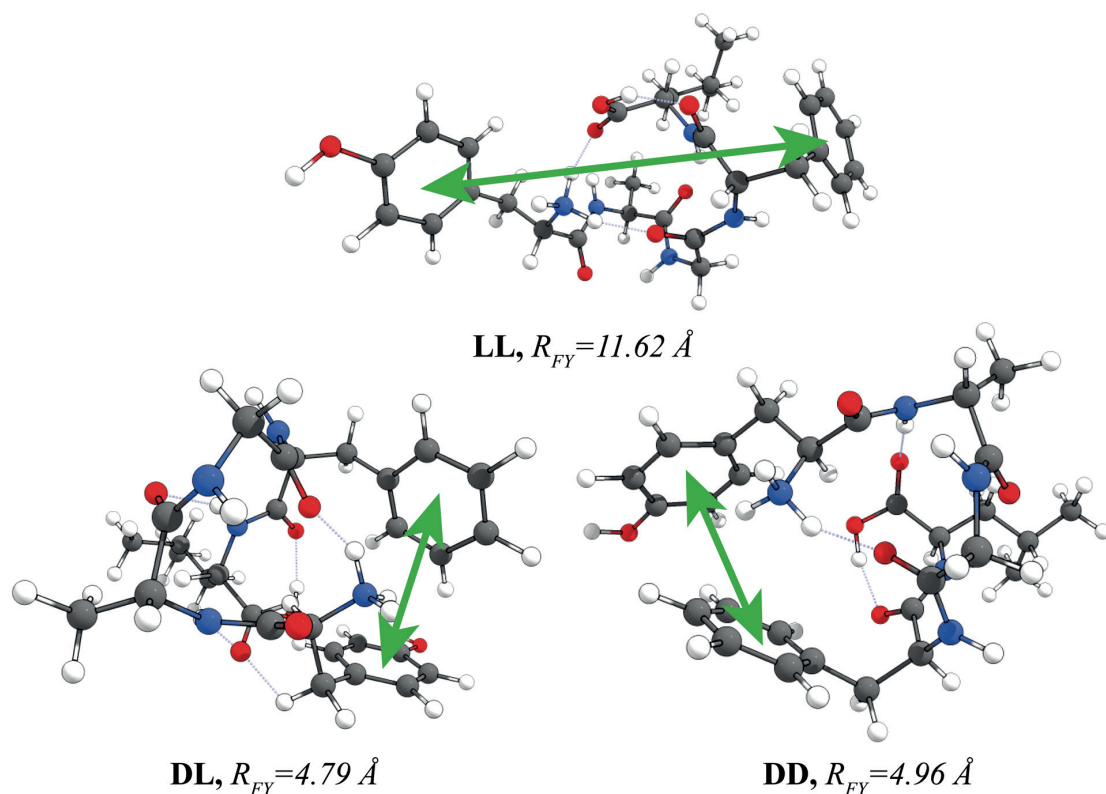**DL,** R_{FY}=4.79 Å   **DD,** R_{FY}=4.96 Å

Figure 5.16. *Structures of the lowest-energy conformers of [Ala^2, Leu^5]-enkephalin stereoisomers.*
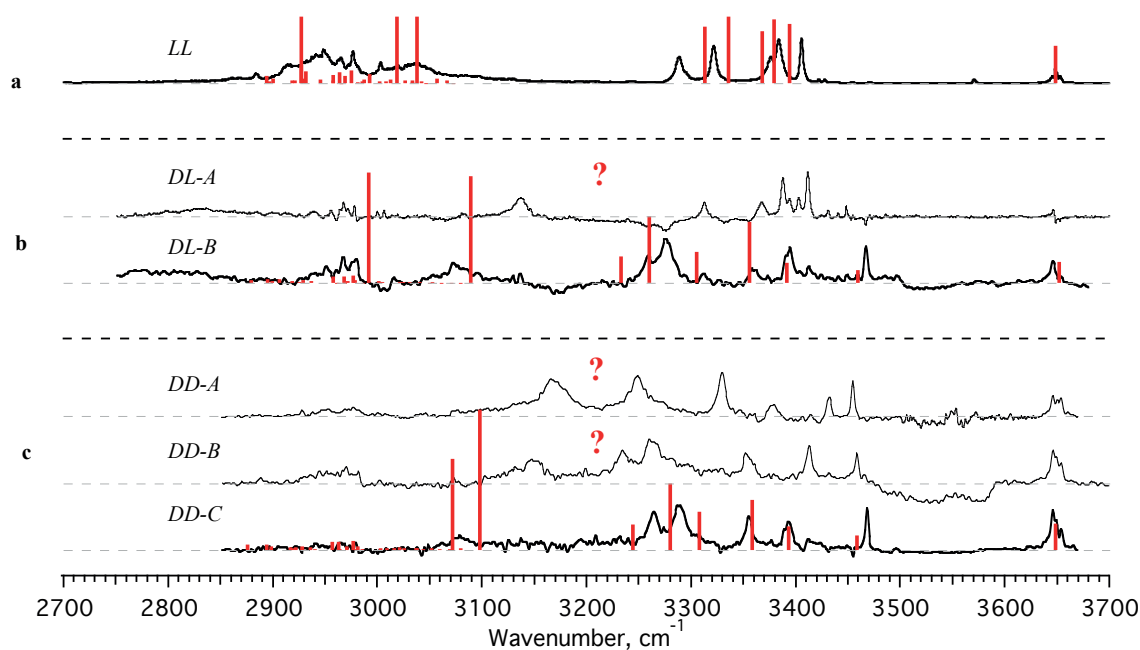

Figure 5.17. *Comparison of experimental conformer-specific vibrational spectra with ones calculated for the lowest-energy structures (figure 5.16).*

Only the spectra of structures with relative energies within 1 kcal/mol window were calculated (3-5 structures for each stereoisomer). As was discussed before, this might not be enough to find all gas-phase structures, present in the gas-phase. Therefore, the origin and structural properties of higher-energy conformers of DALLE and DADLE remain unclear and require further computational effort.

5.2.4. Correlation between CIS and FRET

The distances between chromophores in the validated lowest-energy structure of LALLE and presumably lowest-energy structure of DADLE are indeed in a good agreement with FRET experiments. For LALLE FRET predicted an average distance $R_{LL} = 10.6 \pm 0.7$ Å,[38] while the calculated structure has the distance 11.62 Å. An average distance between DADLE structures yields $R_{DD} = 5.7 \pm 1$ Å,[38] while in the theoretically calculated geometry this distance is 4.96 Å.

In contrast, The DALLE isomer was predicted to have three distinct conformational families with $R = 9.6$, 10.4 and 11.2 Å, similar to LALLE. Experimental data, provided herein, show that this stereoisomer has the structure, which resembles more the one of DADLE, rather than LALLE. However, given some ambiguity in assignment of the found DALLE structure to the most abundant conformer, elucidating all structures of this stereoisomer in the gas-phase could explain the observed discrepancy. Another evidence, supporting the assignment of DL-**B** to the major conformer, is that both distances between chromophore rings and positions of the band origins are very similar.

5.2.5. Summary

We have applied IR-UV gain, depletion, hole-burning, and IR-IR-UV hole-burning cold on spectroscopic techniques to obtain conformer-specific vibrational spectra of all highly-abundant intrinsic conformers of three stereoisomers of the opioid peptide Leu-Enkephalin analogues. They allow for a direct comparison of the previously calculated harmonic vibrational spectra to the experimental ones. For each stereoisomer one structure was identified within the 1 kcal/mol energy range. The verified structures are the lowest-energy ones, which is consistent with previous considerations regarding the fast, non-adiabatic collisional cooling of the thermalized ion ensemble. The inconsistency between the relative populations of the lowest and higher-energy conformers estimated from the relative intensities of IR transitions in the all-conformer IR-UV gain spectrum is explained by the different energy gap between the band origins of each conformer and the UV excitation energy, used in these experiments.

The distances between the Tyr and Phe aromatic rings were calculated for each validated structure. They are in a good agreement with the expected properties of these biological molecules estimated from the gas-phase FRET measurements, especially in cases of LALLE and DADLE. This observation implies that the gas-phase FRET is, indeed, a useful experimental technique for finding structural constraints. The interchromophore distances of LALLE and DADLE show also a reasonable match with the efficiencies of these peptide drugs *in vivo*. So far, enough evidence has been collected indicating that the vacuum and hydrophobic environments induce similar structural motifs in these short linear peptides.

The next step for a more stringent validation of this suggestion is comparing directly the identified intrinsic structures with the ones found in native conditions, which, however, have not been reported so far.

5.3. Cold Ion Spectroscopy of Neurokinin A

In the following section we investigate a doubly protonated neurokinin A (NKA) using IR-UV double resonance cold ion spectroscopy and find only five conformers of this decapeptide in the gas phase. In hydrophobic micelles NKA also adopts a few well-defined structures. In contrast, NMR data show that in aqueous solutions, NKA exhibits high conformational heterogeneity. Do the gas-phase structures of NKA resemble the native structures in a hydrophobic environment? The IR spectra, reported herein, allow for the validation of future structural calculations that may answer this question.

5.3.1. Introduction

The three-dimensional (3D) structure of a decapeptide neurokinin A (NKA) in dodecylphosphocholine (DPC) micelles has been solved by NMR (figure 5.18).[68] In this hydrophobic environment, which mimics the lipid bilayer, NKA adopts biologically relevant structural motif typical for the receptor-selective agonists.[69] NKA (HKTDSFVGLM-NH$_2$) belongs to the tachykinin family of neuropeptides, distributed in the central and peripheral nervous systems. NKA and its N-terminally extended mutants have been identified as very potent bronchoconstrictors[70] and have been implicated as important mediators of inflammatory lung disorders, such as asthma.[71] There is, therefore, a considerable interest in the structures of these peptides, which are potential targets for drug design, especially in the development of novel antiasthmatics.

Tachykinin peptides are characterized by a common C-terminal sequence, Phe-X-Gly-Leu-Met-NH2, where X represents either an aromatic (Phe, Tyr) or a branched aliphatic (Val, Ile) amino acid (figure 5.18). The C-terminal region, the message domain, is considered to be responsible for activating the receptor. The divergent N-terminal region, the address domain, varies in amino acid sequence and length and is postulated to play a key role in determining the receptor subtype specificity.[72] The wide range of physiological activity of tachykinins has been attributed to the conformational flexibility of these short, linear peptides.[73] There are no discernible trends in the conformation of the N-terminal address domains of these peptides. However, the C-terminal message domains are similar in each case. In general, the message domain undergoes conformational averaging in aqueous environments,[74, 75] while in a hydrophobic environment the message domain assumes helical conformations[72, 74, 76-78] or exists as a series of turns in dynamic equilibrium.[75]
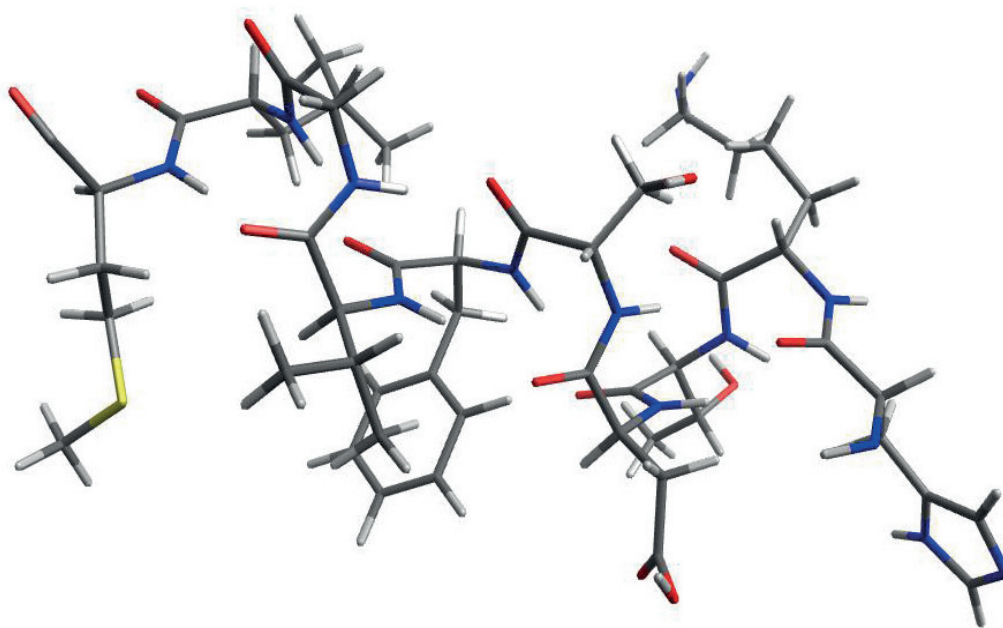
Figure 5.18. Structure of NKA in DPC micelles determined by NMR spectroscopy (PDB ID 1N6T).[68] The pH=5 of the aqueous solution is identical to that in our experiments, in which almost all the peptides are doubly protonated. Note, that the two protons, which are bound to the micelles, and the C-terminal amine group are not shown in the figure.

As the first step towards solving the gas-phase structure of this ligand, herein is reported UV and IR spectroscopy of cold doubly protonated NKA^{2+}. Three types of IR-UV double resonance

spectroscopy were employed to identify all of the highly abundant conformers of NKA^{2+} that are present under our experimental conditions and to assign their individual vibrational fingerprints.

5.3.2. Experimental results

1. Photofragmentation Mass Spectrum of NKA^{2+}

Figure 5.19 shows a UV photofragmentation mass spectrum for NKA^{2+} (m/z=567.7 Th). UV laser wavenumber is fixed at 37431 cm^{-1}. The lightest of the detected fragments corresponds to the side chain loss of the Phe residue, which is a well-known prompt fragmentation channel specific to the electronic excitation of aromatic amino acids.[79-83] The two most abundant fragments correspond to the loss of neutrals with the masses of 17, 18, and 45 Da, corresponding to the loss of NH_3 (ammonia) from the Lys side chain, H_2O loss from Asp or Ser side chains, and COOH loss from Asp side chain, respectively.[84] The peak near 552 Th might correspond to $[b_5 - NH_3]^{1+}$ or $[b_5 - H_2O]^{1+}$ fragment.
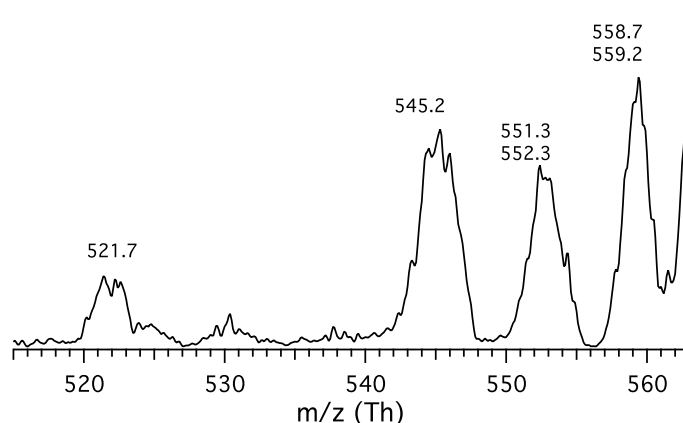
Figure 5.19. *UV-induced photofragmentation mass spectrum of doubly protonated $[NKA+2H]^{2+}$. The rising edge of the largely prevailing parent ion (m/z=567.7 Th) is visible on the right.*

2. UV Photofragmentation Spectroscopy of NKA^{2+}

Figures 5.20a and b show the UV photo fragmentation spectra of NKA^{2+}, measured for the ions electrosprayed from water and from methanol solutions, respectively. The spectra exhibit no noticeable difference, although there is a substantial structural difference of NKA in the two solvents, as revealed by NMR.[85] The observed identity of the spectra, measured for the gas-phase ions that originate from different solution structures, indicates that the intrinsic structure of NKA^{2+} must differ from its solution geometries.

144

The spectra exhibit several sharp vibronic transitions, some of which are baseline-resolved (or almost resolved). UV spectra are, usually, very sensitive to the finer geometry changes in molecules. The relatively low congestion in the UV spectra of a molecule as large as NKA suggests that under the conditions of our experiment the high number of conformers for this peptide is very unlikely.
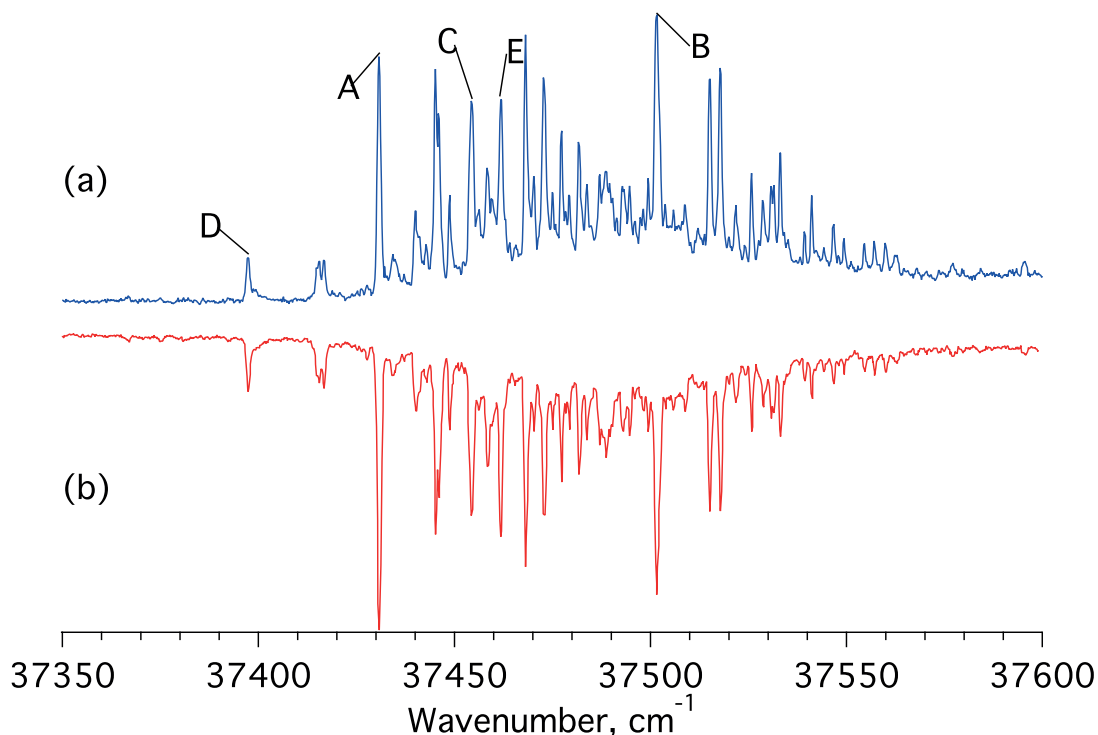
Figure 5.20. *UV photofragmentation spectra of doubly protonated NKA electrosprayed from (a) pure water and (b) pure methanol with 1% of acetic acid. The spectra were measured by detecting all fragments within the 540 to 556 Th window of m/z. The transitions, used for IR-UV depletion spectroscopy (see figure 5.21), are labeled by capital letters.*

3. IR-UV Double-Resonance Spectroscopy of NKA^{2+}

Observation of sharp peaks in the electronic spectrum of NKA^{2+} allows us to perform an IR-UV double resonance vibrational spectroscopy of this peptide. Figure 5.21a displays an IR gain spectrum of NKA^{2+}, measured with the UV laser tuned to the red from the UV band origin. The spectrum contains IR transitions of all the conformers that are highly abundant under the experimental cooling conditions (collisional cooling rate and trap temperature). Similar to the UV photofragmentation spectrum, the IR gain spectrum of NKA^{2+} also exhibits many vibrationally

resolved transitions. These two facts prompt us to conclude that NKA^{2+} in the gas phase does not exhibit the high conformational heterogeneity, observed for tachykinin peptides in aqueous solution by NMR and circular dichroism.[75, 85, 86]
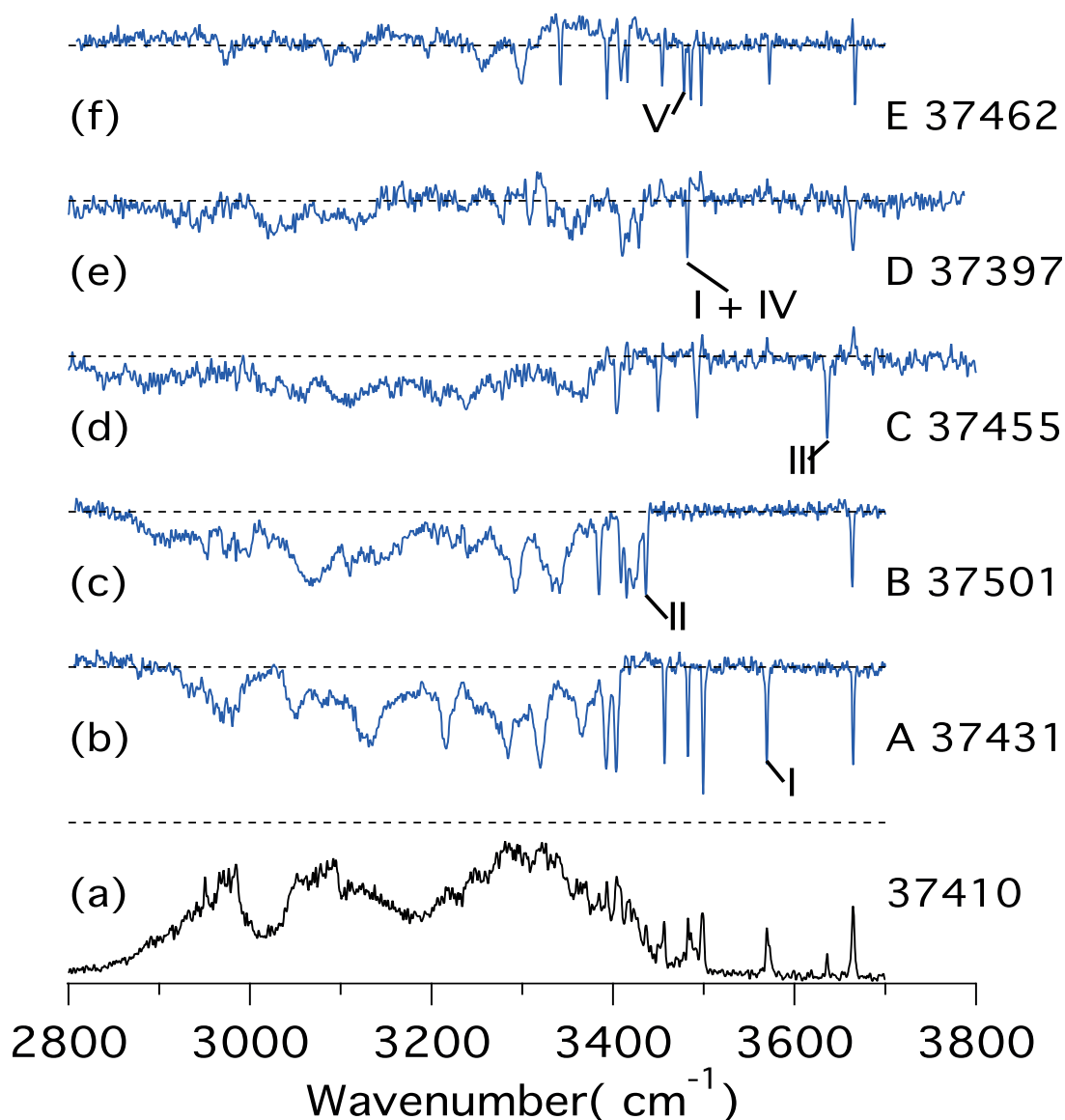
Figure 5.21. *(a) IR gain spectrum, measured as the increase of UV fragmentation yield as a function of IR OPO wavenumber. (b)-(f) IR depletion spectra measured at five different wavenumbers of the UV laser (shown in cm⁻¹ below the depletion traces); each data point of the spectra is generated as a ratio of the UV fragmentation yield measured with and without an IR OPO pulse. The spectra (b) to (f) belong to conformers I to V, respectively. The peaks, labeled by numbers I to V, were used in the hole-burning experiments (figures 5.22 and 5.23).*

Based on the available spectroscopic data for peptides, the three highest wavenumber peaks at 3664.5 cm^{-1}, 3637 cm^{-1}, and 3573 cm^{-1} can be tentatively assigned to the alcohol O-H stretches of either Thr or Ser residues or, else, to the carboxylic acid O-H stretch of Asp residue.[87]   The remaining sharp peaks, some of which stick out of the broad absorption bands, are largely due to the N-H stretch vibrations with possible contribution from hydrogen bound O-H stretches, although in this experiment they cannot be unambiguously assigned to specific residues. The broad absorption band centred at 3300 cm^{-1} is typical for overlapped N-H stretches with hydrogen atoms involved in non-covalent bindings. The two overlapped broad bands centred at 3100 cm^{-1} and 2950 cm^{-1} are, typically, due to the N-H stretch vibrations of protonated amide groups and C-H stretches, respectively.[59]

Figures 5.21b-f show five IR-UV depletion spectra of NKA^{2+}, measured with the UV laser tuned to five different sharp peaks labeled in figure 5.20 as A, B, C, D, and E, respectively. A close inspection of the depletion spectra reveals that they all differ in positions of well-resolved sharp peaks. This observation suggests a co-existence of five distinct conformers, whose IR spectra are distinguishable in the studied IR spectral range with ~2 cm^{-1} spectral resolution of our IR OPO. The fact that the five measured depletion spectra contain all major resolved peaks of the gain spectrum implies that these conformers are, likely, the only ones that are highly abundant under the conditions of our experiment. It still remains possible that some of the conformers are, actually, families of similar conformers, which cannot be distinguished by their IR spectra.

4. IR-UV Hole-Burning Spectroscopy of NKA^{2+}

To confirm our conformational identifications, we finally performed IR-UV hole-burning spectroscopy of NKA^{2+}. Figure 5.22 shows IR depletion spectra of five NKA^{2+} conformers in the 3400-3700 cm^{-1} spectral region, where vibrational transitions are well resolved. For each of the five conformers, except the conformer IV, we have chosen a unique vibrational transition, labeled in figure 5.22 with the corresponding numbers.   All well-resolved vibrational transitions of the conformer IV strongly overlap with transitions of other conformers. We, therefore, recorded the IR-UV hole-burning spectra of these conformers while exciting the transition that belongs to both conformers I and IV. Provided that we have already identified all of the UV peaks, associated with conformer I, we may assume that the additionally removed electronic transitions belong to the conformer IV. The corresponding hole-burning spectra are shown in figure 5.23.
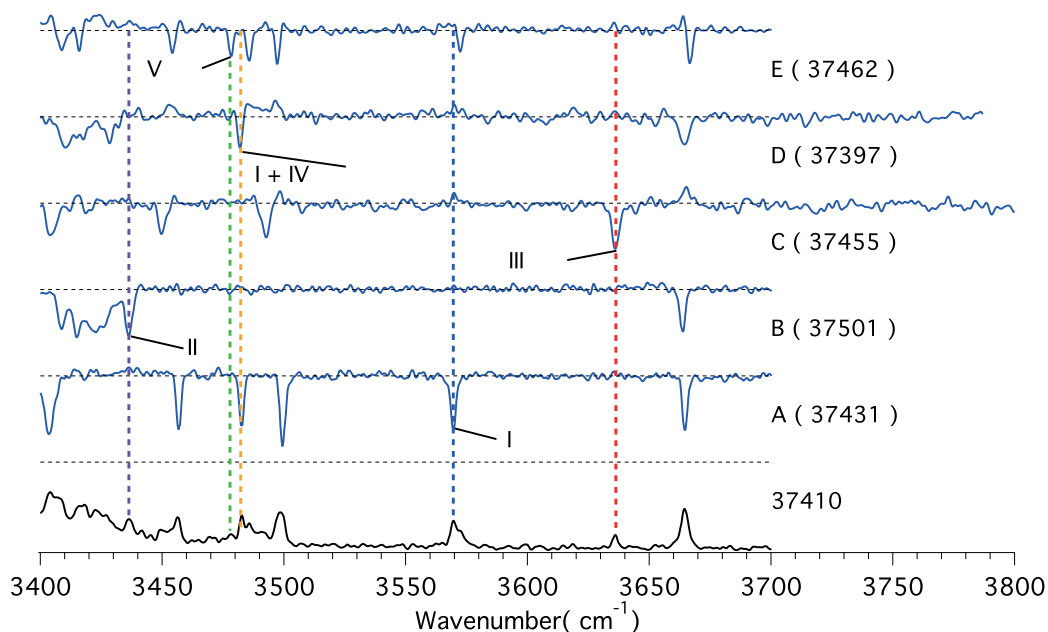
Figure 5.22. *Unique vibrational peaks of each conformer, used for IR-UV hole-burning spectroscopy.*
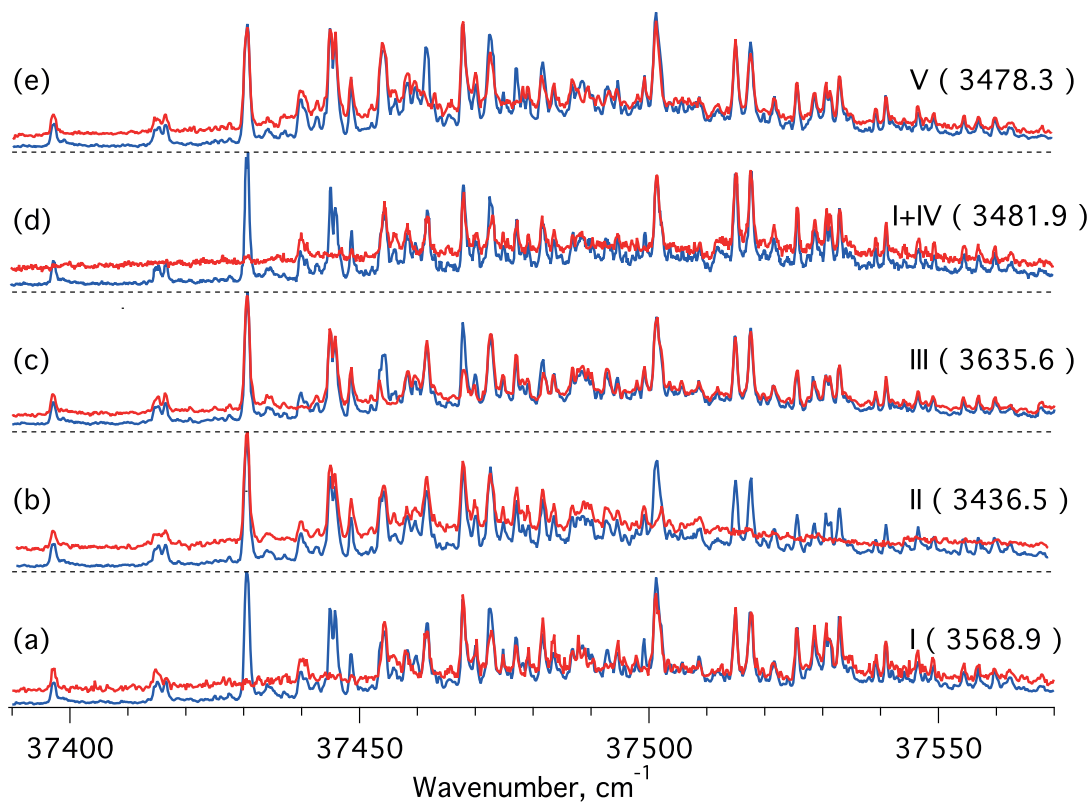
Figure 5.23. *IR-UV "hole-burning" spectra of NKA. (a)-(e) correspond to IR laser wavenumber fixed at vibrational transitions, marked I – V in figure 5.24, respectively.*

Figure 5.24 shows the resulting conformational assignment of the resolved UV transitions. Essentially, all sharp peaks in the spectrum have been assigned to one of the five conformers, identified by IR gain and depletion spectroscopy. The assignment confirms that, under the conditions of our experiment, NKA^{2+} populates only five substantially different conformational states, which differ in their IR spectra.
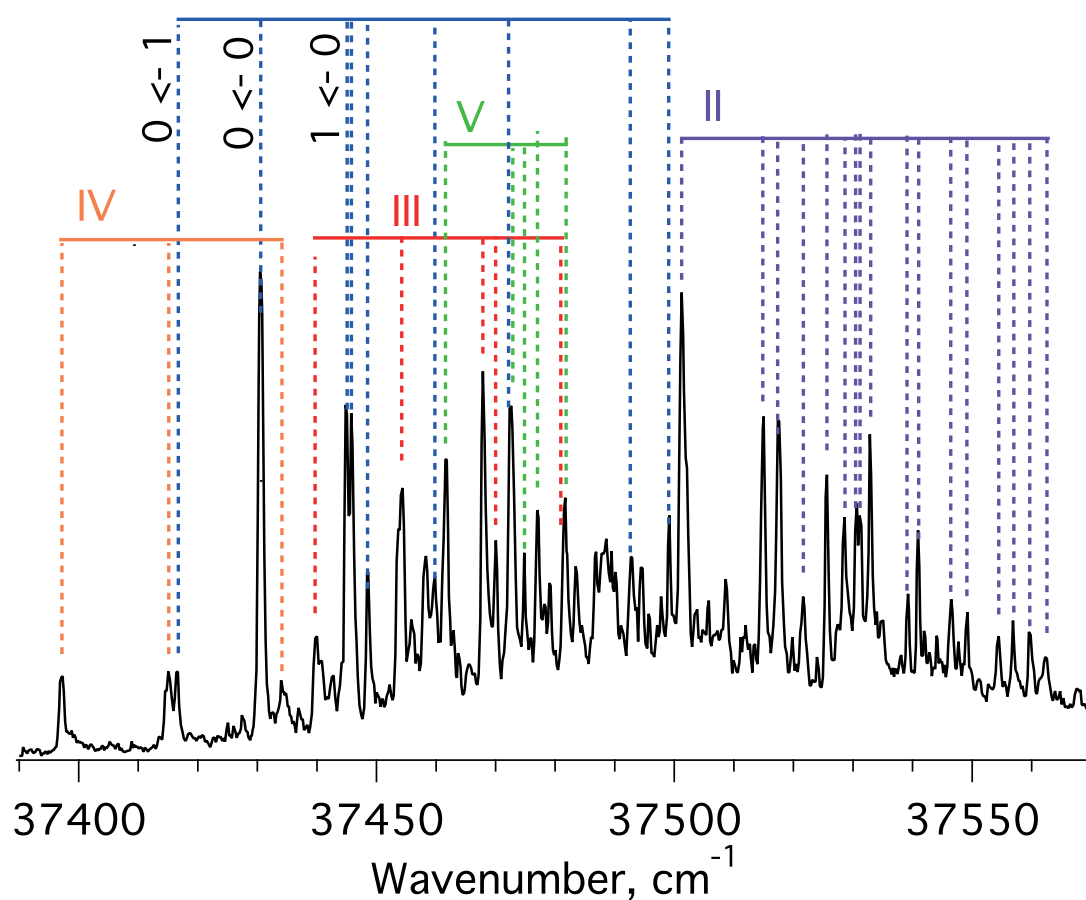
Figure 5.24. *Color-coded assignment of UV transitions in doubly protonated NKA to the detected conformers I-V. The assignment is based on IR-UV hole burning spectra (figure 5.23). The vibronic $S_1 \leftarrow S_0$ transitions of the 14.2 cm^{-1} progression in conformer I are labeled by vibrational quantum numbers.*

In general, one may expect a reduction of conformational heterogeneity upon desolvation of a peptide, which should be stabilized by additional intramolecular hydrogen bonds. For NKA, which contains an intrinsically disordered fragment, this reduction is, indeed, drastic. More rigid peptides may exhibit identical numbers of conformers in the gas phase and in solution, however.

Three gas-phase conformers were spectroscopically revealed, for instance, for doubly charged gramicidin S, which is a rigid cyclic peptide of the same size as NKA.[3, 4] The IR spectra of gramicidin S, which was complexed with up to 15 water molecules and cooled to $T = 12$ K remained vibrationally resolved, suggesting yet a low number of conformers in such microsolvated environment. The fact that NMR study was able to solve the structure of this peptide in aqueous solution implies a low number of (similar) conformers of this peptide *in vitro* even at room temperature.[88] Moreover, apart from minor details, the solution and the gas-phase structures of gramicidin S appeared identical. Our study provides evidence that this is not the case for NKA, for which we expect a resemblance of the gas-phase and the "hydrophobic" structures instead.

Our analysis of the UV spectra in figure 5.24 reveals a 14.2 cm^{-1} vibrational progression that belongs to the NKA^{2+} conformer I. We have used the intensities of the transitions in this progression to estimate the vibrational temperature of the cold peptides, T_{vib}, from the following expression:

$$T_{vib} \cong (1.435 \cdot v)/ ln \left(\frac{I_{1 \leftarrow 0}}{I_{0 \leftarrow 1}}\right)$$
(Eq. 5.1)

where v=14.2 cm^{-1} is the wavenumber of the progression, $I_{0 \leftarrow 1}$ and $I_{1 \leftarrow 0}$ are intensities of the hot band and the $1 \leftarrow 0$ vibronic transition in the observed progression, respectively. The equation (1) with the data in figure 5.24 gives $T_{vib} \sim$ 15 K.

5.3.4. Summary

We have employed gain, depletion, and hole-burning IR-UV double resonance techniques to identify all major conformers of doubly protonated peptide neurokinin A in the gas phase and to measure their vibrational spectra. This peptide ligand, which exhibits high conformational heterogeneity in aqueous and methanol solutions, becomes structurally determined when it performs its biological function by docking into the hydrophobic pocket of the NK2 receptor protein. Our spectra of NKA^{2+}, electrosprayed from water, water/methanol and pure methanol, suggest a low conformational heterogeneity of this peptide in the gas phase: we found only five highly abundant conformers of NKA under the cooling conditions of our experiment. This observation suggests that the gas phase structures are unlikely to resemble the structures of NKA in aqueous or methanol solutions. Whether the gas-phase geometries resemble or differ from the known "hydrophobic" one (figure 5.18), is a subject of the future structural calculations, which are challenging for molecules of this size. Finding structural similarities between the intrinsic and "in-micelles" geometries would support the proposed practical relevance of the gas-phase spectroscopy

to the characterization of "hydrophobically active" biomolecules and would allow assessment of its limitations. The conformer-selective IR spectra, measured herein, are now available for validation of calculated gas-phase structures of doubly protonated decapeptide neurokinin A.

5.4. Conclusions

The relevance of the gas-phase structures to the native ones *in vivo* remains still one of the main questions of structural biology. The structures of small biomolecular ions (i.e., amino acids) in the gas-phase are drastically different from the ones in solution, mainly because of the different charge state. Furthermore, removing the solvent shell from the peptidic ion would, most probably, change its conformation and the intrinsic structure will be determined only by intramolecular interactions.

Kinetic trapping is a holy grail of the gas-phase structural studies. If, following the transfer to the gas-phase, energy barrier between structures is higher compared to the internal energy of ions, there is a good chance to observe the structures that are far above the energy minimum in the gas phase. Such examples were demonstrated by ion mobility experiments for Pro-containing peptides. In most other cases observation of many conformers of peptide ions in the gas-phase is likely explained by a rapid non-adiabatic cooling.

Therefore, it was proposed that the peptides that are biologically active in hydrophobic environment have native structures that are formed in the absence of solvent and might resemble intrinsic ones. The data, provided in this study, suggests that this scenario is possible. Short opioid pentapeptides have intrinsic structures that correlate with their pharmacological activity *in vivo*. In addition, it was shown that a ten amino acid intrinsically disordered peptide in the gas phase is unlikely to resemble itself in aqueous solution. The firm answers to the important questions that were posed above require more effort, mostly computational, though the data provided herein allows unambiguous validation of the calculations.

References

1. T. R. Rizzo, J. A. Stearns and O. V. Boyarkin, *Int. Rev. Phys. Chem.*, 2009, **28**, 481-515.
2. T. R. Rizzo and O. V. Boyarkin, in *Gas-Phase IR Spectroscopy and Structure of Biological Molecules*, eds. A. M. Rijs and J. Oomens, Springer, 2015, vol. 364, pp. 43-98.

3.   N. S. Nagornova, M. Guglielmi, M. Doemer, I. Tavernelli, U. Rothlisberger, T. R. Rizzo and O. V. Boyarkin, *Angew. Chem. Int. Ed.*, 2011, **50**, 5383-5386.

4.   T. K. Roy, V. Kopysov, N. S. Nagornova, T. R. Rizzo, O. V. Boyarkin and R. B. Gerber, *ChemPhysChem*, 2015, **16**, 1374-1378.

5.   N. S. Nagornova, T. R. Rizzo and O. V. Boyarkin, *Angew. Chem. Int. Ed.*, 2013, **52**, 6002-6005.

6.   C. B. Braga and R. Rittner, *J. Phys. Chem. A*, 2017, **121**, 729-740.

7.   M. Yamashita and J. B. Fenn, *J. Phys. Chem.*, 1984, **88**, 4451-4459.

8.   C. M. Whitehouse, R. N. Dreyer, M. Yamashita and J. B. Fenn, *Anal. Chem.*, 1985, **57**, 675-679.

9.   J. B. Fenn, M. Mann, C. K. Meng, S. F. Wong and C. M. Whitehouse, *Mass Spectrom. Rev.*, 1990, **9**, 37-70.

10.   P. Kebarle and L. Tang, *Anal. Chem.*, 1993, **65**, 972A-986A.

11.   L. Konermann, E. Ahadi, A. D. Rodriguez and S. Vahidi, *Anal. Chem.*, 2013, **85**, 2-9.

12.   J. Li, C. Sanatmbrogio, S. Brocca, G. Roseti, P. Carloni and R. Grandori, *Mass Spectrom. Rev.*, 2016, **35**, 111-122.

13.   A. Konijnenberg, A. Butterer and F. Sobott, *Biochim. Biophys. Acta*, 2013, **1834**, 1239-1256.

14.   D. V. D. Spoel, E. G. Marklund, D. S. D. Larsson and C. Caleman, *Macromol. Biosc.*, 2011, **11**, 50-59.

15.   K. Breuker, S. Brüschweiler and M. Tollinger, *Angew. Chem. Int. Ed.*, 2011, **50**, 873-877.

16.   K. Breuker and F. W. McLafferty, *PNAS*, 2008, **105**, 18145-18152.

17.   M. F. Jarrold, *Acc. Chem. Res.*, 1999, **32**, 360-367.

18.   E. Jurneczko and P. E. Barran, *The Analyst*, 2011, **136**, 20-28.

19.   T. Wyttenbach and M. T. Bowers, *J. Phys. Chem. B*, 2011, **115**, 12266-12275.

20.   A. I. Gonzalez Florez, E. Mucha, D. S. Ahn, S. Gewinner, W. Schöllkopf, K. Pagel and G. Von Helden, *Angew. Chem. Int. Ed.*, 2016, **55**.

21.   K. Pagel, P. Kupser, F. Bierau, N. C. Polfer, J. D. Steill, J. Oomens, G. Meijer, B. Koksch and G. von Helden, *Int. J. Mass spectrom.*, 2009, **283**, 161-168.

22.   B. T. Ruotolo, G. F. Verbeck, L. M. Thomson, K. J. Gillig and D. H. Russell, *J. Am. Chem. Soc.*, 2002, **124**, 4214-4215.

23.   J. Li, J. A. Taraszka, A. E. Counterman and D. E. Clemmer, *Int. J. Mass spectrom.*, 1999, **185**, 37-47.

24.   J. A. Loo, J. X. He and W. L. Cody, *J. Am. Chem. Soc.*, 1998, **120**, 4542-4543.

25.   P. J. Wright, J. Zhang and D. J. Douglas, *J. Am. Soc. Mass. Spectrom.*, 2008, **19**, 1906-1913.

26.   H. Shi and D. E. Clemmer, *J. Phys. Chem. B*, 2014, **118**, 3498-3506.

27.   N. A. Pierson, S. J. Valentine and D. E. Clemmer, *J. Phys. Chem. B*, 2010, **114**, 7777-7783.

28.   H. Shi, N. Atlasevich, S. Merenbloom and D. E. Clemmer, *J. Am. Soc. Mass. Spectrom.*, 2014, **25**, 2000-2008.

29. L. Voronina, A. Masson, M. Z. Kamrath, F. Schubert, D. Clemmer, C. Baldauf and T. R. Rizzo, *J. Am. Chem. Soc.*, 2016, **138**, 9224-9233.

30. N. A. Pierson and D. E. Clemmer, *Int. J. Mass spectrom.*, 2015, **377**, 646-654.

31. S.-H. Chen and D. H. Russell, *J. Am. Soc. Mass. Spectrom.*, 2015, **26**, 1433-1443.

32. K. L. Fort, J. A. Silveira, N. A. Pierson, K. A. Servage, D. E. Clemmer and D. H. Russell, *J. Phys. Chem. B*, 2014, **118**, 14336-14344.

33. J. A. Silveira, K. L. Fort, D. Kim, K. A. Servage, N. A. Pierson, D. E. Clemmer and D. H. Russell, *J. Am. Chem. Soc.*, 2013, **135**, 19147-19153.

34. G. Papadopoulos, A. Svendsen, O. V. Boyarkin and T. R. Rizzo, *J. Am. Soc. Mass. Spectrom.*, 2012, **23**, 1173-1181.

35. N. S. Nagornova, T. R. Rizzo and O. V. Boyarkin, *Science*, 2012, **336**, 320-323.

36. B. G. Nielsen, M. Jensen and H. G. Bohr, *Biopolymers*, 2003, **71**, 577-592.

37. S. Granier, A. Manglik, A. C. Kruse, T. S. Kobilka, F. S. Thian, W. I. Weis and B. K. Kobilka, *Nature*, 2012, **485**, 400-404.

38. V. Kopysov and O. V. Boyarkin, *Angew. Chem. Int. Ed.*, 2016, **55**, 689-692.

39. J. A. Lord, A. A. Waterfield, J. Hughes and H. W. Kosterlitz, *Nature*, 1977, **267**, 495-499.

40. M. Waldhoer, S. E. Barlett and J. L. Whistler, *Annu. Rev. Biochem*, 2004, **73**, 953-990.

41. A. Janecka, J. Fichna and T. Janecki, *Curr. Top. Med. Chem.*, 2004, **4**, 1-17.

42. J. R. Deschamps, C. George and J. L. Flippen-Anderson, *Biopolymers*, 1996, **40**, 121-139.

43. J. R. Deschamps, J. L. Flippen-Anderson and C. George, *Biopolymers*, 2002, **66**, 287-293.

44. H. W. Kosterlitz, J. A. H. Lord, S. J. Paterson and A. A. Waterfield, *Br. J. Pharmacol.*, 1980, **68**, 333-342.

45. J. S. Morley, *Annu. Rev. Pharmacool. Toxicol.*, 1908, **20**, 81-110.

46. T. Förster, *Discuss. Faraday Soc.*, 1959, **27**, 7-17.

47. D. L. Dexter and J. H. Schulman, *J. Chem. Phys.*, 1954, **22**, 1063.

48. A. S. Danell and J. H. Parks, *Int. J. Mass spectrom.*, 2003, **229**, 35-45.

49. F. O. Talbot, A. Rullo, H. Yao and R. A. Jockusch, *J. Am. Chem. Soc.*, 2010, **132**, 16156-16164.

50. V. Frankevich, V. Chagovets, F. Widjaja, K. Barylyuk, Z. Yang and R. Zenobi, *PCCP*, 2014, **16**, 8911-8920.

51. S. Daly, F. Poussigue, A.-L. Simon, L. MacAleese, F. Bertorelle, F. Chirot, R. Antoine and P. Dugourd, *Anal. Chem.*, 2014, **86**, 8798–8804.

52. N. G. Hendricks, N. M. Lareau, S. M. Stow, J. A. McLean and R. R. Julian, *J. Am. Chem. Soc.*, 2014, **136**, 13363–13370.

53. A. Kulesza, S. Daly, L. MacAleese, R. Antoine and P. Dugourd, *J. Chem. Phys.*, 2015, **143**, 025101.

54. V. Kopysov, Docteur des Sciences, Ecole Polytechnique Fédérale de Lausanne, 2016.

55. T. Takekiyo, M. Kato and Y. Taniguchi, *J. Mol. Liq.*, 2005, **119**, 147-152.

56. N. L. Burke, J. G. Redwine, J. C. Dean, S. a. McLuckey and T. S. Zwier, *Int. J. Mass spectrom.*, 2015, **378**, 196-205.

57. J. Tennyson, P. F. Bernath, L. R. Brown, A. Campargue, A. G. Csa´sza´re, L. Daumontf, R. R. Gamacheg, J. T. Hodgesh, O. V. Naumenko, O. L. Polyansky, L. S. Rothman, A. C. Vandaele, N. F. Zobov, A. R. Al Derzi, C. Fa´brie, A. Z. Fazliev, T. Furtenbacher, I. E. Gordon, L. Lodi and I. I. Mizus, *J. Quant. Spectrosc. Radiat. Transfer*, 2013, **117**.

58. S. E. Stein, in *NIST Chemistry WebBook, NIST Standard Reference Database Number 69*, eds. P. J. Linstrom and W. G. Mallard, National Institute of Standards and Technology, Gaithersburg MD, 20899.

59. A. Y. Pereverzev, X. Cheng, N. S. Nagornova, D. L. Reese, R. P. Steele and O. V. Boyarkin, *J. Phys. Chem. A*, 2016, **120**, 5598-5608.

60. J. W. Ponder, *Journal*.

61. W. L. Jorgensen, D. S. Maxwell and J. Tirado-Rives, *J. Am. Chem. Soc.*, 1996, **118**, 11225-11236.

62. G. A. Kaminski, R. A. Friesner, J. Tirado-Rives and W. L. Jorgensen, *J. Phys. Chem. B*, 2001, **105**, 6474-6487.

63. H.-J. Lee, H.-M. Park and K.-B. Lee, *Journal of Theoretical and Computational Chemistry*, 2009, **8**, 799-811.

64. M. Elstner, K. J. Jalkanen, M. Knapp-Mohammady, T. Frauenheim and S. Suhai, *Chem. Phys.*, 2001, **263**, 203-219.

65. K. J. Jalkanen, *J. Phys.: Condens. Matter*, 2003, **15**, S1823-S1851.

66. K. J. Jalkanen, M. Elstner and S. Suhai, *Journal of Molecular Structure: THEOCHEM*, 2004, **675**, 61-77.

67. A. A. Granovsky, Firefly, Version 8.0.1. http://classic.chem.su/gran/firefly/index.html).

68. I. R. Chandrashekar and S. M. Cowsik, *Biophys. J.*, 2003, **85**, 4002-4011.

69. I. R. Chandrashekaran, G. S. Rao and S. M. Cowsik, *J. Chem. Inf. Model.*, 2009, **49**, 1734-1740.

70. J. E. Sherwood, P. J. Mauser and R. W. Chapman, *J. Pharmacol. Exp. Ther.*, 1997, **283**, 788-793.

71. G. F. Joos, P. R. Germonpré and R. A. Pauwels, *Clin. Exp. All.*, 2000, **30**, 60-65.

72. R. Schwyzer, *The EMBO Journal*, 1987, **6**, 2255-2259.

73. S. Nakanishi, *Ann. Rev. Neurosci.*, 1991, **14**, 123-136.

74. G. A. Wooley and C. M. Deber, *Biopolymers*, 1987, **26**, 109-121.

75. S. C. J. Sumner, K. S. Gallagher, D. G. Davis, D. G. Covell, R. L. Jernigan and J. A. Ferretti, *J. Biomol. Struct. Dyn.*, 1990, **8**, 687-707.

76. C.-S. C. Wu and Y. T. Yang, *Biochim. Biophys. Acta*, 1983, **746**, 72-80.

77. J. Horne, M. Sadek and D. J. Craik, *Biochemistry*, 1993, **32**, 7406-7412.

78. T. L. Whitehead, S. D. McNair, C. E. Hadden, J. K. Young and R. P. Hicks, *J. Med. Chem.*, 1988, **41**, 1497-1506.

79. H. Kang, C. Jouvet, C. Dedonder-Lardeux, S. Martenchard, G. Grégoire, C. Desfrancois, J.-P. Schermann, M. Barat and J. A. Fayeton, *PCCP*, 2005, **7**, 394-398.

80.   T. Tabarin, R. Antoine, M. Broyer and P. Dugourd, *Rapid Commun. Mass Spectrom.*, 2005, **19**, 2883-2892.

81.   J. A. Stearns, S. Mercier, C. Seaiby, M. Guidi, O. V. Boyarkin and T. R. Rizzo, *J. Am. Chem. Soc.*, 2007, **129**, 11814-11820.

82.   B. Lucas, M. Barat, J. A. Fayeton, M. Perot, C. Jouvet, G. Gregoire and S. B. Nielsen, *J. Chem. Phys.*, 2008, **128**, 164302.

83.   V. Kopysov, N. S. Nagomova and O. V. Boyarkin, *J. Am. Chem. Soc.*, 2014, **136**, 9288-9291.

84.   B. Paizs and S. Suhai, *Mass Spectrom. Rev.*, 2004, **24**, 508-548.

85.   G. Chassaing, O. Convert and S. Lavielle, 1986.

86.   G. Chassaing, O. Convert and S. Lavielle, *Eur. J. Biochem.*, 1986, **154**, 77-85.

87.   C. N. Stedwell, J. F. Galino, A. E. Roitberg and N. C. Polfer, *Ann. Rev. Anal. Chem.*, 2013, **6**, 267-285.

88.   Y. Xu, I. P. Sugar and N. R. Krishna, *J. Biomol. NMR*, 1995, **5**, 37-48.

Chapter 6

Collisional Cooling Efficiency

Vibrational energy relaxation via collisions of biomolecular ions with neutral molecules at low internal energies is a poorly studied field. In this chapter we apply cold ion spectroscopy to evaluate cooling dynamics of an ion ensemble, pre-heated with an IR laser pulse. Following an introduction section, an estimation of the ion-molecule collision rate in our trap is presented. Next, experimental approach is described and the obtained spectroscopic data are shown. Finally, quantitative estimations of the cooling efficiency are discussed.

6.1. Introduction

The relevance of the gas-phase studies for biology was discussed in previous chapter. The possibility to preserve some elements of the 3D structure of biomolecular ions after transferring them from solution to the gas phase allows one to study a bare object without the influence of the solvent and draw some conclusions about its structural features in condensed phase. Many biological ions were shown to adopt "kinetically trapped" conformations, relaxing to lower-energy states upon extensive activation.[1] Obviously, the relative populations of kinetically trapped conformations depend crucially on the cooling rate. Collisional cooling occurs on the timescales faster than conformational relaxation rates.[2, 3] Controlling the cooling rate allows one to switch from adiabatic to non-adiabatic cooling regimes and control isomerisation process. Therefore, the deeper understanding of the cooling constraints may shed more light on the kinetic trapping mechanism and relation between gas-phase and solution conformations of biomolecular ions.

Ion-molecules reactions at very low temperatures are also of fundamental interest because at total energies close to zero the reaction barriers are lower compared to neutral-neutral reactions and the outcome of a collision depends significantly on the excitation of even the lowest states of the reactants. Another consequence of low-energy collisions is that for systems even as large as a few

atoms, intermediates with very long lifetimes can be formed; this can lead to improbable processes such as tunnelling or radiative association.[4] Understanding the mechanisms that govern energy flow at low temperatures is crucial for gas-phase chemistry at low temperatures and may shed light on chemical reactions in space.[4, 5]

On the other hand, cooling in the cold gas bath allows vibrational resolution for cold ion spectroscopy, and even rotational resolution in small systems.[6] Collisional vibrational energy deactivation of biological ions, stored and cooled in multipole ion traps filled with cold buffer gas, quenches statistical fragmentation and, hence, increases the sensitivity of CIS.

The idea to use energy loss of ions to determine their physical properties was postulated more then 100 years ago by Niels Bohr.[7] However, the first application of this idea to biomolecular ions in the gas phase was described by Covey and Douglas in 1993,[8] who used simple elastic collision model to quantify an average translational energy loss and find collisional cross sections of protein ions.

The mechanism of the internal energy transfer in molecular collisions was published 80 years ago by Landau and Teller[9] and still remains the most basic theory of vibrational relaxation, known as Landau-Teller (LT) theory. It explained the reasons for the low rate of the vibrational-translational energy exchange in diatomic gases, which, among other effects, manifests itself in ultrasonic dispersion. LT theory determined the temperature dependence of vibrational state-to-state rate coefficients, set up kinetic equations for the population of molecular states, and provided the relaxation equation for the average vibrational energy of the molecular ensemble. The results of LT theory referred to collinear collisions. Besides, the model was restricted to situations when the vibrational quantum $\hbar\omega$ of the harmonic molecular oscillator was much smaller compared to k_BT.

Schwartz, Slawsky, and Herzfeld[10] were the first who attempted to relax the condition $\hbar\omega/k_BT \ll 1$. The ultimate result of their work is known as the SSH theory.[10, 11] The LT theory has experienced several other generalizations and extensions. The review on its revolution can be found in ref [11].

The LT theory predicts that the probability of the energy transfer to or from a harmonic oscillator of a level v per collision, P_v, is represented by $P_v \propto v \cdot exp(-c|\Delta E_v|)$, where $|\Delta E_v|$ is the vibrational energy transferred from a target molecule to the relative translational motion between the two molecules and c is a constant. Experimental results on collisional deactivation of vibrationally excited diatomic molecules perfectly fit to this model.[12]

Regarding the polyatomic molecules, the statistical treatment was developed to model the evolution of the energy distribution function.[13] Forst and Bhattacharjee developed predictive *ab initio* model for vibrational energy transfer in ion-molecule collisions, based on the energy redistribution during short-lived ion-molecule complex.[14, 15] These models were applied to evaluate energy transfer in highly excited polyatomics.[16-18]

In the present work we studied vibrational energy deactivation of biomolecular ions as large as a decapeptide. Herein, we study energy transfer from vibrationally excited polyatomic ion and suggest several spectroscopic probes to do so. First of all, we estimate the average time between two subsequent ion-atom collisions in our ion trap. Next, we describe the experimental approach, in which the ions are prepared in a well-defined energetic state and their cooling dynamics is monitored. This allows determining the time required to relax the known vibrational energy of ions. Together with the estimated time between collisions, this allows for a rough estimate of the average energy taken away per collision. Though the theoretical model that would fit the experimental data has not yet been found, the simple statistical models are discussed herein.

6.2. Average Time Between Subsequent Ion-Neutral Collisions

The collisional deactivation speed depends on the collision frequency and the average energy, transferred from warm ions to cold He atoms per collision. The latter is a function of the internal energy of an ion and various forms of this dependence will be discussed (see Section 6.4). In this section, an average time between two subsequent collisions of ion and buffer gas atoms is estimated.

6.2.1. Collision Rate of the Trapped Ions with the Buffer Gas Atoms

The ions and buffer gas atoms in the trap can be considered as a mixture of two gases with concentrations n_1 and n_2, radii r_1 and r_2, and mean velocities $\overline{v_1}$ and $\overline{v_2}$. Kinetic theory of gases predicts the following expressions for collision rates z_i ($i, j = 1,2; j \neq i$) for each gas (taking into account Maxwell distribution of velocities)[19]:

$$z_i = \left(n_i \sigma_{ii} \sqrt{2} + n_j \sigma_{ij} \sqrt{1 + \frac{m_i}{m_j}} \right) \overline{v_i} \qquad \text{(Eq. 6.1)}$$

where $\sigma_{ij} = \pi \left(r_i + r_j \right)^2$ and $\sigma_{ij} \equiv \sigma_{ji}$ are the collisional cross-sections. In the following analysis all quantities related to biomolecular ions and buffer gas atoms are denoted by indexes 1 and 2, respectively.

The first term in eq. 6.1 describes the collision rate of particles of the same gas, while the second term stands for the collisions of particles of different gases. Since the concentration of ions in the trap is negligible compared to the one of the buffer gas, we can neglect interaction of ions with each other. Furthermore, typical biomolecular ions are much larger compared to the buffer gas atoms in terms of both mass and size (here, for example, we study doubly-protonated gramicidin S ions (M = 1141 g/mole, $\sigma_{CCS} \approx 300$ Å^2) and He buffer gas (M = 4 g/mole, r = 6.3 Å^2)), we thus can assume $m_1 \gg m_2$, $r_1 \gg r_2$, and $n_1 \ll n_2$. Therefore, equation 6.1 reduces to the following expression:

$$z_1 = n_2 \pi r_1{}^2 \sqrt{\frac{m_1}{m_2}} \overline{v_1} \qquad \text{(Eq. 6.2)}$$

where $\pi r_1{}^2 = \sigma_{CCS}$ is a collisional cross section of the ion. Finally, since at the thermal equilibrium $\sqrt{\frac{m_1}{m_2}} \overline{v_1} = \overline{v_2}$, the collision rate of the trapped ions with He buffer gas is:

$$z = n_{He} \sigma_{CCS} \overline{v_{He}} \qquad \text{(Eq. 6.3)}$$

Note, that the same result can be obtained if one assumes that ions are fixed spheres, while He atoms collide with their surface as with the vessel walls, with collision rate $z = n_{He} \overline{v_{He}} S / 4$, where $S = 4 \pi r_1^2$ is the area of the ion surface.

The mean velocity of the He buffer gas at a given temperature of the trap, T_{tr}, is calculated as follows:

$$\overline{v_{He}(T_{tr})} = \sqrt{\frac{8RT_{tr}}{\pi M_{He}}} = \sqrt{\frac{8 \cdot 8.31}{3.14 \cdot 4 \cdot 10^{-3}}} \sqrt{T_{tr}} = 72.75 \sqrt{T_{tr}} \text{ m/s}, \qquad \text{(Eq. 6.4)}$$

where R is the universal gas constant and M_{He} is the molar mass of helium. (At the temperature of the trap T_{tr} = 6 K, equation 6.4 gives $\overline{v_{He}(6\,K)}$ = 178 m/s.) The ion-atom collision rate at the given He buffer gas concentration n_{He}, trap temperature T_{tr}, and a collisional cross section of an ion σ_{CCS}, can be calculated numerically as follows:

$$z = 7.28 \cdot 10^{-13} \cdot \sqrt{T_{tr}} n_{He} \sigma_{CCS} \text{ s}^{-1} \qquad \text{(Eq. 6.5)}$$

where collisional cross section σ_{CCS} is measured in Å^2 and He buffer gas concentration, n_{He}, is measured in cm^{-3}. For the temperature of the cold ion trap in our setup, T_{tr} = 6 K, equation 6.5 can be reduced to:

$$z = 1.78 \cdot 10^{-12} \cdot n_{He} \sigma_{CCS} \text{ s}^{-1} \qquad \text{(Eq. 6.6)}$$

160

In each machine cycle He buffer gas is injected into the trap during the short pulse and is being pumped out into the surrounding chamber. Hence, concentration of the buffer gas and collision rate change during the cycle. Therefore, for further analysis one needs to find time-dependence of He buffer gas concentration in the octupole ion trap, $n_{He}(t)$. Section 6.2.2 provides numerical estimation of the number of He atoms injected in the trap in each cycle, while section 6.2.3 describes the dynamics of He flow out of the trap into the surrounding chamber.

6.2.2. Number of Helium Atoms Injected in the Trap per Cycle

Method 1. Pumping Speed-based Estimation

He buffer gas is injected into the cold ion trap ($V_{trap} = 34.2 \; cm^3$) through a pulsed valve at the repetition rate $\nu = 20$ Hz. Let N_0 be the number of He atoms injected in the trap in each cycle. He gas is pumped out from the trap into the surrounding vacuum chamber ($V_{ch} \approx 1.5 \cdot 10^4 \; cm^3$) pumped by the Turbo drag Pump TMU 521 (Pfeiffer), with pumping speed $S_p = 520$ l/s for He gas, therefore the helium concentration decreases exponentially with time constant τ_{out}. Collisions of He atoms with the vacuum chamber walls heat them to room temperature after several collisions. Average pressure in the chamber during the operation in $\nu = 20$ Hz cycle equals to $\bar{p} = 3.9 \cdot 10^{-5}$ mbar. During the operation, He concentration reaches quasi equilibrium, and the number of molecules injected in the trap is equal to the number of molecules pumped away for each cycle, thus:

$$N_0 = \frac{S_p \frac{1}{\nu}\bar{p}}{k_B T_{room}} = \frac{520 \cdot 10^{-3} \cdot 3.9 \cdot 10^{-3}}{20 \cdot 1.38 \cdot 10^{-23} \cdot 300} = 2.4 \cdot 10^{16} \qquad \text{(Eq. 6.7)}$$

For a more precise estimation one must also take into account the neighbouring chambers, where the pressure also increases due to He injection (see section 2.1.3). The second quadrupole mass filter is pumped by TurboDrag Pump TMU 261 (Pfeiffer), with pumping speed for He $S_{Q2} = 250$ l/s, $\bar{p}_{Q2} = 9.2 \cdot 10^{-6}$ mbar; the octupole ion guide and the interface for Orbitrap are both pumped by TurboDrag Pump TMU 071P (Pfeiffer), with pumping speed for He $S_{OIG} = S_{IF} = 50$ l/s, the typical pressures are $\bar{p}_{OIG} = 4.8 \cdot 10^{-5}$ mbar and $\bar{p}_{IF} = 3.9 \cdot 10^{-6}$ mbar, respectively. This correction changes the result by approximately 11%:

$$N_0 = \frac{520 \cdot 10^{-3} \cdot 3.9 \cdot 10^{-3} + 250 \cdot 10^{-3} \cdot 9.2 \cdot 10^{-4} + 50 \cdot 10^{-3} \cdot 4.8 \cdot 10^{-3} + 50 \cdot 10^{-3} \cdot 3.9 \cdot 10^{-4}}{20 \cdot 1.38 \cdot 10^{-23} \cdot 300} \approx 3.1 \cdot 10^{16} \quad \text{(Eq. 6.8)}$$

Method 2. Direct Estimation.

Another way to determine N_0 is a direct measurement of the gas flow from the valve. In this experiment we create initial pressure $p_i = 4$ bar in the 8.5 m long pipe with an inner diameter of 4.0 mm, connecting He reservoir with the valve. The volume of the pipe is $V_{pipe} \approx 110$ cm^3. At the normal operating conditions the pressure reduces by $\Delta p = 0.5$ bar in about 40 minutes. We, thus, can estimate N_0 from the following equation:

$$N_0 t \nu = \frac{\Delta p V_{pipe}}{k_B T} = \frac{0.5 \cdot 10^5 \cdot 110 \cdot 10^{-6}}{1.38 \cdot 10^{-23} \cdot 300 \cdot 46 \cdot 60 \cdot 20} = 2.8 \cdot 10^{16} \qquad \text{(Eq. 6.9)}$$

All estimations give approximately the same result. We will thus assume $N_0 = 3 \cdot 10^{16}$ in the following analysis.

6.2.3. Helium Flow Dynamics

Theoretical Estimation of the Characteristic Flow Times for He

He atoms escape the cold ion trap through two electrostatic lenses with inner diameter $d = 6.8$ mm and length $l = 8$ mm. Once injected into the trap the number of buffer gas atoms should decrease exponentially[20] with a characteristic time τ_{out}:

$$N_{He}(t) = N_0 \cdot e^{-\frac{t}{\tau_{out}}} \qquad \text{(Eq. 6.10)}$$

The characteristic time, τ_{out}, is determined as the ratio of the vessel volume and conductance of the tubes, Q:

$$\tau_{out} = \frac{V_{tr}}{Q} \qquad \text{(Eq. 6.11)}$$

The conductance through a short tube, Q, depends on the gas flow regime, which, in turn, depends on the relative value of the mean free path and the characteristic size of the orifices. The minimum mean free path of He, λ_{He}^{min}, is at the highest He concentration, n_{He}^{max}, that is, immediately after the injection:

$$n_{He}^{max} = N_0/V_{tr} = 3 \cdot 10^{16}/34.2 = 8.8 \cdot 10^{14} \text{ cm}^{-3}, \qquad \text{(Eq. 6.12)}$$

$$\lambda_{He}^{min} = 1/\sqrt{2} n_{He}^{max} 4\pi r_{He}^{2} = 3.3 \text{ mm}, \qquad \text{(Eq. 6.13)}$$

where $r_{He} = 1.4$ Å is the Van-der-Waals radius of He atom. The Knudsen number is $K_n = \lambda_{He}^{min}/d \approx 0.5$, which corresponds to the Molecular Flow Regime. Therefore, the conductance for the short tube, Q_{tube} is[21]:

$$Q_{tube} = \alpha \cdot Q_{orifice} \qquad \text{(Eq. 6.14)}$$

where α is the transmission probability ($\alpha \approx 0.4$ for a tube with $l/d \approx 2$ [21]) and $Q_{orifice}$ is the conductance of the orifice:

$$Q_{orifice} = \frac{s\bar{v}}{4} \qquad \text{(Eq. 6.15)}$$

where s is the area of the orifice and $\bar{v}$ is a mean velocity of He atoms at $T_{tr} = 6$ K. Therefore, the characteristic escape time through the two end caps, τ_{out}, is:

$$\tau_{out}^{theor} = \alpha \frac{4V}{s\bar{v}} = 0.4 \frac{4 \cdot 34.2 \cdot 10^{-6}}{2 \cdot 3.14 \cdot 0.0034^2 \cdot 178.2} = 4.23 \text{ ms} \qquad \text{(Eq. 6.16)}$$

This estimation has to be verified experimentally. The following subsection describes the method for evaluating the characteristic escape times in our setup.

Experimental Measurement of Characteristic Times of He Flow from the Trap

He flow out of the trap increases the pressure in the chamber, and is then pumped away by a turbomolecular pump. The time-dependence of the pressure in the vacuum chamber, surrounding the trap, can be measured directly. In order to determine the time constant τ_{out} this time-dependence at different temperatures of the trap was measured with He gas being injected at 1 Hz frequency (figure 6.1).
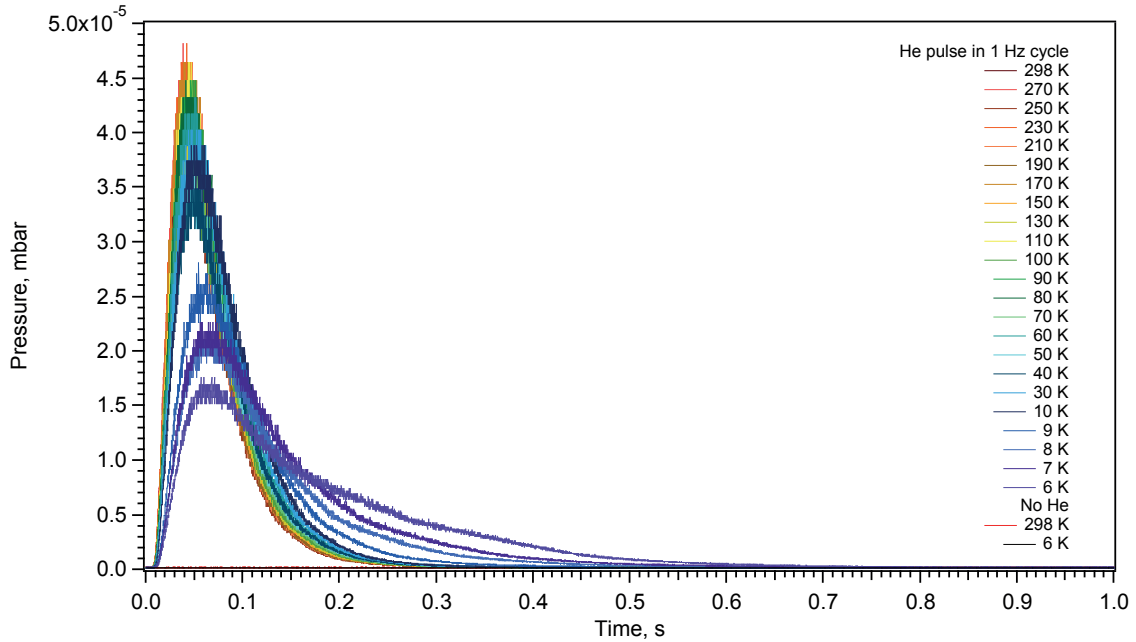

Figure 6.1. *Time-dependence of the He buffer gas pressure in the surrounding chamber, measured in 1 Hz cycle.*

The rapid rise of the pressure in the beginning of each cycle corresponds to the relatively fast He escape from the trap, while the following decrease is determined by the pumping speed of the turbomolecular pump. The rising edge of the curves at high temperature is limited by 9 ms resolution of the pressure gauge. The theoretical pumping rate is defined by the following formula:

$$k_{pump} = \frac{S}{V} = \frac{510 \cdot 10^{-3}}{1.5 \cdot 10^{-2}} = 34 \text{ s}^{-1} \qquad \text{(Eq. 6.17)}$$

where S is the pumping speed and V is the volume of the chamber. Thus the characteristic time for the pumping process is:

$$\tau_{pump}^{theor} = \frac{1}{k_{pump}} = 29.4 \text{ ms} \qquad \text{(Eq. 6.18)}$$

For the times $t \ll \tau_{pump}$ one can neglect the number of atoms pumped away by the pump, and assume that the number of He atoms in the chamber increases by the number of He atoms, that have left the trap:

$$N_{ch}(t) = N_0 - N_{tr}(t) = N_0 \left(1 - e^{-\frac{t}{\tau_{out}}} \right) \qquad \text{(Eq. 6.19)}$$

Thus, while $t \ll \tau_{out}$, the concentration of He atoms in the chamber increases linearly:

$$\Delta n_{ch}(t) \approx \frac{N_0}{V_{ch}} \frac{t}{\tau_{out}} \qquad \text{(Eq. 6.20)}$$

The pressure in the chamber can thus be approximated by the following linear expression:

$$p_{ch}(t) \approx p_{res} + \Delta n_{ch}(t) k_B T = p_{res} + \frac{N_0 k_B T}{V_{ch} \tau_{out}} t \qquad \text{(Eq. 6.21)}$$

where p_{res} is a residual pressure in the chamber. τ_{out} can now be calculated as:

$$\tau_{out}^{exp} = \frac{N_0 k_B T}{V_{ch} B} \qquad \text{(Eq. 6.22)}$$

where B is the coefficient of the linear function, fitting the initial parts of pressure dependencies. Figure 6.2 shows the resulting linear fits with a functions of the $y = A + Bx$ type.

The pressure of the He buffer gas depends on the duration of the valve opening, which is determined by the length of the corresponding electrical pulse, applied to it. The measurements of the pressure in the chamber were performed with 150 μs long pulse, while the experiments with collisional cooling were performed with 145 μs long pulse. The shorter valve opening results in a 4-fold decrease of the pressure in the chamber. On the other hand, the pressure gauge is calibrated for N_2 gas, therefore the actual pressure for He corresponds to the measured pressure, multiplied by a factor of 5.9.
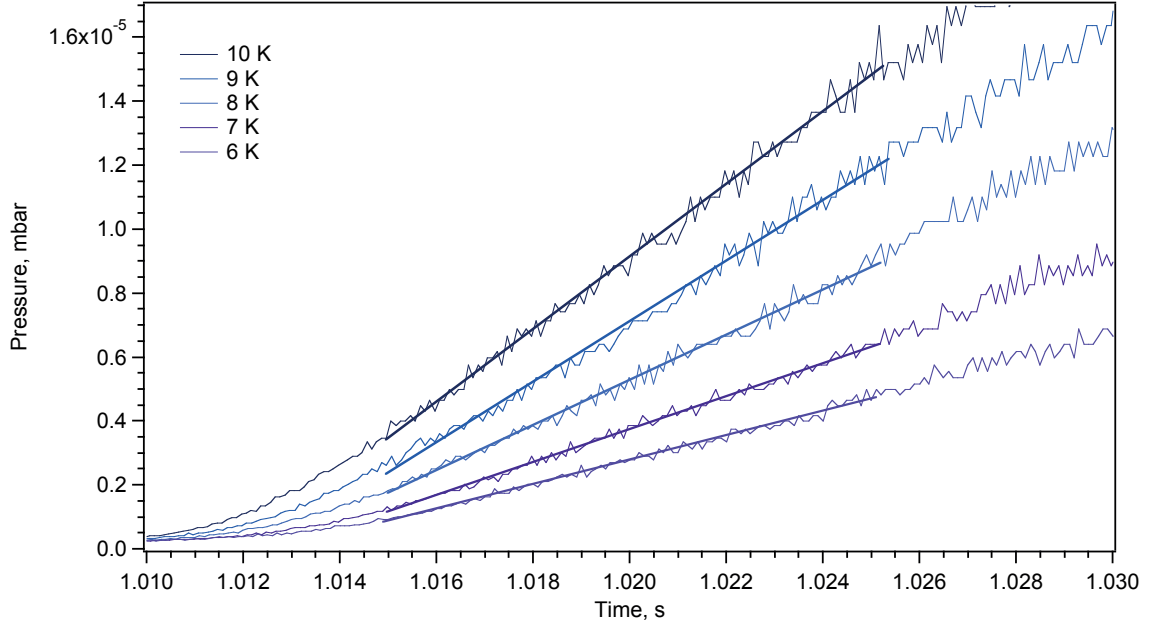
Figure 6.2. *Linear fits of pressure time-dependencies (the data shown only includes pressure measured at small tempretures).*

After applying these corrections, the B coefficient for He gas at 6 K is $B_{He}(6\,K) = 0.16 \pm 0.004$ Pa/s. Substituting this value into Eq. 6.22 one can find an experimental characteristic time for He atoms exiting the trap:

$$\tau_{out}^{exp}(6K) = \frac{N_0 k_B T}{V_{ch} B_{He}} = \frac{2.7 \cdot 10^{16} \cdot 1.38 \cdot 10^{-23} \cdot 300}{1.5 \cdot 10^{-2} \cdot 0.16} = 46.6 \text{ ms} \qquad \text{(Eq. 6.23)}$$

This experimental result differs from the theoretical prediction ($\tau_{out}^{theor} = 4.23$ ms, Eq. 6.16) by an order of magnitude. Furthermore, the time constant for the pumping process, derived from approximating the tail of the pressure dependence with the exponential decay, is $\tau_{pump}^{exp}(6\,K) = 153.5$ ms, which is 5 times higher, compared to the theoretical estimation ($\tau_{pump}^{theor} = 29.4$ ms, Eq. 6.18). These discrepancies, though, vanish at room temperature: the observed values $\tau_{out}^{exp}(298\,K) = 9.3$ ms and $\tau_{pump}^{exp}(298\,K) = 36.0$ ms are close to theoretical estimations! The origin of these effects should stem from the low temperatures. Next section provides a likely explanation.

6.3.4. Helium Freezing

In order to find the reason of the abovementioned discrepancies between theoretical and experimental estimations of the characteristic escape times of He gas from the trap and the vacuum chamber, the temperature dependencies of the experimental characteristic escape time τ_{out} and pumping time τ_{pump} were investigated in more details. Figure 6.3 shows the $\tau_{out}^{exp}(T)$ and $\tau_{pump}^{exp}(T)$ functions in temperature intervals 298-6 K.
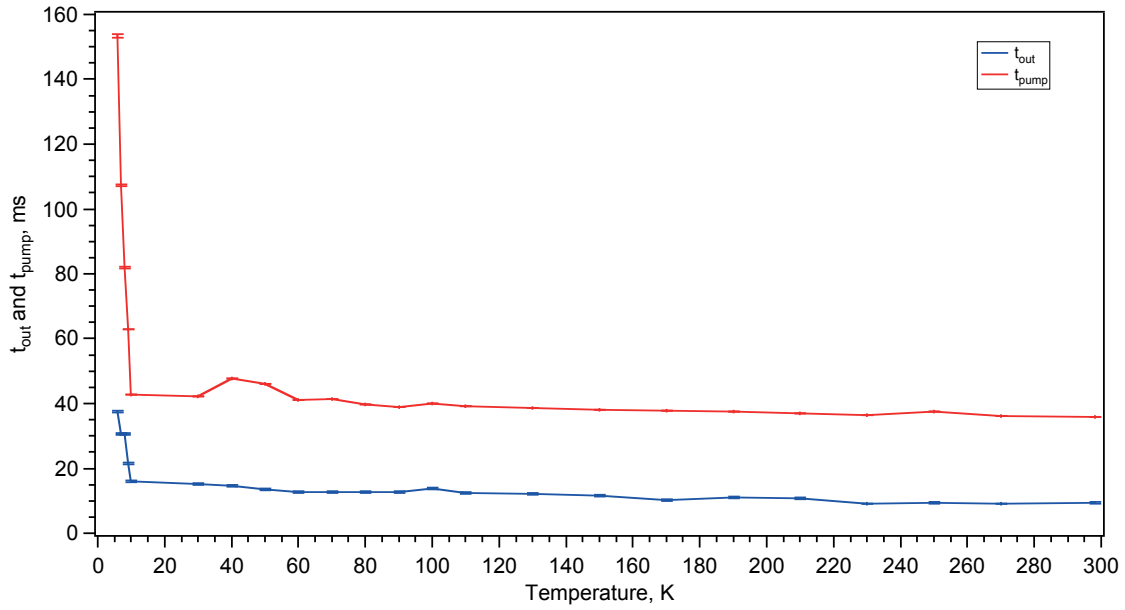

Figure 6.3. *Temperature dependence of $\tau_{out}^{exp}(T)$ and $\tau_{pump}^{exp}(T)$, obtained from the experimental measurement of the pressure in the chamber.*

These temperature dependencies clearly indicate that below 10 K the characteristic times begin to increase, which suggests the occurrence of the temperature dependent phenomenon. Indeed, at temperatures below 10 K He atoms adsorb on the walls of the cold trap.[22] Figure 6.4 schematically shows the He gas flow between number of ions, frozen at the walls, N_W, stored in the trap, N_{tr}, and atoms that left the trap N_{ch}.
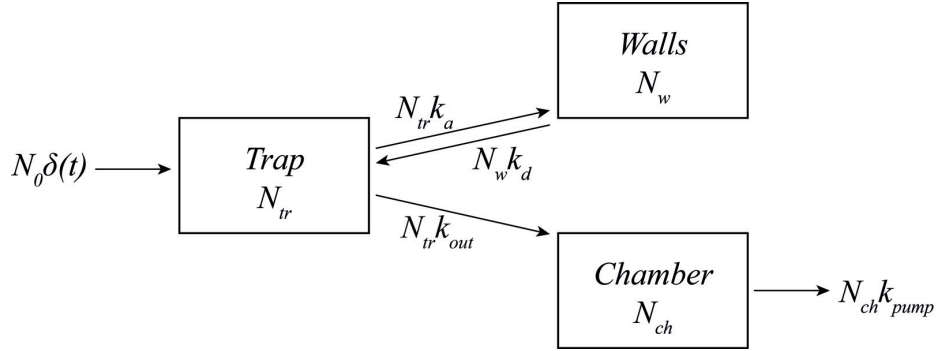
Figure 6.4. *Schematic representation of the He flow between the trap volume, trap walls, and the vacuum chamber.*

The gas flow, depicted schematically in figure 6.4, can be described quantitatively by a system of differential equations:

$$\begin{cases} \frac{dN_{tr}}{dt} = N_0\delta(t) - N_{tr}k_a - N_{tr}k_{out} + N_w k_d \\ \frac{dN_w}{dt} = N_{tr}k_a - N_w k_d \\ \frac{dN_{ch}}{dt} = N_{tr}k_{out} - N_{ch}k_{pump} \end{cases} \quad \text{(Eq. 6.24)}$$

Obviously, the number of He atoms injected in the trap is equal to the number of atoms that escape the trap, and the number of atoms pumped away by the pumps. One, thus, can assume that the number of He atoms in the trap does not change during the cycle:

$$\int_0^T \frac{dN_{tr}}{dt} dt = 0 \quad \text{(Eq. 6.25)}$$

Substituting the first equation from the Eq. 6.24 into Eq. 6.25 gives:

$$\int_0^T (N_0\delta(t) - N_{tr}k_a - N_{tr}k_{out} + N_w k_d)\, dt = 0 \quad \text{(Eq. 6.26)}$$

$$\int_0^T N_{tr}k_a dt - \int_0^T N_w k_d\, dt + \int_0^T N_{tr}k_{out}\, dt = N_0 \quad \text{(Eq. 6.27)}$$

The sum of the first two terms in the Eq. 6.27 is the difference between atoms adsorbed and desorbed from the trap walls in each cycle, and is 0 in quasiequilibrium. Furthermore, provided that the pressure in the chamber does not change much during the cycle, we assume the same condition holds true for the pressure in the trap. Thus, $N_{tr} = \overline{n_{tr}}V_{tr} = const$, and

$$\overline{n_{tr}} = \frac{N_0}{V_{tr}k_{out}T} \quad \frac{3\cdot10^{16}\cdot46.6}{34.2\cdot50} = 8.2\cdot10^{14} \text{ cm}^{-3} \quad \text{(Eq. 6.28)}$$

where T is the duration of the cycle.

The verification of the assumption regarding the constant concentration of He atoms in the trap needs justification. Obviously, it is impossible to find exact solutions for these equations without knowing k_a and k_d. Instead, we will use some typical values to find the time-dependences of N_w, N_{tr}, and N_{ch}. The system reaches quasi-equilibrium, i.e., the number of He atom on the walls, in the trap volume, and in the camber do not change during the cycle:

$$\begin{cases} N_w(t = 0\ ms) = N_w(t = 50\ ms) \\ N_{tr}(t = 0\ ms) = N_{tr}(t = 50\ ms) \\ N_{ch}(t = 0\ ms) = N_{ch}(t = 50\ ms) \end{cases} \qquad \text{(Eq. 6.29)}$$

Figure 6.5 shows the solutions of the system of equations Eq. 6.24 with the boundary conditions from Eq. 6.29 and some typical values k_a and k_d, that can be calculated for each trap geometry.[22] Here, however, the plots are used only to demonstrate the He flow dynamics in each cycle. The slow desorption of He atoms from the walls of the trap (blue curve) supports the constant pressure in the trap (black curve) for almost full duration of the cycle, which supports the assumption that was used to calculate the average concentration of the He gas (Eq. 6.28).

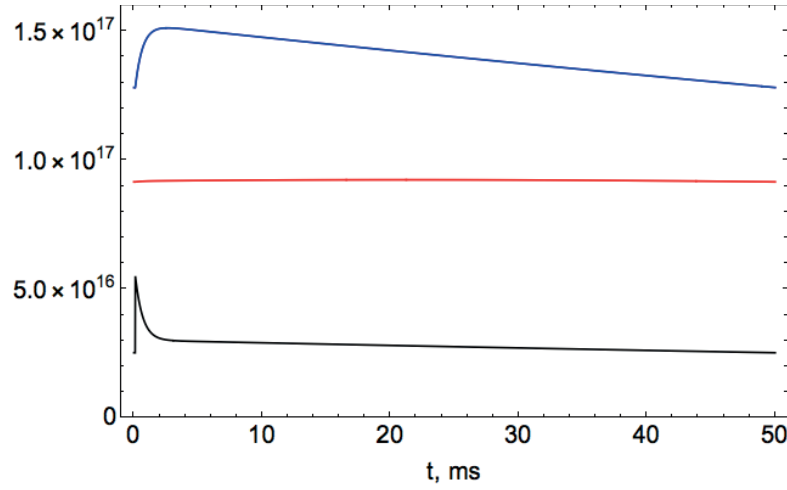**Figure 6.5.** *Time-dependencies of the $N_{tr}(t)$ (black), $N_w(t)$ (blue), and $N_{ch}(t)$ (red).*

6.2.6. Collisional Cross Section of [GS+2H]$^{2+}$

As was shown above, the collision rate of ions with the buffer gas (Eq. 6.6) depends on the concentration of the buffer gas (see Section 6.2.5) and the collision cross section of the ion. The latter will be discussed below.

Langewin Model

The standard model to estimate collision rates of ions with neutral atoms or molecules is the Langevin or capture model.[23-25] This model assumes that a collision occurs with 100% probability when the two collision partners approach each other closer than a critical distance. The Langevin cross section in a simplified picture can be calculated as follows:

$$\sigma_L = \frac{|q|}{2\epsilon_0}\sqrt{\frac{\alpha}{\mu v^2}}, \tag{Eq. 6.30}$$

where α is the polarizability for neutral, μ is the reduced mass, v is the relative velocity, q is the charge of the ion, and ϵ_0 is the electric constant. In our case one can safely assume $\mu = m_{He}$ and $v = \overline{v_{He}}$ (see Section 6.2.1). Furthermore, $|q| = 2|e|$ for doubly protonated gramicidin S and $\alpha_{He} = 2.28 \cdot 10^{-41}$ F·m^2.[26] Therefore,

$$\sigma_L = \frac{|e|}{\epsilon_0 \overline{v_{He}}}\sqrt{\frac{\alpha}{m_{He}}} = \frac{1.6\cdot10^{-19}}{8.85\cdot10^{-12}\cdot178}\sqrt{\frac{2.28\cdot10^{-41}}{6.65\cdot10^{-27}}} = 595\ \text{Å}^2 \tag{Eq. 6.31}$$

The model, however, is applicable for small ions. For a biomolecular ion, as large as gramicidin S, in which the two protons are localized and surrounded my other atoms, such approximation is not valid. On the other hand, calculating a geometrical CCS from the known structure of the ion would underestimate the real cross section, as it does not take into account the charge-dipole interaction. Hence, experimental values have to be used instead.

Experimental Value of the Collisional Cross Section for Gramicidin S

Collisional cross section of singly charged cyclic Gramicidin S in nitrogen buffer gas was taken from literature[27] and is equal to $263\ \text{Å}^2$. For doubly charged Gramicidin S a Coulombic repulsion of the two protons should lead to a more extended geometry. Furthermore, at low temperatures interaction of charges with buffer gas are more efficient. These factors lead to the increase of the CCS. We will thus assume that the CCS of the [GS+2H]$^{2+}$ is $300\ \text{Å}^2$.

6.2.7. Average Time Between Ion-Atom Collisions

Taking into account all of the abovementioned estimations, namely the average concentration of the He gas in the trap (Eq. 6.28) and the collisional cross section of the [GS+2H]$^{2+}$ and substituting it into Eq. 6.6 gives

$$dt_{GS} = \frac{1}{z} = \frac{5.17\cdot10^{17}}{300\cdot8.2\cdot10^{14}} = 2.1\ \mu s \tag{Eq. 6.32}$$

Now that the time between two consecutive collisions is known, one needs to find the total energy, that is taken away from the ion, and exact time, required for such deactivation.

6.3. Experimental Section

In the following section the experimental results will be described. The aim of the experiment was to determine the average time that is required for a deactivation of the known amount of energy from an ion.

6.3.1. Description of the Experiment

General Description of the Experiment

Collisional cooling in our tandem mass spectrometer is arranged as follows. The cold ion trap is mounted on a cold head of a two-stage, closed-cycle refrigerator (RDK-408, Sumitomo). Helium buffer gas at room temperature is pulsed into the trap and cools down to the trap temperature ($T_{tr} = 6$ K) after a few collisions with the trap walls. Ion packet is released from the hexapole trap shortly after the helium injection, so that ions enter the trap when the buffer gas concentration reaches maximum level, which ensures the highest trapping efficiency.

Collisions with neutral buffer gas molecules remove the translational and internal energy of ions until they reach thermal equilibrium with He gas at $T_{He} = 6$ K. The internal energy of ions prior to the collisional cooling depends on many parameters, such as the potential difference between the hexapole and cold ion traps, ion density, RF voltages, etc. The correct estimation of the cooling rate, however, requires that the ions are initially prepared in a well-defined energetic state. One obvious way to do so is to cool the ions down to cryogenic temperature and then excite them with an IR photon of a known energy. The following collisional energy dissipation would bring the ions back to the thermal equilibrium with buffer gas, and the intermediate states of ions can be monitored after varying time delays with respect to the IR pre-excitation (figure 6.6). In this case both the initial and final values of the internal energy of ions can be known precisely.

In our experiments, we study the cooling dynamics of a doubly protonated gramicidin S, [GS+2H]$^{2+}$. The electronic and vibrational spectroscopy of this decapeptide has been studied in details,[28] which allowed unambiguous assignment of its structures in the gas phase.[29, 30] Precise spectroscopic fingerprint allow to derive several metrics to monitor the cooling dynamics.

Figure 6.6. *The schematic model of the experiment, designed to investigate the ion vibrational energy dissipation in collisions with the buffer gas molecules.*

Numerical Parameters for the Cooling Rate Estimation

The UV spectra of biomolecular ions are broad at room temperature, but, if taken at lower temperatures, the resolved transitions appear and the thermal broadening decreases.[31, 32] Cooling to typical temperatures of 10 K in cold ion traps confines ions in their ground vibrational state and removes line broadening, which drastically simplifies electronic and vibrational spectra of biomolecular ions.

The UV spectra can be used for precise measurement of the vibrational temperature of ions close to zero by comparing the intensities of the $(0\leftarrow1)$ and $(1\leftarrow0)$ transitions[33, 34] (the hot band and the first vibrational transition). However, the concept of temperature can only be applied to an ensemble in thermal equilibrium, which is not the case for ions during collisional cooling. This is further confirmed by the lack of thermal broadening of the band origin in our experiments (see Section 6.3.6). Thus, other parameters are required to evaluate cooling process.

The main principle of vibrational cold ion spectroscopy is based on the changes in the UV photofragmentation spectra of cold ions induced by absorption of an IR photon prior to the electronic excitation.[35] Absorption of an IR photon is followed by fast vibrational energy redistribution among all vibrational modes of the ion (IVR), which modifies electronic spectrum as follows. Inhomogeneous broadening of the pre-heated ions results in the unstructured background in the electronic spectra of pre-heated ions, while depopulation of the ground vibrational state causes intensity drop of sharp electronic transitions from this state (so-called "depletion"). If the internal heating does not cause population transfer between conformers during the energy dissipation process, the electronic spectrum fully recovers after the thermal equilibrium is restored between the ions and the buffer gas.

Thus, the vibrational energy dissipation can be extracted from the dynamic changes of electronic spectra. The number of ions with excess vibrational energy as a function of time-delay

between IR pump and UV probe lasers is proportional to the average intensity of the background signal in the UV spectra. This metrics, though, has an important disadvantage – the low intensity of the background signal results in a low signal-to-noise ratio.

Intensity of the band origin, proportional to the population of ions in the ground electronic and vibrational state, on the other hand, can be measured more precisely. Given that the linewidth of this transition does not change during the cooling process (see Section 6.3.6 and Figure 6.11), one can measure either the intensity or the area under the peak (sum of all counts).

In the following sections the different numerical parameters that potentially can be used for evaluating the cooling dynamics, as well as thermal broadening of the transitions (namely, the lack one in our experiments) will be discussed and compared.

Timing of the Experiments

The initial cooling experiment was designed as follows. Each cycle starts with a He pulse. After a short time delay, Δt_{He}, needed for He to reach its maximum pressure, the hexapole trap opens for Δt_{hex}, and the ions are released towards the cold trap. These two times must be as small as possible, because in the long ion packet spatially separated ions would interact with helium for significantly different times on the 1-10 ms timescale.

The optimal time delay between the He pulse and the hexapole trap opening was chosen to be $\Delta t_{He} = 500$ μs. This value was determined from the trapping efficiency. The ions were released from the hexapole trap after different time delays with respect to the He pulse. At each time delay the resulting ion signal was measured. In order to trap the ions they have to loose some energy in collisions with the buffer gas. Thus, the resulting signal depends on the concentration of He gas in cold trap. Minimum Δt_{He} was chosen to correspond to the maximum ion signal.

The duration of the hexapole opening affects the number of ions, entering the trap, since they are not released immediately. For further experiments Δt_{hex} was chosen to be 500 μs.

In the initial cooling experiments the UV spectra were measured as a function of a time delay Δt_{in} with respect to the hexapole trap closure (1 ms after the He pulse) to identify the minimum time required to cool ions to $T_{tr} = 6$ K.

In the second set of experiments IR laser pulse excites ions after a time delay Δt_{IR}, which is enough to ensure ion energy equilibration with the buffer gas. UV spectra of the IR-pre-heated ions were then measured after several time delays $\Delta t_{cooling}$ with respect to the IR pulse.

6.3.2. Initial Cooling of Ions to Cryogenic Temperature

Experimental Measurement of the Initial Cooling Time

Figure 6.7 shows UV photofragmentation spectra of $[GS+2H]^{2+}$, recorded after several time delays Δt_{in} with respect to the hexapole trap closure in the range 37500-37860 cm^{-1} with wavenumber step 0.2 cm^{-1}. Each data point was averaged over 10 measurements. UV laser pulse energy was 3 mJ. The fragmentation signal was normalized on the parent ion signal and UV power.
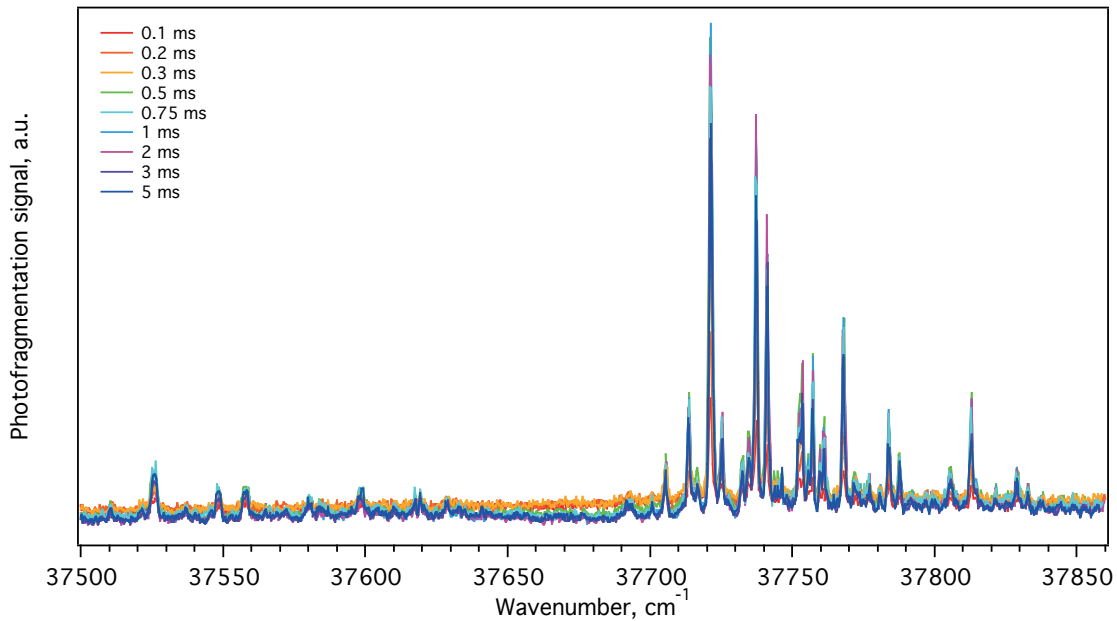

Figure 6.7. *UV photofragmentation spectra of $[GS+2H]^{2+}$, recorded after several time delays with respect to Hex trap closure (1 ms after the He pulse).*

Figure 6.8 shows the comparison of several parameters that can potentially be used for evaluating the cooling dynamics: an average background signal between 37650 and 37680 cm^{-1} (red trace), intensity of the band origin, calculated as the sum of counts between 37719 and 37723 cm^{-1} minus the background (blue trace), and the ratio of these two values (black trace) at different time delays Δt_{in}. All parameters were normalized to reach maximum value of unity. Figure 6.4 indicates that the major part of the molecules is cooled to $T_{tr} = 6$ K within 1 ms, and after 2 ms practically all molecules are internally cold. In the further experiments the time for the initial cooling was chosen to be $\Delta t_{in} = 5$ ms in order to avoid any unambiguity in the initial energetic state of the ion ensemble. Thus we ensure that all of the ions are internally cold.
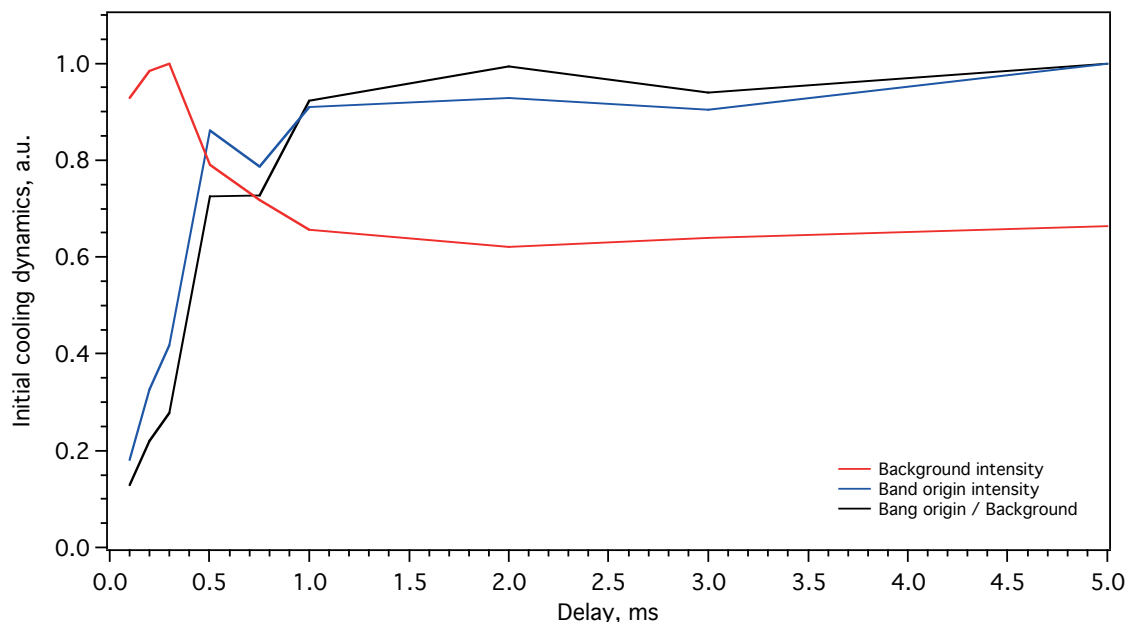
173

Figure 6.8. *Intensities of the background (red curve), band origin (blue curve), and their ratio (black curve), normalized to 1, as a function of the time delay between the hexapole trap closure and the probing UV pulse.*

6.3.6. IR Energy Dissipation

IR Laser Pulse Fired $\Delta t_{cooling}$ ***= 5 ms After the Hexapole Trap Closure***

In the previous section it was shown that after the time delay Δt_{in} = 5 ms with respect to the hexapole trap closure all ions are in thermal equilibrium with the buffer gas. In the following section we describe the cooling dynamics of the ion ensemble, preheated with an IR laser pulse fired after Δt_{in}.

Since our experiments aim to establish the vibrational energy deactivation rate, we excite $[GS+2H]^{2+}$ ions with IR laser beam of 1 mJ energy per pulse, wavelength corresponding to the vibration of conformer **A**, 3341.7 cm^{-1}. We then measure UV spectra of the pre-heated ion ensemble after several time delays $\Delta t_{cooling}$ with respect to the IR pulse. Each data point was averaged over 20 measurements, dye laser scanning step was 0.1 cm^{-1}. Figure 6.9 shows the resulting electronic spectra of $[GS+2H]^{2+}$.
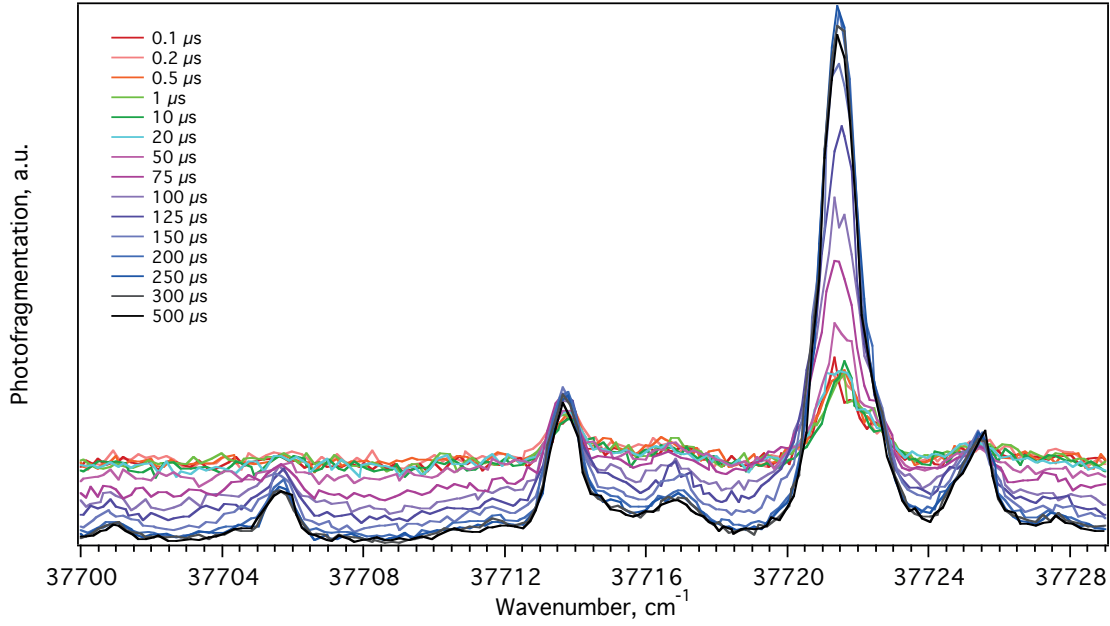
Figure 6.9. *UV photofragmentation spectra of [GS+2H]$^{2+}$ recorded after several time delays $\Delta t_{cooling}$ with respect to the IR laser pulse, fired 5 ms after hexapole trap closure.*

In order to find the intensity of the band origin more precisely, the peaks at 37721.5 cm^{-1} were approximated with a Gaussian function (eq. 6.33) with the offset y_0, intensity A, median x_0, and standard deviation σ:

$$y = y_0 + Ae^{-\frac{(x-x_0)^2}{2\sigma^2}}$$ (Eq. 6.33)

The resulting fits are shown in figure 6.10. The full width at half of the maximum, (FWHM) equals to FWHM $= 2\sqrt{2\ln 2}\,\sigma$. Figure 6.11 shows the dependence of the FWHM on the cooling time $\Delta t_{cooling}$.

Figure 6.11 shows that the linewidth of the band origin transition does not change during the cooling process. In other words, IR pre-excitation does not cause thermal broadening. The explanation of this phenomenon will be given later (see section 6.4). Since the linewidth of the Gaussian peaks does not change, we can use either the intensities obtained from the fits, or the ones measured directly from the experiment, or even the area under the peak (calculated as the sum of counts between 37719 and 37723 cm^{-1} minus the background) to quantify the cooling dynamics. Figure 6.12 shows the comparison of these parameters, plotted for all $\Delta t_{cooling}$. All the curves

were normalized to reach the maximum value of unity. Both the slope and the point of saturation are very similar in all cases.
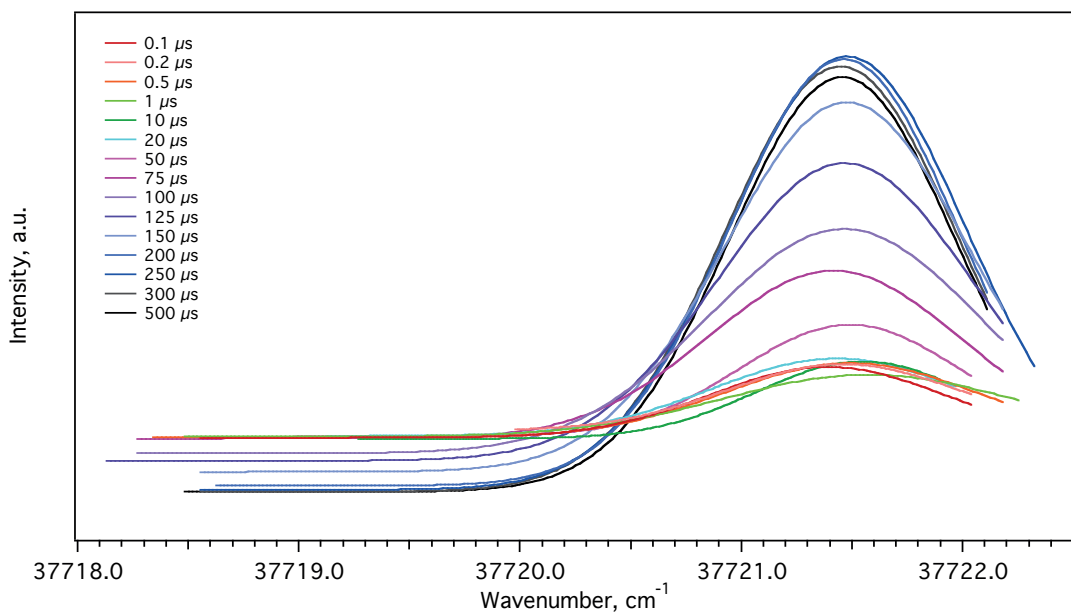
Figure 6.10. *Gaussian fits of the band origin transitions of [GS+2H]$^{2+}$ conformer **A**. IR laser pulse fired 5 ms after hexapole trap closure.*
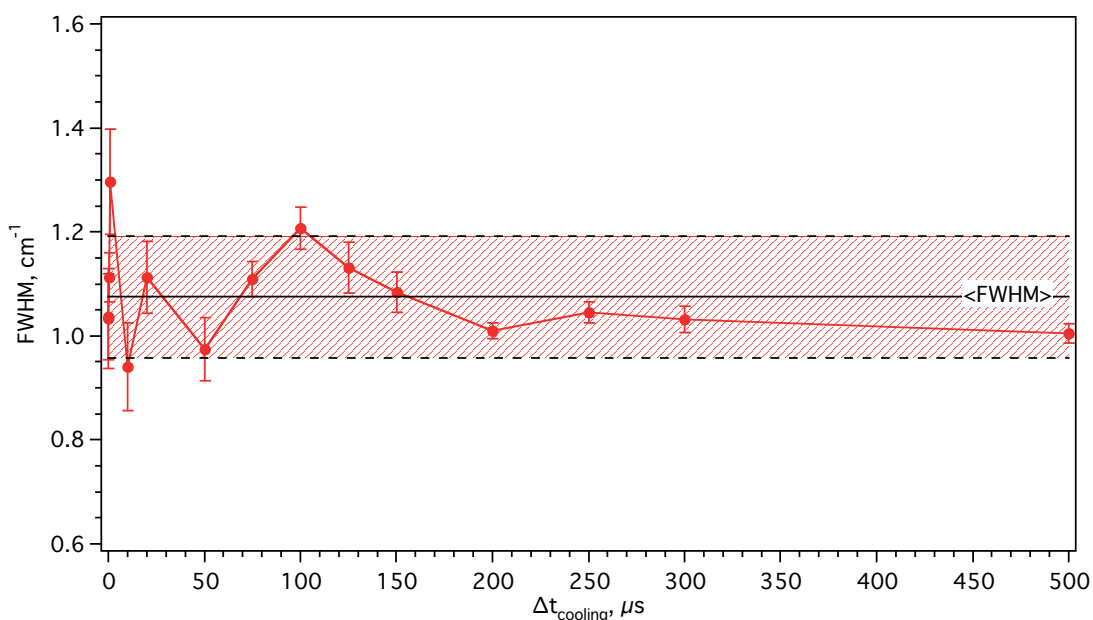

Figure 6.11. *FWHM of the band origin peak of [GS+2H]$^{2+}$ conformer **A**. IR laser pulse fired 5 ms after hexapole trap closure. Solid black line corresponds to the average value of FWHM and dashed area covers range from $\overline{FWHM} - \Delta FWHM$ to $\overline{FWHM} + \Delta FWHM$.*
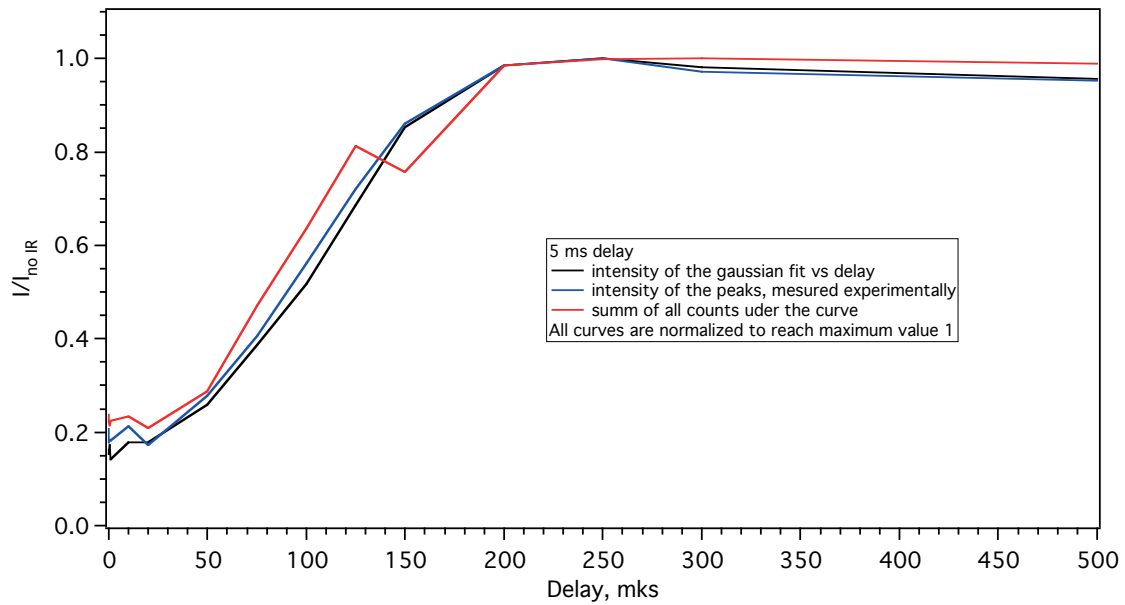
Figure 6.12. *Comparison of the cooling dynamics obtained via different methods.*

Given that the numerical fits allow for an estimation of the errors, the intensities of the Gaussian fits of the band origins were chosen as the most convenient parameter for the evaluation of the cooling dynamics. Figure 6.13 shows this metrics together with the errors.
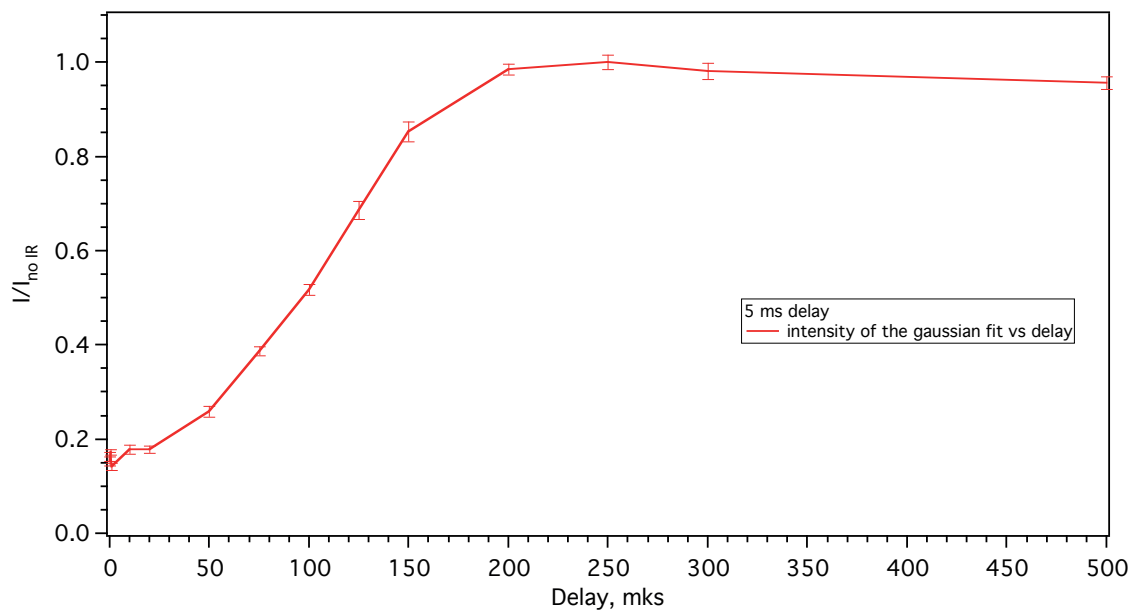

Figure 6.13. *Intensity of the Gaussian fits of the GS band origin taken 5 ms after Hex trap closure.*

6.3.7. Mixing of Cold and IR Pre-heated Ions in the Trap

All of the abovementioned numerical parameters give approximately the same estimations of the cooling time. These data are already enough to make rough estimations of the buffer gas cooling efficiency. However, for a more detailed analysis the comparison of the experimentally obtained curves with theoretical modeling is required.

The intensity of the band origin transition depends on the concentration of the ions that have been cooled to the equilibrium temperature and thus is the most convenient parameter for such comparison. However, $[GS+2H]^{2+}$ ions in an inhomogeneous RF field constantly move, and cold ions can penetrate the volume that is probed by a UV pulse. This factor can affect the slope of the cooling dynamics curve and the ion diffusion rate has to be taken into account separately. Indeed, figure 6.13 shows that the increase of the fraction of cold ions starts almost immediately after the IR pre-excitation. This means that a considerable amount of ions can lose about 3400 cm^{-1} of their internal energy in several collisions, which seems unrealistic.

In order to estimate the mixing rate of ions in the trap for further computer modeling, the following experiment was designed. The machine was switched to 1 Hz cycle repetition rate, in which all He gas is pumped away in every cycle. The spectroscopy of $[GS+2H]^{2+}$ was performed near the end of each cycle. Since the collisional cooling efficiency was significantly decreased, the observed increase of the band origin intensity has to be accounted only by ion mixing. The results are shown in figure 6.14.
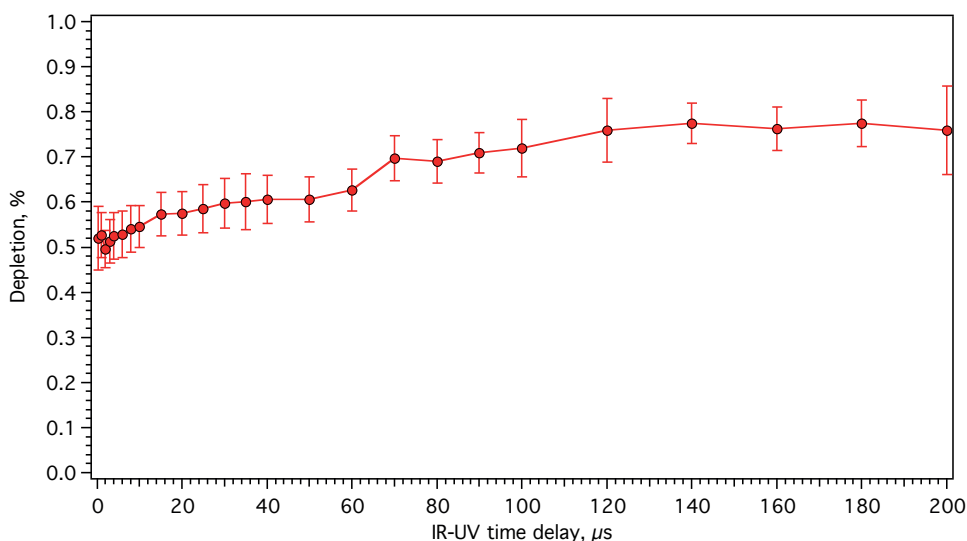

Figure 6.14. *The fraction of the cold ions in the volume probed by UV laser as a function of time delay between IR pre-excitation and UV pulse fired in 1 Hz machine cycle.*

This data suggest that the relative concentration of IR pre-heated ions decreases approximately twice during 200 μs due to the ion motion. This fraction is replaced by cold ions that have not been excited, which accounts for cooling dynamics at short time-delays.

6.3.8. Energy Transfer per Collision

Employing Monte-Carlo simulations or solving the Fokker-Planch equation can numerically model the slope of the curve shown in figure 6.13. However, the data in figure 6.13 can give a rough estimation of the average energy taken away from He atoms in each collision. The ions almost cold after 200 μs which corresponds to approximately 100 collisions.

One can assume several possible functions, describing the time-dependence of the average energy of ions during collisional cooling.

1. Linear model

Herein we assume that the average energy, transferred from a hot ion to the He buffer gas does not depend on the internal energy of ion.[13] Each ion loses the internal energy, equal to the IR photon energy, or 3400 cm^{-1} after 100 collisions. Thus an average energy per collision is $\sim$34 cm^{-1}. This model can make sense if one takes into account that the vibrational energy on an ion is distributed among high number of modes, therefore an average energy per mode in [GS+2H]$^{2+}$ is small, and the mode quantum numbers are not high.

Furthermore, the initial cooling of ions at room temperature ($\sim$19,000 cm^{-1} [35]) is dissipated during 2 ms or $\sim$1000 collisions. Given the fact that the ions can reach internal temperatures up to 500 K in our ion source, an average energy per collision remains of the same order of magnitude.

2. Power law model

Another scenario is when an energy taken per collision is proportional to the internal energy.[16, 36] In other words, each He atoms takes away a fixed portion of the total ion energy, α. The ion energy after N collisions is, therefore, defined as:

$$E_N = E_0(1 - \alpha)^N. \tag{Eq. 6.34}$$

Thus, α can be found as:

$$\alpha = 1 - \sqrt[N]{E_N/E_0}. \tag{Eq. 6.35}$$

179

After $N = 100$ collisions the average internal energy of $[GS+2H]^{2+}$ at $T = 15$ K can be calculated based on the known vibrational frequencies (Eq. 3.2) and is approximately $E_N = 20$ cm^{-1}. The initial internal energy is essentially the internal energy of cold $[GS+2H]^{2+}$ and the energy of the IR photon: $E_N \approx 3400$ cm^{-1}. Therefore,

$$\alpha \approx 1 - \sqrt[100]{20/3400} = 5\%. \tag{Eq. 6.36}$$

Extrapolated to the internal energies at room temperature, an average energy transferred after the first collision after entering the trap would be $\Delta E_1 = 900$ cm^{-1}. Such a high value is rather unrealistic.

No firm conclusion regarding the exact energy transfer mechanism can be done until detailed theoretical modeling is compared with experiment, because it is exactly the slope of the curve in figure 6.13, that depends on the evolution of the ion internal energy probability distribution function.

6.4. Statistical Energy Deactivation Models

The rough estimations, made above, allow assessment of an average energy, transferred per collision. However, collisional deactivation is a statistical process, in which a probability for energy E before collision to become E' after one, is $P(E', E)$. The Monte-Carlo simulations allow comparing the resulting cooling dynamics with the one measured experimentally (figure 6.13).

In 1982 Troe has derived a formalism, which describes collisional deactivation sequence of highly excited polyatomic molecules.[13] According to his derivation, the collisional transition probability, $P(E', E)$, is determined by:

$$P(E', E) = \frac{k(E', E)}{Z(E)} \tag{Eq. 6.37}$$

where

$$Z(E) = \int_0^\infty k(E', E) dE' \tag{Eq. 6.38}$$

is the total energy transfer collision frequency, and $k(E', E)$ is a collisional transition rate coefficient. The average energy transferred in all up and down transitions, $\langle \Delta E(E) \rangle$, can be calculated as follows:

$$\langle \Delta E(E) \rangle = \int_0^\infty (E' - E) P(E', E) dE' \tag{Eq. 6.39}$$

Provided that ion-ion collision rate is negligible compared to of ion-neutral and since He atoms are cold the possibility of the activating transitions can be neglected. The average energy, transferred per collision is thus given by:

$$\langle \Delta E(E)\rangle = \int_0^E (E' - E)P(E',E)dE' \qquad \text{(Eq. 6.40)}$$

In the experiments, described above, biomolecular ions were initially prepared in a well-defined initial stated.   If the exact form of $k(E',E)$ one could easily model the statistical deactivation process.   Several simple models for the transition rate coefficients $k(E',E)$ are considered herein.

Transition Rate Coefficients

Troe studied two energy transfer models for highly excited toluene: (i) exponential down model (Eq. 6.41) and (ii) Poisson type down model (Eq. 6.42) with energy independent parameters α.[13]

$$k(E',E) \propto exp\left(-\frac{E-E'}{\alpha}\right) for \ 0 \le E' \le E \qquad \text{(Eq. 6.41)}$$

$$k(E',E) \propto \left(\frac{E-E'}{\alpha}\right)exp\left(-\frac{E-E'}{\alpha}\right) \ for \ 0 \le E' \le E \qquad \text{(Eq. 6.42)}$$

Model (i) stands for situations where energy transfer probabilities are peaked at $E' = E$, model (ii) characterizes energy transfer probabilities peaked at $E' < E$. The parameter α was varied between values around 100 cm^{-1} and values near to 1000 cm^{-1}.   Higher α values correspond to strong collisions where the average energy transferred in up transitions is much smaller than that for down transitions. The smaller α value represents weak collisions where up transitions are not much less efficient than down transitions.

Subsequently substituting Eq. 6.41 and 6.42 together with Eqs. 6.37 and 6.38 into Eq. 6.40 and performing simple integration (NOTE: since we neglect activating collisions, integration is made from 0 to E), one arrives to the following dependencies for the average energy transferred in down collisions $\langle \Delta E(E)\rangle$ on the internal energy E for the two models:

$$\langle \Delta E(E)\rangle = -\alpha\left(1 - \frac{\frac{E}{\alpha}}{e^{\frac{E}{\alpha}}-1}\right) \qquad \text{(Eq. 6.43)}$$

$$\langle \Delta E(E)\rangle = -\alpha\left(2 - \frac{\left(\frac{E}{\alpha}\right)^2}{e^{\frac{E}{\alpha}}-\frac{E}{\alpha}-1}\right) \qquad \text{(Eq. 6.44)}$$

Both models predict very similar linear energy decrease for the region where $E \geq 2\alpha$: $\langle \Delta E(E) \rangle = -\alpha$ and $\langle \Delta E(E) \rangle = -2\alpha$ for exponential and Poisson type models, respectively. These results, compared with simple estimates in the previous section suggest that α is ~30-40 and 15-20 cm^{-1} for the two models, respectively, which corresponds to extremely weak collisions.

In addition to these energy independent deactivation models, energy-dependent models were also considered, in which α was a linear, exponential, etc. function of the internal energy. In the previous section it was determined, that IR-preheated ion ensemble fully relaxes back to the ground state after approximately 100 collisions on average. Therefore, a simple calculation can give a good estimate of parameter α for any model, so that it meets the cooling time criterion.

These statistical models suggest that initial energy distribution function, following excitation, turns into the Gaussian one after several collisions. While the average value decreases, the width of the distribution increases until is reaches the final thermal distribution.[13]

Of course, the described energy transfer models are representative for a broad field of possible cases at energies in the vibrational quasicontinuum[37, 38] they are not applicable for discrete energies, where very specific types of $k(E', E)$ will dominate.[39-41] They, however, are beyond the scope of the present work, which is to find a simple expression that quantitatively describes the cooling dynamics.

The Lack of Thermal Broadening.

So far the model, that would describe the observed cooling dynamics, has not been found. Yet in all models, tried so far, the general trend is observed: the energy distribution function during the cooling process becomes much broader, compared to Boltzmann distribution at typical internal temperature of $T = 12$ K. The thermal broadening of the UV transitions, observed previously at slightly elevated temperatures of the trap,[35] results from ions at thermal equilibrium, while the collisional cooling is a non-equilibrium process. Therefore, the relative population of ions with internal energies higher than an average value at equilibrium is much lower compared to the relative population of thermally equilibrated ions at $T = 12$ K, which contribute to the intensity of the band origin transition.

6.5. Conclusions

The main goal of this study was the assessment of the cooling speed of ions in cold ion trap. Numerous evidences suggest that the presence of several populated conformers of an ion is a result

of a non-adiabatic cooling; therefore, the energy deactivation rate competes with isomerization speed.

In order to obtain numerical estimates of a typical energy that is taken away from the molecule per collision the experiment was designed where ion ensemble was initially cooled to cryogenic temperatures, than it was excited with IR photons of a known energy, and a cooling dynamics was monitored in terms of restoration of the electronic spectrum. This experiment allowed to estimate the time required to deactivate a typical energy of ~ 3400 cm^{-1} to be approximately 200 μs.

The collision rate of ions with buffer gas atoms was also estimated. First the number of buffer gas atoms that were injected in the cold ion trap in each cycle was determined by two different methods with a high precision. Next, the He flow dynamics from the trap was assessed. At the conditions of the experiment the He concentration was assumed to be almost constant during the 20 Hz cycle because of He freezing on the trap walls and slowly desorbing during the cycle. Finally, the average time between collisions was calculated to be ~2 μs.

Therefore the average energy of ~3400 cm^{-1} is extracted from the ions in approximately 100 collision events. Several simplest models were assessed. The average energy decrease per collision is ~30-40 cm^{-1}/col. in power model He atom was estimated to deactivate 5% of the vibrational energy. These rough estimates are useful in practice. The currently ongoing Monte-Carlo simulations will allow for a more precise assessment of the possible energy transfer models. The cooling dynamics curves allow comparison of the simulation with a highly precise experiment.

References

1. L. Voronina, A. Masson, M. Z. Kamrath, F. Schubert, D. Clemmer, C. Baldauf and T. R. Rizzo, *J. Am. Chem. Soc.*, 2016, **138**, 9224-9233.
2. G. K. Drayna, C. Hallas, K. Wang, S. R. Domingos, S. Eibenberger, J. M. Doyle and D. Patterson, *Angew. Chem. Int. Ed.*, 2016, **55**, 4957-4961.
3. B. C. Dian, G. M. Florio, J. R. Clarkson, A. Longarte and T. S. Zwier, *J. Chem. Phys.*, 2004, **120**, 9033-9046.
4. D. Gerlich, 1994.
5. D. Gerlich, *Phys. Scr.*, 1995, **T59**, 256-263.
6. D. Newnham, J. Ballard and M. Page, *Rev. Sci. Instrum.*, 1995, **66**, 4476-4481.
7. N. Bohr, *Philosophical Magazine Series 6*, 1913, **25**, 10-31.
8. T. Covey and D. J. Douglas, *J. Am. Soc. Mass. Spectrom.*, 1993, **4**, 616-623.

9.   L. Landau and E. Teller, *Phys. Zeitschr. Sow.*, 1936, **10**, 34-43.

10.   R. N. Schwartz, Z. I. Slawsky and K. F. Herzfeld, *J. Chem. Phys.*, 1952, **20**, 1591.

11.   E. E. Nikitin and J. Troe, *Phys. Chem. Chem. Phys.*, 2008, **10**, 1483-1501.

12.   J. Yamashita, H. Goto, K. Fujihara, A. Hara, H. Kohguchi and K. Yamasaki, *Chem. Phys. Lett.*, 2016, **657**, 95-101.

13.   J. Troe, *J. Chem. Phys.*, 1982, **77**, 3485-3492.

14.   R. C. Bhattacharjee and W. Forst, *Chem. Phys. Lett.*, 1978, **30**, 217-241.

15.   W. Forst and R. C. Bhattacharjee, *Chem. Phys.*, 1979, **37**, 343-353.

16.   A. T. Barfknecht and J. I. Brauman, *J. Chem. Phys.*, 1986, **84**, 3870-3881.

17.   H. Hippler, J. Troe and H. J. Wendelken, *J. Chem. Phys.*, 1983, **78**, 6709-6717.

18.   M. S. Ahmed and R. C. Dunbar, *J. Am. Chem. Soc.*, 1987, **109**, 3215-3219.

19.   D. V. Sivukhin, *Thermodynamics and Molecular Physics*, PHYSMATLIT, Moscow, 5th edn., 2005.

20.   M. Vargas, S. Naris, D. Valougeorgis, S. Pantazis and K. Jousten, *Vacuum*, 2014, **109**, 385-396.

21.   R. G. Livesey, in *Foundations of Vacuum Science and Technology*, 1998.

22.   E. Wallén, *J. Vac. Sci. Technol., A*, 1997, **15**, 265-274.

23.   G. Gioumousis and D. P. Stevenson, *J. Chem. Phys.*, 1957, **29**, 294-299.

24.   R. Wester, *J. Phys. B: At., Mol. Opt. Phys.*, 2009, **42**, 154001.

25.   J. Turulski and J. Niedzielski, *Int. J. Mass Spectrom. Ion Processes*, 1994, **139**, 155-162.

26.   M. A. Thomas and J. W. Humberston, *J. Phys. B: At. Mol. Phys.*, 1972, **5**, L229.

27.   B. T. Ruotolo, C. C. Tate and D. H. Russell, *J. Am. Soc. Mass. Spectrom.*, 2004, **15**, 870-878.

28.   N. S. Nagornova, T. R. Rizzo and O. V. Boyarkin, *J. Am. Chem. Soc.*, 2010, **132**, 4040-+.

29.   N. S. Nagornova, M. Guglielmi, M. Doemer, I. Tavernelli, U. Rothlisberger, T. R. Rizzo and O. V. Boyarkin, *Angew. Chem. Int. Ed.*, 2011, **50**, 5383-5386.

30.   T. K. Roy, V. Kopysov, N. S. Nagornova, T. R. Rizzo, O. V. Boyarkin and R. B. Gerber, *ChemPhysChem*, 2015, **16**, 1374-1378.

31.   O. V. Boyarkin, S. R. Mercier, A. Kamariotis and T. R. Rizzo, *J. Am. Chem. Soc.*, 2006, **128**, 2816-2817.

32.   N. L. Burke, J. G. Redwine, J. C. Dean, S. a. McLuckey and T. S. Zwier, *Int. J. Mass spectrom.*, 2015, **378**, 196-205.

33.   O. V. Boyarkin and V. Kopysov, *Rev. Sci. Instrum.*, 2014, **85**, 033105.

34.   A. Y. Pereverzev and O. V. Boyarkin, *Phys. Chem. Chem. Phys.*, 2017, **19**, 3468-3472.

35.   N. S. Nagornova, T. R. Rizzo and O. V. Boyarkin, *Angew. Chem. Int. Ed.*, 2013, **52**, 6002-6005.

36.   G. A. Zalesskaya, D. L. Yakovlev, E. G. Sambor and D. V. Prikhodchenko, *Opt. Spectrosc.*, 2001, **90**, 526-533.

37.   D. C. Tardy and B. S. Rabinovitch, *Chem. Rev.*, 1977, **77**, 369-408.

38.   M. Quack and J. Troe, *Int. Rev. Phys. Chem.*, 1981, **1**, 97-147.

39.   R. S. Sheorey and G. Flynn, *J. Chem. Phys.*, 1980, **72**, 1175-1186.

40.   B. L. Earl, L. A. Gamms and A. M. Ronn, *Acc. Chem. Res.*, 1978, **11**, 183-190.

41.   R. V. Serauskas and E. W. Schlag, *J. Chem. Phys.*, 1965, **43**, 898-902.

Chapter 7

Outlook and Conclusions

Various methods to study structures of biological molecules and ions were described in the Introduction chapter in a historic context. Cold Ion Spectroscopy – the main objective of the present work – is an extremely powerful technique in terms of amount of information it is able to provide about the studied species. However, it is only applicable in a very small number of specific cases, at least compared to X-ray crystallography and NMR techniques. The main purpose of this work was two-fold: showing that the biological relevance of spectroscopic studies in the gas phase spans much further than simply providing benchmark spectroscopic data for validation of theoretical calculations, and expanding the applicability of Cold Ion Spectroscopy to a wider range of peptides.

Several evidence was collected, showing that after electrospray ionization process biomolecular ions adopt energetically the most favorable conformations in the gas phase, determined by their intramolecular interactions. All possible structures are, likely, in thermal equilibrium at typical temperatures of $300 - 600$ K, but only a few lowest energy structures can be significantly populated at these conditions. This ensemble of gas-phase conformations, when injected in the cold octupole ion trap, is rapidly cooled via collisions with He buffer gas. The presence of several conformers under the cooling conditions of the experiment suggests that collisional internal energy deactivation of ions is a rapid, non-adiabatic process.

The cooling speed in our octupole ion trap was estimated by designing an experiment, in which ion ensemble was initially prepared in a well-defined energetic state, subjected to the controlled excitation, and the cooling dynamics was monitored using high-resolution spectroscopic UV probe. The cooling dynamics accounts for the origin of the multiple gas-phase conformers observed in experiments. However, even the fast cooling of an ion ensemble down to cryogenic temperatures does not guarantee the possibility to obtain conformer-specific signatures for structural analysis.

One of the most crucial limitations of the Cold Ion Spectroscopy is a lack of vibrational resolution in electronic spectra of many ions, which precludes the use of an IR-UV "depletion" technique. In this work a novel IR-IR-UV hole-burning technique was developed. It has many important advantages. First of all, it is essentially a gain, rather than depletion, technique. Therefore, the signal-to-noise ratio is significantly improved. Furthermore, it is applicable to any peptide, even the ones with broad, unresolved electronic spectra where depletion is precluded. The power of the IR-IR-UV hole-burning spectroscopy was demonstrated by providing conformer-specific vibrational spectra of individual conformers of the protonated aromatic amino acids tryptophan and histidine. These spectra together with high-level quantum chemical calculations allowed for a structural assignment of these ions.

Nevertheless, since the gas-phase spectroscopy is, essentially, an "action" technique, the conceptual limitation of Cold Ion Spectroscopy – the necessity to contain at least one aromatic amino acid in the sequence in order to absorb a UV light for further photofragmentation – remained strong. Another important achievement in this work is a clear demonstration that a peptide bond can be used as a natural chromophore, present in almost any peptide! The UV photofragmentation spectra (down to 192 nm) as well as all-conformer vibrational gain spectra were recorded for several model and natural peptides. The parameters that affect the quality of the vibrational gain spectra were explored and a specific procedure was developed, that allows to determine automatically the settings at which the experimental signal-to-noise ratio is the highest. Furthermore, it was demonstrated that it is possible to obtain even the conformer-selective spectra of peptides that do not contain any aromatic amino acid.

The advances in experimental techniques allowed studying structural preferences of many biomolecular ions. An improved understanding of the origin of the structures in the gas phase, namely, non-adiabatic cooling and lack of kinetic trapping, allowed to reconsider one of the most important questions in gas-phase structural studies – what is the relation between the intrinsic structures and biologically active geometries *in vivo*?

It was hypothesized that since the intrinsic structures in the absence of the solvent are determined solely by the intramolecular interactions, they may be a good reflection of the 3D structures of peptides that are active only in the hydrophobic environments such as receptor pockets, cell membranes, etc. It was previously stated that FRET experiments in the gas-phase correlate with physiological activity of opioid peptide drugs, while the X-ray crystallography does not. Hence, the structures of these peptides in vacuum might be similar to the native ones. It was not until the IR-IR-UV hole-burning spectroscopy became a routine spectroscopic tool, that the

conformer-specific vibrational signatures of individual conformers of these peptides were obtained. It was demonstrated in this work that the lowest energy gas-phase structures of stereoisomers of an opioid drug (namely, the distances between chromophores) correlate with the differences in the physiological activity of these peptides *in vivo*.

Therefore, the main output of this thesis is the evidence, that intrinsic structures of peptides that are biologically active in hydrophobic environments may resemble native-like geometries. The novel technique developed in this work, IR-IR-(D)UV hole-burning spectroscopy, allows now studying such peptides even if they do not contain aromatic residues.

ALEKSANDR PEREVERZEV

Rue de Pontarlier 1
1337 Vallorbe
+41 78 843 4864
aleksandr.pereverzev@epfl.ch

Born: 26.07.1988 in Tbilisi (Georgia)
Citizenship: Georgian

Key competences: UV and IR multi-laser spectroscopies,
Scanning confocal microscopy, Mass spectrometry,

RESEARCH AND EDUCATION

09.2013 – PRESENT   **ECOLE POLYTECHNIQUE FÉDÉRALE DE LAUSANNE
(EPFL) – LAUSANNE, SWITZERLAND**
PhD in Physical Chemistry (expected in 08.2017)

- Developed IR-IR-UV Hole-Burning spectroscopic approach for conformer-selective vibrational spectroscopy of gas-phase biomolecular ions
- Developed IR-VUV spectroscopy approach based on peptide-bond electronic excitation for double-resonance spectroscopy of peptides without chromophores
- Experimental investigation and numerical modelling (Mathematica) of the buffer gas collisional cooling in the ion trap
- Senior Teaching Assistant in General Physics courses
- Co-authored 2 published articles (4 are currently being prepared)

09. 2009 – 06-2013   **LEBEDEV PHYSICAL INSTITUTE OF THE RUSSIAN
ACADEMY OF SCIENCES – MOSCOW, RUSSIA**
Research Assistant

- Won the 1st prize in the Scientific Research Competition in 2012
- Developed correlational analysis method to study blinking luminescence of quantum dots based on photon emission times of individual photons recorded with MT 200 confocal microscope (PicoQuant)
- Photoluminescence kinetics of thin crystalline films
- Co-authored 3 publications

09.2005 – 06.2012   **MOSCOW INSTITUTE OF PHYSICS AND TECHNOLOGY
(STATE UNIVERSITY) (MIPT) – MOSCOW, RUSSIA**
M.S. in Quantum Radiophysics
B.S. in General and Applied Physics

- Tuition fees 100% financed from academic scholarship
- GPA 4.8 / 5 at the Master level

09.2003 – 06.2005   **GEORGIAN LYCEUM OF SCIENCE AND TECHNOLOGY –
TBILISI, GEORGIA**
Graduate

- GPA 4.9 / 5
- Bronze Medal at International Physics Olympiad in 2005, Spain
- Numerous prizes at Georgian State Olympiads in mathematics and physics

LIST OF PUBLICATIONS

2017

- A.Y. Pereverzev, V.N. Kopysov and O.V. Boyarkin. "High Susceptibility of Histidine to Charge Solvation Revealed by Cold Ion Spectroscopy". *Angewandte Chimie*. Submitted

- A.Y. Pereverzev and O.V. Boyarkin. "Exploring the relevance of gas-phase structures to biology: cold ion spectroscopy of the decapeptide neurokinin A". *Physical Chemistry Chemical Physics Communication*, 2017, 19, 3468-3472.
http://pubs.rsc.org/is/content/articlehtml/2017/cp/c6cp07953a

2016

- A.Y. Perevezev, X. Cheng, N.S. Nagornova, D.L. Reese, R.P. Steele and O.V. Boyarkin. "**Vibrational Signatures of Conformer-Specific Intramolecular Interactions in Protonated Tryptophan**". *The Journal of Physical Chemistry A*, 2016, **120**, 5598-5608.
http://pubs.acs.org/doi/abs/10.1021/acs.jpca.6b05605

2014

- V.A. Postnikov, Y.I. Odarchenko, A.V. Iovlev, V.V. Bruevich, A.Y. Pereverzev, L.G. Kudryashova, V.V. Sobornov, L. Vidal, D. Chernyshov, Y.N. Luponosov, O.V. Borshchev, N.M. Surin, S.A. Ponomarenko, D.A. Ivanov and D.Yu. Paraschuk. "**Molecularly Smooth Single-Crystalline Films of Thiophene-Phenylene Co-Oligomers at the Gas-Liquid Interface**". *Crystal Growth and Design*, 2014, **14**, 1726-1737.
http://pubs.acs.org/doi/abs/10.1021/cg401876a

2012

- A.G. Vitukhnovskii, A.Yu. Pereverzev, V.V. Fedyanin, S.A. Ambrozevich, R.B. Vasiliev and D.N. Dirin. "**Correlation between Photon-Emission Intervals in Blinking Luminescence of Single CdSe/CdS Nanocrystals**". *Letters to Journal of Experimental and Theoretical Physics*, 2012, **96**, 1, 17-20.
http://link.springer.com/article/10.1134%2FS0021364012130139?LI=true

- A.Yu. Pereverzev, A.V. Iovlev, N.S. Vlasova, Yu.N. Luponosov, A.V. Bogdanov, V.A. Postnikov, S.A. Ponomarenko and D.Yu.Parashchuk. "**The Photoluminescence Kinetics of Oligothiophene-Phenylenesilane Crystalline Films**". *Moscow University Physics Bulletin*, **67**, 4, 409-411.
http://link.springer.com/article/10.3103%2FS002713491204011X?LI=true

SKILLS

- Language skills:
  English – fluent; Russian and Georgian – native; French – B1/B2; German – A1;

- Computer skills:
  Programming on Mathematica, Python; data analysis with different software: IGOR, Origin, Excell;

- Excellent public speaking skills

VOLUNTEERING AND EXTRACURRICULAR ACTIVITIES

- Volunteered at the International Physics Olympiad 2016 in Zurich as a member of the Academic Committee